University of Kent

Kent Academic Repository

Eastwood, Tara Ann (2019) *An investigation into the effect of N-terminal acetylation upon the human neuronal protein, alpha Synuclein, and influence of NatH on actin function in C. elegans*. Doctor of Philosophy (PhD) thesis, University of Kent,.

Downloaded from

https://kar.kent.ac.uk/76622/ The University of Kent's Academic Repository KAR

The version of record is available from

This document version

Author's Accepted Manuscript

DOI for this version

Licence for this version

UNSPECIFIED

Additional information

Versions of research works

Versions of Record

If this version is the version of record, it is the same as the published version available on the publisher's web site. Cite as the published version.

Author Accepted Manuscripts

If this document is identified as the Author Accepted Manuscript it is the version after peer review but before type setting, copy editing or publisher branding. Cite as Surname, Initial. (Year) 'Title of article'. To be published in ***Title of Journal*** , Volume and issue numbers [peer-reviewed accepted version]. Available at: DOI or URL (Accessed: date).

Enquiries

If you have questions about this document contact ResearchSupport@kent.ac.uk. Please include the URL of the record in KAR. If you believe that your, or a third party's rights have been compromised through this document please see our Take Down policy (available from https://www.kent.ac.uk/guides/kar-the-kent-academic-repository#policies).

An investigation into the effect of N-terminal acetylation upon the human neuronal protein, alpha Synuclein, and influence of NatH on actin function in C. elegans.

A thesis submitted to the University of Kent for the degree of PhD in the Faculty of Science, Technology and Medical Studies

2019

Tara Ann Eastwood

School of Biosciences



DECLARATION

No part of this thesis has been submitted in support of an application for any degree or qualification of the University of Kent or any other University or Institute of learning.

_____

Tara Ann Eastwood

Date:

ACKNOWLEDGMENTS

I would like to thank Dr Dan Mulvihill for all of his support and guidance throughout this project. I would also like to thank all the members of the Mulvihill lab for their help and support. I would also like to thank Dr Jennifer Tullet and the members of her lab for their help with investigations using C. elegans, and Prof. Stan Botchway and the staff at the Central Laser Facility, Harwell for their help with FLIM and SIM, imaging and analysis.

Lastly I would like to thank my family for all their help and support during my studies.

TABLE OF CONTENTS

Declaration I

Acknowledgments II

Table of Contents III

List of Figures VIII

List of Tables XVIII

List of Films XVIII

List of Abbreviations XIX

Abstract XXII

Chapter 1: Introduction

1.1	Cellular regulation.	1
1.2	Post translational modifications.	1
1.3	Acetylation.	2
1.4	Amino Terminal acetylation (Nt-acetylation).	3
1.5	Acetylation and Disease.	5
1.6	N-terminal acetyltransferases (NATs).	7
1.6.1	NatA	8
1.6.2	NatB	9
1.6.3	NatC	9
1.6.4	NatD	10
1.6.5	NatE	10
1.6.6	NatF	10
1.6.7	NatG	10
1.6.8	NatH	10
1.7	Co-translational and Post-translational Nt-acetylation.	12
1.8	Limitations with in vivo Nt-acetylation research.	12
1.9	NatH/NAA80 substrate specificity.	13
1.10	Phenotype of HAP1 cells with NAA80 knockout.	14
1.11	The effect of NAA80 knockout in HAP1 cells on actin turnover and cell motility	15
1.12	Actin isoforms.	16
1.13	Caenorhabditis elegans as a model organism.	19
1.14	*E. coli* as an *in vivo* test tube.	20

1.15	Alpha Synuclein (aS).	20
1.15.1	Post translational modifications of aS.	23
1.15.2	Proposed functions of aS.	24
1.15.3	aS association with Parkinson's Disease (PD).	25
1.15.4	Nt-acetylation of aS.	27
1.16	Tyrosine kinase inhibitors.	29
1.17	Bacterial Membranes.	30
1.18	Bacterial membrane vesicles.	32
1.19	Microscopy techniques.	34
1.19.1	Live cell imaging	34
1.19.2	Widefield microscopy	34
1.19.3	Spinning Disk microscopy	34
1.19.4	Structured Illumination Microscopy (SIM)	35
1.19.5	Super-Resolution Radial Fluctuations (SRRF)	36
1.19.6	Deconvolution	36
1.20	Forster Resonance Energy Transfer (FRET) and Fluorescence Lifetime Imaging (FLIM).	36
1.21	Biomolecular Fluorescence Complementation (BiFC).	37
1.22	Optogenetics.	38
1.23	Aim of this project.	38

Chapter 2: Methods and Materials

2.1	Media and Buffers	39
2.2	Cell Culture Techniques	41
2.2.1	*E. coli* cultures	41
2.2.2	Preparation of competent cells	41
2.2.3	Transformation of Chemically competent E. coli	42
2.2.4	Starter cultures	42
2.2.5	Acquisition of Growth curves	42
2.2.6	Staining live cells with Congo red and NIAD-4	42
2.2.7	Purification of vesicles from cell culture	43
2.3	Protein expression and purification	43
2.3.1	Small scale protein expression for preparation of cell extracts and live cells for imaging	43
2.3.2	Preparation of cell extracts for Coomassie Blue stained SDS-PAGE gel and western blots	43
2.3.3	Precipitation of protein from cell cleared media	44
2.3.4	Large scale expression of protein for purification of aS-Cerulean3-His_6	44
2.3.5	His tag purification of aS-Cerulean3-His_6	44
2.3.6	Purification of aS-Cerulean3-His6 by Fast Protein Liquid Chromatography (FPLC)	45
2.4	Biochemistry Techniques	46
2.4.1	Gel electrophoresis of proteins	46

2.4.2	Western Blot	47
2.4.3	Lipid binding assays using PIP Strips™ Membranes	47
2.4.4	Size Exclusion Chromatography(SEC)	48
2.4.5	Isothermal Titration Calorimetry (ITC)	49
2.4.6	Dynamic Light Scattering (DLS)	50
2.5	Molecular Biology Techniques	51
2.5.1	Plasmid DNA purification	51
2.5.2	Restriction digests of DNA	51
2.5.3	Separation of DNA using Gel electrophoresis	52
2.5.4	Gel purification of DNA fragments	52
2.5.5	Klenow treatment for blunt end ligation	52
2.5.6	Ligation of DNA fragments	53
2.5.7	Polymerase Chain Reaction (PCR)	53
2.5.8	Quantitative PCR	54
2.5.9	CRISPR-Cas9	56
2.5.10	*C. elegans* Genotyping PCR	56
2.6	*C. elegans* Techniques	58
2.6.1	Maintenance of *C. elegans* strains	58
2.6.2	Producing and maintaining male *C. elegans*	58
2.6.3	Back-crossing naa-80 knockout C. elegans into N2H control strain *C. elegans*	59
2.7	*C. elegans* Phenotype assays	61
2.7.1	Brood size assays	61
2.7.2	Age specific fecundity assays	61
2.7.3	Unfertilised eggs assays	61
2.7.4	Larvae length comparison	62
2.7.5	Body bend frequency as a motility assay	62
2.7.6	Embryonic developmental timing comparison	63
2.7.7	Microscopy image comparison	64
2.8	Microscopy techniques	64
2.8.1	Fluorescent proteins used in this investigation	64
2.8.2	Fluorescent amyloid staining dyes used in this investigation	65
2.8.3	Preparation of *E. coli* slides for fluorescent microscopy	66
2.8.4	Preparation of slides for imaging *C. elegans*	67
2.8.5	Preparation of slides for time lapse imaging of *C. elegans*	67
2.8.6	Widefield Microscopy	68
2.8.7	Spinning disk Confocal Microscopy	68
2.8.8	Transmitted Electron Microscopy (TEM) and Immuno EM	68
2.8.9	Measurement of Förster Resonance Energy Transfer (FRET) using Fluorescent Lifetime Imaging (FLIM)	69
2.7.10	Structured Illumination Microscopy (SIM)	69
2.9	Image analysis	70
2.9.1	Fluorescent intensity measurements	70
2.9.2	FLIM analysis of FRET	70
2.9.3	Larvae length measurement	70
2.9.4	Embryo developmental timing measurements	71

2.10	Safety	72
2.11	Strains, Plasmids and Oligonucleotides	72
2.11.1	*E. coli* strains	72
2.11.2	*C. elegans* strains	73
2.11.3	Plasmids used in this study	73
2.11.4	PCR primers for DNA amplification	77
2.11.5	genotype PCR and qPCR primers	77

Chapter 3: The effect of Nt-acetylation on aS oligomerisation

3.	aS Oligomerisation	78
3.1	The impact of Nt-Acetylation on aS conformation and oligomerisation *in vitro*	78
3.2	The use of Förster Resonance Energy Transfer (FRET) in live *E. coli*	84
3.3	Measurement of FRET using Fluorescent Lifetime Imaging (FLIM)	87
3.4	Development of an aS-Venus-Biomolecular Fluorescence Complementation (BiFC) construct to monitor oligomerisation	91
3.4.1	Optimisation of aS induction	95
3.4.2	Optimisation of starting OD_{595}	97
3.4.3	Optimisation of 96 well plates and plate position	99
3.5	Congo Red and NIAD-4 staining of live cells	102
3.6	The use of BiFC to screen for aS-drug interactions	104
3.7	Use of Venus-BiFC as a reporter of Nt-acetylation effects on Cdc8	108
3.8	Discussion	111

Chapter 4: The effect of Nt-acetylation on aS membrane interactions

4.	aS Membrane Interactions	112
4.1	Comparison of Nt-acetylated versus non Nt-acetylated aS localisation using Widefield microscopy and TEM imaging	112
4.2	Comparison of vesicle number and size with varying C-terminal fluorophore	119
4.3	The use of FLIM to examine membrane interactions	121
4.4	The use of Structured Illumination Microscopy (SIM) Super resolution microscopy	127
4.5	The use of recombinant protein enhanced vesicle formation to facilitate large scale protein production	130
4.6	aS induced vesicles and human Growth Hormone (hGH)	132
4.7	Purification of vesicles from cell culture	135
4.8	Targeting of recombinant protein into vesicles	138
4.9	Lipid specific interactions	141
4.10	aS and Microcompartments	143
4.11	Discussion	145

Chapter 5: The effect of *naa-80* knockout in C. elegans

5.	The effect of *naa-80* knockout in C. elegans	146
5.1	Acquisition and conformation of CRISPR/CAS9 deletion strains	146
5.2	Initial assays with knockout strains	147
5.3	Initial assays at 25oC with knockout strains	149
5.4	Production of outcrossed strains	152
5.5	Assays with outcrossed deletion strains	155
5.6.	Optimisation of conditions for Time lapse imaging	160
5.7	Embryo developmental timing	160
5.8	Rapid time lapse imaging to examine actin dynamics in early embryo development	165
5.9	Comparison of images of C. elegans larvae and adult	165
5.10	Discussion	171

Chapter 6: Discussion

6.1	The effect of naa-80 knockout in C. elegans	172
6.2	Contradictory aS research	173
6.3	BiFC development	174
6.4	aS Oligomerisation	174
6.5	aS Membrane interactions	176
6.6	Summary of aS	179
6.7	Future work	180

Bibliography 182

Appendices

List of Figures

Figure 1.1	Nt-acetylation of a protein or peptide is the transfer of an acetyl moiety from Acetyl-CoA to the N-terminal α-amino group catalysed by a NAT.	4
Figure 1.2	Ribosome associated NAT's A to F.	8
Figure 1.3	The structure of Nat A.	9
Figure 1.4	The structure of DmNAA80/CoA-Ac-DDDI-NH2.	11
Figure 1.5	The Nt-acetylome of yeast and humans, showing the N-terminal amino acid sequences Nt-acetylated by NATs A to F.	11
Figure 1.6	The Co-translational and Post-translational Nt-acetylation of actin.	13
Figure 1.7	Actin filament showing exposed actin N-termini with myosin bound in a cleft between two actin subunits.	16
Figure 1.8	Actin monomers, filaments, structures and interacting proteins.	18
Figure 1.9	Tropomyosin binding along an actin filament	18
Figure 1.10	Double helix structure of alpha-Synuclein bound to lipid vesicles.	21
Figure 1.11	A proposed aS double anchor mechanism.	22
Figure 1.12	Post-translational modifications of aS including Nt-acetylation, phosphorylation, ubiquitination, nitration and truncations.	23
Figure 1.13	Cellular membranes, targets and pathways, potentially involved in the normal, physiological functions of alpha-Synuclein.	25
Figure 1.14	Six SNCA point mutations linked to familial PD and dementia with Lewy bodies.	26
Figure 1.15	Model for a compact aS tetramer.	28
Figure 1.16	Proposed structure of Multimeric membrane-bound helical aS.	28
Figure 1.17	Schematic to show 'initiation-elongation' model of aS binding to vesicles.	29
Figure 1.18	Schematic to show the differences between Gram +ve and Gram –ve bacteria cell wall structure.	31
Figure 1.19	The formation of different types of bacterial membrane vesicles.	33
Figure 1.20	Schematic drawing of a spinning disk confocal microscope.	35
Figure 2.1	Schematic of a size exclusion column (SEC).	49
Figure 2.2	Schematic showing the procedure for back crossing of C. elegans strains.	60
Figure 2.3	Slide preparation for Time lapse imaging of *C. elegans*.	67

Figure 2.4	Screen shot of Metamorph software as used for measurement of larval lengths.	70
Figure 2.5	Embryo development time lapse images, showing the time points used for timing measurements.	71
Figure 3.1	Coomassie Blue stained SDS-PAGE gel showing post FPLC purification fractions.	79
Figure 3.2	Western blot of post His tag affinity column purification of aS.	79
Figure 3.3	Graph from size exclusion assays showing the retention volume, where either Nt-acetylated or non Nt-acetylated aS-Cerulean3-His6 was eluted from the column.	80
Figure 3.4	Coomassie Blue stained SDS-PAGE gel and western blot of extracts from *E. coli* cells expressing aS-Cerulean3-His6, Nt-acetylated or Non Nt-acetylated for 90 hours.	83
Figure 3.5	Vector map of the FRET construct pET1.aS-Cerulean aS-mNeonGreen-Pif6.	82
Figure 3.6	eGFP and CFP Excitation and Emission spectra.	83
Figure 3.7	Schematic to show when FRET occurs.	83
Figure 3.8	FRET images of cells producing aS-Cerulean3 and aS-mNeonGreen.	85
Figure 3.9	Coomassie Blue stained SDS-PAGE gel showing relative amounts of protein in E. coli cells producing Nt-acetylated or non Nt-acetylated, aS-Cerulean3 alone, aS-mNeonGreen alone or our aS-FRET construct which produces each fluorophore attached to aS simultaneously.	86
Figure 3.10	Corrected relative average aS-Cerulean3 signal of E. coli producing aS-Cerulean3 or aS-FRET construct.	86
Figure 3.11	Coomassie Blue stained SDS-PAGE gel showing production of aS-mNeonGreen as a control and the FRET construct producing aS-mNeonGreen and aS-mCherry.	87
Figure 3.12	Average fluorescent lifetime in pico seconds (ps) for single fluorophore controls and FRET constructs.	88
Figure 3.13	FLIM image of *E. coli* cells producing non Nt-acetylated, aS-mNeonGreen-Pif6 and aS-mCherry simultaneously.	89
Figure 3.14	Fluorescent lifetime in pico seconds (ps) for individual cells in overnight stationary *E. coli* cultures producing either Nt-acetylated or non Nt-acetylated aS-mNeonGreen-Pif6 and aS-mCherry simultaneously	90
Figure 3.15	Illustration of how BiFC works	91
Figure 3.16	Phase and yellow, Venus fluorescence images of *E. coli* cells producing one half of the Venus BiFC construct, either aS-Venus-(start-154) or aS-Venus-(155-end) and cells producing the complete aS-Venus BiFC, [aS-Venus-(start-154) and aS-Venus-(155-end)].	92

Figure 3.17	Graphs showing fluorescence and simultaneous OD_{595} readings over time, of *E.coli* cells producing aS-Venus-BiFC with or without the NatB complex.	93
Figure 3.18	Coomassie Blue stained SDS-PAGE gel and matching western blot using Rabbit anti-aS primary antibody, of extracts from E.coli cells producing either Nt-acetylated or non Nt-acetylated aS-Venus BiFC.	94
Figure 3.19	Graph showing the level of fluorescence over time of E.coli cells producing aS-Cerulean3 having been induced with varying concentrations of IPTG.	96
Figure 3.20	Graph showing OD_{595} over time of *E.coli* cells producing aS-Cerulean3 having been induced with varying concentrations of IPTG.	96
Figure 3.21	Coomassie Blue stained SDS-PAGE gel showing the level of protein produced by E.coli cells producing aS-Cerulean3 having been induced for 3 hours with varying concentrations of IPTG.	97
Figure 3.22	Graph showing the level of fluorescence over time of *E.coli* cells producing either Nt-acetylated or non Nt-acetylated aS-Venus BiFC, with an initial OD_{595} of 0.1 or 0.01.	98
Figure 3.23	Graph showing OD_{595} values over time of *E.coli* cells producing either Nt-acetylated or non Nt-acetylated aS-Venus BiFC, with an initial OD_{595} of 0.1 or 0.01.	98
Figure 3.24	Graph showing the level of Venus fluorescence over time of a single culture of *E.coli* cells producing non Nt-acetylated aS-Venus BiFC.	100
Figure 3.25	Graph showing OD_{595} values over time of a single culture of *E.coli* cells producing non Nt-acetylated aS-Venus BiFC.	100
Figure 3.26	Heat map showing the average relative difference in fluorescence from the lowest fluorescence value at the time point when the highest level of fluorescence was reached, shown as position on a 96 well plate.	101
Figure 3.27	Graph showing average relative difference in fluorescence from the lowest fluorescence value at the time point when the highest level of fluorescence was reached.	101
Figure 3.28	Images of *E. coli* producing aS-Venus BiFC induced with 100 μg/ml IPTG for 4 hours, with 0.001% Congo Red.	102
Figure 3.29	Graph showing the percentage of *E.coli* cells with some Congo Red fluorescence indicating some amyloid formation versus the number of *E. coli* cell with no red fluorescence indicating the absence of any amyloid formation.	103

Figure 3.30	Graph showing the level of fluorescence over time of *E.coli* cells producing non Nt-acetylated aS-Venus-BiFC + DMSO controls, Nt-acetylated aS-Venus BiFC + DMSO controls or with the addition of a FDA approved drug at a final concentration of 1μM.	104
Figure 3.31	Graph showing the level of fluorescence over time of *E.coli* cells producing Nt-acetylated aS-Venus BiFC in the presence of Tyrosine kinase inhibitors.	106
Figure 3.32	Graph showing the level of fluorescence over time of *E.coli* cells producing Nt-acetylated aS-Venus BiFC, in the presence of 0.5 μM Tyrosine kinase inhibitors.	106
Figure 3.33	ITC graphs showing energy transfer with time as Gefitinib was titrated into non Nt-acetylated aS.	107
Figure 3.34	Graph showing the level of fluorescence over time of *E.coli* cells producing either Nt-acetylated or non Nt-acetylated cdc8-Venus BiFC.	109
Figure 3.35	Graph showing the OD_{595} over time of *E.coli* cells producing either Nt-acetylated or non Nt-acetylated cdc8-Venus BiFC.	109
Figure 3.36	Schematic of proposed theory for differences in fluorescence between Nt-acetylated and non Nt-acetylated Cdc8-Venus-BiFC.	110
Figure 4.1	Widefield images of BL21 DE3 *E.coli* producing either non-Nt-acetylated or) Nt-acetylated aS-Cerulean3, 3 hours post induction.	113
Figure 4.2	Widefield images of BL21 DE3 E.coli producing non Nt-acetylated aS-Cerulean3 with CydAB-mCherry, 3 hours post induction.	114
Figure 4.3	Widefield images of BL21 DE3 E.coli producing Nt-acetylated aS-Cerulean3 with CydAB-mCherry 3 hours post induction.	115
Figure 4.4	Immuno-EM images of BL21 DE3 *E.coli* producing either non Nt-acetylated aS-Cerulean3 or Nt-acetylated aS-Cerulean3 2 hours 40 minutes post induction.	116
Figure 4.5	TEM images of JM109 *E.coli* producing non Nt-acetylated aS.	117
Figure 4.6	TEM images of BL21 DE3 *E.coli* producing either non Nt-acetylated or Nt-acetylated aS-Cerulean3, 2 hours post induction.	118
Figure 4.7	Montage of time lapse images, showing the formation of an aS induced vesicle (green arrows).	119
Figure 4.8	Comparison of size and number of vesicles in 1 image each of *E. coli* BL21 DE3 producing aS-Cerulean3 or aS-mNeonGreen-Pif6.	120

Figure 4.9	Donor fluorophore fluorescent lifetime in pico seconds (ps) in E. coli cells producing non Nt-acetylated aS-Cerulean3 alone or aS-Cerulean3 with Citrine-MinD.	122
Figure 4.10	Donor fluorophore fluorescent lifetime in pico seconds (ps) in E. coli cells producing Non Nt-acetylated aS-mNeonGreen alone or aS-mNeonGreen with OmpA-mCherry.	123
Figure 4.11	FLIM heat map image of *E. coli* producing non Nt-acetylated aS-Cerulean3 with Citrine-MinD.	124
Figure 4.12	Average donor fluorophore fluorescent lifetime in pico seconds across *E.coli* cells producing either Non Nt-acetylated or Nt-acetylated aS-Cerulean3 with Citrine-MinD, an inner membrane marker, or Non Nt-acetylated or Nt-acetylated aS- mNeonGreen with OmpA-mCherry, an outer membrane marker.	126
Figure 4.13	SIM image of *E.coli* producing Citrine-MinD, inner membrane marker (green) and OmpA-mCherry, outer membrane marker (magenta).	128
Figure 4.14	Images of *E.coli* producing non Nt-acetylated aS-mNeonGreen (green) and OmpA-mCherry, (red and magenta) using widefield microscopy (a) and SIM (b).	128
Figure 4.15	Images of *E.coli* producing non Nt-acetylated aS-mNeonGreen (not shown) and mScarlet-MinD inner membrane marker (magenta) obtained using SIM.	129
Figure 4.16	*E. coli* producing non Nt-acetylated aS-mNeonGreen (green) with mScarlet-MinD (red).	130
Figure 4.17	Coomassie Blue stained SDS-PAGE gel and matching western blot of protein precipitated from cell cleared media from aS-Venus BiFC cultures producing Non Nt-acetylated and Nt-acetylated aS.	131
Figure 4.18	Coomassie Blue stained SDS-PAGE gels of cell extracts from *E. coli* strains DH10β and BL21 DE3 producing Non Nt-acetylated aS-mNeonGreen-FLAG-hGH	133
Figure 4.19	Images of *E. coli* induced for 5 hours with 0.01% Rhamnose producing non Nt-acetylated aS-mNeonGreen-FLAG-hGH.	134
Figure 4.20	Anti-FLAG western shows expression and export to vesicles/media of αS-hGH fusion (highlighted by *) in four Ambr250 bioreactor runs	134
Figure 4.21	Images of supernatant from cell cultures centrifuged to remove cells from vesicle containing media.	136
Figure 4.22	DLS graph of control supernatant from a culture of BL21 DE3 *E. coli* cells expressing OmpA-mCherry, centrifuged for 30 minutes at 1000rcf.	137

Figure 4.23	DLS graph of supernatant from a culture of BL21 DE3 *E. coli* cells expressing non Nt-acetylated aS-mNeonGreen-Pif6 and OmpA-mCherry, centrifuged for 30 minutes at 1000rcf.	137
Figure 4.24	Widefield images of *E.coli* producing non Nt-acetylated aS-mNeonGreen (green) and cytoplasmic mCherry (magenta),	138
Figure 4.25	SIM images of E.coli producing non Nt-acetylated aS-mNeonGreen-FLAG-hGH (green) and OmpA-mCherry (magenta) outer membrane marker, show aS-mNeonGreen-FLAG-hGH packaged into the vesicle.	139
Figure 4.26	Schematic of optogenetics	145
Figure 4.27	Widefield images of *E.coli* producing aS-mNeonGreen-Pif6 (green) and PhyB-mCherry (magenta).	140
Figure 4.28	PIP strips showing aS-Cerulean3 binding to specific lipids.	141
Figure 4.29	DLS measurements of vesicle size when either Nt-acetylated of non Nt-acetylated aS is added.	142
Figure 4.30	Widefield images of JM109 *E.coli* producing non Nt-acetylated aS-mCherry-PduABJKNU.	143
Figure 4.31	TEM images of JM109 *E.coli* producing non Nt-acetylated aS-mCherry-PduABJKNU.	144
Figure 4.32	17% SDS PAGE gel stained with Coomassie Blue, showing protein present in cell extracts from JM109 E.coli producing non Nt-acetylated aS-mCherry-PduABJKNU.	144
Figure 5.1	qPCR showing relative amounts of *naa-80* mRNA in N2H control and *naa-80* KO *C. elegans* strains COP1594, COP1595 and COP1596.	147
Figure 5.2	Average number of offspring for brood size assays carried out at 20oC using N2H control and naa-80 knockout C. elegans strains COP1594, COP1595 and COP1596.	148
Figure 5.3	Age specific fecundity assay from a timed egg lay, at 20oC using N2H control and naa-80 knockout C. elegans strains COP1594, COP1595 and COP1596.	149
Figure 5.4	Brood size assays carried out at 25oC using N2H control and naa-80 knockout C. elegans strain COP1594.	150
Figure 5.5	Averaged results from three Age specific fecundity assays at 25^{o}C using N2H control and *naa-80* knockout *C. elegans* strain COP1594.	151
Figure 5.6	Average number of unfertilised eggs laid during the 25^{o}C brood size assays	151
Figure 5.7	Average larvae lengths in pixels of N2H control and *naa-80* knockout larvae.	152
Figure 5.8	Genotyping PCR.	154

Figure 5.9	Results of brood size assays carried out at 20^{o}C using N2H control and outcrossed *naa-80* knockout *C. elegans* strain.	155
Figure 5.10	Averaged results from three Age specific fecundity assays at 20^{o}C using N2H control and outcrossed *naa-80* knockout *C. elegans.*	156
Figure 5.11	Average larvae length in pixels.	157
Figure 5.12	Average larvae length in pixels of outcrossed *naa-80* knockout and N2H control *C. elegans* from age synchronised parents.	159
Figure 5.13	Average number of body bends per minute, of outcrossed *naa-80* knockout and N2H control *C. elegans.*	159
Figure 5.14	Single frames from a time lapse film of an outcrossed naa-80 knockout *C. elegans* embryo.	161
Figure 5.15	Average minutes until three different embryonic developmental stages are reached in N2H controls (n=12) and outcrossed *naa-80* knockout (n=11) *C. elegans.*	162
Figure 5.16	Single frames from a time lapse film of a *C. elegans* embryo producing LifeAct-mRFP	163
Figure 5.17	Single frames from a time lapse film of a *C. elegans* embryo producing mCHERRY-ACT-1.	164
Figure 5.18	L2 larvae of LifeAct-mRFP *C. elegans* (left) and outcrossed *naa-80* knockout x LifeAct-mRFP C. elegans (right) showing filamentous actin.	166
Figure 5.19	Heads of adult LifeAct-mRFP *C. elegans* (left) and outcrossed *naa-80* knockout x LifeAct-mRFP *C. elegans* (right).	167
Figure 5.20	Developing embryos inside adult of LifeAct-mRFP *C. elegans* (left) and outcrossed *naa-80* knockout x LifeAct-mRFP *C. elegans* (right).	167
Figure 5.21	L3 larvae of mCherry-Act-1 *C. elegans* (left) and outcrossed *naa-80* knockout x mCherry-Act-1 *C.elegans* (right) showing mCherry-ACT-1.	168
Figure 5.22	Heads of L4/young adult mCherry-Act-1 *C. elegans* (top) and outcrossed *naa-80* knockout x mCherry-Act-1 *C. elegans* (bottom).	169
Figure 5.23	GFP image of L4/young adult mCherry-Act-1 *C. elegans* heads (top) and outcrossed *naa-80* knockout x mCherry-Act-1 C.elegans (bottom).	169
Figure 5.24	Adult mCherry-Act-1 *C. elegans* (top) and mCherry-Act-1 x outcrossed *naa-80* knockout *C.elegans* (bottom)	170
Figure 6.1	A proposed scheme for the stepwise mechanism of vesicles assembly.	178

List of Tables

Table 2.1	Media and buffer recipes used in this investigation	39
Table 2.2	Recipe table for SDS Page gels.	46
Table 2.3	Basic Genotype PCR master mix recipe.	57
Table 2.4	Optimised Genotype PCR, thermocycler setting.	57
Table 2.5	Expected DNA fragment sizes for each genotype PCR primer pair.	58
Table 2.6	E. coli strains used throughout this project and their use.	72
Table 2.7	*C. elegans* strains used throughout this project.	73
Table 2.8	Plasmids used during this project	73
Table 2.9	PCR primers and template for amplification of DNA fragments.	77
Table 2.10	Genotype PCR primers for identification of wild type *naa-80 C. elegans*, homozygous *naa-80* knockout *C. elegans* and heterozygous wildtype and *naa-80* knockout *C. elegans* and primers used for the amplification of cDNA during qPCR.	77
Table 3.1	Polymer lengths of Cdc8 non Nt-acetylated and Cdc8 Nt-acetylated, calculated from electron micrographs (n>200).	110
Table 6.1	Summary of aS findings.	179

List of Films: Films can be accessed as stand alone video format or embedded within MS Powerpoint files within the data files at https://data.kent.ac.uk/id/70/

Film 1	Forming vesicle on BL21 DE3 E. coli cell producing aS-mNeonGreen. Time lapse filmed using a Cellasics microfluidic system. Over 6, 1 minute frames a vesicle is seen forming growing and then leaves the cell.
Film 2	Time lapse film of outcrossed *naa-80* KO C. elegans embryo development from 2 cells to hatching. 999 Images were taken at 1 per minute.
Film 3	Time lapse film of LifeAct-mRFP C. elegans embryo development from 3 cells to hatching. 999 Images were taken at 1 per minute.
Film 4	Time lapse film of mCherry-Act-1 C. elegans embryo development from 4 cells to just prior to hatching. 999 Images were taken at 1 per minute.
Film 5	Time lapse film of LifeAct-mRFP C. elegans early embryo development. Images were taken at 10 frames per second.

List of Abbreviations

Ala	Alanine (A)
APS	Ammonium persulfate
Arg	Arginine (R)
aS	Alpha Synuclein
Asn	Asparagine (N)
Asp	Aspartic acid (D)
BiFC	Bimolecular Fluorescence Complementation
BOG	β-octyl-glucoside
C. elegans	*Caenorhabditis elegans*
cDNA	Complementary DNA
CMV	Cytoplasmic membrane vesicles
CRISPR	Clustered regularly interspaced short palindromic repeats
Cys	Cysteine (C)
DMSO	Dimethyl sulfoxide
DNA	Deoxyribonucleic acid`
DLS	Dynamic light scattering
E.coli	*Escherichia coli*
EDTA	Ethylendiamineteraacetic acid
EGFR	Epidermal growth factor receptor
FLIM	Fluorescence Lifetime Imaging
EM	Electron Microscopy
EMMG	Edinburgh minimal media with 20 mM L-Glutamic acid
EOMV	Explosive outer membrane vesicles
FPLC	Fast Protein Liquid Chromatography
FRET	Forster Resonance Energy Transfer
GFP	Green Fluorescent Protein
Gln	Glutamine (Q)
Glu	Glutamic acid (E)

Gly	Glycine (G)
GNAT	GNC5-related acetyltransferase
GNC5	General control non-derepressible 5
HAT	Histone acetyltransferase
HDAC	Histone deacetylase
His	Histidine (H)
HYPK	Huntingtin yeast two-hybrid protein K
Ile	Isoleucine (I)
IPTG	Isopropyl β-D-1-thiogalactopyranoside
KAT	Lysine acetyltransferase
KDAC	Lysine deacetylase
LB	Luria Bertani Broth
Leu	Leucine (L)
Lys	Lysine (K)
Met	Methionine (M)
MV	Membranous Vesicle
NAC	Non-Amyloid beta Component
NAD	Nicotinamide adenine dinucleotide
NAT/Nat	Nt-acetyltransferase
NGM	Nematode Growth Medium
Nt	N-terminal
OD	Optical Density
OIMV	Outer-inner membrane vesicles
OMV	Outer-membrane vesicles
PAGE	Polyacrylamide gel
PBS	Phosphate Buffered Saline
PCB	Phycocyanbilin
PCR	Polymerase Chain Reaction
PD	Parkinson’s Disease
Phe	Phenylalanine (F)

PhyB	Phytochrome B
Pif6	Phytochrome interaction factor 6
Pro	Proline (P)
Ps	Pico seconds
PTM	Post Translational Modification
RNA	Ribonucleic acid
S. cerevisiae	*Saccharomyces cerevisiae*
S. pombe	*Schizosaccharomyces pombe*
SDS	Sodium dodecyl sulfate
SEC	Size Exclusion Chromatography
Ser	Serine(S)
sgRNA	single guide RNA
SIM	Structured Illumination Microscopy
SRRF	Super-Resolution Radial Fluctuations
TAE	Tri-acetate-EDTA
TEM	Transmission Electron Microscopy
TEMED	Tetramethylethylenediamine
Thr	Threonine(T)
Tris	Tris(hydroxymethyl)aminomethane
Trp	Tryptophan (W)
Tyr	Tyrosine (Y)
Val	Valine (V)
Ub	Ubiquitin
WB	Western Blot

Abstract

N-terminal (Nt) acetylation is one of the most common post-translational modifications of proteins, which occurs on 70-90% of human proteins. The effect of Nt-acetylation of the Parkinson's disease associated protein, alpha Synuclein (aS), is poorly understood. Nt-acetylation of aS is generally believed to increase the helicity of the N-terminal 10-12 amino acids of the protein and to effect protein-protein interactions and membrane binding, though previous studies are contradictory. It is difficult to investigate the effect of aS Nt-acetylation in eukaryote cells, as the knockout of either of the genes (*naa*20 or *naa*25) which code for the two sub-units of N-terminal acetyltransferase B (NatB), which catalyses the Nt-acetylation of aS, also prevents the Nt-acetylation of many other proteins. In this investigation aS was produced within *E. coli*, with or without the co-expression of NatB, using a plasmid coding for both *naa*20 and *naa*25 from S. pombe, to enable direct comparison of the protein with and without Nt-acetylation, *in vivo* and *in vitro*. Differences were consistently seen between the two forms of aS, in protein-protein interactions and in membrane and lipid interactions. Nt-acetylation of aS resulted in a different oligomer conformation, which was more stable and liable to form amyloid *in vivo*, compared to oligomers produced when aS was not Nt-acetylated. *E. coli* expressing Nt-acetylated aS form internal structures with a tubular appearance, whereas cells expressing non Nt-acetylated aS, produced large extracellular vesicles. The toxic form of aS has not been identified and differences identified here may have relevance in the disease state. The formation of large aS-induced vesicles, which can be harvested from media, have potential for use in the enhancement of therapeutic protein production.

The effect of knockout, of the recently characterised actin specific N-terminal acetyltransferase, NAA80, within C. elegans, was also investigated. No NAA80 knockout-specific phenotype could be identified.

Chapter 1: Introduction

1.1 Cellular regulation

Cellular regulation is most commonly thought of in terms of regulation of the cell cycle, but includes the interaction of many different cellular pathways involved in the maintenance of homeostasis. Regulation can take place at a genetic level, with different genes expressed or repressed in response to environmental triggers. Transcription can be regulated by histone acetylation, a post-translational modification which is linked via Acetyl-CoA to metabolism (Hole *et al*., 2011; Drazic *et al*., 2016). Other post translational modifications are also vital for cellular regulation, as are protein-protein interactions, cyclin-dependant kinases which drive cell cycle progression, are serine/threonine kinases that phosphorylate key substrates to promote DNA synthesis and mitotic progression. They also as their name suggests, require binding to a regulatory protein called cyclin, to gain its enzymatic activity (Barnum and O'Connell, 2014). Most of the regulatory processes within cells are a triggered response to some form of signal. Changes in a cell's environment cause signalling proteins or chemicals to bind to signal receptors in order to indicate the need for some form of regulatory response. Alternatively a simple ion, as with calcium signalling, can also act via changes in cytosolic concentration, as a messenger, regulating numerous and diverse cellular processes, for example, transcription and muscle contraction (Bootman *et al.*, 2001).

1.2 Post-translational modifications

Post-translational modifications (PTMs) occur on most proteins, for example 70-90 % of human protein is Nt-acetylated (Starheim, Gevaert and Arnesen, 2012). Multiple PTMs can occur on the same protein and PTMs may also inhibit other PTMs (Schiza *et al.*, 2013). PTMs can be reversible, such as phosphorylation, and lysine acetylation or irreversible as for N-terminal acetylation.

The most common PTM is phosphorylation. This involves the addition of a phosphate group to the side chain of an Arg, Lys, His, Tyr, Ser or Thr. This is a reversible modification, which plays a key role in metabolism, division, organelle trafficking, membrane transport, immunity, learning and memory (Audagnotto and Dal Peraro, 2017). Acetylation is the second most common PTM and involves the addition of an acetyl moiety from acetyl Co-A to either the α-amino terminal group of the N-terminal residue of the ε-amino group of internal lysine. Glycosylation is a modification where glycans such as oligosaccharides or polysaccharides, are attached to Asn, Arg, Ser, Tyr or Thr residues of proteins, protein which can effect folding, conformation, distribution, stability and activity (Audagnotto and Dal Peraro, 2017). Nitration of Tyr residues is a less common modification which can occur for example on alpha Synuclein (Paleologou and El-Agnaf, 2012). Ubiquitination is a PTM which involves the addition of Ubiquitin, a small protein, to lysine residues. Ubiquitination is targeted according to the Ac/N-end rule (Varshavsky, 2011).

1.3 Acetylation

Protein acetylation is one of the major post translational modifications in eukaryotes. It involves the addition of an acetyl moiety from acetyl-CoA to a protein, this can be either amino terminal acetylation (Nt-acetylation) or lysine acetylation, where the ε-amino group of lysines are acetylated. Acetylation of lysine residues was first identified in histones and this is why lysine acetyltransferases (KAT's) are also called histone acetyltransferases (HAT's). There are at least 17 human KAT's which form three different families, including the GCN5 (general control non-derepressible 5)-related acetyltransferase (GNAT) family, into which the Nt-acetyltranferases (NATs) belong and which share conserved sequence motifs including the Ac-CoA binding motif Q/RxxGxG/A. Unlike Nt-acetylation which is not reversible, lysine acetylation is reversible with several lysine deacetylases (KDAC's) (also called histone deacetylases (HDAC's)) able to remove the acetyl moiety from lysine residues. There are two groups of KDAC's, Zn^{2+} -dependant KDAC's and NAD^{+} -dependant sirtuins (Drazic *et al.*, 2016).

Most KAT's belong to multiprotein complexes with various associated subunits, which define their catalytic activities and substrate specificities. KAT's have many targets, the best known of which are histone proteins. A high degree of histone acetylation leads to increased transcriptional activation. Histone acetylation destabilises DNA-histone interactions leading to an open, lightly packed chromatin structure and consequently to an increase of gene transcription (Drazic *et al.*, 2016).

Both hypoacetylation and hyperacetylation have been linked to various neurodevelopmental, neurodegenerative and psychiatric disorders (Malnou, Bonnaud and Suberbielle, 2016). Many different transcription factors and transcriptional co-regulators are modified by KAT's, these may be general transcriptional factors or proteins specific to cellular signalling pathways such as p53, β-catenin, NF-κB or MyoD (Yang, 2004). Acetylation of the cytoskeletal protein actin has been shown to effect actin filament stability. Myosin and other actin and myosin interacting proteins are also acetylated (Drazic *et al.*, 2016). Acetylation has been shown to be important for microtubule architecture and maintaining microtubule integrity, due to recruitment of tubulin binding proteins and effects on their localisation(Li and Yang, 2000).

1.4 Amino Terminal acetylation (Nt-acetylation)

Nt-acetylation is the addition of an acetyl moiety from acetyl-CoA to the N-terminal α-amino group of a protein, eliminating the positive charge (**Figure 1.1**). This reaction is catalysed by N-terminal acetyltransferases (NATs) which Nt-acetylate proteins with specific N-terminal sequences. The majority of eukaryote proteins are Nt-acetylated, 50-70 % of the protein in the lower eukaryote *Saccharomyces cerevisiae*, 70-75 % of protein in the plant *Arabidopsis thaliana* and 70-90 % of human protein is Nt-acetylated (Starheim, Gevaert and Arnesen, 2012).

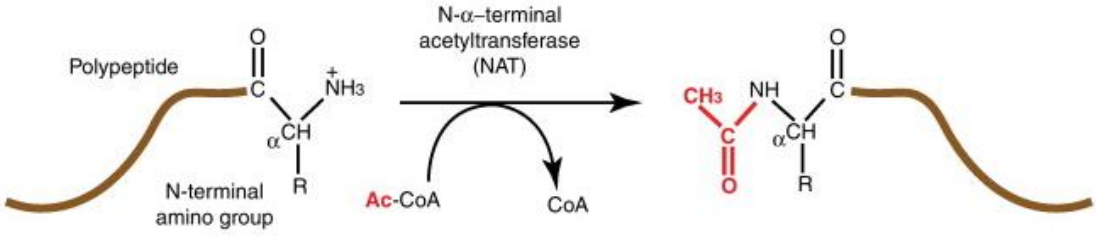


Figure 1.1. Nt-acetylation of a protein or peptide is the transfer of an acetyl moiety from Acetyl-CoA to the N-terminal α-amino group catalysed by a NAT. From Starheim, Gevaert and Arnesen (2012).

Unlike the acetylation of lysine side chains of proteins by KATs, which can be reversed by KDACs, Nt-acetylation is considered irreversible, no N-terminal deacetylase has yet been discovered (Ree, Varland and Arnesen, 2018).

Nt-acetylation affects proteins in various ways including stability, degradation, folding, protein-protein interactions, sub cellular targeting and in transcriptional control.

Nt-acetylation of alpha Synuclein (aS) effects protein folding, with Nt-acetylated aS obtained from human red blood corpuscles and *Escherichia coli* co-expressing the NatB complex being more α-helically folded, as shown by circular dichroism spectra, compared to aS produced in *E. coli* without Nt-acetylation which has only minimal α-helical content (Bartels *et al.*, 2014). Further membrane-induced α-helical folding was also enhanced by Nt-acetylation of aS (Maltsev, Ying and Bax, 2012).

Nt-acetylation effects protein-protein interactions and protein localisation. Within *S. cerevisiae,* Nt-acetylation of the Arl3 GTPase is essential for Golgi targeting, where it associates with the Golgi integral membrane protein Sys1p (Setty *et al.*, 2004).

NatD which specifically Nt-acetylates histones H4 and H2A, has been shown to have a role in the control of transcription. Nt-acetylation antagonises histone H4 serine phosphorylation which results in elevated expression of the transcription factor Slug (Ju *et al.*, 2017). H4 Nt-acetylation blocks dimethylation of Arg3 on H4 in *S. cerevisiae* resulting in ribosomal DNA silencing (Schiza *et al.*, 2013).

Nt-acetylation can target proteins for degradation via the Ac/N-end rule pathway (Nguyen *et al.*, 2018). Conversely Nt-acetylation can have a stabilising effect, an increase in protein degradation is linked to a reduction in methionine cleavage and Nt-

acetylation in Rett syndrome (Sheikh *et al.*, 2017). The N-end rule associates a proteins *in vivo* half life with its N-terminal residue or modifications, this regulated degradation is performed by the ubiquitin (Ub)-proteasome-system (UPS). UPS recruits a cascade of reactions, Ub-activating E1's, Ub-conjugating E2's and Ub-ligase E3's, which covalently attach Ub to the target proteins, following recognition of target substrates termed degradation signals (degrons). Polyubiquitinated proteins are targeted to the proteasome for degradation (Varshavsky, 2011). There are two main branches to the N-end rule, the Arg/N-end rule, where the dedicated N-degrons include N-terminal Arg, Lys, His, Leu, Trp. Phe, Ile, Tyr or Met with a hydrophobic residue at position 2 and Asp or Glu following N-terminal arginylation. The second branch of the N-end rule, the Ac/N-end rule pathway, conducts the degradation of N-terminally acetylated proteins by directly targeting the N-terminal acetyl moiety. Nt-acetylation is an abundant protein modification which predominantly takes place co-translationally and thus most proteins retain the Ac/N-degron from birth to death, however most Nt-acetylated proteins are stable and long lived. This apparent discrepancy could be explained by steric shielding of the Ac/N-degron by rapid intramolecular folding and intermolecular sequestration by binding partners or subcellular compartmentalisation, protecting the Nt-acetylated protein from degradation by the Ac/N-end rule pathway. Nt-acetylation has also been shown to impede Ub attachment to the α-amino group of Met by linear Ub chain assembly complex, E3 ligase or Ub-conjugating Ube2W E2 enzyme, showing that competition between Nt-acetylation and Ubiquitination could provide another, protein degradation regulatory mechanism (Nguyen *et al.*, 2018).

1.5 Acetylation and Disease.

Changes in lysine acetylation have been linked to various diseases. Decreases in tubulin acetylation have been linked to numerous neurological disorders and both increases and decreases in acetylation are linked to cancers, heart disease, lung disease and inflammation and immunity diseases (Li and Yang, 2000). Changes in levels of histone

acetylation in neurones have been linked to various disorders, including Rett syndrome, Rubinstein-Taybi syndrome, Alzheimers, Huntington's disease, depression and schizophrenia (Malnou, Bonnaud and Suberbielle, 2016).

Changes in levels of Nt-acetylation, either up or down, also affect cells in many ways. This can be seen in studies using cells with deletions of the genes encoding for NAT subunits and in analysis of cancer cells with increased expression of NAT subunits. Deletion of the NatB sub unit, Naa25, in *Schizosaccharomyces pombe* results in a loss of Nt-acetylation of tropomyosin and this is believed to be the major contributing factor in a disrupted septation phenotype (Coulton *et al.*, 2010). Links have also been made with several human diseases including cancers, developmental conditions and neurodegenerative disease.

There are numerous studies which have investigated links between NAA10, NatA activity and cancer. The majority indicate that NAA10 and NatA are pro-proliferative and anti-apoptotic, ensuring the survival of cancer cells, others show NAA10 to be anti-proliferative and pro-apoptotic (Kalvik and Arnesen, 2013). Human NAA10 potentially targets up to 40 % of the human proteome, meaning that numerous pathways are simultaneously affected by varying NAA10 levels, thus multiple variables down-stream of NAA10 will determine the end point phenotype of cancer cells.

Nt-acetylation of histone H4 is linked to lung cancer prognosis, where patients with more elevated levels of Nat D and Slug were found to have shorter overall survival (Ju *et al.*, 2017).

The first reported human genetic disorder associated with a mutation in a NAT gene was Ogden syndrome. This is caused by a Ser37Pro substitution in the gene encoding for NAA10 (Rope *et al.*, 2011). This is an X-linked lethal syndrome in males, characterised by severe global developmental delays, craniofacial anomalies, hypotonia, cardiac arrhythmia and cardiomyopathy resulting in infant mortality. Several de novo missense mutations in NAA10 have also been linked to moderate, to severe intellectual disability, together with variable other anomalies (Saunier *et al.*, 2016).

Rett syndrome, which has symptoms including problems with language, coordination, and repetitive movements, is caused by an Ala2Val substitution of Methyl CpG-binding

protein 2 which results in a reduction in methionine cleavage and Nt-acetylation, this is linked to an increase in protein degradation (Sheikh *et al.*, 2017).

Investigations have also suggested that together with the chaperone-like protein, Huntingtin yeast two-hybrid protein K (HYPK), the presence of functional NatA prevents Huntingtin aggregation (Arnesen *et al.*, 2010). Aggregation of aS is associated with Parkinson's disease (PD), studies have shown that Nt-acetylation of aS by NatB increases α-helicity and small oligomer formation and reduces aggregation (Trexler and Rhoades, 2012) (Bartels *et al.*, 2014).

1.6 N-terminal acetyltransferases (NATs)

Eight NATs have been identified, each Nt-acetylates proteins with specific N-terminal amino acid sequences and thus are responsible for Nt-acetylating differing percentages of the proteome. Early research into Nt-acetylation in different species, resulted in different names for orthologous genes in different species. Here the nomenclature system where by the orthologous genes from different species have the same name is used (Polevoda, Arnesen and Sherman, 2009). Five of these NAT's, A to E, are associated with ribosomes where they Nt-acetylate protein co-translationally (**Figure 1.2**). NatF associates with the Golgi apparatus, NatG is associated with chloroplasts and NatH acts within the cytoplasm.

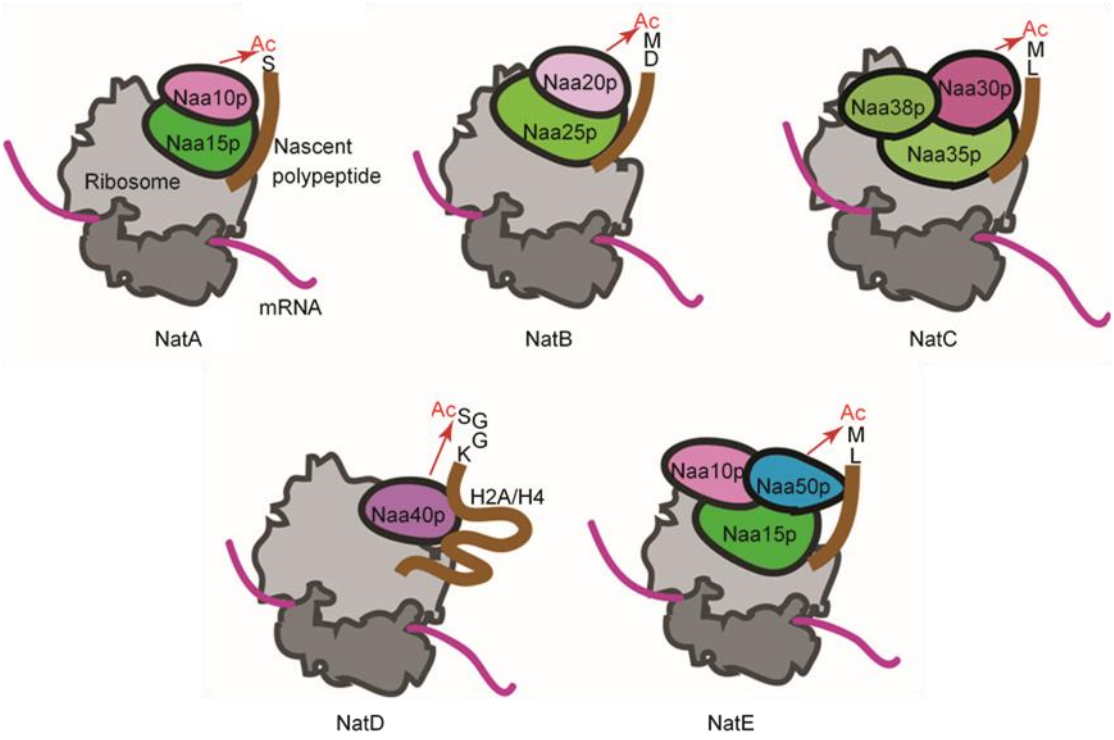


Figure 1.2. Ribosome associated NAT's A to F. Catalytic subunits are shown in pink and auxiliary subunits green. NatE, subunit Naa50p (blue) is responsible for altering NatA to NatE substrate specificity. Adapted from Starheim, Gevaert and Arnesen, (2012).

1.6.1 NatA

NatA is responsible for the largest proportion of Nt-acetylation, approximately 38% of the human proteome. It consists of a catalytic subunit NAA10 and an auxiliary subunit NAA15, which can anchor the NatA complex to ribosomes. NAA15 has 37 α-helices arranged into a ring like tertiary structure, which wraps completely around the NAA10 subunit (Liszczak *et al.*, 2013) (**Figure 1.3**). NAA10 and NAA15 are also found without ribosome association in humans where NAA10 on its' own, is able to Nt-acetylate acidic N-termini. The NatA complex is responsible for the co-translational Nt-acetylation of proteins with the N-terminal amino acids, Ala, Ser, Thr, Cys, Val and Gly, following cleavage of the terminal methionine by methionine aminopeptidases (**Figure 1.5**) (Arnesen *et al.*, 2009) NatA has several interaction partners such as Huntingtin interaction protein K, the deletion of which or the deletion of NAA10 or NAA15, increases the aggregation of Huntingtin (Arnesen *et al.*, 2010).

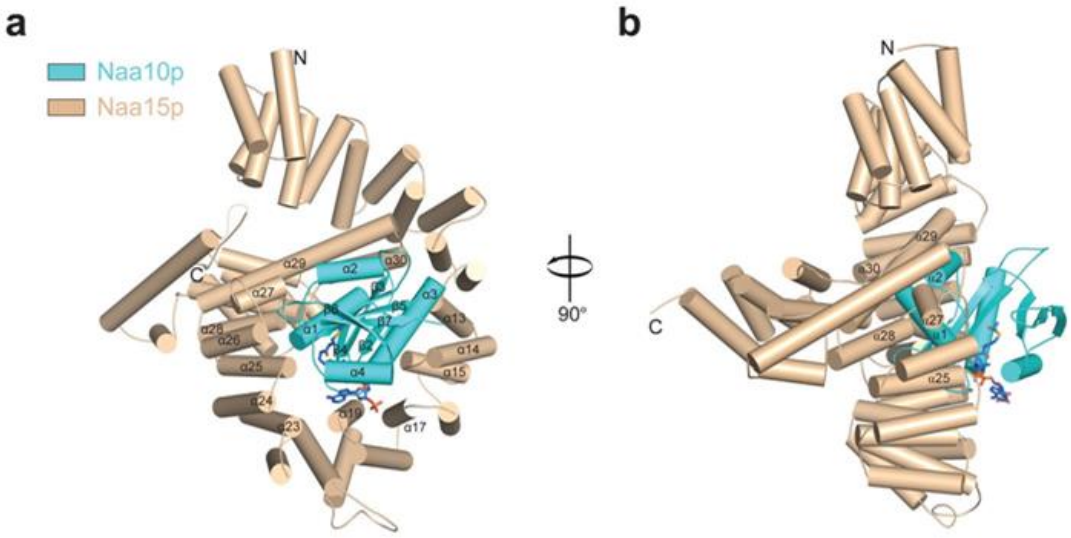


Figure 1.3. The structure of Nat A. NatA consists of the subunit Naa15, which has 37 α-helices, which form a tertiary structure around the Naa10 subunit (a) and 90^{o} rotational view (b). Adapted from Liszczak *et al.*, (2013).

1.6.2 NatB

NatB Nt-acetylates the second largest proportion of the proteome, approximately 26% of the human proteome. It consists of a catalytic subunit NAA20 and an auxiliary subunit NAA25, which can also act as a ribosomal anchor, a large proportion of the NatB units can be found in a non-ribosomal associated form in humans. The NatB complex is responsible for the co-translational Nt-acetylation of proteins with the N-terminal amino acid sequence of Methionine followed by an acidic or hydrophobic amino acid, Met-Asp-, Met-Glu-, Met-Asn- or Met-Gln- (**Figure 1.5**) (Van Damme *et al.*, 2012).

1.6.3 NatC

NatC is composed of the catalytic subunit NAA30 and auxiliary subunits NAA35 which act as a ribosomal anchor and NAA38. NatC Nt-acetylates proteins with the N-terminal amino acid sequences, Met-Leu-, Met-Phe-, Met-Ile- and Met-Trp- (**Figure 1.5**)(Van Damme *et al.*, 2016)

1.6.4 NatD

NatD is a highly selective NAT which consists of just a catalytic unit, NAA40 and only Nt-acetylates the histones H2A and H4 (Hole *et al.*, 2011).

1.6.5 NatE

NatE is formed when NAA50 physically interacts with the NatA complex. NatE Nt-acetylates a completely different set of N-terminal amino acid sequences compared to NatA. *In vitro* studies revealed a partial overlap with NatC specificity and studies using human NAA50 produced in *S. cerevisiae* revealed that NAA50 can potentially Nt-acetylate methionine followed by a small amino acid, however these N-termini are normally Nt-acetylated by NatA following cleavage of the terminal methionine (**Figure 1.5**) (Van Damme *et al.*, 2015).

1.6.6 NatF

NatF is another highly specific NAT which has a single catalytic unit NAA60. This Nat is also unusual in that it is anchored to the cytosolic side of the Golgi membrane, where it specifically Nt-acetylates transmembrane proteins (Aksnes *et al.*, 2015) (Aksnes *et al.*, 2017). NatF is only present in higher eukaryotes (**Figure 1.5**).

1.6.7 NatG

NatG has a single catalytic unit NAA70, it is a NAT which has been identified within the chloroplasts of Arabidopsis thaliana (Dinh *et al.*, 2015).

1.6.8 NatH

NatH has a single catalytic unit NAA80. The structure of Drosophila melanogaster NAA80, bound to the bisubstrate inhibitor CoA-Ac-DDDI NH_2, has a GNAT fold with a conserved Ac-CoA binding core region similar to other NAT structures (Goris *et al.*, 2018)(**Figure 1.4**). It Nt-acetylates class I, β and γ myosin following cleavage of Nt-acetylated methionine by an unknown acetylaminopeptidase (Drazic *et al.*, 2018) It is also expected to Nt-acetylate the class II myosins following a similar cleavage of Nt-acetylated cysteine (Arnesen, Marmorstein and Dominguez, 2018)

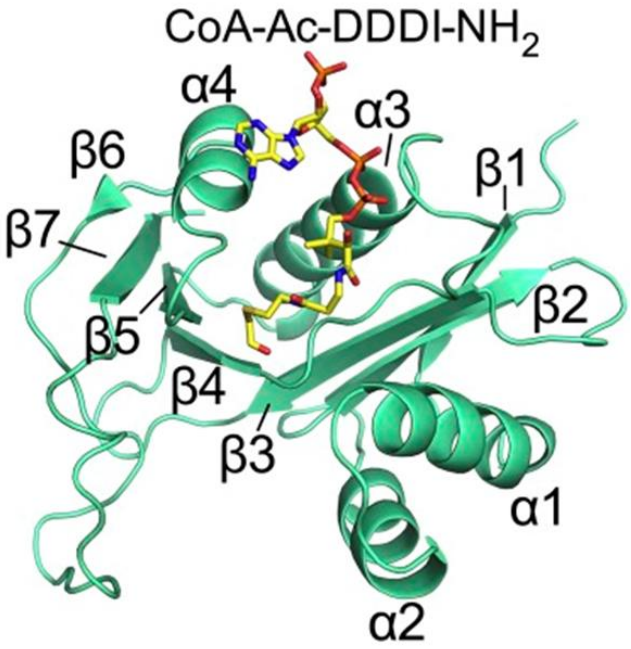


Figure 1.4. The structure of DmNAA80/CoA-Ac-DDDI-NH_2. The structure consists of four α-helices and seven b-strands with a conserved Ac-CoA binding core region similar to other NAT structures (Goris et al., 2018).

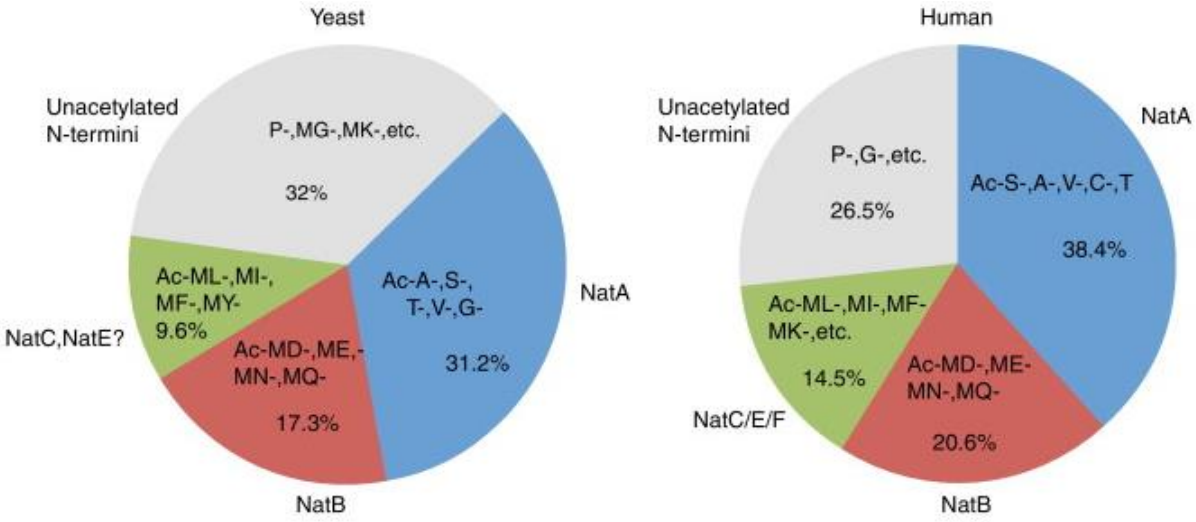


Figure 1.5. The Nt-acetylome of yeast and humans, showing the N-terminal amino acid sequences Nt-acetylated by NATs A to F. From Starheim, Gevaert and Arnesen, (2012).

1.7 Co-translational and Post-translational Nt-acetylation.

Nt-acetylation of the majority of the acetylome occurs co-translationally, where NatA, NatB, NatC and NatE are anchored to ribosomes by axillary subunits. NatD may Nt-acetylate both co-translationally where it is associated with ribosomes, but may also Nt-acetylate post-translationally as a large proportion is not ribosome associated and some is also found within the nucleus (Hole *et al.*, 2011). NatF post-translationally Nt-acetylates transmembrane proteins, where it is anchored to the Golgi. NatG, within chloroplasts and NatH, within the cytoplasm, Nt-acetylate post-translationally.

1.8 Limitations with *in vivo* Nt-acetylation research.

In eukaryotes the large number of substrates Nt-acetylated by the majority of NAT complexes makes investigation into the effect of loss of Nt-acetylation *in vivo* difficult. Knock out of a Nat subunit affects numerous different pathways. Comparisons may be made in cells with a Nat subunit deletion, by over expression of the protein of interest with or without an acetylation mimic N-terminal (Coulton *et al.*, 2010). However, that numerous other proteins will be effected by loss of N-terminal acetylation, often effecting cell growth, must be considered.

Recombinant protein produced in *E. coli* is commonly used for *in vitro* investigations as this is a fast, easy and relatively cheap method for producing target proteins and can also be used for *in vivo* investigations. However prokaryotes are unable to Nt-acetylate most recombinant proteins. Novel recombinant bacterial N-terminal acetylation systems, exploit the co-expression of *S. pombe* NatA or NatB, together with a recombinant protein within *E.coli*. (Johnson *et al.*, 2010). This system can produce Nt-acetylated protein for *in vitro* investigation (Trexler and Rhoades, 2012; Bartels, *et al*., 2011) and also for *in vivo* investigations. Consideration must be given to the fact that endogenous proteins not normally Nt-acetylated within *E. coli,* could now be Nt-acetylated. However investigations examining growth, by measurement of change of OD_{600} with time, show expression of NatA or NatB within *E. coli* does not appear to have any detrimental effect on growth.

1.9 NatH/NAA80 substrate specificity

NatH, which was recently characterised (Drazic *et al.*, 2018)(Goris *et al.*, 2018), has a single catalytic unit NAA80. Nt-acetylation of a representative library of peptides found that only peptides with acidic amino acids in the second and third position were Nt-acetylated, strongly suggesting that NAA80 Nt-acetylates all six human actin isoforms, however this has only been formally demonstrated with class I, β and γ actin. That actins are the target of NAA80 Nt-acetylation was confirmed using N-terminal proteomics by quantitatively assessing the N-terminal acetylation status of 402 protein N-termini from HAP1 control and NAA80 knockout cell lysates. Only DDDI and EEEI N-termini corresponding to processed β and γ actin showed altered Nt-acetylation levels in the knockout cells (Drazic *et al.*, 2018). Unlike the Nt-acetylation of the majority of proteins, NAA80 Nt-acetylates actin post-translationally. This occurs following cleavage of the N-terminal Nt-acetylated methionine of class I actin, by an unknown acetylaminopeptidase (Drazic *et al.*, 2018), or following a similar cleavage of Nt-acetylated cysteine of class II myosins (Arnesen, Marmorstein and Dominguez, 2018) (**Figure 1.6**).

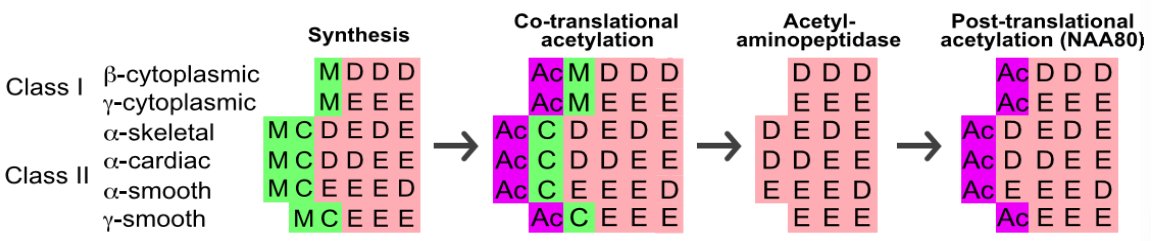


Figure 1.6. The Co-translational and Post-translational Nt-acetylation of actin. Actin Nt-maturation begins with co-translational Nt-acetylation of the N-terminal methionine of class I actin or the N-terminal cysteine following cleavage of the N-terminal methionine of class II actin is followed by cleavage of the N-terminal Acetylated methionine or cysteine by an unknown acetylaminopeptidase and finally Nt-acetylation of the N-terminal acidic amino acid by NAA80. From Arnesen, Marmorstein and Dominguez, (2018).

Crystal structures have been obtained for an N-terminal deletion construct of *Drosophila melanogaster* NAA80, bound to either Ac-CoA or the bisubstrate inhibitor CoA-Ac-DDDI-NH_2. NAA80 has a typical Gcn5-related Nt-acetyltransferase (GNAT) fold as found in many acetyltransferases (Goris et al., 2018). The substrate binding region is wider in NAA80 than other NAT's, with an electrostatic surface with many positively charged residues, indicating substrate specificity towards acidic residues particularly residues 2 and 3 (Goris *et al.*, 2018). NAA80 Nt-acetylates some NatB substrates within *naa20Δ* yeast, but due to the co-translational mode and high processivity of NatB, the only *in vivo* substrates of NAA80 are processed actins (Drazic *et al.*, 2018). Human NAA80 differs from *Drosophila melanogaster* NAA80 in that it has an extended N-terminal and a proline rich loop before the C-terminal β-strand which may further effect the substrate specificity of human NAA80.

1.10 Phenotype of HAP1 cells with NAA80 knockout.

Studies using, mammalian HAP1 cells have identified a phenotype for NAA80 knockout. In HAP1 NAA80 knockout cells where actin is not Nt-acetylated, cells are seen to have an increase in the number of filopodia and lamellipodia and have an increase in cell motility, with at least a doubling of speed for random cellular movement and with the gap in wound healing assays closing approximately 12 hours ahead of control HAP1 cells (Drazic et al., 2018; Aksnes et al., 2018).

1.11 The effect of NAA80 knockout in HAP1 cells on actin turnover and cell motility

The Nt-acetylation of actin was found not to affect actin filament nucleation, however a significant effect on polymerisation has been observed. Cytoplasmic actin, a mixture of both β and γ isoforms, isolated from HAP1 and HAP1 NAA80 knockout cells had elongation and depolymerisation rates approximately two-fold faster for Nt-acetylated actin compared to Non Nt-acetylated actin. This suggests that Non-Nt-acetylated actin filaments may be more stable, cells containing Non Nt-acetylated actin also had a decrease in their ratio of monomeric to filamentous actin (Drazic *et al.*, 2018) (Aksnes *et al.*, 2018).

Images of NAA80 knockout cells with decreased monomeric to filamentous actin show a fourfold increase in the numbers of filopodia seen with an average length of 5 μm compared to those of HAP1 control cells which had an average length of 1 μm. NAA80 knockout cells also formed twice as many lamellipodia compared to controls.

In NAA80 knockout cells a significant difference was seen in cell motility. In wound-healing assays, cell front velocity was increased in NAA80 knockout cells, chemotaxis and random cell migration assays also show increased motility for NAA80 knockout cells with single cell analyses demonstrating at least a doubling in speed for random cellular movement (Drazic *et al.*, 2018) (Aksnes *et al.*, 2018).

Whole cell effects may also be due to interactions other than actin filament turnover. In actin filaments the actin N-termini are exposed and may participate in interactions with many actin binding proteins, such as myosin as indicated by cryo-EM structures of actin-bound myosin (Arnesen, Marmorstein and Dominguez, 2018) (Mentes *et al.*, 2018) (**Figure 1.7**), Changes in proteins binding to actin could also have an effect on cell adhesion and contraction thus effecting cell motility.

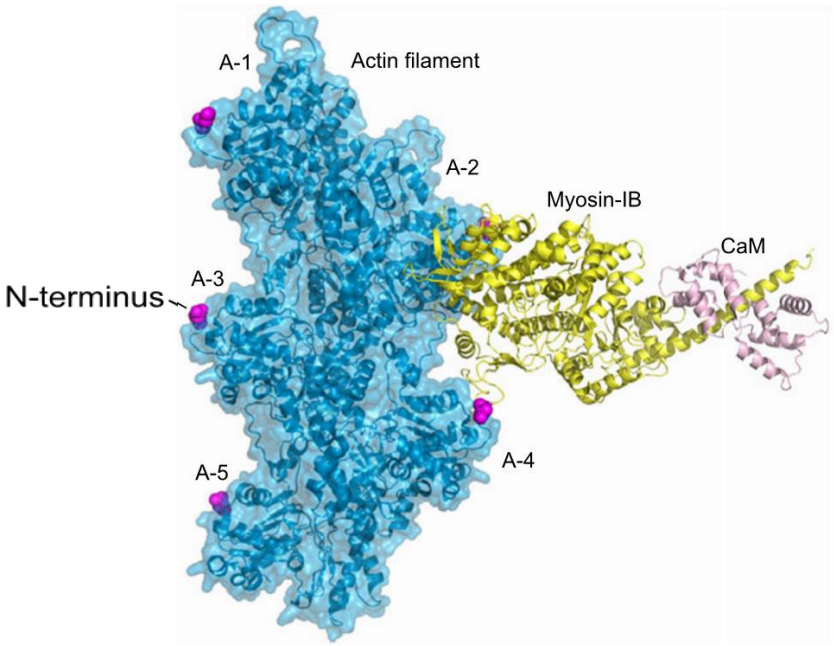


Figure 1.7. Actin filament showing exposed actin N-termini with myosin bound in a cleft between two actin subunits. The bound myosin is within contact distance of the N-termini of both units. From Arnesen, Marmorstein and Dominguez, (2018) (from a cryo-EM structure determined by Mentes *et al*., 2018)

1.12 Actin isoforms

There are six different human actin isoforms which share 93-99 % sequence identity. There are two cytoplasmic class I actins; β-cytoplasmic and γ-cytoplasmic and four class II actins; α-skeletal, α-cardiac, α-smooth and γ-smooth. Despite a high percentage sequence identity the different actin isoforms appear to have different cellular functions with all knockout mice so far reported having distinct phenotypes, some of which are fatal (Perrin and Ervasti, 2010). Different localisation is also seen, with α-skeletal-actin found in the sacromeric thin filament, β and γ cytoplasmic actin have also been shown to have different localisation within neurones and differentially effect neuronal growth (Moradi *et al.*, 2017). Actin forms a variety of different structures which are vital in a number of cellular processes (**Figure 1.8**), including interactions with myosin motor proteins, intracellular transport, muscle contraction, cytokinesis,

endocytosis and cellular structure and motility, including cell adhesion and contraction and the formation of lamellipodia and filopodia.

The formation, disassociation and regulation of filamentous actin structures are controlled by actin-binding proteins (Pollard, 2016). Actin monomers polymerise into filaments which when associated with myosin form an arrow shaped complex, the ends of the filament are therefore defined as 'barbed' and 'pointed'. Profilin bound to the barbed end of actin monomers sterically inhibits nucleation and elongation at pointed ends of filaments, high concentrations can promote dissociation. Actin filament severing proteins, such as cofilin and some formins, can sever actin filaments. Motility and cytokinesis are dependant on actin filament severing by cofilin. Formins interact with the barbed end of an actin filament via a formin homology 2 domain. Most formins nucleate actin filaments, by stabilising actin dimers, for the contractile ring, stress fibres and filopodia. Some formins are associated with the plasma membrane, intracellular membranes or microtubules. In addition to nucleation of actin filaments, formins can both promote and inhibit actin fibre elongation. Profilin overcomes inhibition where the formin has a formin homology 1 domain, such as with the formin mDia1, where elongation can be five times faster than for a free barbed end.

The Arp2/3 complex is formed of seven subunits. The Apr2/3 complex produces actin side branches. When Arp2/3 binds to the side of an actin filament it forms the base for the growth of a new branch, anchoring the pointed end to the mother filament enabling the elongation of the free barbed end. Capping protein prevents elongation of filaments at the barbed end of filaments. Arp2/3 also acts as a capping protein on disassociated branches, similar to tropomodulin, which is an exclusively pointed-end capping protein, preventing the elongation of filaments at the pointed end. Cross linking proteins connect actin filaments and also stabilise higher order structures such as bundles, as in filopodia, and networks as at the leading edge of motile cells.

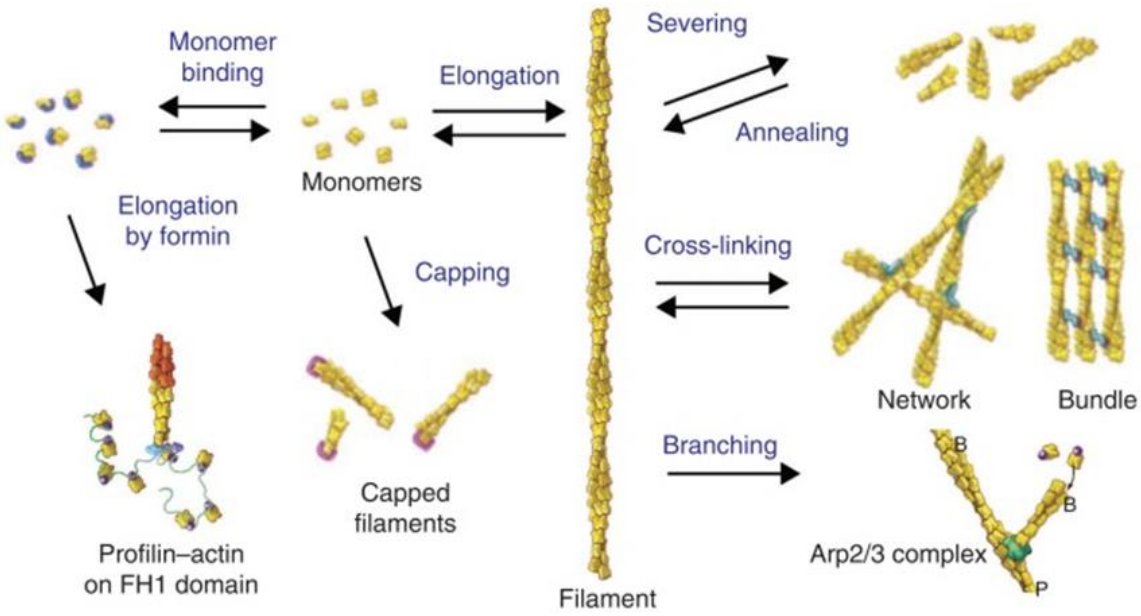


Figure 1.8. Actin monomers, filaments, structures and interacting proteins. From Pollard, (2016).

Tropomyosin is a dimeric α-helical coiled coil protein that associates with actin filaments. Tropomyosin dimers associate in an end to end fashion, creating an unbroken polymer that binds along each of the two long-pitch helices of the actin filament. This protects the actin filament from severing by cofilin and influences myosin interactions with the actin filament (**Figure 1.9**).

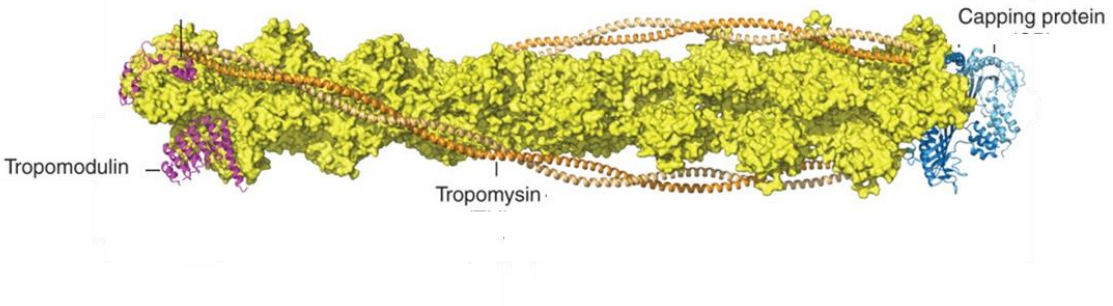


Figure 1.9. Tropomyosin binding along an actin filament. Actin filament shown with tropomyosin binding and actin capping protein including tropomodulin. Adapted from Pollard, (2016).

Cdc8

Cdc8 is the single tropomyosin isoform produced in *S. pombe.* Cdc8 can be Nt-acetylated to increase its affinity for actin and enhance its' ability to regulate myosin function (East *et al.*, 2011).

1.13 *Caenorhabditis elegans* as a model organism

The model organism used within this investigation was *C. elegans.* Model organisms such as this are all well understood, they are used to study human disease for a number of reasons, including ethical reasons, cost and time. A disease may take several years to develop in a human, but in an organism with a much shorter lifespan effects may be seen far more rapidly. Model organisms are frequently used due to their speed of growth, ease of use and the range of genetic tools that can be used with them. *C. elegans* is well characterised, and its genetic manipulation is relatively easy, making it attractive as a multicellular model organism with a simple nervous system and a fast life cycle. *C. elegans* is transparent and its size makes them suitable for localisation studies using fluorescent microscopy.

C. elegans is valuable in investigations into possible effects on actin due to changes in Nt-acetylation, as it is a tractable multicellular organism with muscles and a simple nervous system, which together with general changes in health may highlight differences in phenotype due to *naa-80* knockout. Many different assays have been used to investigate phenotype in *C. elegans* including brood size, movement and sensory assays (Hart, 2006). *C. elegans* can be either hermaphrodite or male. This enables cross mating of strains to establish consistent background genotype of knockdown and control strains. Hermaphrodite stocks also produce offspring which are genetic clones, ensuring minimal genetic variation within strains used for investigations.

1.14 *E. coli* as an in vivo test tube

E. coli has been used extensively to produce recombinant protein for purification and use in, *in vitro* investigations which has predominantly involved the production of non Nt-acetylated protein. *E.coli* does not however appear to have been used in its own right as a system for the *in vivo* study of aS, i.e. using *E. coli* as an *in vivo* test tube. The folding of aS within *E. coli* has been investigated, though this was conducted at a high IPTG induction rate which may have had a toxic effect on the E. coli cells (McNulty, Young and Pielak, 2006). One other investigation was also carried out into aS translocation into the periplasm (Ren *et al.*, 2007). *E.coli* provides a very simple system for gaining insight into mechanisms regulating protein-protein and protein-membrane interactions. It has no internal membranes, only membranes at the periplasmic region, which is in contrast to eukaryotic systems. The co-expression of *S. pombe* NatB and aS within *E.coli* (Johnson *et al.*, 2010) provides a simple system for investigation of the effect of Nt-acetylation *in vivo* on aS protein-protein and protein-membrane interactions.

1.15 Alpha Synuclein (aS)

aS is a protein which is highly enriched in the brain and is predominantly distributed in the presynaptic terminals of neurones (Baltic, 2004). It can also be found in red blood corpuscles (Bartels, Choi and Selkoe, 2011), the heart, muscles and other tissues (Baltic, 2004). aS is a small 140 amino acid protein, which is coded for on the SNCA gene. aS is normally soluble, but forms aggregates in several disease states. aS was first identified in β–amyloid plaques in the brain of patients with Alzheimer's disease, but is mostly associated with Parkinson's disease. Parkinson's disease is one of a number of neurodegenerative disorders called α-Synucleinopathies which also include dementia with Lewy bodies and multiple system atrophy (Kim, Kagedal and Halliday, 2014). aS is subject to many different post-translational modifications and is also known to interact with lipids, phospholipids and other proteins. It is not fully understood how these interactions affect aS structure and function (Paleologou and El-Agnaf, 2012).

aS was long thought to exist primarily as a natively unfolded protein monomer, though studies are now reporting an α-helix structure for approximately the first 10 N-terminal residues. The protein is made up of three domains, the N-terminal region (residues 1 to 60) which contains lysine-rich, imperfect 11 amino acid repeats, which are important in membrane binding and α-helix formation. The central non-amyloid beta component (NAC) region (residues 61 to 95) which is predominantly composed of hydrophobic residues and is the region required for aS aggregation. The third domain is the C-terminal region (residues 96 to 140) which is acidic and proline rich and is found in a disordered conformation and has been implicated in interactions with proteins, metals and small molecules (Kim, Kagedal and Halliday, 2014)(Pratt *et al.*, 2015).

The N-terminal region undergoes a change into an amphipathic α-helix on membrane binding (Maltsev, Ying and Bax, 2012). The lipid composition and curvature of vesicles, can affect aS binding to these membranes, with enhanced binding of aS to vesicles with increased curvature and negative charge. Different helical membrane-bound conformations have been observed, including a short helix at the N-terminal which is membrane bound with most of the N-terminal domain remaining disordered and unbound, on phospholipid vesicles. An extended helix of approximately 100 residues and a broken-helix conformation in which the extended-helix is broken into two distinct helices separated by a non-helical linker region (residues 39 to 45) (**Figure 1.10**) have both been observed in the context of detergent micelles and lipid vesicles (Snead and Eliezer, 2014).

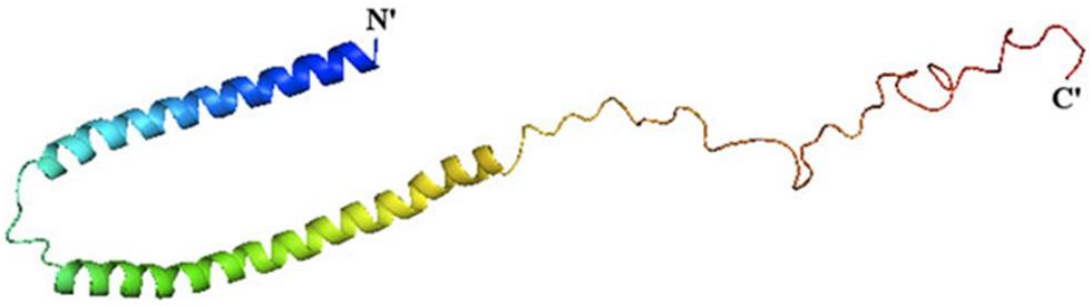


Figure. 1.10. Double helix structure of alpha-Synuclein bound to lipid vesicles. From Ritchie and Thomas, (2012).

A double anchor mechanism has also been proposed where an N-terminal amphipathic α-helix anchor can bind to one vesicle and a further amphipathic α-helix (residues 65-97) binds to a second vesicle (Fusco *et al.*, 2016)(**Figure 1.11**).

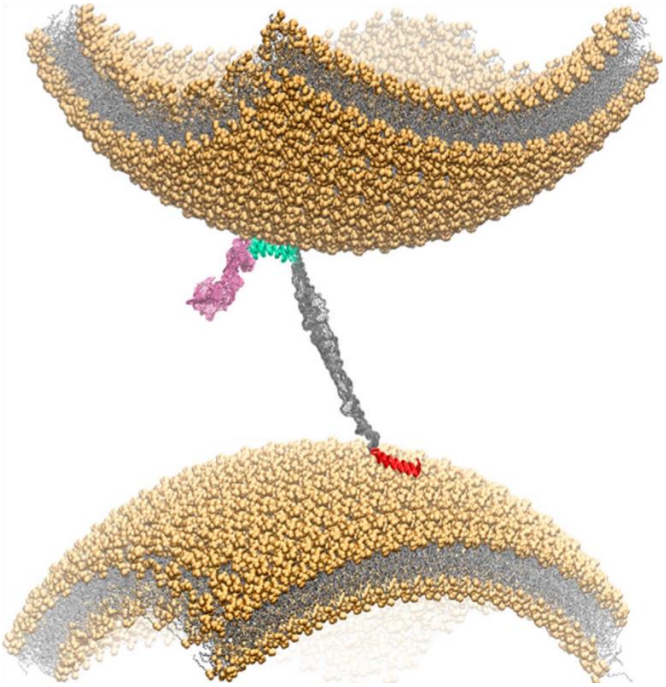


Figure. 1.11. A proposed aS double anchor mechanism. An N-terminal amphipathic α-helix anchor (red) can bind to one vesicle and a further amphipathic α-helix (residues 65-97 within the NAC and C-terminal regions)(cyan) binds to a second vesicle Fusco *et al.*,(2016).

aS has the N-terminal sequence Met-Asp and is therefore Nt-acetylated by NatB. N-terminal acetylation also increases helicity at the N terminus, electrostatic charge and increases membrane affinity with moderately charged vesicles (Dikiy and Eliezer, 2014)(Maltsev, Ying and Bax, 2012).

aS is known to oligomerise and to form fibrils and large aggregates, which are associated with disease states, though there is ongoing debate as to which form is the toxic species.

1.15.1 Post-translational modifications of aS

There are several post-translational and co-translational modifications that aS can undergo, which have been identified in aS from Lewy bodies and *in vitro studies*, including phosphorylation, ubiquitination, nitration and Nt-acetylation (Kim, Kagedal and Halliday, 2014)(Pratt *et al.*, 2015)(Schmid *et al.*, 2013) (**Figure. 1.12**).

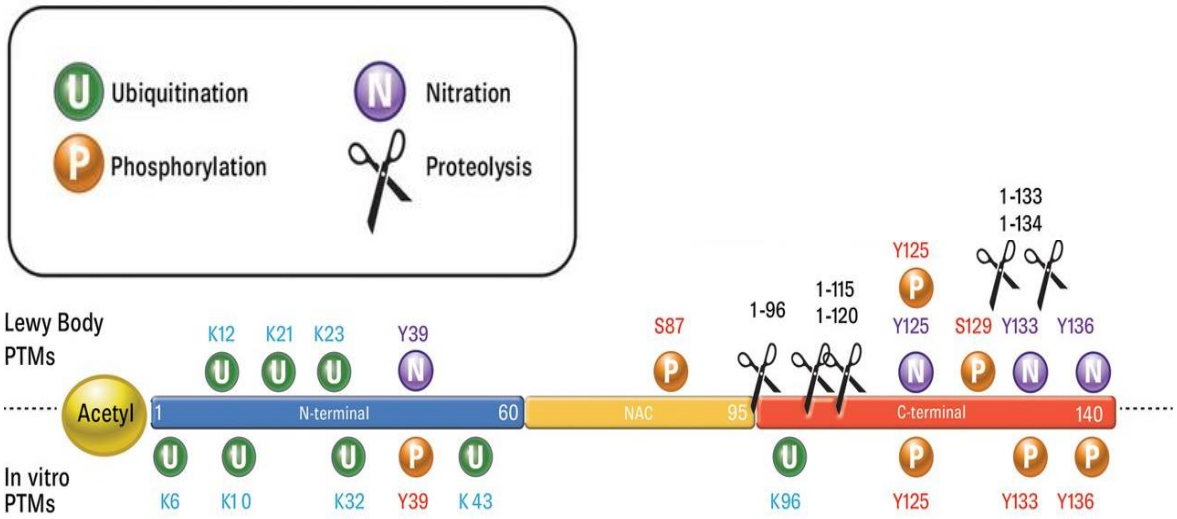


Figure. 1.12. Post-translational modifications of aS including Nt-acetylation, phosphorylation, ubiquitination, nitration and truncations. Adapted from (Schmid et al., 2013).

Phosphorylation is seen as the most common post-translational modification, though levels of phosphorylation vary. In dementia with Lewy Bodies, approximately 90% of insoluble aS is phosphorylated at S129, compared to 4% in soluble cytosolic aS. Phosphorylation also occurs at S87, Y39, Y125, Y133 and Y135. This implicates phosphorylated aS in aggregate formation and has led to more research into this modification than any other. Other post translational modifications including ubiquitination of lysine residues, nitration of tyrosine residues and truncations have been investigated (Pratt *et al.*, 2015)(Schmid *et al.*, 2013)(Ritchie and Thomas, 2012).

Nt-acetylation has also been investigated, but with varying results. It has been reported that Nt-acetylation does not have prominent effects on the biophysical and membrane-binding properties of aS, *in vitro* and *in vivo* (Fauvet *et al.*, 2012). But other papers have reported that Nt-acetylation can have an effect on α–helicity of the N-terminal, membrane interactions (Maltsev *et al*., 2012; Dikiy and Eliezer, 2014) and oligomer formation (Trexler and Rhoades, 2012).

1.15.2 Proposed functions of aS

The exact action of aS is unknown, but there are several theories (**Figure 1.13**) (Snead and Eliezer, 2014). As aS is predominantly found in the presynaptic terminals of neurons and is known to bind synaptic vesicles it is largely thought to be involved in maintaining a supply of synaptic vesicles in presynaptic terminals (Fusco *et al.*, 2016) and to act as a chaperone in the formation of SNARE complexes. Experiments using SNCA knockout mice have also shown an effect on memory and cognitive function (Kim, Kagedal and Halliday, 2014)(Burré, Sharma and Südhof, 2014). However aS is also found in Red blood corpuscles (Bartels *et al.*, 2014) and to a lesser extent in other tissues and is also thought to potentially interact with other cellular membranes, including the inner nuclear membrane, mitochondrial membranes, plasma membrane and with lipid rafts and fatty acids. These other potential sites of aS action could indicate a more widespread or general function for aS

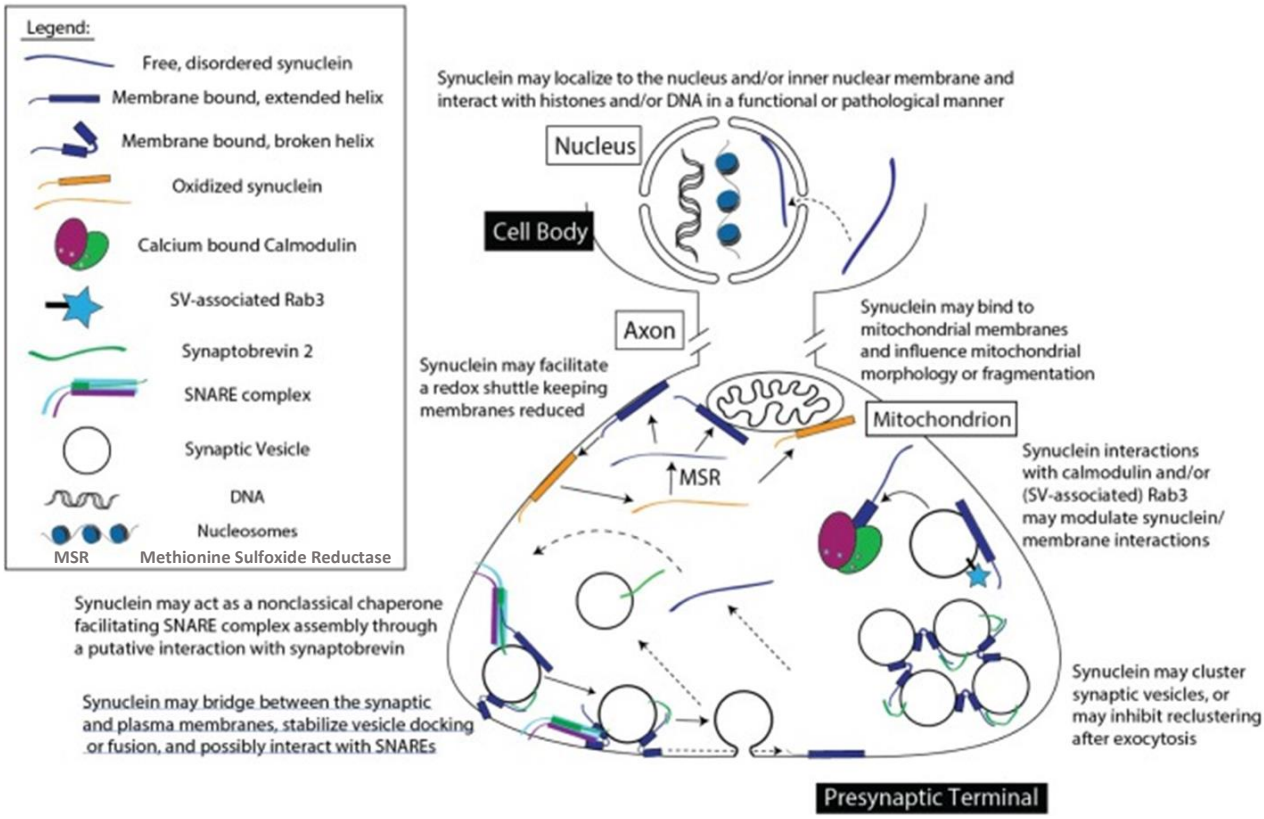


Figure. 1.13. Cellular membranes, targets and pathways, potentially involved in the normal, physiological functions of alpha-Synuclein. From Snead and Eliezer, (2014)

1.15.3 aS association with Parkinson's Disease (PD)

Parkinson's Disease (PD) is a neurodegenerative disorder, caused by the selective loss of dopaminergic neurones in the substantia nigra. PD has a prevalence of 315 per 100,000 people aged 40+ The main symptoms are tremor, slowness of movement (bradykinesia) and muscles stiffness (rigidity), though there are many other symptoms that can vary from person to person. PD is an age-related condition with prevalence increasing from 41 per 100,000 in people aged 40 to 49 years of age to 1087 per 100,000 people aged 70 to 79 years of age and, 1903 per 100000 people 80+ years of age (Prigsheim, Jette, Frolkis, 2014). The cause of Parkinson's is unknown and there is no cure.

A defining feature of PD is the presence of Lewy Bodies, cytoplasmic inclusions within the neurones of the substantia nigra, which consist mainly of aS. There is no consensus as to when aS is most toxic in PD. Some believe it is the soluble protofibrils or oligomers which are the most toxic, whereas others believe it is the matured aggregates (Bengoa-Vergniory *et al.*, 2017) The concentration of aS within dopaminergic cells, also seems to be linked to toxicity, as duplications and triplications of the SNCA gene, which codes for aS, are linked to early onset Parkinson's disease.

A small number of people develop early onset or familial PD, which has been linked to several point mutations in, as well as duplications and triplications of the SNCA gene (Kim et al., 2014; Bengoa-Vergniory et al., 2017) (**Figure 1.14**) .

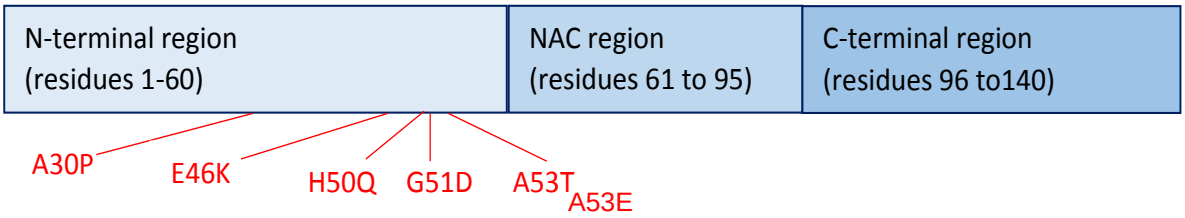


Figure. 1.14. Six SNCA point mutations linked to familial PD and dementia with Lewy bodies. Disease associated point mutations are found in the N-terminal region of aS but not in the non-amyloid beta component (NAC) or C-terminal regions

Research has primarily focussed on three of these point mutations, A30P and A53T which have also been linked to an increase in the production of C-terminally truncated aS (Ritchie and Thomas, 2012), which may also play a role in aS aggregation. Truncated aS has been found in Lewy bodies, from dementia with Lewy bodies, brains and other associated neurodegenerative diseases (Paleologou and El-Agnaf, 2012) and E46K (Fiske *et al.*, 2011). Phosphorylation of S129 and S87 has also been the focus of many investigations as these residues are phosphorylated in Lewy bodies (Paleologou and El-Agnaf, 2012; Schmid et al., 2013). Until recently, relatively little research has been carried out into the effect of Nt-acetylation and other post translational modifications.

1.15.4 Nt-acetylation of aS

Investigations into the effect of Nt-acetylation of aS, on its' conformation and membrane binding, has predominantly used purified protein. One study which conducted NMR using live *E.coli* found that the spectra with and without the presence of the NatB construct were nearly identical, but that in lysates obtained from the same cells where NatB was co-expressed, aS was quantitatively modified (Fauvet *et al.*, 2012). NMR studies using purified aS have found that the impact of Nt-acetylation is seen as an increase in helicity, limited to the first approximately 10-12 residues(Trexler and Rhoades, 2012; Maltsev *et al*., 2012; Bartels *et al*., 2014). An investigation using native cell derived aS (therefore Nt-acetylated), found that aS occurs as a helically folded tetramer (Bartels, Choi and Selkoe, 2011) and studies using recombinant aS with an additional 10 residue N-terminal extension also found that aS formed a dynamic tetramer (Wang *et al.*, 2011)(**Figure 1.15**), as opposed to a disordered monomer as non Nt-acetylated recombinant aS has often been described. A different multimeric membrane-bound aS structure has also been proposed (Burré, Sharma and Südhof, 2014) (**Figure 1.16**). Recombinant Nt-acetylated aS also forms a partially α-helical, oligomeric form of the protein when purified in the presence of glycerol and β-octyl-glucoside (BOG) (Trexler and Rhoades, 2012). Nt-acetylation of aS has been shown to slow aggregation (Bartels *et al*., 2014; Ruzafa *et al*., 2017).

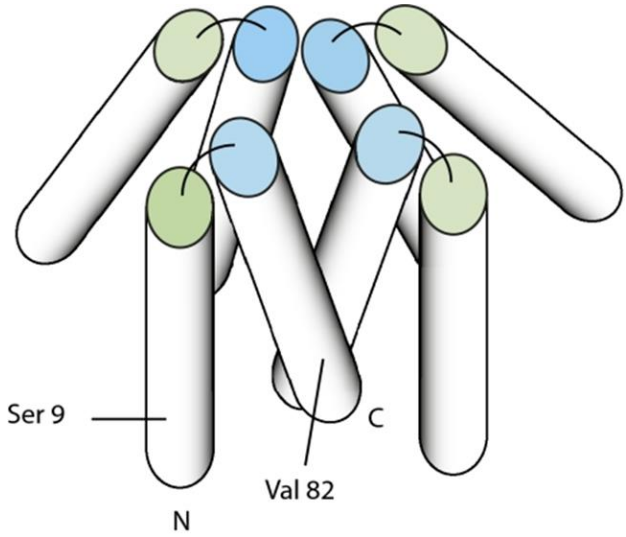


Figure. 1.15. Model for a compact aS tetramer. Helices are represented as cylinders. N indicates the N-terminal of the protein, with the first helix (α1, represented by green-ended cylinder) ending at ~residue 43. The second helix (α2, blue ended) starts ~residue 50 and ends at residue 103 (marked C). The remainder of the polypeptide, which is expected to be disordered, is not represented. From (Wang W, *et al* 2011).

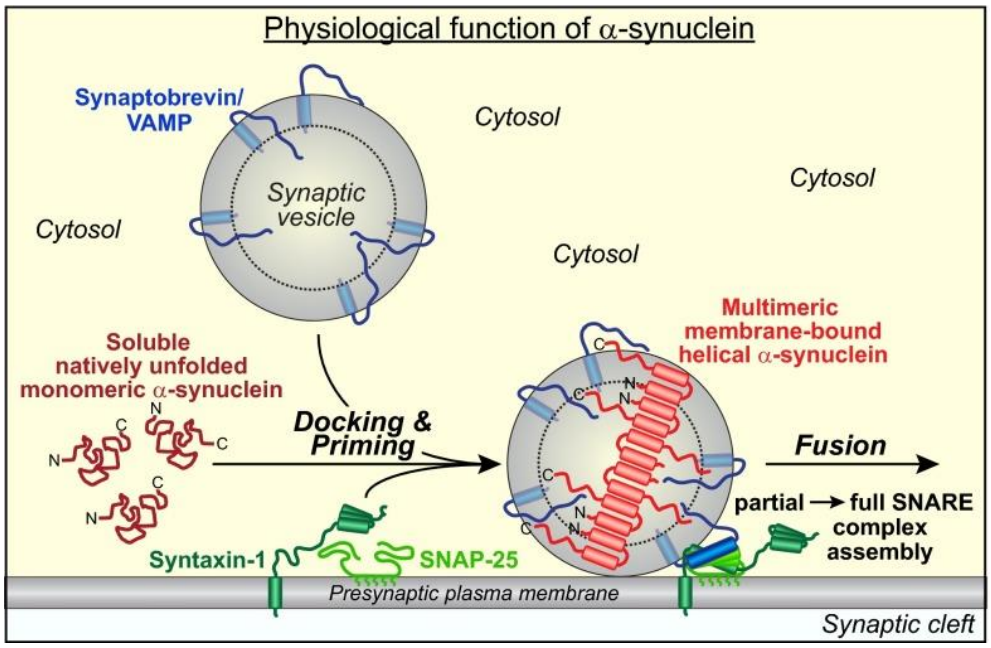


Figure. 1.16. Proposed structure of Multimeric membrane-bound helical aS. From Burré, Sharma and Südhof, (2014)

Investigations into the effect of Nt-acetylation on membrane binding show an increase in N-terminal helicity on membrane binding of both forms of aS. The majority of these also report a greater membrane binding affinity with Nt-acetylated compared to non Nt-acetylated aS (Bartels *et al*., 2014; Maltsev *et al*., 2012)(**Figure 1.17**) (Dikiy and Eliezer, 2014), however not all studies have found differences (Fauvet *et al.*, 2012). Some of these inconsistencies may be due to the investigations using different sizes of synthetic vesicles, 40-120 nm which would have differing curvature (Dikiy and Eliezer, 2014) and different lipid compositions (Bartels *et al*., 2014; Pirc and Ulrih, 2015; Varkey *et al*., 2010) or rat synaptic vesicles (Fusco *et al.*, 2016).

Unfortunately investigations into synaptic vesicle assembly promoted by aS (Fusco *et al.*, 2016), and into membrane binding to promote SNARE complex formation (Burré, Sharma and Südhof, 2014), only used non Nt-acetylated aS, so that the effect of Nt-acetylation of aS, in these aS membrane binding situations cannot be compared.

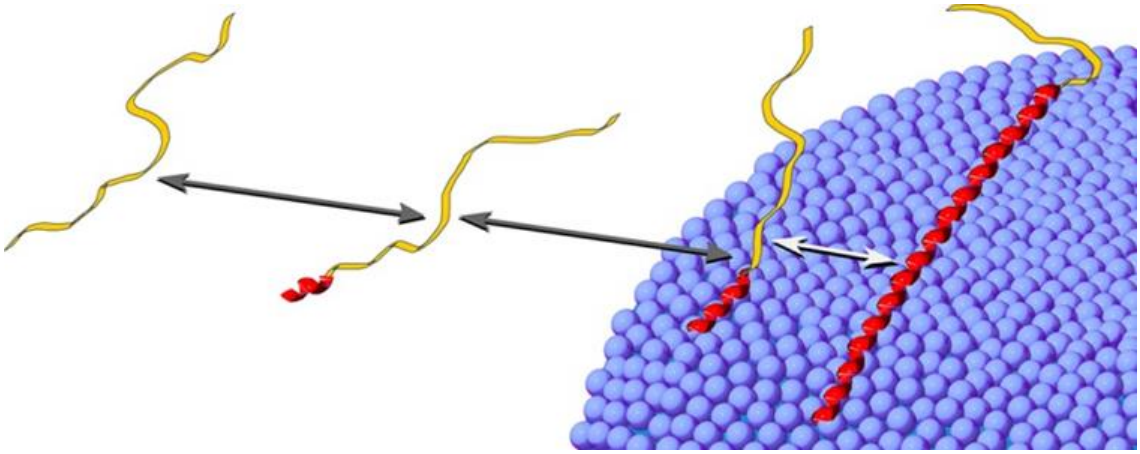


Figure. 1.17. Schematic to show 'initiation-elongation' model of aS binding to vesicles. The N-terminal amphipathic α-helix binds to membranes, initiating elongation of the α-helix and further binding to the membrane. From Maltsev, Ying and Bax, (2012).

1.16 Tyrosine kinase inhibitors

Several drugs used in the treatment of adult cancers are tyrosine kinase inhibitors. Gefitinib is an inhibitor of epidermal growth factor receptor's (EGFR) tyrosine kinase,

Lapatinib is an inhibitor of EGFR and ErbB-2 (HER-2) tyrosine kinases and Nilotinib inhibits Bcr-Abl tyrosine kinase activity. Levels of the tyrosine kinase, Abl, are increased in the nigrostriatal region of PD patients and in mouse models lentiviral expression of aS lead to Abl activation and lentiviral expression of Abl increased aS levels (Hebron, Lonskaya and E-H Moussa, 2013). In mouse models, tyrosine kinase inhibitors, including Nilotinib, have been shown to reduce brain and peripheral aS (L. Hebron, 2014). *In vitro* studies have shown that c-Abl exclusively phosphorylates tyrosine 39 of aS, which falls within the range of point mutations, A30P to A53T/A53E, which are linked to familial PD and dementia with Lewy bodies,.

1.17 Bacterial Membranes

Bacteria are divided into two groups according to their cell wall structure, Gram +ve bacteria retain the primary Gram stain, crystal violet, within the thick peptidoglycan wall following an alcohol wash step and so appear purple viewed on a microscope whereas Gram –ve bacteria loose the crystal violet stain, which is not held in the thin peptidoglycan layer and take up the second Gram stain, safranin, and so appear pink viewed on a microscope (**Figure 1.18**). These two groups also differ in several other ways, most significantly Gram +ve bacteria only have one membrane, whereas Gram –ve bacteria have both an inner and outer membrane which enclose the periplasmic space. The outer membrane is an asymmetrical bilayer composed of an inner phospholipid layer and outer lipopolysaccharide layer, the outer membrane also contains porins. Different bacterial species contain different membrane lipid compositions which can also change according to environmental conditions. *E. coli* as used in this study have three major membrane lipids, phosphatidylethanolamine, phosphatidylglycerol and cardiolipin, but also contain several other lipopolysaccharides including, lysophosphatidic acid, phosphatidic acid and phosphatidylserine (Sohlenkamp and Geiger, 2016). Bacterial membranes contain structures similar to the lipid rafts found in eukaryotic cells. These structures called functional membrane microdomains consist of two structural elements polyisoprenoid lipids and flotillin,

which acts as a scaffold protein. The third functional component is the protein cargo, which consists of a number of functional membrane microdomain associated proteins that oligomerise into functional complexes and signal transduction cascades (Lopez, 2015). The periplasm can contain more than 300 proteins and is essential for the maturation of many proteins which are translocated into the periplasm in an unfolded state. Both membranes contain many different proteins which perform a wide variety of functions.

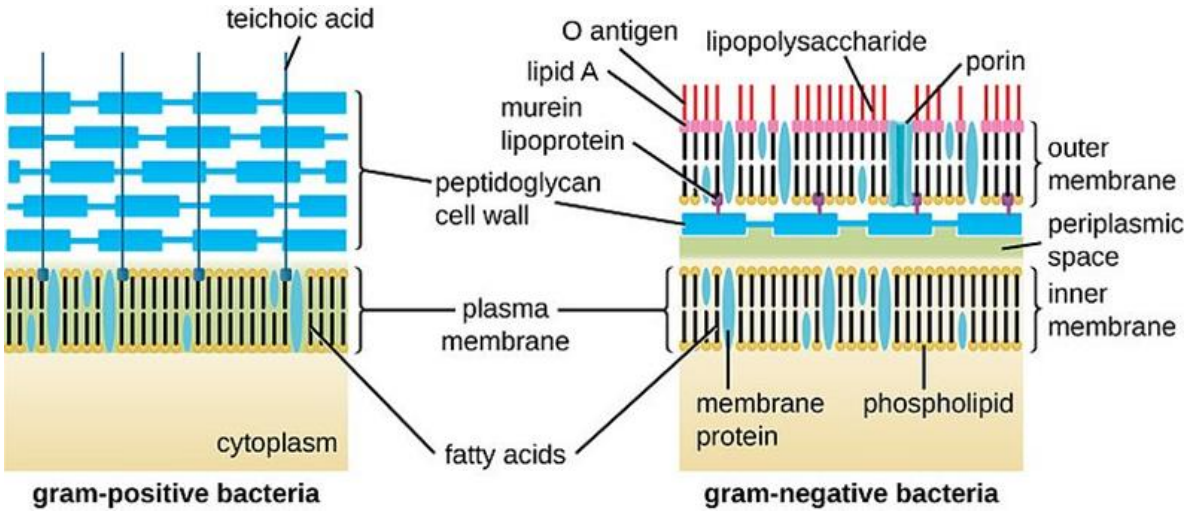


Figure. 1.18. Schematic to show the differences between Gram +ve and Gram –ve bacteria cell wall structure. From www.easybiologyclass.com.

Three membrane proteins were utilised during this investigation:

Cytochrome d, encoded for by CydAB

CydAB encodes for CydA which is the cytochrome d, subunit I, and CydB which is the cytochrome d, subunit II, together they form an inner membrane trans membrane complex. In proteobacteria a third approximately 4kDa subunit, CydS, which has a crucial role in enzyme activity is also present, this was not included in the construct used in this investigation. Cytochrome d is an aerobic terminal oxidase that catalyses the oxidation of ubiquinol-8 and the reduction of oxygen to water (Safarian *et al.*,

2016). For use in this investigation the fluorophore mCherry was attached to the C-terminus.

OmpA

Outer Membrane protein A (OmpA) is one of the major outer membrane proteins of *E. coli,* it has multiple structural and physiological functions including as a bacteriophage receptor, participating in biofilm formation and in maintaining cell shape and stability. OmpA is thought to exist as a two-domain structure, with 171 N-terminal residues creating an eight β-barrel narrow pore in the outer membrane with 154 C-terminal residues remaining in the periplasm, where they associate with the peptidoglycan layer (Koebnik, Locher and Van Gelder, 2000). However there appears to be some disagreement as to whether this is the native state (Reusch, 2012). The fluorophore mCherry was attached to the C-terminus for use in this investigation.

MinD

MinD forms part of the MinCDE System which is involved in division site placement in bacteria and chloroplasts, it is the best conserved of the Min proteins being found in bacteria, archaea and eukaryotes (Rothfield, Shih and King, 2001). MinD associates with the inner membrane of *E. coli*, this localisation is mediated by a highly conserved sequence at the C-terminal region of the protein which is predicted to form an amphipathic helix (Szeto *et al.*, 2002). Due to the C-terminus being essential for membrane binding, fluorophores were only attached to the N-terminal of this protein.

1.18 Bacterial membrane vesicles

Several different forms of extracellular bacterial membrane vesicles (MV) have been described. The best known of these are Outer-membrane vesicles (OMV) which are formed by the outer membrane of Gram-negative bacteria blebbing. Outer-inner membrane vesicles (OIMV) are proposed to be formed by explosive cell lysis, where OIMV contain chromosomal DNA or by autolysin weakening of the peptidoglycan layer

allowing the inner membrane to protrude through the periplasm enabling cytoplasmic cell contents to enter the vesicle before it is pinched off from the cell surface with a surrounding outer membrane. Explosive outer membrane vesicles (EOMV) are formed by self-assembly of shattered membrane fragments and randomly contain cytoplasmic contents. Cytoplasmic membrane vesicles (CMV) are formed by Gram-positive bacteria and contain cytoplasmic contents (Toyofuku, Nomura and Eberl, 2019) (**Figure 1.19**). These naturally occurring bacterial MVs range in size from 20 to 400 nm and affect biological processes including virulence, horizontal gene transfer, export of cellular metabolites, phage infection and cell to cell communication.

Neurone-like cells overexpressing aS, can secrete aS within exosomes (Lööv *et al.*, 2016), a form of extracellular vesicle released on exocytosis of a multivesicular body (Cocucci and Meldolesi, 2015).

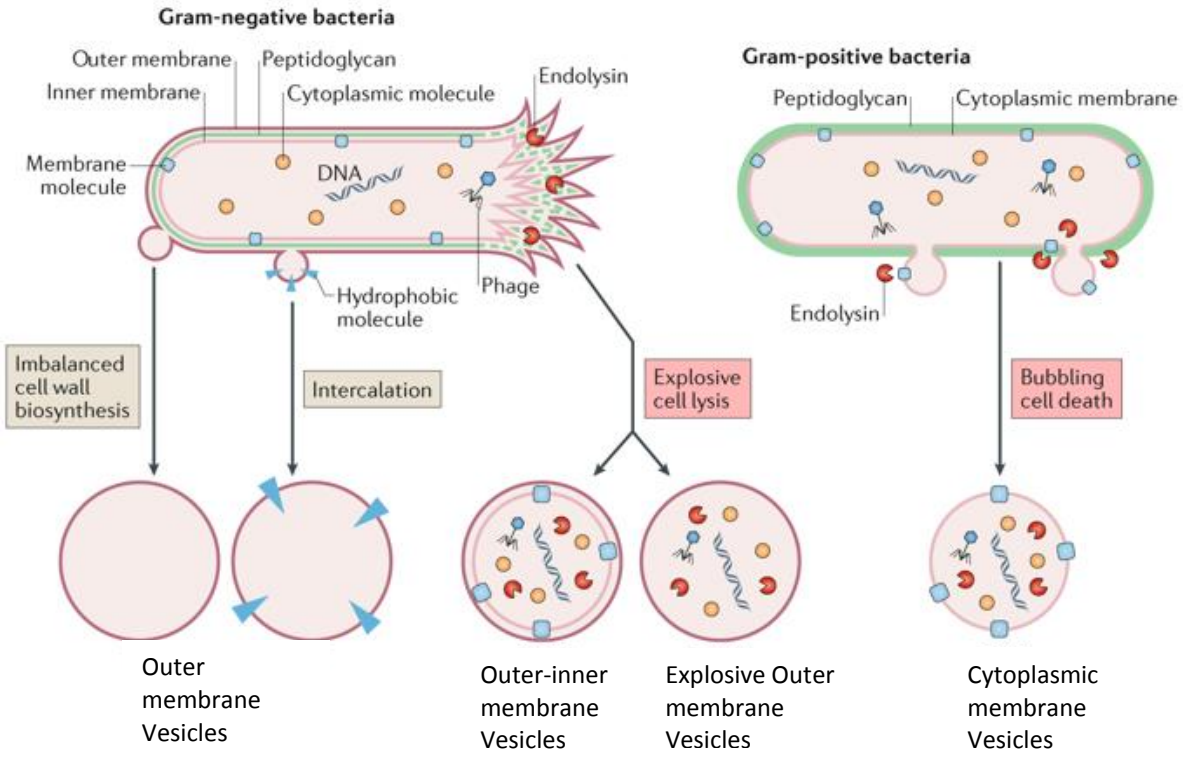


Figure. 1.19. The formation of different types of bacterial membrane vesicles. Adapted from Toyofuku, Nomura and Eberl, (2019).

1.19 Microscopy techniques

1.19.1 Live cell Imaging

Live cell imaging is used to investigate cellular dynamics and combined with fluorescent microscopy is used to investigate protein localisation and interactions within live cells. Fluorescent dyes which can be used to fluorescently stain specific structures and the use of fluorescent proteins, which can be expressed attached to proteins of interest, can be used to visualise the location of these structures and proteins within live cells. The wide range of different colour dyes and fluorescent proteins available, means that when combined with time lapse imaging, the movements and co-localisation of proteins can be observed. During live cell imaging it is important to consider cell viability. The environment of the cell must be maintained with regard to media and temperature, so as not to induce stress responses, which can alter the cellular process of interest. Over expression of fluorescent proteins can also cause a stress response. Care must also be taken not to induce stress due to the light being used. Ultra violet light can damage DNA, infrared light can cause localised heating and fluorescent excitation can cause phototoxicity (Ettinger and Wittmann, 2014).

1.19.2 Widefield Microscopy

In widefield microscopy, the whole specimen on the microscope stage is exposed to a light source, either white light for brightfield microscopy or of a specific wavelength, for fluorescent microscopy. Microscopes can be standard upright or in an inverted configuration, with a camera attached. Samples can emit fluorescence outside of the focal plane of the objective which can make the capturing of fine detail above out-of-focus signal difficult, in particular with thicker samples.

1.19.3 Spinning Disk Confocal Microscopy

In confocal microscopy, out-of-focus light is rejected by using a pinhole. Only light from the focal plane is able to pass through the pinhole, cutting out, out of focus fluorescence from above and below the focal plane, allowing imaging of discreet optical regions in thicker samples (**Figure 1.20 inset**)

In spinning disk microscopy, a disk is used with multiple pinholes arranged so that when it rotates this allows every part of a sample to be imaged (**Figure 1.20**). This allows rapid imaging of samples compared with scanning confocal microscopy and is more suitable for imaging live samples.

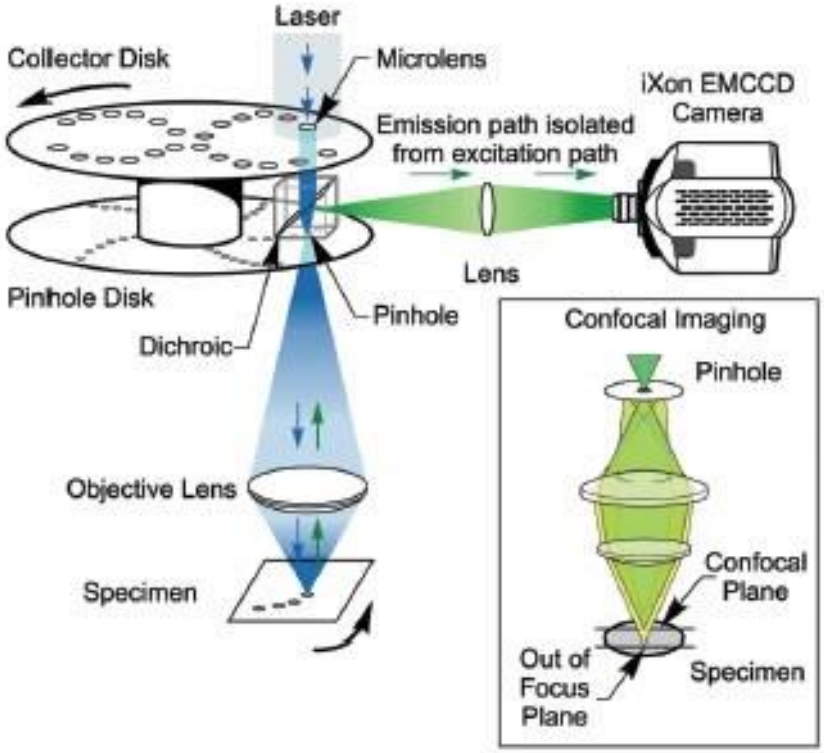


Figure. 1.20. Schematic drawing of a spinning disk confocal microscope.
From Oxford Instruments Learning centre.
(https://andor.oxinst.com/learning/view/article/spinning-disk-confocal).

1.19.4 Structured Illumination Microscopy (SIM)

SIM is a super resolution microscopy technique which enables the acquisition of images with approximately double the resolution of a conventional fluorescent microscope Optical diffraction imposes a limit on resolution in the conventional microscope, which is doubled in SIM. Confocal fluorescent microscopes can achieve resolutions of approximately 200-250nm, SIM however can achieve a resolution of approximately 100nm (Reusch, 2012)

SIM is a widefield microscopy technique which involves imaging a grating onto the sample to produce Moiré fringes. An algorithm is then used to analyse the data

produced, resulting in an image, enabling more fine structure to be observed. This technique is comparatively fast with imaging in the order of seconds and uses much lower laser powers than other Super resolution microscopy techniques and hence is suited to applications where limiting phototoxicity is important, such as when imaging live cells.

1.19.5 Super-Resolution Radial Fluctuations (SRRF)

SRRF is an analytical program which can be used for live cell super-resolution imaging. A sequential series of frames of an imaged structure is required as the input data, this can be acquired using a range of different microscopes (Culley *et al.*, 2018).

1.19.6 Deconvolution

Deconvolution is the use of a computer algorithm to either subtract or reasign out of focus blur from a fluorescent microscopy image (Wallace, Schaefer and Swedlow, 2001).

1.20 Forster Resonance Energy Transfer (FRET) and Fluorescence Lifetime Imaging (FLIM)

FRET is a method which can be used to investigate the distance between two fluorophores when they are within close proximity (<10nm). FRET occurs when the emission spectra of a donor fluorophore overlaps the excitation spectra of an acceptor fluorophore. When these two fluorophores are in close proximity and are exposed to light at the excitation wavelength of the donor fluorophore, non-radiative energy transfer occurs between the fluorophores resulting in the acceptor fluorophore fluorescing and a decrease in the donor fluorophore fluorescence lifetime (De *et al.*, 2015). Various fluorophore pairings may be used in FRET investigations (Bajar *et al.*, 2016).

FLIM is a way of examining FRET at a single molecule level with minimal variation, measurements taken monitor the fluorescent lifetime of a single donor fluorophore. A

short pulse of light is used to excite the donor fluorophore with either a single photon or two photons where non-linear absorption of two or more photons with a longer wavelength is used. Photodamage is reduced in live cells by using longer wavelengths to excite the donor fluorophore (Peter and Ameer-Beg, 2004). FLIM has been used previously to investigate aS oligomerisation within H4 neuroglioma cells (Klucken *et al.*, 2006)

1.21 Biomolecular Fluorescence Complementation (BiFC)

BiFC is a method which involves attaching half a fluorophore to a protein and the complementary half of the same fluorophore to a protein which is believed to interact with the first protein. These can be two different proteins or separate copies of the same protein. If the two proteins interact, the two halves of the fluorophore are brought into close proximity and can reform creating a functional fluorophore. Several different fluorophores have been used including eYFP, eCFP, Citrine, Venus, cerulean and eGFP (Shyu *et al.*, 2006; Outeiro *et al.*, 2008). BiFC is most commonly used with fluorescent microscopy to visualise the cellular localisation of protein interactions within live cells. Within this investigation, BiFC was used in conjunction with a fluorescent plate reader to examine differences in levels of fluorescence within whole cell cultures over time. This method enables a continuous measurement of differences in protein-protein interaction over several hours within live cell cultures and by taking simultaneous OD_{595} measurements these interactions can be compared to cell growth. Within this investigation an improved Venus BiFC construct was used (Yutaka Kodama and Hu, 2010). A pET DUET plasmid was used to simultaneously produce aS-N-Venus (aS attached at its C-terminal to the first 154 amino acids of the Venus fluorophore) and aS-C-Venus (aS attached at its C-terminal to the Venus fluorophore, amino acid 155 to the end). Results obtained in this investigation suggest that if an aS oligomer forms in a parallel conformations it can bring the two halves of the fluorophore together, enabling the production of yellow Venus fluorescence or if anti-parallel oligomer formation occurs, holding the two halves of the fluorophore apart, this prevents the

formation of Venus fluorescence. A previous study into aS oligomerisation, using GFP-BiFC observed a lower level of fluorescence on oligomer formation when using C-terminally tagged aS, compared to when they used one C-terminal tag and one N-terminal tag joined to aS with a linker region, the method used predominantly within their study, which was carried out using eukaryotic cell lines (Outeiro *et al.*, 2008). In this investigation aS was only tagged at the N-terminal to allow the effect of Nt-acetylation to be studied.

1.22 Optogenetics

Optogenetic methods such as the Phy-Pif system used in this investigation use light to control cells. The Phy-Pif system uses a light controllable binding interaction between a fragment of *Arabidopsis thaliana* phytochrome B (PhyB) and a fragment of phytochrome interaction factor 6 (Pif6) in the presence of phycocyanbilin (PCB) (Toettcher *et al*, 2011). Phy B becomes light-responsive following conjugation with the membrane-permeable small molecule chromophore PCB. Once light responsive, PhyB associates with Pif6 when exposed to 650 nm red light and disassociated upon exposure to 750 nm far red light. By anchoring the larger PhyB to specific areas of the cell, for example to the plasma membrane (Levskaya *et al.*, 2009) or mitochondria (Jost and Weiner, 2015) proteins attached to Pif6 can be sequestered from other areas of the cell by exposure to 650 nm red light, due to the PhyB-Pif6 association. The sequestered proteins can then be released by exposure to 750 nm far red light.

1.23: Aim of this project

The aim of this project was to investigate the effect of Nt-acetylation on the oligomerisation and membrane interactions of aS and to attempt to identify a *naa-80* knockout specific phenotype in *C. elegans*.

CHAPTER 2: MATERIALS AND METHODS

2.1: Media and Buffers

A. C. elegans Lysis buffer	Final concentration
Potassium chloride	50mM
Tris (pH 8.3)	10mM
Magnesium chloride	2.5mM
NP40	0.45%
Tween20	0.45%
Gelatin	0.01%
Add proteinase K to a final concentration of 0.1mg/ml before use.	

B. Coomassie gel Destain	Final concentration
Methanol	50%
Acetic acid	10%

C. Coomassie stain	Final concentration
Coomassie brilliant blue	0.1%
Methanol	50%
Acetic acid	10%

D. FPLC Buffer A		Final concentration
Tris Base	2.42g	20mM
Make up to 1L with distilled water whilst adjusting to pH7.5		

E. FPLC Buffer B		Final concentration
Tris Base	2.42g	20mM
Sodium Chloride	58.44g	1M
Make up to 1L with distilled water whilst adjusting to pH7.5		

F. His tag Binding buffer		Final concentration
Tris Base (1M stock)	5ml	50mM
Sodium Chloride (5M stock)	10ml	500mM
TritonX100	1ml	1%
Imidazole (1M stock)	1ml	10mM
Make up to 100ml with distilled water whilst adjusting to pH7.8		
Add PMSF just before use		1mM

G. His tag Elution buffer		Final concentration
Tris Base (1M stock)	5ml	50mM
Sodium Chloride (5M stock)	10ml	500mM
Imidazole (1M stock)	15ml	150mM
Make up to 100ml with distilled water whilst adjusting to pH6.0		

H. His tag Wash buffer		Final concentration
Tris Base (1M stock)	5ml	50mM
Sodium Chloride (5M stock)	10ml	500mM
TritonX100	1ml	1%
Imidazole (1M stock)	1ml	10mM
Make up to 100ml with distilled water whilst adjusting to pH6.0		

I. Luria Bertani (LB) medium	
Distilled water	1L
Sodium Chloride	10g
Tryptone	10g
Yeast extract	5g
Agar (optional- if solid media required)	15g
Antibiotic (as appropriate, added after autoclaving)	25 to 100μg/ml as appropriate

J. M9 salts (for use with C. elegans)	
Disodium hydrogen phosphate	7g
Potassium dihydrogen phosphate	3g
Sodium chloride	5g
Magnesium sulphate	0.25g
Make up to 1L with distilled water	

K. M9 salts (for use with *E. coli*)	
Disodium hydrogen phosphate	12.8g
Potassium dihydrogen phosphate	3g
Sodium chloride	0.5g
Ammonium Chloride	1g
Make up to 1L with distilled water	

L. Nematode Growth Medium (NGM) agar	
Distilled water	1.6 L
Sodium Chloride	4.8 g
Agar	27.2 g
Bactopeptone	4 g
Once cooled to 50°C post Autoclaving	
Potassium dihydrogen phosphate pH6	40 ml of 1M
Magnesium sulphate	1.6 ml of 1M
Calcium chloride	1.6 ml of 1M
Cholesterol (in Ethanol)	1.6 ml of 5 mg/ml

M. PBS		Final concentration
Phosphate buffer		10mM
K_2HPO_4	1.82g	
KH_2PO_4	0.23g	
Sodium Chloride	8.7g	150mM
Make up to 1L with distilled water whilst adjusting to pH7.4		

N. PIP Strip® Blocking buffer	Final concentration
1xPBS	
Tween 20	0.1%
BSA	3%

O. PIP Strip® Wash buffer	Final concentration
1xPBS	
Tween 20	0.1%

P. Protein loading buffer	Final concentration
Tris –HCl pH6.8	50mM
SDS	2%
Glycerol	10%
Mercaptoethanol	1%
EDTA	12.5mM
Bromophenol blue	0.02%

Q. TAE buffer	Final concentration
Tris base	0.4mM
Glacial Acetic acid	0.4mM
EDTA	0.01mM

R. Tris Running buffer for SDS Page gels	
Tris Base	3g
Glycine	14.4g
SDS	1g
Make up to 1L with distilled water	

S. Western blot detection buffer		Final concentration
Tris pH9.6	4ml of 1M	100mM
Sodium Chloride	800ml of 5M	100mM
Magnesium Chloride	200ml of 1M	5mM
Make up to 40ml with distilled water		

T. Western blot milk solution	
Milk powder	1.5g
1x PBS	50ml
Tween20	100µl

U. Western blot transfer buffer		Final concentration
Tris Base	3g	25mM
Glycine	14.4g	200mM
Make up to 1L with distilled water		

Table 2.1. Media and buffer recipes used in this investigation

2.2: Cell Culture Techniques

2.2.1: *E. coli* cultures

E. coli cultures were grown at 37 ^{o}C unless otherwise stated, in Luria Bertani (LB) broth (**Table 2.1. I**.), with shaking at 120 rpm. Plasmid selection was achieved by addition of the appropriate antibiotic. Selection antibiotics used were diluted 1 in 1000 to their final concentration from stock solutions of, Ampicillin at 100 mg/ml in distilled water, Chloramphenicol at 25 mg/ml in ethanol or Kanamycin at 50 mg/ml in water.

2.1.2: Preparation of competent cells

Strains of *E.coli* (either DH10β, BL21DE3 (**Table 2.6**), or BL21DE3 transformed with plasmids 310 or 657 (**Table 2.8**)), were streaked out onto LB agar plates, containing the appropriate antibiotic if the cells possessed a plasmid and grown at 37 ^{o}C overnight. From this, a single colony was inoculated into 5 ml of LB medium with antibiotic where required and grown with shaking at 120 rpm, at 37 ^{o}C overnight. 0.5 ml of this pre culture was then inoculated into 50ml of fresh LB medium with appropriate antibiotics and grown with shaking at 120 rpm at a temperature of 37 ^{o}C until an OD_{600} of 0.6 to 0.8 was reached. The cells were cooled on ice for 10 minutes, before being centrifuged at 1000 rcf at 4^{o}C for 10 minutes. The pelleted cells were resuspended in 10 ml of ice cold 0.1M $CaCl_2$ (filter sterilised)/10%Glycerol sterile solution and kept on ice for a further 15 minutes. The cells were then centrifuged again at 1000 rcf at 4 ^{o}C for 10 minutes. The pelleted cells were resuspended in 1 ml of the 0.1 M $CaCl_2$ / 10 % Glycerol solution and 50 μl aliquots (in 500 μl sterile prefrozen -80 ^{o}C tubes) were frozen in liquid nitrogen, then stored at -80 ^{o}C.

2.2.3: Transformation of chemically competent *E. coli*

An aliquot of chemically competent cells were defrosted on ice, then up to 5µl of plasmid was added and stirred gently with a sterile pipette tip. Cells were incubated on ice for 30 minutes, heat shocked for 90 seconds at 42 ^{o}C and immediately returned to ice for 2 minutes. 100 µl of LB medium was added to the cells which were then incubated in a shaking incubator (120 rpm) at 37 ^{o}C for 1 hour. Cells were plated onto LB agar supplemented with the appropriate antibiotic and incubated at 37 ^{o}C overnight.

2.2.4 Starter cultures

5 ml starter cultures were prepared the afternoon prior to assays being carried out using *E. coli* cell cultures. Appropriate plasmid selection antibiotics were added to 5 ml of LB broth which was then inoculated with a single colony from a transformation plate. This was incubated at 37^{o}C with shaking at 120 rpm overnight to produce a cell culture that has reached stationary phase.

2.2.5: Acquisition of growth curves

Growth curves were obtained using a CLARIOstar fluorescent plate reader. Overnight 5ml starter cultures were used to inoculate LB broth with appropriate selection antibiotics which was then incubated at 37 ^{o}C with shaking at 120 rpm until mid log phase growth was reached. This log phase culture was sub cultured to the required starting OD_{595} of either 0.1 or 0.01 in LB broth, with appropriate antibiotics. Isopropyl β-D-1-thiogalactopyranoside (IPTG) was added to the cultures as required and 200ml of cell culture was added to the required wells of a sterile 96 well plate, with any required additions. A lid was placed on the plate and sealed with parafilm to reduce evaporation. The plate was incubated in the plate reader at 37^{o}C with shaking between readings, which were taken every 15 minutes.

2.2.6: Staining live cells with Congo red and NIAD-4

Cell cultures were induced as for small scale protein expression, for the last hour of induction 1 µl per ml of cell culture of either 1 % Congo Red in sterile distilled water or 2.5 % NIAD-4 in DMSO was added.

2.2.7: Purification of vesicles from cell culture

Vesicles were purified from cell cultures, for analysis by Dynamic light scattering (DLS) and fluorescent microscopy. 1 ml samples were taken from cell cultures and centrifuged at 1000 rcf for 30 minutes. The vesicle containing supernatant was gently removed by pipetting.

2.3: Protein expression and purification

2.3.1: Small-scale protein expression for preparation of cell extracts and live cells for imaging

Overnight 5 ml starter cultures were used to inoculate LB broth at a ratio of 1 in 50 with appropriate selection antibiotics, this was then incubated at 37 ^{o}C with shaking at 120 rpm until an OD_{595} of 0.4 to 0.5 was reached. IPTG was then added to a final concentration of 100 or 20 μg/ml or Rhamnose at a concentration of 0.01 % unless stated otherwise. After the required period of time, cells were prepared for imaging or 1 ml samples were taken for cell extract preparation for protein gels following measurement of OD_{595}.

2.3.2: Preparation of cell extracts for Coomassie Blue stained SDS-PAGE gels and western blots

1 ml samples were taken from the *E. coli* cell culture to be examined and their OD_{595} measured. The cells were then centrifuged at 0.8 rcf at 4 ^{o}C for 5 minutes and the supernatant removed, pelleted cells were then frozen at -20 ^{o}C. Defrosted pellets were then resuspended in 1 x Phosphate Buffered Saline (PBS) buffer according to the OD_{595} measured, e.g. a pellet from a culture with an original OD_{595} of 1.2 would be resuspended in 120 μl of 1 x PBS.

2.3.3: Precipitation of protein from cell cleared media

Protein was precipitated from the supernatant removed from centrifuged cell cultures during the preparation of cell extracts. 400 µl of the supernatant was placed in a 2 ml tube with 1.6 ml of acetone, this was then frozen at -80 ^{o}C. On thawing precipitated protein was centrifuged at 16100 rcf at 4 ^{o}C for 30 minutes, and pellet dried. The pellet was resuspended in 40µl of 1 x PBS ready for analysis.

2.3.4: Large-scale expression of protein for purification of aS-Cerulean3-His_6

1ml of an overnight starter culture was used to inoculate 1L of LB broth with appropriate antibiotic in a sterile 2 L conical flask, this was incubated with shaking at 120 rpm, at 37 ^{o}C. Once the culture reached an OD_{595} of 0.4 to 0.5, protein production was induced by the addition of IPTG to a final concentration of 20 µg/ml and then incubated with shaking at 120 rpm at 25^{o}C for a further 2 to 3 hours. The cell culture was then spun at 1800 rcf for 20 minutes and the resultant cell pellet was frozen at -20 ^{o}C.

2.3.5: His tag purification of aS-Cerulean3-His_6

Frozen cell pellets were defrosted on ice and then resuspended in 16ml of *His* tag Binding buffer (**Table 2.1, F**). The cells were sonicated on ice for a total of 2 minutes, made up of 20 second pulses with a 59 second gap between them. The resulting suspension was then centrifuged at 4400 rcf for 30 minutes and the protein containing supernatant kept.

A Cobalt column was prepared for *His* tag purification by sealing a 5 ml syringe with glass wool, approximately 3 ml of TALON® Superflow metal affinity resin, from Clontech laboratories Inc, was then added to the syringe. This Cobalt purification column was equilibrated with approximately 5 volumes of *His* tag binding buffer. The buffer ran through the column by gravity and the flow was stopped by placing a cap on the syringe. At no time was the column allowed to run dry.

The protein-containing supernatant was loaded onto the pre-equilibrated column, all liquid that flowed through the column was collected in case not all the protein bound to the column. Once the protein had bound to the Cobalt column it was washed with 5 resin volumes of His tag binding buffer (**Table 2.1, F**.) followed by 5 resin volumes of His tag wash buffer(**Table 2.1, H.).** Protein was then eluted from the Cobalt column by the addition of His tag elution buffer (**Table 2.1, G.).** The elution buffer flow through was collected in 1ml fractions until the column had returned to a bright pink colour and the flow through returned from green to colourless. The presence of aS-mCerulean3-His_6 in the fractions was confirmed SDS-PAGE analysis, alternatively if placed in UV light the mCerulean3 containing fractions were seen to fluoresce.

The aS-mCerulean3-His_6 containing fractions were pooled for further purification by FPLC.

2.3.6: Purification of aS-Cerulean3-His_6 by Fast Protein Liquid Chromatography (FPLC)

Due to the high salt content of the His tag elution buffer, the aS-mCerulean3-His_6, pooled post His tag purification protein, was first dialysed into aS FPLC buffer A (**Table 2.1, D.**) prior to further purification by FPLC.

The dialysed protein was then purified by FPLC. The samples were run through a 5 ml HiTrapQ ion exchange column using a GE Healthcare, AKTA FPLC system, bound protein was then eluted from the column using an increasing concentration gradient of FPLC Buffer B (**Table 2.1, E.).** Protein containing fractions were determined by absorbance at 260 nm and 280 nm and this was confirmed by fluorescence when exposed to UV light.

2.4: Biochemistry Techniques

2.4.1: Gel electrophoresis of proteins

Protein samples were analysed by gel electrophoresis using 10 % or 17.5 % SDS-PAGE gels. Gels were cast using a BioRad minPROTEAN® 3 System

	10 % resolution gel	17.5 % resolution gel	Stacking gel
Distilled water (ml)	2.55	0.15	7.0
1.5M Tris pH8.7 (ml)	3.75	3.75	0
1M Tris pH6.8 (ml)	0	0	1.25
10%SDS (µl)	100	100	50
30% Acrylamide (ml)	3.2	5.6	1.7
APS (µl)	100	100	50
TEMED (µl)	15	15	15

Table 2.2. Recipe table for SDS Page gels.

The appropriate percentage resolution gel was mixed (**Table 2.2**) and pipetted between two clean, glass casting plates, to just below the level of the comb insert. Isopropanol was gently pipetted onto the surface to level the gel interface. The resolving gel was then allowed to set at 37 ^{o}C. Once the gel was set the isopropanol was poured off and the surface of the resolving gel rinse 6x with distilled water. The Stacking gel was then mixed (**Table 2.2**) and pipetted onto the resolving gel and a well forming comb inserted into the stacking gel, which was then allowed to set at 37 ^{o}C. Gels were run in Tris running buffer (**Table 2.1, R.)**

Protein samples, cell extracts or purified protein, were mixed 4 parts sample to 1 part 5x Protein loading buffer (**Table 2.1, P.)** and heated at 95 ^{o}C for 30 minutes with vortexing. 10 µl of each sample was run alongside 5 µl of Thermo Scientific PageRuler Unstained Protein Ladder (Catalogue number #26614), at 150 volts for 50 minutes.

When gels were for use in Western Blotting, Thermo Scientific PageRuler Prestained Protein Ladder #26616 or Bio-Rad Kaleidoscope Prestained Standards were used.
Bands were visualised when required using Coomassie Blue stain, gels were placed in Coomassie Blue stain (**Table 2.1, C.)** for at least 1 hour and then in Coomassie Blue gel destain (**Table 2.1, B.)** for at least 24 hours.

2.4.2: Western Blot

Gels were run as outlined above and protein then transferred to a methanol activated PVDF, Imobilon®P Transfer Membrane, using a Bio-Rad Trans-Blot®Semi-Dry Electrophoretic Transfer Cell, following the manufacturer's protocols at 10 volts for 30 minutes, using western blot transfer buffer (**Table 2.1, U.).** The membrane was blocked using western blot milk solution (**Table 2.1, T**.) at room temperature for 1 hour. The membrane was then incubated in milk solution with primary antibody diluted 1 in 1000 (abcam ab155038) anti aS primary antibody at room temperature for 1 hour. The membrane was rinsed four times in 1 x PBS before having milk solution added until the membrane was just covered. 2µl of secondary antibody, anti-rabbit IgG Alkaline Phosphatase produced in goat (Sigma A9919) was added and this was incubated at room temperature for 1 hour. The membrane was then rinsed with 1xPBS and then covered with fresh, Western Blot Detection Buffer (**Table 2.1, S**.) for 5 minutes. 1 ml of BCIP®/NBT Purple liquid substrate from Sigma, was then added and colour allowed to develop to visualise antigen on the membrane.

2.4.3: Lipid binding assays using PIP Strips™ Membranes

The membrane was first blocked by covering the membrane with 5-10 ml of PIP Strip® Blocking buffer (**Table 2.1, N.)** and gently agitated for 1 hour at 25 °C or overnight at 4 °C. The blocking buffer was poured off and protein added at a concentration of 0.5 µg/ml in 5-10 ml of fresh Blocking buffer and incubated for 1 hour at room temperature with gentle agitation. The protein solution was poured off and the membrane washed with 5 ml of Wash buffer with gentle agitation at 25°C for 10 minutes, this was repeated three times. Primary antibody (abcam ab155038) anti-alpha-Synuclein primary

antibody was added, diluted 1:1000 in the PIP Strip® blocking buffer and incubated for 1 hour at 25°C with gentle agitation. The membrane was then washed three times with 5 ml of PIP Strip® wash buffer (**Table 2.1, O.).**

The wash buffer was discarded and secondary anti-rabbit antibody was added to the membrane diluted 1 in 1000 in blocking buffer and then incubated for 1 hour at 25°C or overnight at 4°C with gentle agitation. The membrane was then again washed three times in 5 ml wash buffer and then rinsed in 1xPBS. The membrane was covered with fresh western blot Detection buffer (**Table 2.1, T.)** for 5 minutes, then transferred to an empty dish and washed with 1 ml of BCIP®/NBT Purple liquid substrate from Sigma, until colour developed visualising the presence of aS on the lipid. The membrane was then washed three times in distilled water and scanned.

2.4.4: Size Exclusion Chromatography (SEC)

Size exclusion chromatography (SEC) also known as gel filtration is used to separate molecules according to differences in size. The SEC media consists of spherical particles with pores of different sizes. As a sample passes through a column packed with SEC media small molecules enter these pores slowing their passage through the SEC media. Large molecules are therefore eluted from the column faster that smaller molecules (GE Healthcare, 2015) (**Figure 2.1**). Size exclusion assays were carried out with the help of Dr Karen Baker (University of Kent), using a Superdex75 10/300 column (24ml volume) run at 0.75 ml/min using PBS.

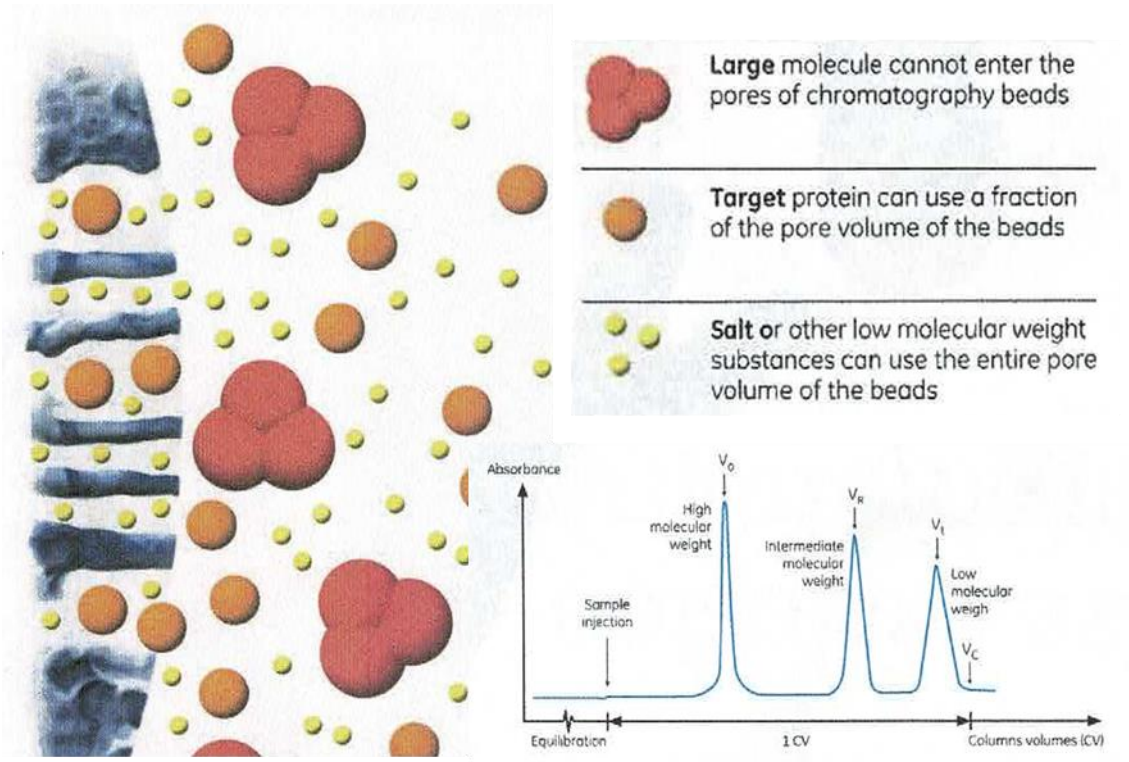


Figure 2.1. Schematic of a size exclusion column (SEC). SEC media consists of spherical particles with pores of different sizes. Small molecules enter these pores slowing their passage through the SEC media. Large molecules are therefore eluted from the column faster that smaller molecules (GE Healthcare, 2015).

2.4.5: Isothermal Titration Calorimetry (ITC)

Isothermal titration calorimetry (ITC) is a technique used to study protein binding for example to examine interactions with drugs, ITC directly measures the energy associated with a chemical reaction triggered by the mixing of two components. In this process two identical cells. A reference cell is used as a control and contains the buffer in which the sample is dissolved. Proteins to be studied are placed in the sample cell and ligand is titrated into the sample cell in precisely known aliquots. An exothermic reaction causes the temperature in the sample cell to increases upon addition of ligand or to decrease if an endothermic reaction occurs. Sensitive thermopile/thermocouple circuits detect temperature differences between the reference cell and sample cell and the number of microcalories required to maintain equal temperatures between the

sample and reference cells is measured for each aliquot of ligand added. The amount of available protein decreases with each aliquot of ligand added and thus the temperature change on each addition will decrease until saturation is reached. The heat flow pulses are integrated with respect to time, giving the total heat exchanged per injection. The pattern of these heat effects as a function of the molar ratio of the ligand and protein can then be analysed to give the thermodynamic parameters of the interaction under study. ITC was conducted by and data analysed by Charles River Ltd.

2.4.6: Dynamic Light Scattering (DLS)

DLS is a technique that primarily measures the Brownian motion of macromolecules in solution and relates this to the size of these particles. The motion of particles depends on their size, temperature and solvent viscosity, large particles diffuse slowly compared to small particles. To take measurements, a monochromatic beam of light is shone through a solution and light is scattered in all directions as a function of the size and shape of the macromolecules within it, scattering intensity is recorded by a detector. A digital autocorrelator then correlates intensity fluctuations of scattered light with respect to time, to determine how rapidly the intensity fluctuates, which is related to the diffusion behaviour of particles and thus their size (Stetefeld, McKenna and Patel, 2016). DLS measurements were obtained with the help of Nyasha Manyanya (University of Kent), using either a Malvern Zetasizer nano ZS or Anton Paar Litesizer 500 Particle analyser.

2.5: Molecular Biology Techniques

2.5.1. Plasmid DNA purification

5 ml of LB medium with appropriate antibiotic was inoculated with a single colony from a transformation plate and grown with shaking at 120 rpm at 37 ^{o}C overnight. This was then centrifuged at 1000 rcf for 5 minutes and DNA preparation was then carried out using a Qiagen, QIAprep® Spin Miniprep Kit, using the manufacturer's reagents and protocol. This kit is based on an alkaline lysis of bacterial cells followed by the use of a DNA affinity column purification.

2.5.2: Restriction digests of DNA

Restriction digests were carried out, either for isolating DNA to subsequently be gel purified and ligated to form new constructs (large scale digests) or in order to check newly made plasmids produced bands of the correct sizes, after digestion with restriction enzymes, when run on agarose gel (small scale digest). Different restriction enzymes were used depending on the restriction sites present, restriction enzymes and buffers used were manufactured by Promega and New England Biolabs and were used at the concentrations supplied.

A typical small scale digest consisted of:

2 μl DNA at least 0.05 μg/μl

2 μl 10x enzyme buffer

14/15 μl water

1 μl Restriction enzyme 1

1 μl Restriction enzyme 2 (if double digest required)

A Typical large scale digestion consisted of:

10 μl DNA at least 0.05 μg/μl

10 μl 10x enzyme buffer

76/78 μl water

2 μl Restriction enzyme 1

2 μl Restriction enzyme 2 (if double digest required)

2.5.3: Separation of DNA using gel electrophoresis

In order to check the size of DNA fragments, either from small scale check digests or for isolating DNA from large scale digests to subsequently be gel purified, restriction digests of DNA were run on agarose gels. 1 % agarose gels were made by dissolving 1 g of agarose per 100 ml of 0.5x TAE buffer. This was then heated until the solution was completely clear then allowed to cool slightly and poured into a casting tray, where Ethidium Bromide was added to a final concentration of 0.001%. The DNA preparation was then run alongside 5 μl of Bioline Hyperladder™ 1 kb at 50 Volts for 1 hour in 0.5 % TAE buffer (**Table 2.1, Q.**). DNA bands were then visualised under ultraviolet light, using appropriate safety equipment such as a full face UV visor or enclosed UV imaging system.

2.5.4: Gel purification of DNA fragments

DNA from digests or PCR product was run on an agarose gel as described previously and the appropriate band excised from the gel. The gel piece was weighed and then purified using the Quiagen QIAquick® Gel Extraction Kit, using the manufacturer's reagents and protocol.

2.5.5: Klenow treatment for blunt end ligation

Large scale restriction enzyme digests for blunt end ligation were treated with Klenow from Promega to truncate the stepped ends of the DNA. 1 μl of 10mM dNTPs and 1 μl of Klenow were added to the 100 μl digest and incubated at 25^{o}C for 15 minutes. 2 μl of 0.5 M EDTA was then added and incubated at 75 ^{o}C for 20 minutes to denature the

Klenow. The required DNA fragment was then purified by gel electrophoresis and gel purification.

2.5.6: Ligation of DNA fragments

DNA was used for ligations where clear bands of purified DNA fragments could be seen in an agarose gel when compared to bands obtained for Bioline Hyperladder™ 1 kb , concentrations were not measured. Ligations of purified insert fragments and vectors were typically carried out as follows:

4 μl Insert DNA (appropriate amount according to length)
4 μl Vector DNA (at least 0.1μg)
1 μl 10x ligase buffer (Promega)
1 μl T4 DNA ligase (Promega)

2.5.7: Polymerase Chain Reaction (PCR)

PCR was used to amplify genes encoding for target proteins, using Expand™ High Fidelity PCR System reagents from Roche, allowing them to be cloned into bacterial expression systems.

PCR products were ligated into the pGEM T-Easy vector (Promega) or pCR™4-TOPO® (Invitrogen), using the manufacturer's reagents and protocols. An example of this ligation reaction is:
3 μl PCR product
1 μl pGEM T-Easy
4 μl water
1 μl 10x ligase buffer
1 μl T4 DNA ligase
All ligations were kept at 4 ^{o}C overnight before use in bacterial transformations.

2.5.8: Quantitative PCR (qPRC)

qPCR was used to confirm the knock out (KO) of NAA-80 production in *C. elegans* strains. Wearing gloves at all times and keeping reagents on ice, RNA was first extracted from *C. elegans,* followed by production of cDNA and qPCR.

RNA extraction from *C. elegans*

For each biological replicate, three NGM plates (**Table 2.1. L**.), heavily populated with non-starved adult and L4 *C. elegans*, were washed with M9 (**Table 2.1. J**.) into a 15 ml falcon tube. The *C. elegans* were allowed to settle with gravity, then the supernatant carefully removed. 2 ml of M9 was added to wash the *C. elegans* which were again allowed to settle and the supernatant removed. This wash step was repeated twice, leaving no more than 5 minutes between washes. The pelleted *C. elegans* were then transferred into a 1.5 ml Eppendorf tube.

In a fume hood, 300 µL of Trizol was added to each Eppendorf and inverted to mix thoroughly. A Disruptor Genie was then used, 2 x 15 minute cycles, until the *C. elegans* had dissolved. 75 µl of 1-Bromo-3-chloropropane was added within a fume hood and inverted to mix thoroughly. The samples were allowed to rest at room temperature for 3 minutes before centrifugation at 13400 rcf for 15 minutes at 4^{o}C. The top layer, approximately 200 µl, was carefully pipetted into a new Eppendorf tube. An equal volume of isopropanol was added and inverted to mix, this was then left at room temperature for 10 minutes before centrifugation at 13400 rcf for 10 minutes at 4 ^{o}C.

The majority of the supernatant was carefully removed, taking care not to disturb the pellet. The pellet was then washed with 400 µl 70 % ethanol and centrifuged at 15700 rcf for 5 minutes at 4 ^{o}C. As much supernatant as possible was removed from the pellet which was then left to air dry until no supernatant was left. The pellet was then reconstituted in 10 µl distilled water and heated for 10 minutes at 60 ^{o}C to help dissolve the RNA. The extracted RNA was stored at -80 ^{o}C prior to cDNA synthesis.

Complementary DNA (cDNA) synthesis

DNA complementary to the RNA extracted from C. elegans was synthesised using a RevertAid H Minus First Strand cDNA Synthesis Kit from Thermo Scientific, using the manufacturers protocol. For each RNA extract, 2 μg was used as a template.

Quantitative PCR (qPCR) using cDNA

Keeping all reagents on ice a Master mix was prepared for each of the primer sets used (**Table.2.10**). Primers O653 and O654 were used to amplify cDNA coding for NAA-80 together with primer sets for cDNA coding for the genes *Cdc-42, Pmp-3* and Y45F10D.4 as qPCR controls.

Master mix for each primer set

SYBR green	75 μl
Primer mix	6 μl
water	39 μl
Total	120 μl

8 μl of each master mix was added to 14 wells of a 96 well plate. 2 μl of each of the three biological replicates, of each of the 4, *C. elegans* strains being examined and two repeats of 2 μl of distilled water for no sample controls (NSC) was added one of each, to the 14 wells containing master mix. When all 56 samples had been added to wells they were sealed with a film cover, shaken vigorously to mix and centrifuged briefly to ensure samples were at the bottom of each well.

The qPCR was then run using a BioRad CFX system. The cycle used was:

Step	Temperature in ^{o}C	Time in seconds
1	95	120
2	95	20
3	65	20
4	70	20
Repeat steps 2 to 4, 44 times then end.		

Data was analysed using BioRad CFX manager software.

2.5.9: CRISPR-Cas9

CRISPR (Clustered regularly interspaced short palindromic repeats) is a microbial adaptive immune system, which can be targeted to a genomic location of choice by the use of single guide RNA (sgRNA) (Hsu, Lander and Zhang, 2014). In this study, the CRISPR-Cas9 system was used to create *naa-80* knockout strains of *C. elegans* using two sgRNAs to guide cutting of genomic DNA by the Cas9 endonuclease and removing 52 base pairs from the genome. An oligonucleotide donor homology guided repair of the cut genome, introduced an early stop (3 frame stop sequence-TAGATAGATAGA) after Proline 46, within Exon 2. *naa-80* knockout *C. elegans* strains produced using CRISPR-Cas9 were obtained from Knudra Transgenics (Utah USA).

2.5.10: *C. elegans* Genotyping PCR

To confirm the genotype of each new strain of *C. elegans,* produced by crossing N2H with *naa-80* disruption *C. elegans,* a single F2 *C. elegans* was placed onto an individual NGM plate. Once eggs had been laid and larvae started to hatch, the adult parental worm was lysed while keeping the eggs and offspring to continue the lines, until genotype PCR identification of the required line.

Single F2 parental or at least 12, F3 offspring *C. elegans* were placed in 5 µl of *C. elegans* lysis buffer (**Table 2.1, A**.) with 0.1 mM proteinase K within the lids of PCR tubes, the lids were then fixed onto PCR tubes and spun, so that both *C. elegans* and buffer were now in the bottom of the tubes. The “Lysis” protocol on a PCR thermocycler was then used to lyse the *C. elegans*.

Lysis Protocol

Lid temp 105^{o}C

Vol: 5 µl

70^{o}C: 60 min

95^{o}C: 15 min

12^{o}C: hold

A master mix was first prepared by using the following volumes, multiplied by the number of *C. elegans* lysates to undergo genotype PCR plus one (**Table 2.3**).

Master mix- multiply volumes by the number of samples + 1	
PCRBIO Taq Mix Red from PCR Biosystems	10 μl
Primer mix- containing 2μM of each required primer	3 μl
Distilled water	2 μl

Table 2.3. Basic Genotype PCR master mix recipe.

15 μl of Master mix was added to each tube containing *C. elegans* lysate and the lids resealed.

Each sample was then run in a PCR thermocycler following the appropriate protocol for the primer set used (**Table 2.4**).

Time	**Primers 6499 and 5600**	**Primers 6041 and 6500**
60 seconds	**94°C**	**94°C**
30 seconds	**94°C**	**94°C**
30 seconds	**65°C**	**68°C**
60 seconds	**72°C**	**72°C**
	Repeat last 3 steps x32	
7 minutes	**72°C**	**72°C**
hold	**12°C**	**12°C**

Table 2.4. **Optimised Genotype PCR, thermocycler setting.**

The PCR amplified DNA fragments were then separated and visualised using Gel electrophoresis. Samples were run through a 2 % agarose gel with a final concentration of 0.001% ethidium bromide. This was run at 50 V for approximately 2 hours, DNA bands were visualised using UV light (**Table 2.5**).

Primers	N2H	*naa-80* KO
6499+6500	439 bp	399 bp
6041+6500	250 bp	No band

Table 2.5. Expected DNA fragment sizes for each genotype PCR primer pair.

The PCR protocol was optomised for each pair of primers used. Multiple N2H control *C. elegans* were lysed and PCR mixes prepared as above. These were run in a thermocycler using a temperature gradient across the heat block, samples were then run on a 2 % agarose gel to identify the optimum temperature set for DNA fragment amplification.

2.6: *C. elegans* Techniques

2.6.1: Maintenance of *C. elegans* strains

C. elegans strains were maintained on 60 mm petri dishes containing 15 ml of Nematode Growth Medium (NGM) (**Table 2.1, L.)** agar, surface seeded with 200 µl of stationary phase OP50 *E. coli* which has been grown to form a lawn of bacteria to act as a food source for the *C. elegans* (Stiernagle, 2006). Strains were incubated at 20 ^{o}C unless otherwise stated. Strains were kept in a clean, well fed state, for at least two generations prior to use in assays.

2.6.2: Producing and maintaining male *C. elegans*

To produce male N2H *C. elegans* for back crossing with *naa-80* knockout *C. elegans*, NGM plates containing L4 hermaphrodite N2H *C. elegans* were heat shocked at 30 °C for 3-4 hours. All the male offspring produced by the heat shocked parents, were used to set up male maintenance plates. A small amount of OP50 *E.coli* was placed on the

centre of an unseeded NGM plate, approximately 5 males to one L4 hermaphrodite were then placed onto this *E. coli* (Fay, 2013)

This process was repeated to produce male *LifeActmRFP* and *mCh-Act-1 C. elegans* to cross with 6x back crossed, *naa-80* knockout O/C *C. elegans,* to produce strains for imaging.

2.6.3: Back-crossing *naa-80* knockout *C. elegans* into N2H control strain *C. elegans*

Hermaphrodite *naa*-80 knockout *C. elegans* were back crossed with male N2H control strain *C. elegans* six times to achieve >98 % genetic identity with the N2H control strain, using a standard genetic cross protocol (Fay, 2013).

Hermaphrodite *naa*-80 knockout *C. elegans* were placed on a small amount of OP50 *E. coli* with male N2H control strain *C. elegans* in the ratio of at least 1:5. The First generation (F1) progeny were examined, if 25-50 % of the adult offspring were seen to be male the cross was deemed to have been successful. As both parents were homozygous, Either N2H wild type or *naa-80* knockout, the F1 offspring will all be heterozygous.

6, L4, hermaphrodite F1 offspring were then placed on a fresh NGM plate with a lawn of OP50 *E. coli*. These *C. elegans* were allowed to produce second generation offspring (F2). Following Mendilian genetics, 25 % of the F2 generation will be homozygous N2H wild type, 50 % heterozygous N2H wild type and *naa-80* knockout and 25% homozygous *naa-80* knockout. 20 of the F2 *C. elegans* were then individually plated onto separate NGM plates with OP50 and allowed to produce a third generation (F3). The Homozygous F2 *C. elegans* produce identical homozygous (F3) offspring, the heterozygous F2 *C. elegans* produce a mixture of offspring, the same as produced by the F1 generation. As soon as the F3 offspring began to hatch, the F2 parental *C. elegans* were removed from the plates and lysed for genotype PCR using primers 6499 and 6500 to identify homozygous F2 *Naa-80* knockout *C. elegans.* The offspring of these *C. elegans* will all be homozygous for *Naa-80* knockout, now called *naa-80* knockout O/C, following the 6th out cross, and could then be used for further crosses.

After the third and sixth crosses, at least 12 adult F3 *C. elegans* were lysed for each F2 parental line and the lysates were split into two identical samples which were used to preform two separate genotype PCR assays using primer sets 6499 with 6500 and 6041 with 6500, to both check and confirm the genotype of each F3 population (**Figure 2.2**).

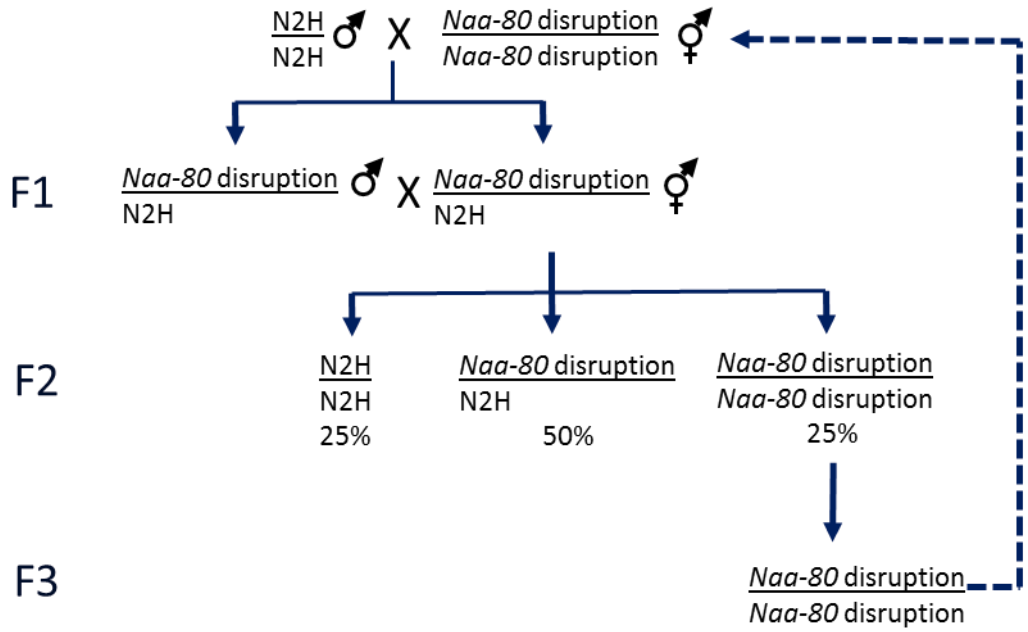


Figure 2.2. Schematic showing the procedure for back crossing of *C. elegans* strains. N2H males were crossed with *naa-80* knockout hermaphrodites. Heterozygous hermaphrodite F1 progeny were allowed to produce a mixed F2 generation. The F3 generation produced by isolated F2 parental *C. elegans* were analysed by Genotype PCR to identify homozygous *naa-80* disruption lines, which were then used for the following cross. Six consecutive crosses were performed.

The 6th cross once confirmed to be homozygous for the *naa-80* knockout was used to repeat the early phenotype assays and was also used to cross with *LifeActmRFP* or *mCh-Act-1 C. elegans* strains, for use in imaging assays. LifeActmRFP or mCh-Act-1 males were crossed with *naa-80* knockout O/C hermaphrodites. Due to time constraints the LifeActmRFP x *naa-80* knockout O/C cross was performed four times and the mCh-Act-1 x *naa-80* knockout O/C cross was performed once.

2.7: *C. elegans* Phenotype assays

2.7.1: Brood size assays

Brood size assays were carried out using age-synchronised parental *C. elegans*. 20 gravid *C. elegans* worms were placed on a NGM plate with an OP50 *E. coli* lawn and placed at 20°C for 2 hour to lay eggs. After 2 hours the parental *C. elegans* were removed from the plate, which was then placed at 20 °C. Once larvae began to hatch 12 *C. elegans* larvae from each strain were placed onto individual NGM plates with an OP50 *E. coli* lawn and placed at 20 °C or 25 °C as specified, these larvae developed into synchronised parental *C. elegans*, the live offspring of which were subsequently counted to establish self progeny brood sizes.

The age synchronised parental *C. elegans* were moved onto fresh NGM plates with an OP50 *E. coli* lawn at the same time each day and the plates from which they were removed and any eggs laid upon them, were then incubated at 20°C. Each day plates were observed and any larvae hatched from these eggs were counted, removed from the plate and their numbers recorded. Once no new larvae were observed the total number of live offspring produced by each synchronised parental *C. elegans* was calculated. Average self progeny brood sizes were then calculated for each strain.

2.7.2: Age specific fecundity assays

Age specific fecundity assays were carried out as part of the brood size assays. As *C. elegans* were moved at the same time each day, the larvae hatched on each plate all came from eggs laid within a 24 hour timespan. By comparing the larvae counted from each plate, the offspring produced during each 24 hour period can be compared, to obtain an Age specific fecundity for each *C. elegans* and an average for each strain.

2.7.3: Unfertilised eggs assays

Once hatched larvae were removed from brood size plates, the number of unfertilised eggs remaining on each plate were counted and compared. Unfertilised eggs are identifiable as they are darker and more spherical than fertile eggs and have a small white dot in them.

2.7.4: Larvae length comparison

The length of *C. elegans* larvae at 1, 2, 3 and 4 days post hatch, were measured and compared. Timed egg lays were carried out by placing 20 gravid adults onto a NGM plate with an OP50 *E. coli* lawn for 2 hours, the adult *C. elegans* were then removed and the eggs laid on the plates were incubated for 24 hours. After each 24 hour period a portion of the resultant larvae were removed from the plates and used to prepare slides for imaging using widefield microscopy.

One comparison was conducted using synchronised parent *C. elegans* for this timed egg lay, as older gravid *C. elegans* had been observed to lay more developed eggs. These parent *C. elegans* were obtained from an earlier timed egg lay.

2.7.5: Body bend frequency as a motility assay

Investigation comparing body bends were carried out with outcrossed *naa-80* knockout and N2H control *C. elegans,* to look for differences in motility. One run was carried out using the body bend assay protocol as described in wormbook (Hart, 2006). For each strain 10 late L4 *C. elegans* were placed on individual NGM plates with an OP50 *E. coli* lawn and incubated at 20 ^{o}C. The following day the plates were gently placed on a dissecting microscope so as not to mechanically disturb the *C. elegans*. Over a three minute period, each time the part of the worm just behind the pharynx reached a maximum bend in the opposite direction from the last bend, this was counted as one bend. If a *C. elegans* dwelled at the edge of the bacterial lawn or the edge of the plate, that 3 minute count was discarded. Three separate, three minute counts were obtained for each *C. elegans*. An average number of bond bends per minute per worm and an average number of body bends per minute for each strain was calculated.

These measurements included a considerable amount of dwelling time. Two further runs were carried out counting body bends during active movement only. In an amended protocol young adult *C. elegans* were observed on a NGM plate with a thin OP50 *E. coli* lawn which covered the entirety of the plate, to prevent dwelling at the edge of the lawn. Body bends were counted during a timed period of active movement,

of 17 to 24 minutes per run. The number of body bends per minute per strain were calculated.

2.7.6: Embryonic developmental timing comparison

Time lapse images were taken over a 16 hour 39 minute time period and used to compare embryo developmental timings. 10 gravid *C. elegans* were removed from a NGM plate and placed into a drop of M9 salts on a clean microscope slide using a fine hypodermic needle attached to a 1 ml syringe. The edge of the point of the needle was then used to cut the *C. elegans* in half, some eggs were released into the M9 salts at this point. *C. elegans* halves and released eggs were then placed onto a prepared 2% agarose pad on a microscope slide. The *C. elegans* halves were then gently tapped with the side of the needle to remove the remaining eggs and the empty half then removed from the agarose. The dissected eggs were then used to prepare slides for time lapse imaging.

For each slide, 999 time lapse images were taken at a rate of 1 per minute over 16 hours 39 minutes. This is long enough for a healthy embryo to develop from a single cell to hatch at 21^{o}C.

When imaging LifeACT-mRFP and mCHERRY-ACT1 producing *C. elegans,* fluorescent images were taken together with transmitted light images at each time point for direct comparison. When taking fluorescent images it was essential to minimise laser intensity and exposure times so as to minimise phototoxicity and photobleaching during the experiment.

Timings were measured from the last image with 4 cells, to three separate developmental stages; 1. The end of the first fold, when tail reaches the opposite end of the egg. 2. The start of the 2nd fold, when tail starts to move back towards the head. 3. The start of circling, when the head has moved from one end of the egg to the other. Live developing embryos move, bend and stretch, so by measuring three different time points for multiple *C. elegans,* it was hoped to minimise the variation due to this.

2.7.7: Microscopy image comparison

Images were taken of adult and different larval stages of *C. elegans*, using spinning disk, confocal fluorescent microscopy. Images of *C. elegans* producing LifeAct-mRFP and mCHERRY-ACT1 both with and without having been back crossed with *naa-80* knockout O/C were compared to look for any differences between the strains that could be due to the *naa-80* knockout. Multiple images were taken of late stage embryos and adult *C. elegans* which were then stitched together using Power Point.

2.8: Microscopy techniques

2.8.1: Fluorescent proteins used in this investigation

mCerulean3

mCerulean3 is a bright photostable cyan fluorescent protein, which has proved to be very popular as a donor fluorophore in FRET experiments (Markwardt *et al.*, 2011). It was developed via Cyan fluorescent protein, from Green fluorescent protein from the hydrozoan jellyfish, *Aequorea Victoria*. Excitation 433 nm, Emission 475 nm.

mNeonGreen,

mNeonGreen is a fast maturing, monomeric, bright green fluorescent protein, with good photostability. It was developed from the tetrameric fluorescent protein LanYFP from the cephalochordate, *Branchiostoma lanceolatum* (Shaner *et al.*, 2013). Excitation 506 nm, Emission 517 nm.

Venus

The Venus fluorescent protein used in this investigation was a mutated version created specifically to reduce spontaneous self assembly and thus increase the signal to noise ration of the BiFC assay in which it was used. Venus was originally developed from

Green fluorescent protein from the hydrozoan, jellyfish, *Aequorea Victoria*. Excitation 515 nm, Emission 528 nm.

Citrine

Citrine is a yellow fluorescent protein which forms a weak dimer. It was developed from the Green fluorescent protein of the hydrozoan, *Aequorea Victoria* (Griesbeck *et al.*, 2001). Excitation 516 nm, Emission 529 nm.

mRFP

mRFP is a red monomeric fluorescent protein which has been reported to be slow maturing, it was developed from the tetrameric fluorescent protein DsRed, from the corallimorpharia, *Discosoma sp.*(Campbell, Robert E,et al., 2002). Excitation 584 nm, Emission 607 nm.

mScarlet

mScarlet is a bright, but slow maturing monomeric red fluorescent protein, which is a synthetic construct (Bindels *et al.*, 2016). Excitation 569 nm, Emission 594 nm.

mCherry

mCherry is a fast maturing monomeric red fluorescent protein, with one of the longest emission wavelengths of the commonly used fluorescent proteins, 610 nm. It was developed from mRFP, which was developed from the tetrameric fluorescent protein DsRed, from the corallimorpharia, *Discosoma sp.* (Shaner *et al.*, 2004). Excitation 587 nm, Emission 610 nm.

2.8.2: Fluorescent amyloid staining dyes used in this investigation

To investigate amyloid formation within live E. coli cells producing aS, two different fluorescent dyes were used. Both are commonly used amyloid dyes and fluorescent microscopy images with similar areas of staining, were obtained using each.

Congo Red

Congo Red stain, apple-green birefringence under polarised light, is the most popular method for detecting amyloid. This method is not always effective for detecting low levels of amyloid. The presence of Red fluorescence in samples stained with Congo Red and observed by fluorescent microscopy, has been shown to be more sensitive for the detection of amyloid (Clement and Truong, 2014). There is some disagreement as to the specificity of Congo Red as an amyloid dye, however this dye was found to be very useful for staining live cells due to its' high solubility in aqueous solution and was found to be effective when incubated with live cell cultures at 0.001% final concentration.

NIAD-4

NIAD-4 was used to confirm the results obtained with Congo Red. This is a more recently developed amyloid dye (Brandenburg, Berlepsch and Koksch, 2012a). Images were obtained showing the same pattern of amyloid staining as seen with Congo Red, however this dye was not as easy to use with live cell cultures due to its lower aqueous solubility. NIAD-4 was first dissolved in DMSO before adding to aqueous cell cultures. This reduction in DMSO concentration resulted in some of the dye falling out of solution and creating a higher level of background fluorescence in the images obtained.

2.8.3: Preparation of *E. coli* slides for fluorescent microscopy

Agarose slides were used when *E.coli* had to be kept extremely still for Z stack imaging. A spacer slide was prepared by placing three bands of masking tape around a slide to form a lower space between the tapes. 2 % agarose was then made in distilled water and heated until dissolved. Approximately 30 μl of hot liquid 2 % agarose was then placed onto the slide being made and the spacer slide placed quickly and firmly on top, so as to form a thin flat disc of agarose between the tapes. The spacer slide was then slid off leaving the agarose disc on the required slide. 8-15 μl of the cells to be viewed were then spread across the disc and allowed to dry until sticky, but not completely dry, a coverslip was then placed on top and fixed to the slide with masking tape or Unibond Repair extreme glue. Unibond Repair extreme glue, N-(3-

(Trimethoxysilyl)propyl)ethylenediamine., was used to adhere glass to glass, as it had no detectable toxic effect on the organisms.

2.8.4: Preparation of slides for imaging *C. elegans*

Agarose slides were used for imaging anaesthetised *C. elegans*. An agarose pad was prepared as for imaging *E. coli,* preparing the 2 % agarose in M9 salts instead of distilled water. 15 µl of anaesthetic (0.06% tetramisole hydrochloride) was then placed on the agarose pad and the *C. elegans* to be imaged were placed in the anaesthetic. Once the anaesthetic had dried/soaked into the agarose to the point of being moist but not wet, a coverslip was gently placed on top and held in place with masking tape or glue as for *E. coli*.

2.8.5: Preparation of slides for time lapse imaging of C. elegans

Agarose slides were initially prepared as for immediate imaging of *C. elegans,* however a large 22 mm x 50 mm coverslip was gently placed on top of the dissected eggs instead of a more normal 22x22 coverslip. This was held in place temporarily with masking tape over 3 mm of each end Unibond repair extreme glue was then run along both long sides in between, but not touching the masking tape. The masking tape was then removed and 1xM9 salts was then placed on the slide touching the coverslip so as the liquid is drawn under the coverslip by capillary action. The 1xM9 salts prevents the agarose from drying out and the unsealed ends allow for gaseous exchange (**Figure 2.3**).

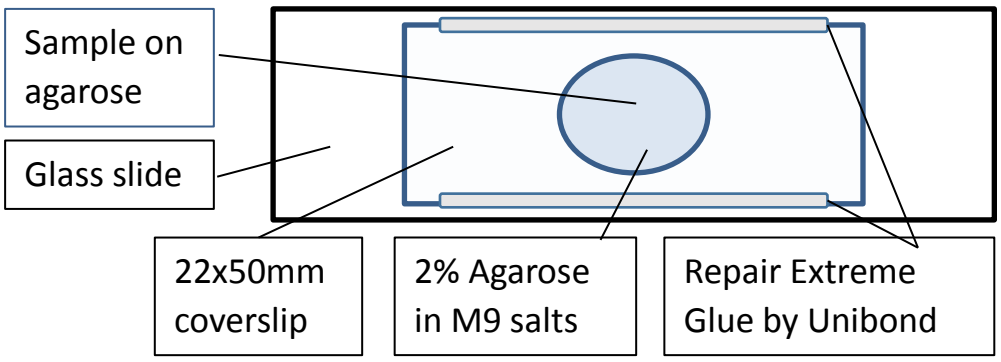


Figure 2.3. Slide preparation for Time lapse imaging of *C. elegans*.

2.8.6: Widefield Microscopy

Samples were visualised using an Olympus IX71 microscope with UApoN 100x TIRF 1.49 NA lens or UPlanFI 20x 0.50NA air lens mounted on a PIFOC z-axis focus drive (Physik Instrumente, Karlsruhe, Germany), and illuminated using LED light sources (Cairn Research Ltd, Faversham, UK) with appropriate filters (Chroma, Bellows Falls, VT). An Optosplit device (Cairn Research Ltd) was used to allow simultaneous acquisition of signals from two fluorophores that emitted light of different wavelengths. Samples were visualised using a Zyla 4.2 (Andor) CMOS camera and the system was controlled with Metamorph software (Molecular Devices). Each 3D-maximum projection of volume data for *E. coli* was calculated from 11 z-plane images, each 0.2 µm apart and analysed using Metamorph and Autoquant X software. A single z-plane image was taken when obtaining transmitted light images of *C. elegans*.

Sample slides were fitted onto an ASI motorised stage (ASI, Eugene, OR) on the above system.

2.8.7: Spinning disk Confocal Microscopy

Samples were visualised using an Olympus IX73 microscope with UApoN 100x TIRF 1.49 NA lens, 100x TIRF 1.45NA lens or Plan Apo 60x 1.40 NA lens mounted on a PIFOC z-axis focus drive (Physik Instrumente, Karlsruhe, Germany) and illuminated using LDI light sources (89 North) with appropriate filters in line with a CrEST.optics spinning disk unit. Samples were visualised using a Photometrics® Evolve EMCCD camera and the system was controlled with Metamorph software (Molecular Devices). Each 3D-maximum projection of volume data of *C. elegans* was calculated from 21 z-plane images, each 0.2 µm apart and analysed using Metamorph and Autoquant X software. A single z-plane image was taken when obtaining transmitted light images of *C. elegans*. Sample slides were fitted onto an ASI motorised stage (ASI, Eugene, OR) on the above system.

2.8.8: Transmitted Electron Microscopy (TEM) and Immuno EM

E.coli cells were fixed, stained and thin sectioned by Ian Brown (Microscopy Suite Facility Manager, University of Kent), to allow high resolution visualisation of the

interior of the cells. Two different preparation techniques were used including the use of an immunogold-staining technique post thin sectioning, using 1 in 500 anti-aS antibody and a secondary anti-rabbit antibody attached to 15 nm gold discs. Methods used were as described in (Parsons *et al.*, 2010).

2.8.9: Measurement of Förster Resonance Energy Transfer (FRET) using Fluorescent Lifetime Imaging (FLIM)

FRET was measured using FLIM at the Central Laser Facility (CLF), Research Centre at Harwell (RCaH), with the assistance of Prof. S Botchway. Using Single photon FRET-FLIM and Multiphoton Confocal –FLIM.

Single photon FRET-FLIM was used when Cerulean3 acted as a donor fluorophore. The system uses a LEICA SP8 3X SMD inverted microscope, with a HC PL APO 100x oil immersion 1.40 NA lens and motorized Märzhäusser stage with Leica Galvo stage.

Multiphoton confocal-FLIM was used when mNeonGreen acted as a donor fluorophore. Multi photon excitation and confocal used near Infra-red to excite the sample and does not need a pin-hole as the two-photon excitation arises from a simultaneous absorption of two photons in a single quantitised non-linear event within 10E-18 seconds. This method uses lower, less phototoxic light levels than standard confocal microscopy. The multiphoton Confocal-FLIM system uses an inverted Nikon EC1, EC2, Becker and Hickl DCS120 system, with 100x oil immersion 1.49 NA lens.

2.8.10: Structured Illumination Microscopy (SIM)

Sim was carried out at the CLF (RCaH) with the assistance of Dr Lin Wang using **a** Zeiss Elyra PS1 microscope, with 100x oil immersion lens.

2.9: Image analysis

2.9.1: Fluorescent intensity measurements

For use in FRET calculations, measurements of Cerulean3 fluorescence intensity within cells were taken using Metamorph software (Molecular Devices) using the Region tool properties function. A circular region of 10 pixel diameter in the centre of each cell was measured. 420 to 700 cells were measured from images of each culture from three different slides.

2.9.2: FLIM analysis of FRET

SPC Image 6.0 (Becker & Hickl GmbH) was used to collect and analyse FLIM data. Mean fluorescent lifetime measurements of whole field of view, selected areas within fields of view and individual pixel lifetimes were analysed from at least 3 different slides.

2.9.3: Larvae length measurement

Larvae lengths were measured using widefield microscopy images and Metamorph software (Molecular Devices) using the Linescan function. A line was manually drawn along the centre line of each *C. elegans* to obtain lengths in pixels for direct comparison between strains (**Figure 2.4**).

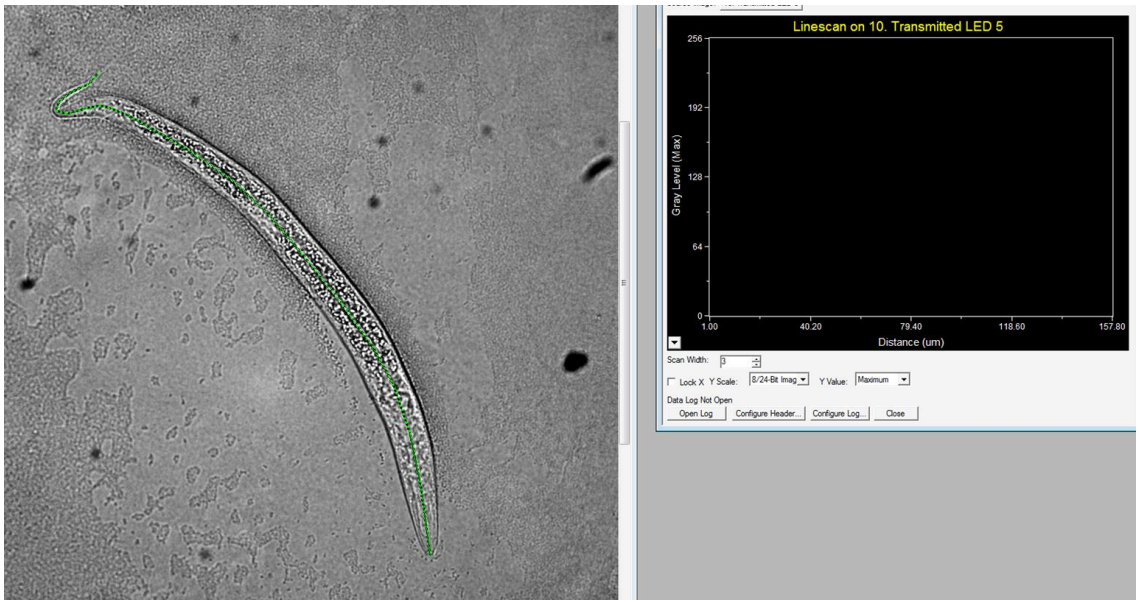


Figure 2.4. Screen shot of Metamorph software as used for measurement of larval lengths. A line was drawn along the centre of larvae to obtain length measurements in pixels.

2.9.4: Embryo developmental timing measurements

Time lapse images of developing *C. elegans* embryos were analysed using Metamorph software (Molecular Devices). Individual images were examined to identify four time points for each embryo. The time point for the last image where four cells are present, the end of the first fold when tail reaches the opposite end of the egg, start of 2nd fold when tail starts to move back towards the head and start of circling when head has moved from one end of the egg to the other (**Figure 2.5**). The time taken for each embryo to progress from the four cell stage to each of the other stages was calculated and compared.

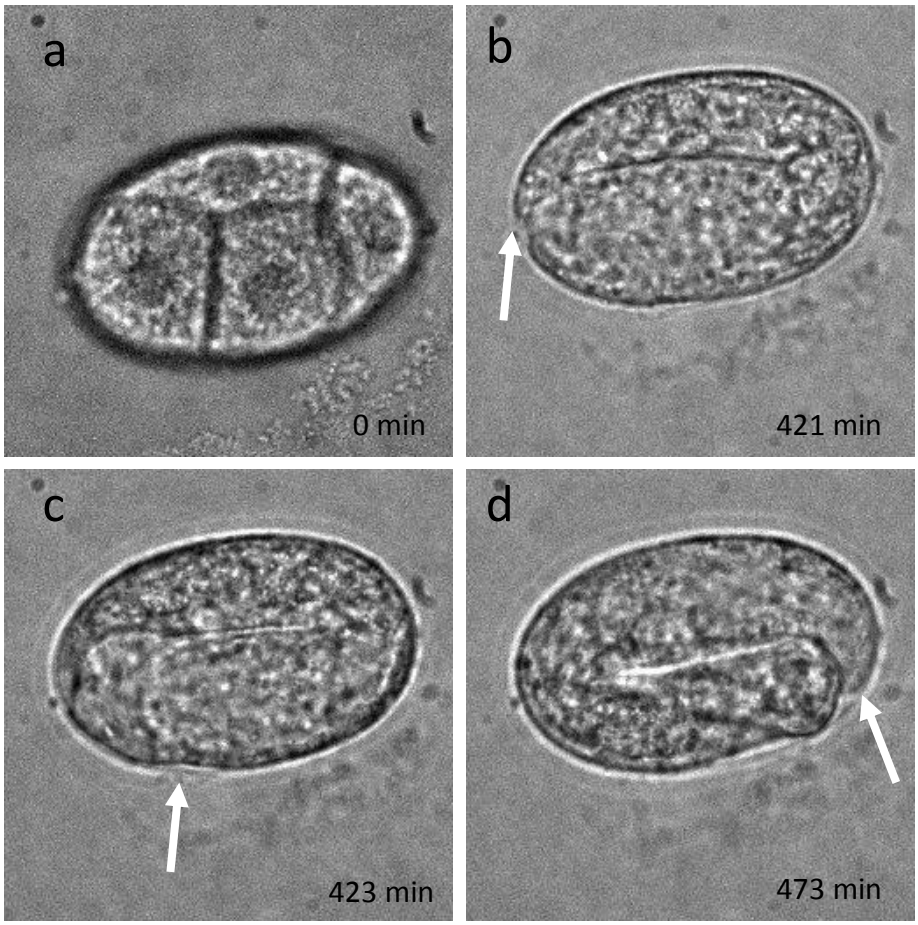


Figure 2.5. Embryo development time lapse images, showing the time points used for timing measurements. a. the last image showing 4 cells was used for the start time point for each film. **b**. The end of the first fold (when tail reaches the opposite end of the egg) was used as the end time point for the first set of measurements. **c**. The start of the 2nd fold (when tail starts to move back towards the head) was used as the end point for the second set of measurements. **d**. The start of circling (when head has moved from one end of the egg to the other) was used as the end point for the third set of measurements. Scale bar 10 μm.

2.10 Safety

All relevant safety precautions were taken when handling chemicals and equipment.

Only non-pathogenic strains of *E. coli* were used during this investigation.

All organisms used during this investigation were within biological hazard group 1 defined as unlikely to cause human disease.

2.11: Strains, Plasmids and Oligonucleotides

2.11.1: *E. coli* strains

Strain	Use
DH10β – *K-12 F– Δ(ara-leu)7697[Δ(rapA'-cra')] Δ(lac)X74[Δ('yahH-mhpE)] duplication(514341-627601)[nmpC-gltI] galK16 galE15 e14–(icdWT mcrA) φ80dlacZΔM15 recA1 relA1 endA1 Tn10.10 nupG rpsL150(StrR) rph+ spoT1 Δ(mrr-hsdRMS-mcrBC) λ– Missense(dnaA glmS glyQ lpxK mreC murA) Nonsense(chiA gatZ fhuA? yigA ygcG) Frameshift(flhC mglA fruB)*	Production of plasmid DNA stock
JM10 - *Δ(lac-proAB), [F', traD36,proAB, laqI^{q}ZΔM15]*	Production of plasmid DNA stock, to prevent leaky expression of the Tac promoter in pMK-RQpTac-aS-mNeonGreen-FLAG-hGH. (Grown in M9 media- 20 % Glucose, 5 mM $MgSO_4$, 1 x M9 salts for *E. coli* (**Table 2.1, K**.), 0.1 mM $CaCl_2$, 0.01 % thiamine) Production of microcompartments.
BL21DE3 - *B F– ompT gal dcm lon hsdSB(rB–mB–) λ(DE3 [lacI lacUV5-T7p07 ind1 sam7 nin5]) [malB+]K-12(λS)*	Protein expression
OP50 - Uracil auxotroph. *E. coli B*. Biosafety Level: BSL-1 (The Caenorhabditis Genetics Center (CGC) University of Minnesota).	Food for *C. elegans*

Table 2.6. *E. coli* strains used throughout this project and their use.

2.11.2: *C. elegans* strains

Strain	Genotype	Short name
N2H	*C. elegans* wild type CGCH	N2H
COP1594	*C56G2.15(knu548 [early stop])*	COP1594
COP1595	*C56G2.15(knu549 [early stop])*	COP1595
COP1596	*C56G2.15(knu550 [early stop])*	COP1596
WX8490	*YqIs100(Pced-1mCHERRY::ACT1)* From Zhang lab, National Institute of Biological Sciences, Beijing (Huang *et al.*, 2012)	*mCh-Act-1*
BU70	*zbIs2(Ppie-1::LifeACT::mRFP)* From Zhang lab (Huang *et al.*, 2012)	*LifeAct-mRFP*
JMT38	*Hum-1(ok634)1:[Phum-1::gfp::hum::hum-1 3'UTR} yqIs100(Pced-1mCXHERRY::ACT-1)*	*Hum-1-GFP;mCh-Act-1*
JMT71	*naa-80* KO*(knu548) O/C strain*	*naa-80* KO O/C
JMT72	*naa-80 KO;zbIs2(Ppie::LifeACT::mRFP)*	*naa-80* KO LifeAct-mRFP
JMT73	*naa-80 KO;YqIs(Pced-1mCHERRY::ACT-1)*	*naa-80* KO mCh-Act-1

Table 2.7. ***C. elegans* strains used throughout this project.** Column 1 gives the lab stock name. JMT strains were produced within the lab of Dr J Tullet. Column 2 gives the strain genotypes. Column 3 gives the short name used when referring to each strain.

2.11.3: Plasmids used in this study

Stock Number	Plasmid	Source
310	pACYC Duet-naa20-naa25 (pNatB)	This lab
567	pJC20 mCherry	This lab
622	pRSFDuet-1 Empty vector	Invitrogen
657	pACYC Duet-naa10-naa15 (pNatA)	This lab
692	pMA-T Nde1cdc8BglII	GeneArt
693	pMA-T NcoICdc8BamHI	GeneArt
694	pMA-T NcoIaSBamHIVC155BglII	GeneArt
695	pMA-T NdeIaSBglIIN Venus154BamHIKpnI	GeneArt
696	pET Duet-1 aS-Cerulean3	This lab
698	pETpRha-aSkTm	This lab

702	pET23bCycABGFP	LH
708	pET Duet-1 aS-C Venus 155 Nco1, BglII v694 fragment (aS-C Venus 155) into Nco1, BamHI vector from v618 (pET Duet empty vector)	This lab
712	pET Duet-1 aS-C Venus 155 aS-N Venus 154 (BiFC) NdeI, KpnI v695 fragment (aS-N Venus 154) into NdeI, KpnI (aS-C Venus 155) vector from v708	This lab
713	pGEM SalImCherryNotI PCR insert (amplified using primers O548 and O549 and v702 template) ligated into pGEM (Promega)	This lab
714	pGEM NcoICydABSalI PCR insert (amplified using primers O550 and O551 and v567 template) ligated into pGEM (Promega)	This lab
718	pET Duet aS-Cerulean3 CydAB NcoI, SalI (CydAB) insert from v714 into NcoI, SalI (aS-Cerulean3) vector from v696	This lab
721	pET Duet-1 aS-N Venus154 NcoI, SacI (aS N Venus 154 only) vector from v712, treated with Klenow for blunt end ligation	This lab
722/3	pET Duet-1 aS-Cerulean3 CydAB-mCherry NotI, SalI (mCherry) insert from v713 into NotI, SalI (aS-Cerulean3 CydAB) vector from v718	This lab
745	pMA-T aS-mNeonGreen-Pif6	GeneArt
748	pET Duet-1 Cdc8-C Venus 155 NcoI, BamHI (Cdc8)insert from v693 into (C Venus 155) NcoI, BamHI vector from v708	This lab
750	pMA-T NdeICdc8BglIIN Venus154BamHIKpnI NdeI, BglII (Cdc8) insert from v692 into NdeI, BglII (N Venus 154) vector from v695	This lab
758	pET Duet-1 Cdc8-C Venus 155 Cdc8-N Venus 154 (BiFC) NdeI, BamHI (Cdc8-N Venus 154) insert from v750 into NdeI BglII (Cdc8-C Venus 155) vector from v748	This lab
759	pET Duet-1 aS-mNeonGreen-Pif6	This lab

	NdeI XhoI (aS-mNeonGreen-Pif6) insert from v745 into NdeI XhoI (empty) vector from v696	
760	PRS305_PhyB-mCherry-NLS	Addgene
772	pET Duet-1 aS-mNeonGreen NheI SpeI vector ligated to remove Pif6	This lab
779	pMK-RQ OmpA-mCherry	Invitrogen
783/4	pET Duet-1 aS-mNeonGreen-Pif6 PhyB-mCherry NotI, AscI (PhyB-mCherry) insert from v787 into NotI, AscI (aS-mNeonGreen-Pif6) vector from v759	This lab
787	pTOPO PhyB-mCherry PCR insert (amplified using primers O589 and O551 and v760 template ligated into pCR™4-TOPO® (Invitrogen))	This lab
798/9	pET Duet-1 aS-mNeonGreen-Pif6 OmpA-mCherry BspHI, BglII (OmpA-mCherry)insert from v779 into NcoI, BamHI (aS-mNeonGreen-Pif6) vector from v759	This lab
800	pET Duet-1 aS-mNeonGreen mCherry SalI, NotI (mCherry) insert from v713 into SalI, NotI (aS-mNeonGreen) vector from v772	This lab
813	pCR4-TOPO NcoIaS-Cerulean3BglII PCR insert (amplified using primers O593 and M13 and v760 template ligated into pCR™4-TOPO® (Invitrogen))	This lab
814/5	pET Duet-1 aS-Cerulean3 aS-mNeonGreen NcoI, BglII (aS-Cerulean3) insert from v813 into NcoI, BamHI (aS-mNeonGreen-Pif6) vector from v759	This lab
827	pCR4-TOPO NcoIaS-GGSG*-SalI PCR insert (amplified using primers O593 and O594 and v696 template ligated into pCR™4-TOPO® (Invitrogen))	This lab
832	pET Duet-1 NcoIaSSalI aS-mNeonGreen-Pif6 NcoI, SalI (aS-GGSG*)insert from v827 into NcoI, SalI (aS-mNeonGreen-Pif6) vector from v759	This lab
834/5	pET Duet-1 aS-mCherry aS-mNeonGreen-Pif6 SalI, NotI (mCherry)insert from v713 into SalI, NotI (aS-GGSG* aS-mNeonGreen-Pif6) vector from v832	This lab

838	pMK-RQ aS-mNeonGreen-FLAG-hGH	Invitrogen
845	pET-Di-C-His-Citrine-MinD-BS	Prof. M Warren, UKC
850/1	pET Duet-1 Citrine-MinD OmpA-mCherry NdeI, AvrII (Citrine-MinD) insert from v845 into NdeI, AvrII (OmpA-mCherry) vector from v799	This lab
857	pETpRha aS-mNeonGreen-FLAG-hGH NdeI, BamHI (aS-mNeonGreen-FLAG-hGH) insert from v838 into NdeI, BamHI (empty) vector from v698	This lab
880	pETpRha aS-mCherry-PduABJKNU	Dr S. Frank, UCL
885	pETpRha PduABJKNU	Dr S. Frank, UCL
906/7	pGEM mScarletMinD PCR insert (amplified using primers O623 and O624 and O652 template) ligated into pGEM (Promega)	This lab
910	pRSF Duet mScarlet-MinD NcoI, BamHI (mScarlet) insert from v907 into NcoI, BamHI (empty) vector from v622	This lab
913/4	pET Duet-1 Citrine-MinD aS-Cerulean3 NdeI, AvrII (Citrine-MinD) insert from v850 into NdeI, AvrII (aS-Cerulean3) vector from v814	This lab
915/6	pRSF Duet mScarlet-MinD aS-mNeonGreen-Pif6 NdeI, XhoI (aS-mNeonGreen-Pif6) insert from v759 into NdeI, XhoI (mScarlet-MinD) vector from v910	This lab

- GGSG – Flexible quadra-peptide linker

Table 2.8. Plasmids used during this project. Column 1 gives the lab stock number. Column 2 gives plasmid information. Column 3 gives the origin of each plasmid.

2.11.4: PCR primers for DNA amplification

Stock No.	Primer Name	Primer Sequence (5' to 3')	Target Gene
O548	Pci1cydABF	ACATGTTAGATATAGTCGAACTGTCGCGC	cydAB
O549	Sal1cydABR	GTCGACGTACAGAGAGTGGGTGTTACG	cydAB
O550	Sal1mCherryF	GTCGACATGGTGAGCAAGGGCGAGGAGG	mCherry
O551	Not1mCHerryR	GCGGCCGCTTACTTGTACAGCTCGTCCATGCC	mCherry
O589	PhyBAscIF	GGCGCGCCATGGTTTCCGGAGTCGGGGG	PhyB
O593	NcoIaSF	CCATGGATGTATTCATGAAAGG	aS
O594	SalIaSGGSGR	GTCGACTCCGCTTCCTCCGGCTTCAGGTTCGTAGTC	aS
O623	pFASTBACK-FOR	TCCGGATTATTCATACCGTCCC	
O624	pFASTBACK-REV	CCTCTACAAATGTGGTATGGCTG	
O626	M1 rev(-29)	CAGGAAACAGCTATGACC	

Table 2.9. PCR primers and template for amplification of DNA fragments.

2.11.5: genotype PCR and qPCR primers

Primer name	Primer sequence (5' to 3')	Target gene
6499	TCGGTGAGTTGTATTCTAGAGTGG	*Naa-80* forwards
6500	CAATCCATAAGGCATGGTCACTG	*Naa-80* reverse
6041	ATGACGAGATACTAGGCCAC	*Naa-80* reverse within removed section of *Naa-80* gene
O653	GTCAGTCCCCTCCAATGTCG	Naa-80 transcript checkF
O654	GTCCAAGGCCACGTTGATCC	Naa-80 transcript checkR
JT212	CTGCTGGACAGGAAGATTACG	qPCR control *Cdc-42* F
JT213	CTCGGACATTCTCGAATGAAG	qPCR control *Cdc-42* R
JT214	GTTCCCGTGTTCATCACTCAT	qPCR control *Pmp-3* F
JT215	ACACCGTCGAGAAGCTGTAGA	qPCR control *Pmp-3* R
JT216	GTCGCTTCAAATCAGTTCAGC	qPCR control, Y45F10D.4 F
JT217	GTTCTTGTCAAGTGATCCGACA	qPCR control, Y45F10D.4 R

Table 2.10. Genotype PCR primers for identification of wild type *naa-80 C. elegans*, homozygous *naa-80* knockout *C. elegans* and heterozygous wildtype and *naa-80* knockout *C. elegans* and primers used for the amplification of cDNA during qPCR.

Chapter 3: The effect of Nt-acetylation on aS oligomerisation

aS aggregates and fibrils have an established link with PD. There is however a growing body of work suggesting that protofibrils and or smaller oligomers may be the toxic form of aS (Ross and Poirier, 2004; Guerrero-Ferreira *et al.*, 2018). Several studies using purified aS have shown that Nt-acetylation increases the helicity of the N-terminus, lipid binding and can effect aggregation into amyloid fibrils (Bartels *et al.*, 2014). To examine the affect of Nt-acetylation on aS conformation and oligomerisation, investigations were carried out using both *in vitro* and *in vivo* techniques. By using a combination *of in vitro* and *in vivo* techniques, it was hoped to gain a greater understanding of how Nt-acetylation affects aS oligomerisation in a purified state and in a cytosolic environment in the presence of other proteins and membranes.

3.1 The impact of Nt-Acetylation on aS conformation and oligomerisation *in vitro*

A two stage purification of both Nt-acetylated and non Nt-acetylated recombinant aS-Cerulean3-His_6 was carried out, for use during *in vitro* assays. Protein was expressed in *E. coli* BL21 DE3 cells with or without co-expression of the Nat B complex, to produce both Nt-acetylated and non Nt-acetylated forms of the protein. An initial purification was carried out, making use of the His tag at the C-terminus of this recombinant protein, and a cobalt resin, metal affinity column as detailed in section 2.2.5. A second FPLC purification using an Anion Exchange Column was then performed and the protein containing fractions as shown by coomassie Blue stained SDS-PAGE gel (**Figure 3.1**) were pooled for analysis. A western blot (WB) was also carried out on samples of both proteins following each purification step, to confirm the presence of aS, using a rabbit polyclonal anti aS primary antibody (**Figure 3.2**).

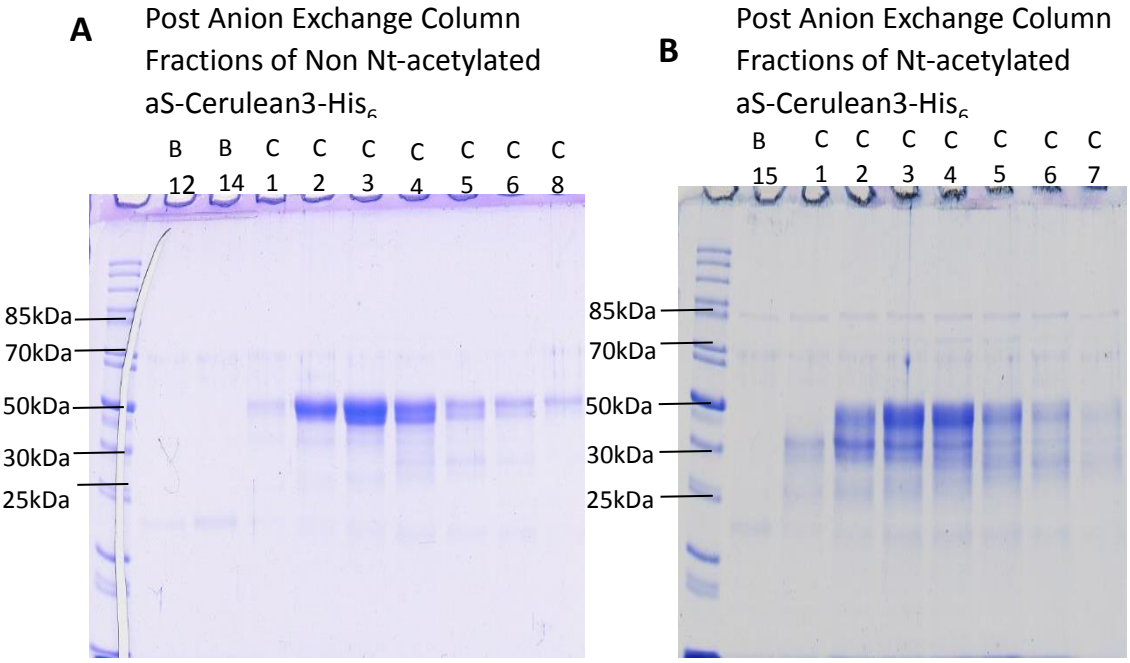


Figure 3.1. Coomassie Blue stained SDS-PAGE gel showing post FPLC purification fractions. (A) Non Nt-acetylated fractions (B12-C8) and (B) Nt-acetylated aS-Cerulean3-$His_{6.}$ Fractions (B15-C7) of each protein were pooled for use in *in vitro* studies. Expected molecular weight for aS-Cerulean3-His_6 - 42.5 kDa.

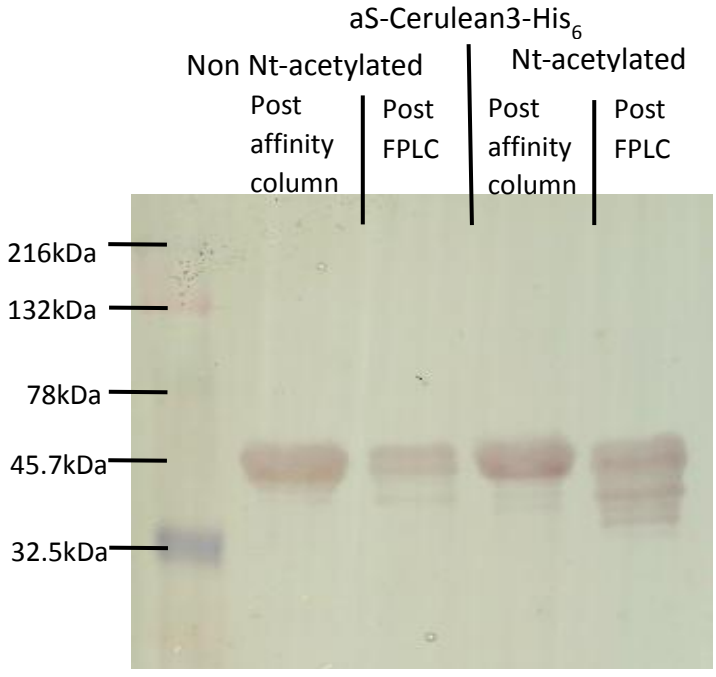


Figure 3.2. Western blot of post His tag affinity column purification of aS. Nt-acetylated and Non Nt-acetylated aS-Cerulean3-His_6 and post FPLC purified aS-Cerulean3-$His_{6,}$ pooled fractions C2 to C6, for both Nt-acetylated and Non Nt-acetylated protein, using Rabbit anti-aS primary antibody. Pooled post FPLC protein was used in *in vitro* analysis. Expected molecular weight for aS-Cerulean3-His_6 - 42.5

To investigate the possibility of size differences between the two purified proteins, the two post Anion exchange column pooled protein samples were run through a size exclusion column. The two peaks obtained for the Nt-acetylated aS, indicates two different forms are present, with the majority being in a larger state, where the protein forms either a larger conformation or oligomeric state which is less able to enter the pores of the SEC media. The shoulder and peak obtained for the non Nt-acetylated aS, which align with the two peaks obtained for Nt-acetylated aS, indicates the presence of the same two different forms but this time the majority is in a smaller state, which may be due to most of the protein being in a smaller conformation or monomeric form which can more easily enter the pores of the SEC media. (**Figure 3.3**).

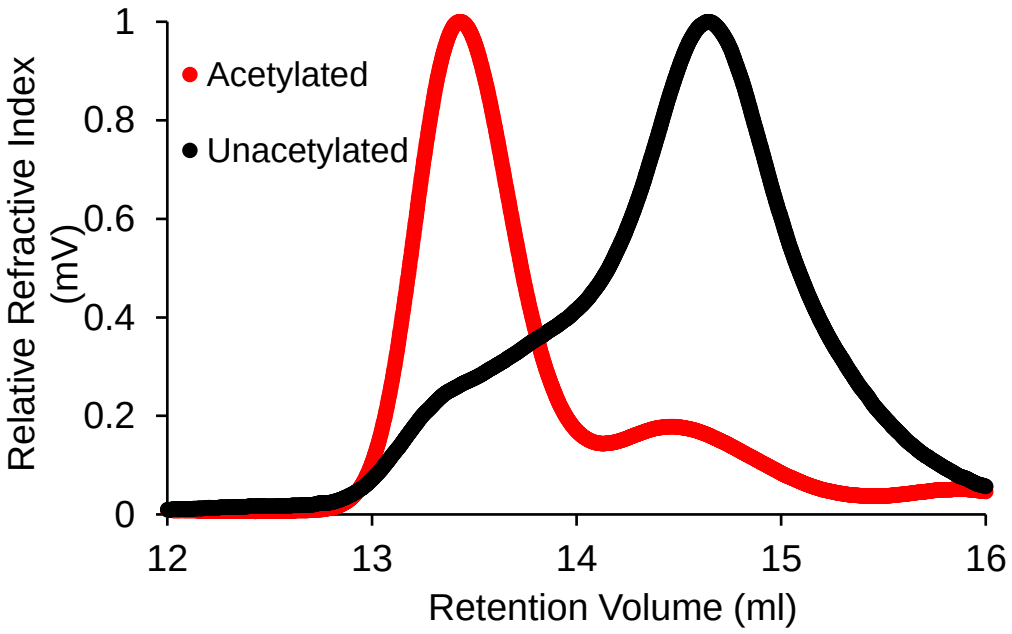


Figure 3.3. **Graph from size exclusion assays showing the retention volume, where either Nt-acetylated or non Nt-acetylated aS-Cerulean3-His$_6$ was eluted from the column.** Nt-acetylated aS-Cerulean3-His$_6$ was eluted from the column at an earlier stage than non Nt-acetylated aS-Cerulean3-His$_6$, indicating differences in structure.

Coomassie Blue stained SDS-PAGE gels and western blots of purified protein and cell extracts containing both Nt-acetylated and non Nt-acetylated aS, sometimes show

additional bands, indicating the possible presence of oligomers, these are seen more often with gentle sample preparation techniques and with older stationary cell cultures. These additional bands are most clearly seen in Coomassie Blue stained SDS-PAGE gels and western blots of cell extracts from stationary *E.coli* Bl21 DE3 cell cultures, having expressed either Nt-acetylated or non Nt-acetylated aS for at least 5 hours (**Figure 3.4**).

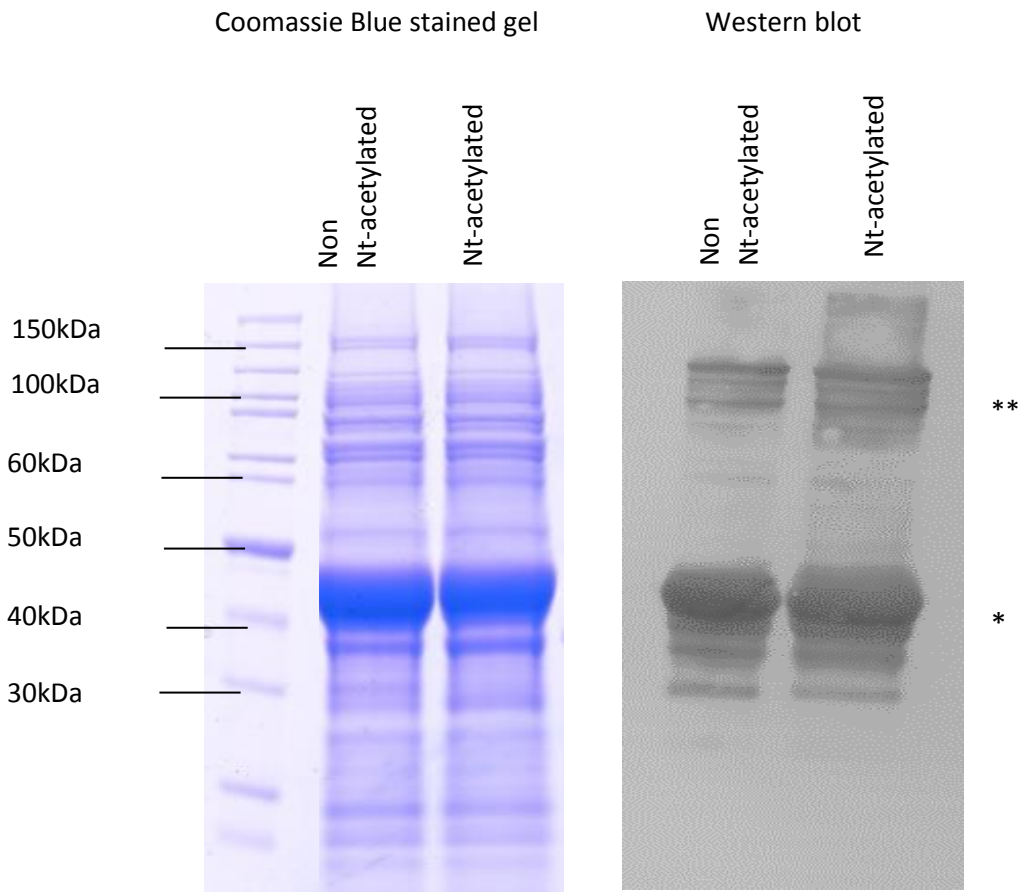


Figure 3.4. **Coomassie Blue stained SDS-PAGE gel and western blot of extracts from *E. coli* cells expressing aS-Cerulean3-His_6, Nt-acetylated or Non Nt-acetylated for 90 hours.** Western blot carried out using Rabbit anti-aS primary antibody. Expected molecular weight for aS-Cerulean3-His_6 - 42.5 kDa (*). The western blot suggests the presence of larger oligomers (**).

3.2 The use of Förster Resonance Energy Transfer (FRET) in live *E. coli*

FRET was used to examine whether this size difference is most likely due to a conformational change and or due to differences in oligomerisation. A pET Duet vector was produced to enable the simultaneous expression of aS-Cerulean3 and aS-mNeonGreen within *E. coli* cells (**Figure 3.5**). As the emission wavelength for Cerulean3 overlaps the excitation wavelength for mNeonGreen, (**Figure 3.6**) if these two fluorophores are within close proximity (<10nm) then FRET should occur when cells are exposed to light at the excitation wavelength of the donor fluorophore, Cerulean3. If oligomerisation of aS is occurring within the *E. coli* cells, bringing the two fluorophores within 10nm of each other, excitation at 440nm should result in energy transfer resulting in mNeonGreen fluorescence (**Figure 3.7**).

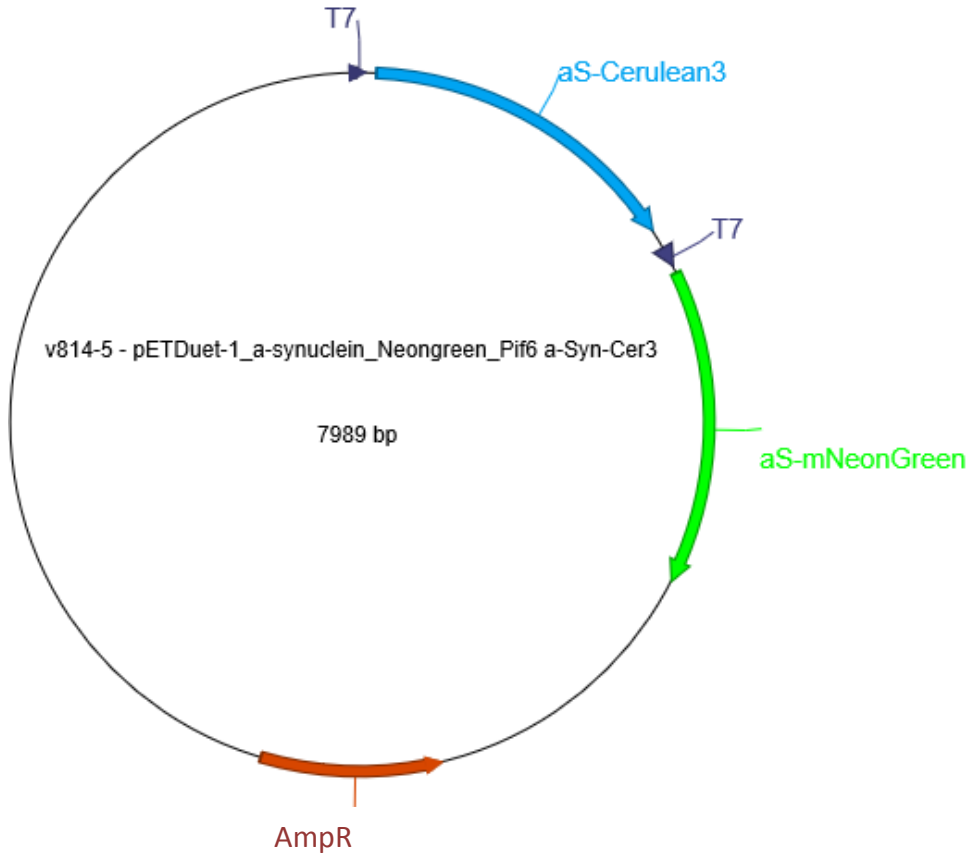


Figure 3.5. Vector map of the FRET construct pET1.aS-Cerulean3 aS-mNeonGreen-Pif6.

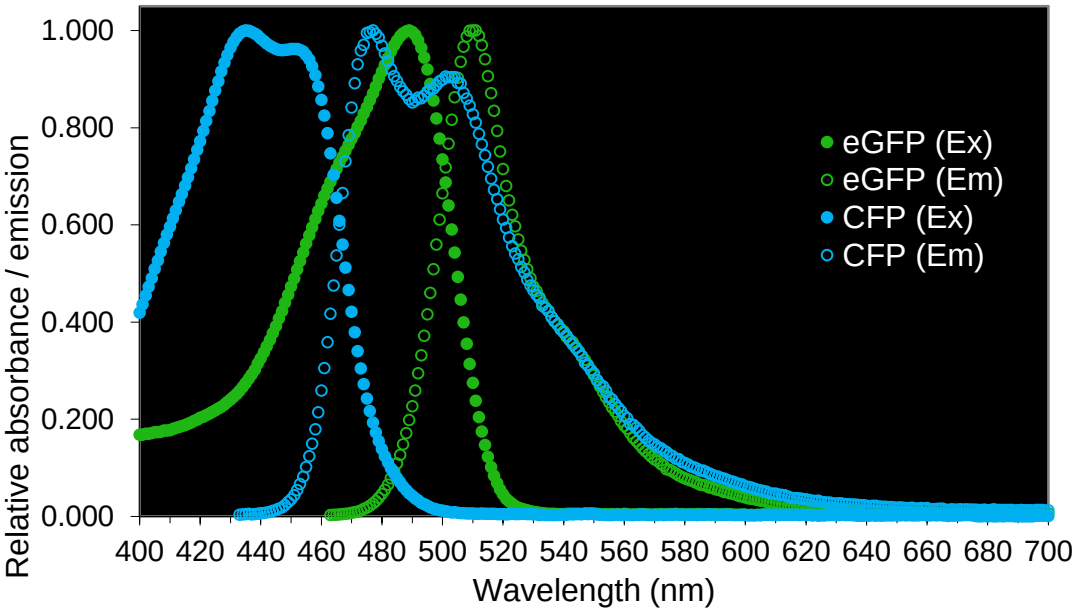


Figure 3.6. eGFP and CFP Excitation and Emission spectra. FRET occurs where the emission spectra of a donor fluorophore overlaps the excitation spectra for an acceptor fluorophore, as with eGFP and CFP and the two fluorophores are in close proximity enabling energy transfer. The spectra for eGFP and mNeonGreen and for CFP and Cerulean3 are almost identical.

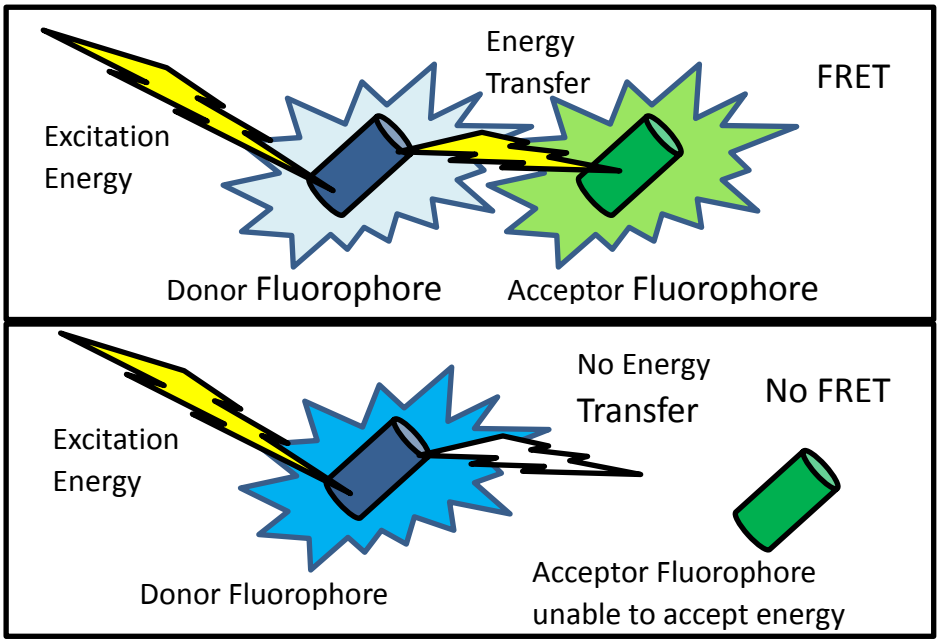


Figure 3.7. Schematic to show when FRET occurs. FRET occurs where a donor and acceptor fluorophore are in very close proximity (<10nm apart) so that a photon emitted from the donor fluorophore is able to excite the acceptor fluorophore. Where FRET occurs the acceptor fluorophore will fluoresce and the level of fluorescence given off by the donor fluorophore will decrease.

FRET was examined using *E. coli* cells expressing the FRET construct, or either aS-Cerulean3 or aS-mNeonGreen alone. Each construct was expressed with or without the co-expression of the NatB complex, to produce the FRET construct proteins or control single fluorophore proteins with or without Nt-acetylation. Cells were imaged using fluorescent microscopy, and samples from the same cultures were used to prepare cell extracts, to examine by gel electrophoresis using a SDS-PAGE gel and stained with Coomassie Blue, to measure the amounts of aS-Cerulean3 protein per ml of each culture. Using the measured levels of protein, the relative fluorescent intensities produced in each cell culture could be calculated (**Figures 3.8, 3.9 and 3.10**). Measurements of relative amounts of protein were made using Scion Image. This gel also confirmed the co-expression of the FRET construct proteins (**Figure 3.9**).

The fluorescent images were then used to measure the Cerulean3 fluorescence intensity in individual cells (400 to 800 cells per sample from 6 to 8 fields of view) (**Figure 3.8**). The average cell fluorescence intensity was calculated for each cell culture using Metamorph software and this was used together with the relative amount of Cerulean3 protein in each culture, to calculate the relative average Cerulean3 fluorescent signal for each culture.

In the fluorescent images shown (**Figure3.8**) the cells producing aS-mNeonGreen alone, only produced mNeonGreen fluorescence, showing that no signal at the emission wavelength for Cerulean3 fluorescence detected, was due to the mNeonGreen protein. The cells producing aS-Cerulean3 alone show a brighter Cerulean3 image in comparison with the Cerulean3 image for the FRET construct producing cells. The FRET construct mNeonGreen image is brighter than the mNeonGreen image obtained for cells producing aS-Cerulean3 alone, the low level of fluorescence at the emission wavelength for mNeonGreen is due to the overlap for Cerulean3 expression spectra with the mNeonGreen expression spectra.

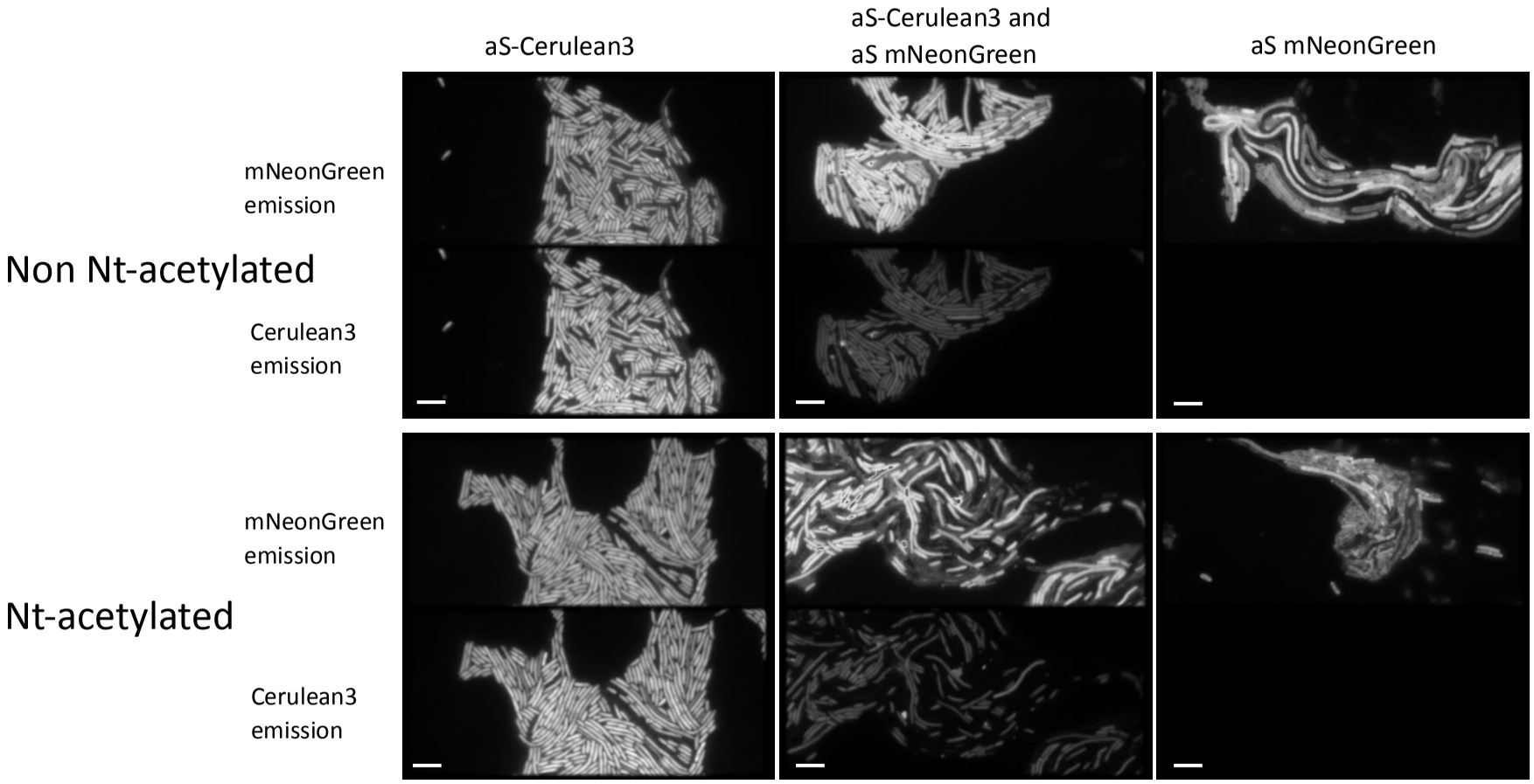


Figure 3.8. FRET images of cells producing aS-Cerulean3 and aS-mNeonGreen. Images of mNeonGreen (green) fluorescence in the top of each pair of images and Cerulean3 (blue) fluorescence bottom of each pair of images. For all images the excitation wavelength for Cerulean3 (440nm) was used. Live *E. coli* cells producing either aS-mCerulean3 or aS-mNeonGreen or both proteins together as a FRET construct, were imaged keeping all microscope settings constant. The intensity of mNeonGreen fluorescence seen increased with the FRET construct compared with single protein expression. The intensity of mCerulean3 fluorescence is seen to decrease significantly when the FRET construct was expressed, compared to when mCerulean3 alone was expressed. Individual fluorescent intensity readings (422 to 766 cells per culture) were taken for individual cells using Metamorph software for calculations of relative fluorescence adjusted for protein concentration. Scale bar 5 μm

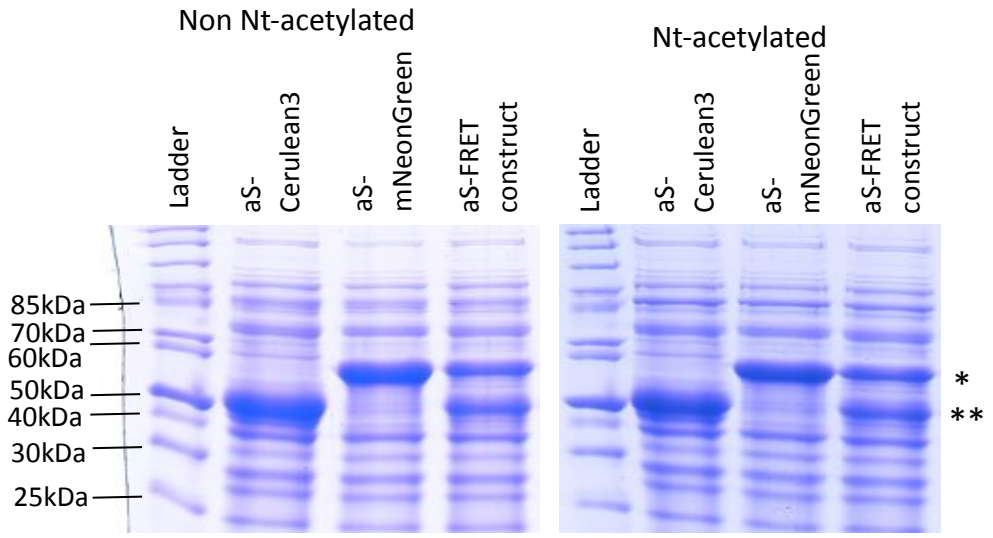


Figure 3.9. Coomassie Blue stained SDS-PAGE gel showing relative amounts of protein in *E. coli* cells producing Nt-acetylated or non Nt-acetylated, aS-Cerulean3 alone, aS-mNeonGreen alone or our aS-FRET construct which produces each fluorophore attached to aS simultaneously. Scion Image was used to measure the relative amounts of protein produced for FRET calculations. Protein production was induced with 100 μg/ml IPTG for 2 hours. Expected molecular weights, aS-mNeonGreen-Pif6 - 53.1 kDa(*) and for aS-Cerulean3 - 42.5 kDa(**).

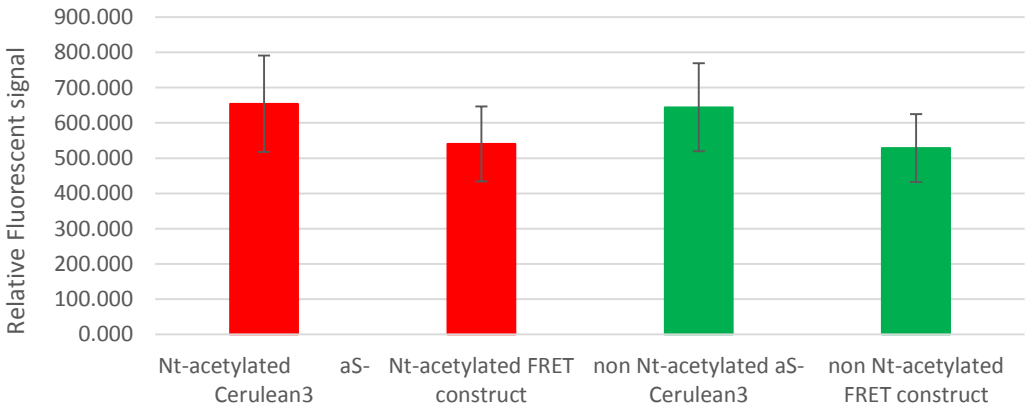


Figure 3.10. Corrected relative average aS-Cerulean3 signal of *E. coli* producing aS-Cerulean3 or aS-FRET construct. A clear reduction in signal is seen with both Nt-acetylated and non Nt-acetylated aS-FRET constructs, compared with aS-Cerulean3 controls, showing that FRET is occurring in both aS-FRET cultures indicating that aS-Cerulean3 and aS-mNeonGreen are interacting.

Once the relative average Cerulean3 fluorescent signal for each culture was calculated, a clear reduction could be seen when the FRET construct was expressed, compared to when the aS-Cerulean3 alone was expressed. This showed that FRET was occurring in cells producing the FRET construct pET Duet-1 aS-Cerulean3 aS-mNeonGreen (**Figure 3.10**).

3.3 Measurement of FRET using Fluorescent Lifetime Imaging (FLIM)

To confirm the FRET measurements taken using wide field microscopy and to obtain further evidence of interactions, FRET was measured using FLIM. FLIM measurements were obtained at the Central Laser Facility at Harwell. FLIM is a way of examining FRET very precisely at a single molecule level with minimal variation, due to the measurements taken, just monitoring the fluorescent lifetime of a single donor fluorophore. Preliminary data was obtained using the aS-Cerulean3 with aS-mNeonGreen FRET construct, used previously, without the co-expression of NatB. As Green-Red FRET pairs can offer advantages over Blue-Green/Yellow pairs, including less phototoxicity and greater spectral separation (Bajar *et al.*, 2016), a second FRET construct to produce aS-mNeonGreen simultaneously with aS-mCherry was created. Cell extracts from cells expressing the second construct were run on a Coomassie Blue stained SDS-PAGE gel to confirm production of both aS-mNeonGreen and aS-mCherry (**Figure 3.11**).

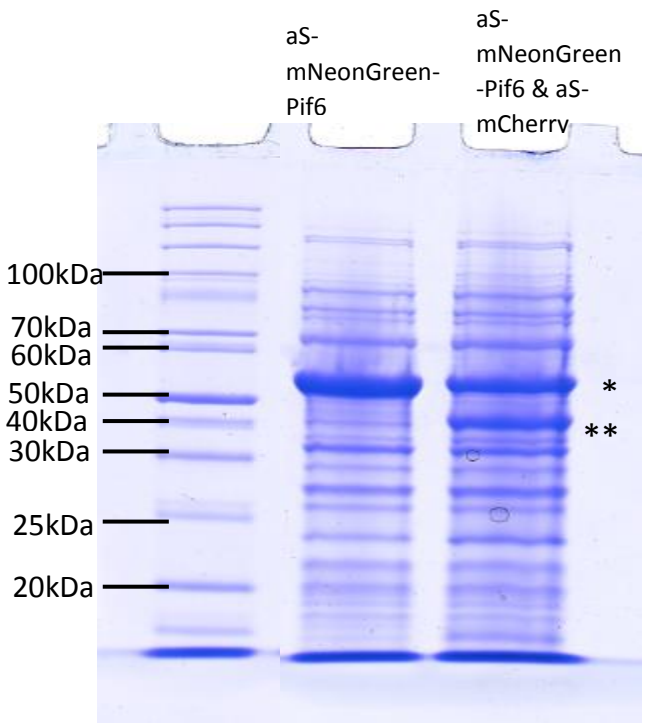


Figure 3.11. Coomassie Blue stained SDS-PAGE gel showing production of aS-mNeonGreen as a control and the FRET construct producing aS-mNeonGreen and aS-mCherry. Expected molecular weights aS-mNeonGreen- 53.1 kDa (*), aS-mCherry- 41.5 kDa (**).

The new FRET construct was expressed to produce aS-mNeonGreen simultaneously with aS-mCherry in live *E. coli*, both with or without expression of the NatB complex to produce both Nt-acetylated and non Nt-acetylated forms of the FRET construct proteins. These cells were examined for FRET using FLIM. Controls could be introduced by photo bleaching the acceptor fluorophore within a restricted area of a field of view (**Figure 3.13**) Here the photo bleached rectangle can be seen to have a higher level of fluorescence and the fluorescence lifetime image can be seen to have a longer fluorescent lifetime.

A clear reduction in averaged fluorescent lifetimes between single fluorophore controls and FRET constructs was observed, confirming FRET as measured by FLIM. This was seen in cells producing both FRET constructs, with and without NT-acetylation, when expressed in cells during log phase growth and for stationary cells (**Figure 3.12**).

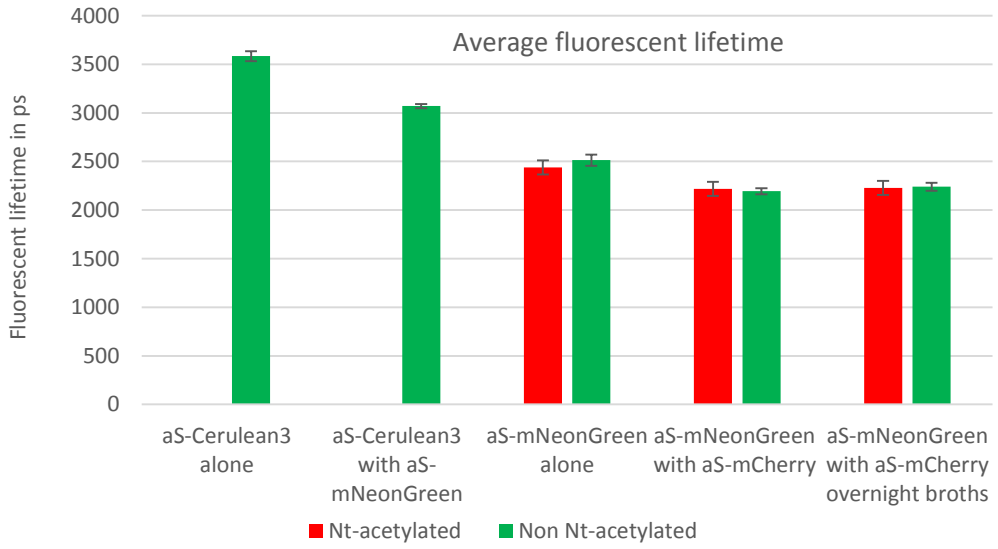
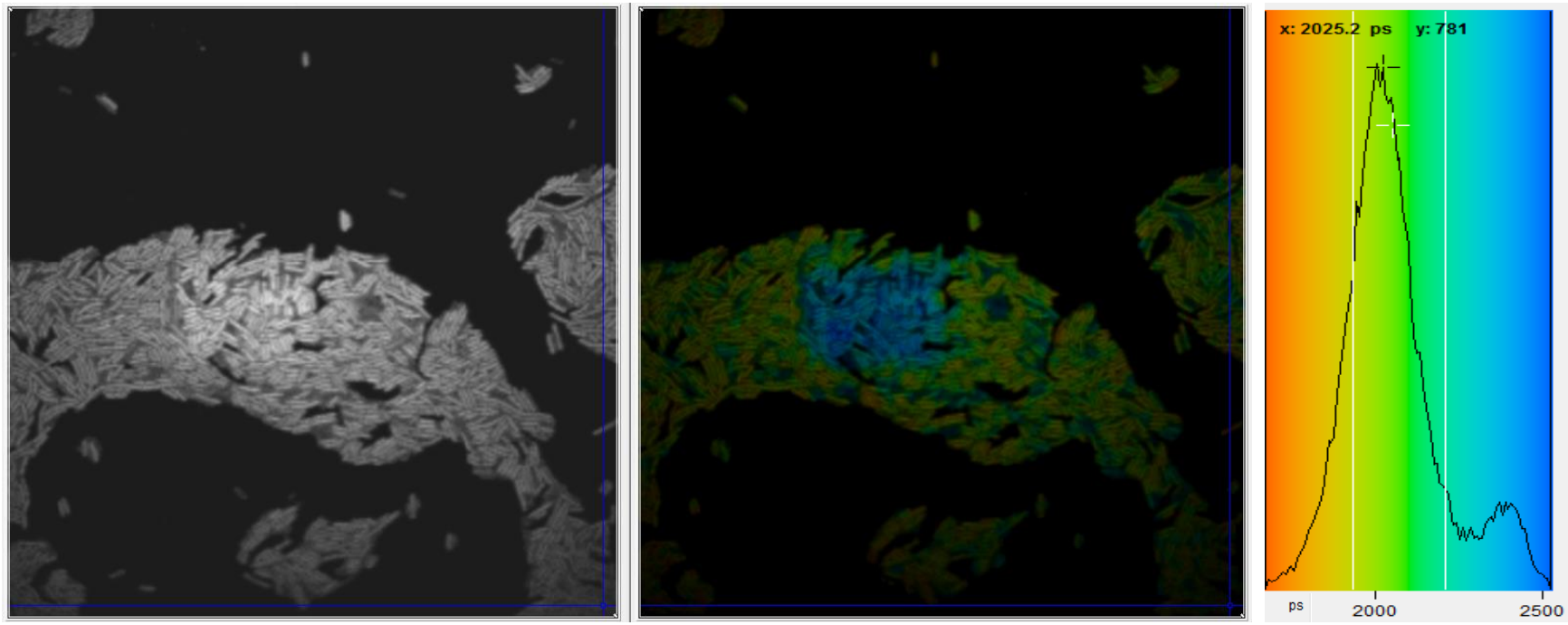


Figure 3.12. Average fluorescent lifetime in pico seconds (ps) for single fluorophore controls and FRET constructs.

However when analysing the fluorescent lifetime of individual stationary cells, two peaks were obtained for fluorescent lifetime, in cells producing Nt-acetylated aS-mNeonGreen and aS-mCherry and only one peak was obtained for cells producing non Nt-acetylated aS-mNeonGreen and aS-mCherry. This indicates the presence of two



aS-mNeonGreen fluorescence | Fluorescent lifetime | Fluorescent lifetime in ps

Figure 3.13. FLIM image of *E. coli* cells producing non Nt-acetylated aS-mNeonGreen-Pif6 and aS-mCherry simultaneously. A central rectangle has had the mCherry fluorophore photo bleached so that it can no longer act as an acceptor and FRET cannot occur in this area as a control. In the left image, these cells can be seen to have a brighter mNeonGreen fluorescence. In the central image the control square can be seen to have a longer fluorescent lifetime, this also shows as a second peak in the chart to the right, which shows the number of pixels with each fluorescent lifetime.

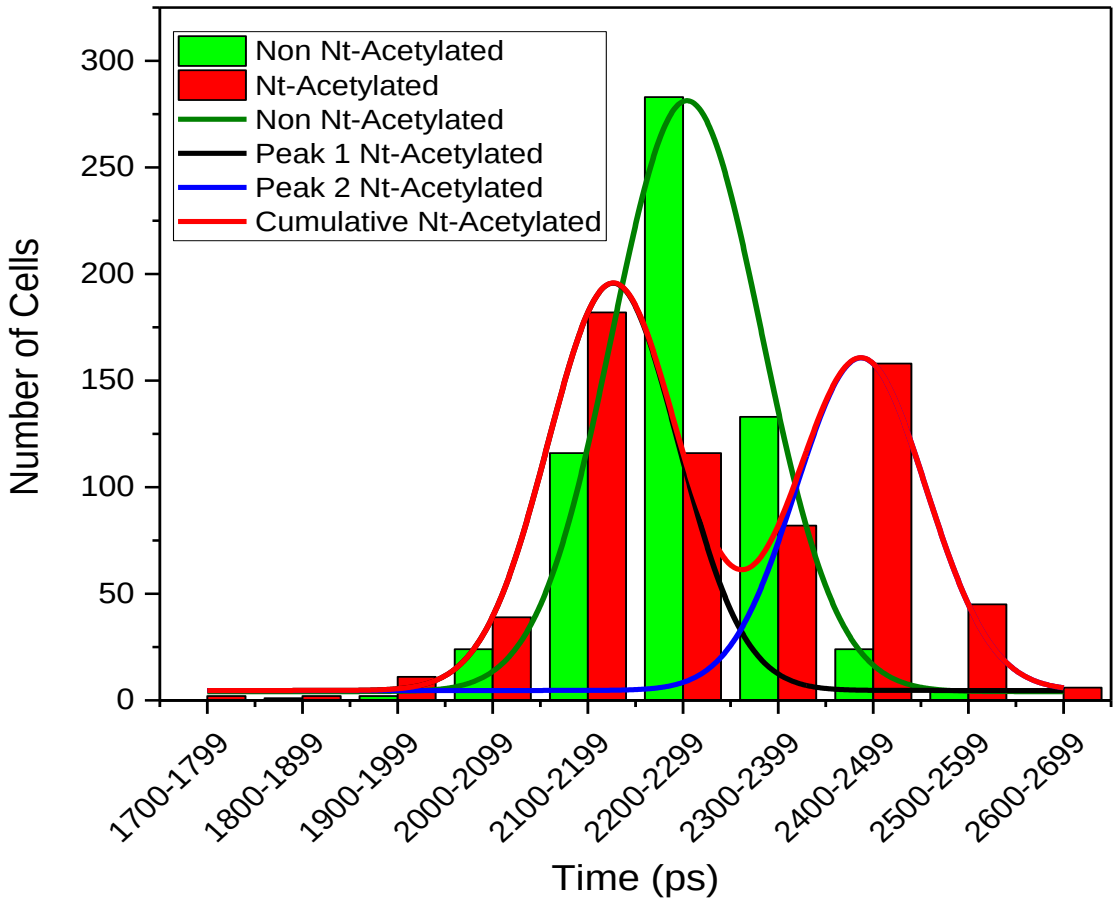


Figure 3.14. Fluorescent lifetime in pico seconds for individual cells in overnight stationary *E. coli* cultures producing either Nt-acetylated or non Nt-acetylated aS-mNeonGreen-Pif6 and aS-mCherry simultaneously. A single lifetime peak was obtained for non Nt-acetylated aS and two for Nt-acetylated aS, indicating the presence of two different forms of oligomerisation.

different forms of oligomerisation when Nt-acetylated aS is produced in older stationary cells, but only one when aS is non Nt-acetylated (**Figure 3.14**).This change in the oligomerisation of aS during stationary phase in live cells, *in vivo*, could correlate with the larger size of purified Nt-acetylated aS, as seen in the *in vitro* size exclusion assay.

3.4 Development of an aS-Venus-Biomolecular Fluorescence Complementation (BiFC) construct to monitor oligomerisation

Having observed differences in oligomerisation due to the presence or absence of Nt-acetylation of aS, this was further investigated, using Biomolecular Fluorescence Complementation (BiFC)(Yutaka Kodama and Hu, 2010). BiFC is a method that enables a continuous measurement of differences in oligomerisation over several hours within live cells. An aS-Venus-BiFC construct was produced and a pET DUET plasmid was used to simultaneously produce aS-N-Venus (aS attached to the first 154 amino acids of the Venus fluorophore) and aS-C-Venus (aS attached to the Venus fluorophore amino acid 155 to the end).

If an aS oligomer forms in a parallel conformation it can bring the two halves of the Venus fluorophore together, enabling the production of yellow Venus fluorescence. If an anti-parallel conformation forms, holding the two halves of the Venus fluorophore apart prevents the production of Venus fluorescence (**Figure 3.15**).

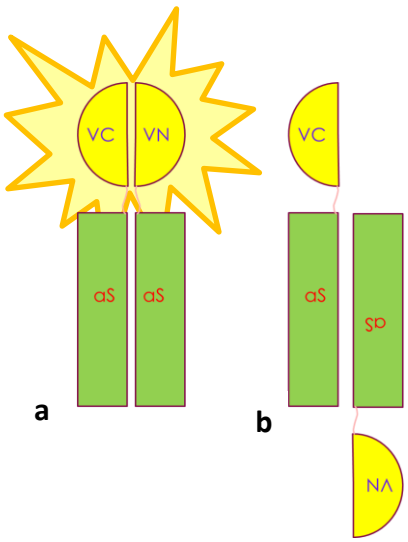


Figure 3.15. Illustration of how BiFC works. If two aS proteins oligomerise in such a way as to bring the two halves of the Venus protein together, they can form a functional fluorophore (a). If the two aS proteins do not closely interact or oligomerise in such a way as to hold the two halves of the fluorophore apart, the fluorophore cannot reform and no fluorescence is seen (b).

Images were taken of *E. coli* cells expressing either aS-N-Venus or aS-C-Venus, both of which show no Venus fluorescence on their own. Images of *E. coli* expressing the complete aS-Venus-BiFC construct show Venus fluorescence within the cells (**Figure 3.16**).

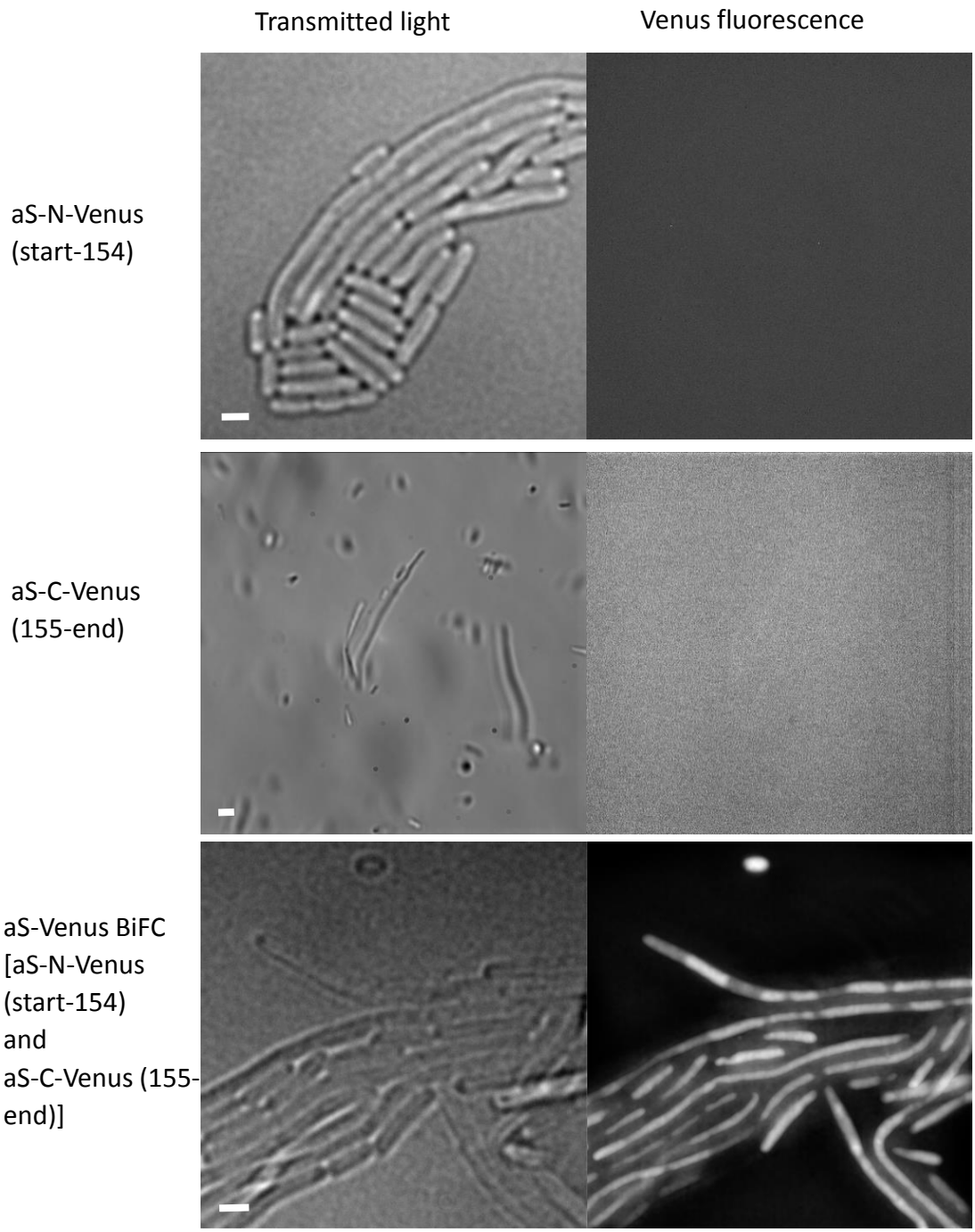


Figure 3.16. Phase and yellow, Venus fluorescence images of *E. coli* cells producing one half of the Venus BiFC construct, either aS-Venus-(start-154) or aS-Venus-(155-end) and cells producing the complete aS-Venus BiFC, [aS-Venus-(start-154) and aS-Venus-(155-end)]. Venus fluorescence is only seen when the complete aS-Venus BiFC construct is expressed. Scale bar 1 μm.

By growing *E. coli* in a fluorescent plate reader, it was possible to follow the development of fluorescence within live culture simultaneously with OD_{595}, to monitor cell growth.

E. coli BL21 DE3 aS-Venus-BiFC cell cultures were induced with 100µg/ml IPTG both with and without the plasmid to produce the NatB complex, enabling production of either Nt-acetylated or non Nt-acetylated forms of the protein (**Figure 3.17**).

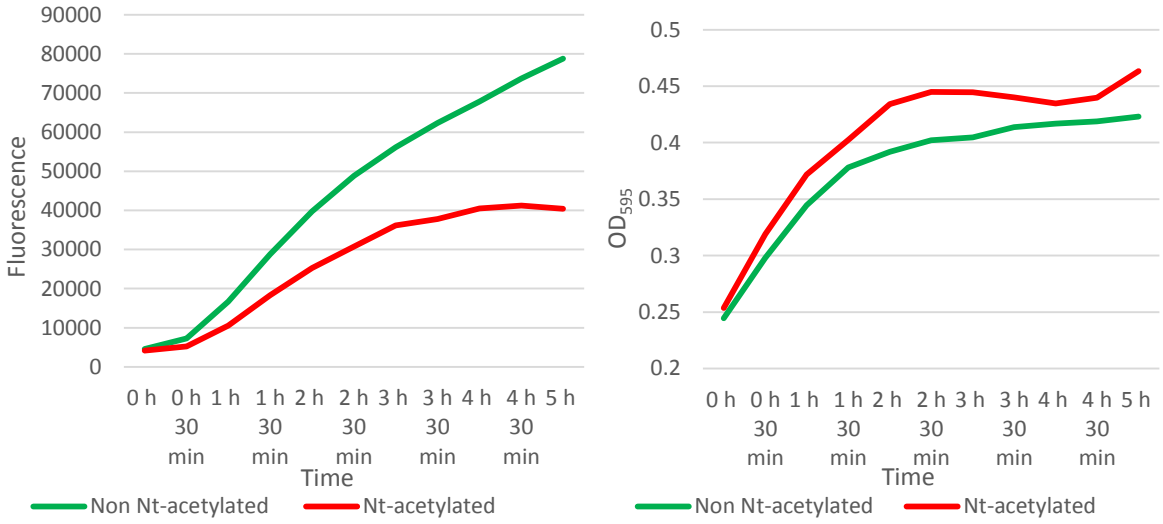


Figure 3.17. Graphs showing fluorescence and simultaneous OD_{595} readings over time, of *E.coli* cells producing aS-Venus-BiFC with or without the NatB complex. Cells were induced with 100µg/ml IPTG to produce either Nt-acetylated or non Nt-acetylated forms of the protein.

Samples were taken from identical cultures at pre-induction and 1, 3, 5 and 7 hours post-induction with IPTG, both with and without Nt-acetylation as used in the plate reader. Cell extracts were prepared from samples taken and a coomassie stained gel and western blot carried out. These gels show no significant difference in the levels of protein produced in cells, either able or unable to Nt-acetylate aS (**Figure 3.18**). Faint bars were also seen at a higher than expected level on the western blot, indicating the presence of oligomers, these were most clearly seen with cell extracts from cultures producing Nt-acetylated aS-Venus BiFC.

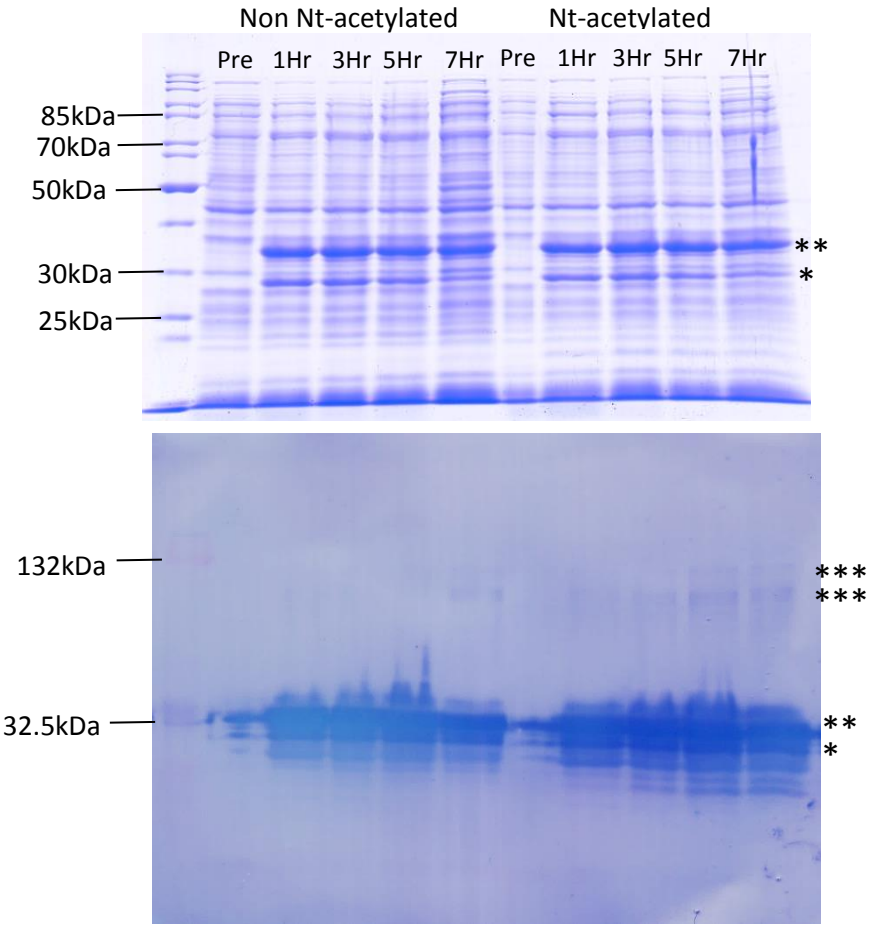


Figure 3.18. Coomassie Blue stained SDS-PAGE gel and matching western blot using Rabbit anti-aS primary antibody, of extracts from *E.coli* cells producing either Nt-acetylated or non Nt-acetylated aS-Venus BiFC. Comparable levels of protein show this is not the reason for the differing levels of BiFC fluorescence. Expected molecular weights aS-Venus C terminal- 24.1 kDa (*) and aS-Venus N terminal 32.1 kDa (**).Faint bands at a higher than expected level on the western blot, indicate the presence of oligomers(***)

Differences were seen in fluorescence, according to whether the NatB complex was co-expressed enabling the NT-acetylation of the aS produced. This difference in fluorescence was shown not to be due to different levels of cell growth or protein production (**Figures 3.17 and 3.18**).

Inconsistencies in early assays, where large differences in fluorescence readings were seen between plates and between wells of single plates with replicate samples, meant that optimisation of this technique was required.

3.4.1: Optimisation of aS induction

In order to develop the use of aS-Venus-BiFC into a sensitive, consistently repeatable assay, induction rates were first optimised. A culture of *E. coli* BL21 DE3 cells containing a plasmid to produce aS-Cerulean3 was split into 8 separate cultures that were induced with varying concentrations of IPTG ranging from zero to 100μg/ml. Fluorescence and OD_{595} readings were taken simultaneously to compare cell growth with the fluorescence produced.

IPTG concentrations from zero to 0.2 μg/ml, resulted in maximum rates of growth but minimal fluorescence. Concentrations of 2μg/ml and 1 μg/ml IPTG resulted in maximum rates of growth, but a delayed production of fluorescence. An IPTG concentration of 100μg/ml resulted in a significantly reduced rate of growth and very little fluorescence. IPTG concentrations of 10 and 20 μg/ml had the fastest rates of fluorescence production, despite a reduction in growth rate (**Figures 3.19 and 3.20**).

Cell extracts from samples of *E. coli* BL21 DE3 cell cultures producing aS-Cerulean3, induced for 3 hours with the same IPTG concentrations as used for the growth curves, were run on a Coomassie stained gel. This also shows the largest amount of aS-Cerulean3 being produced within 3 hours, in the cultures induced with IPTG concentrations of 10 and 20 μg/ml (**Figure 3.21**)

A final concentration of 20μg/ml (83.9μM) was used for future aS-Venus-BiFC assays.

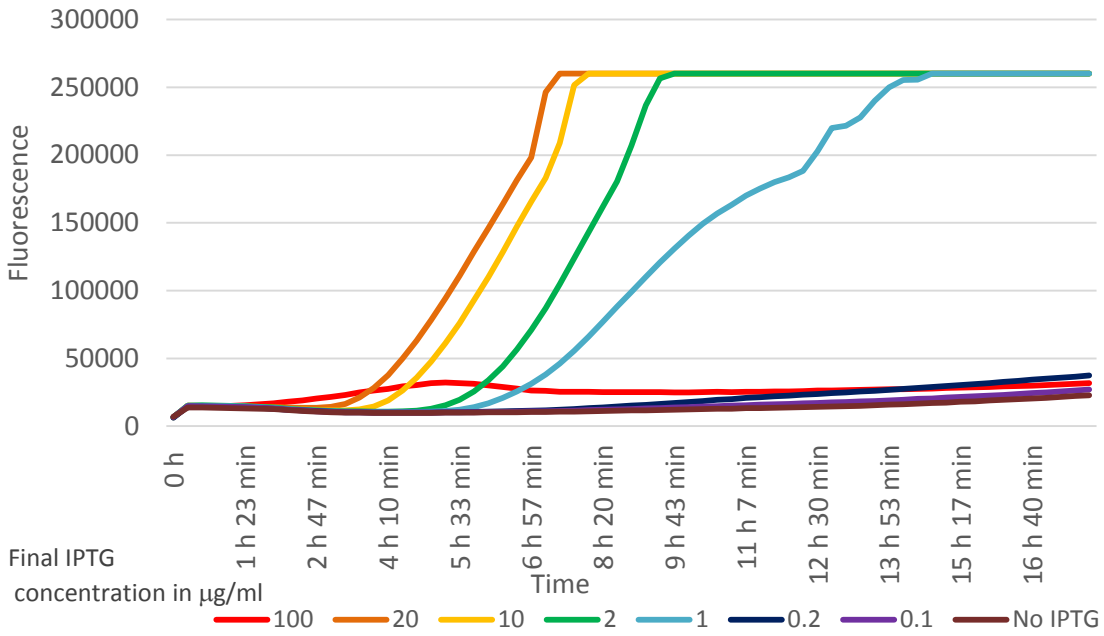


Figure 3.19. Graph showing the level of fluorescence over time of *E.coli* cells producing aS-Cerulean3 having been induced with varying concentrations of IPTG.

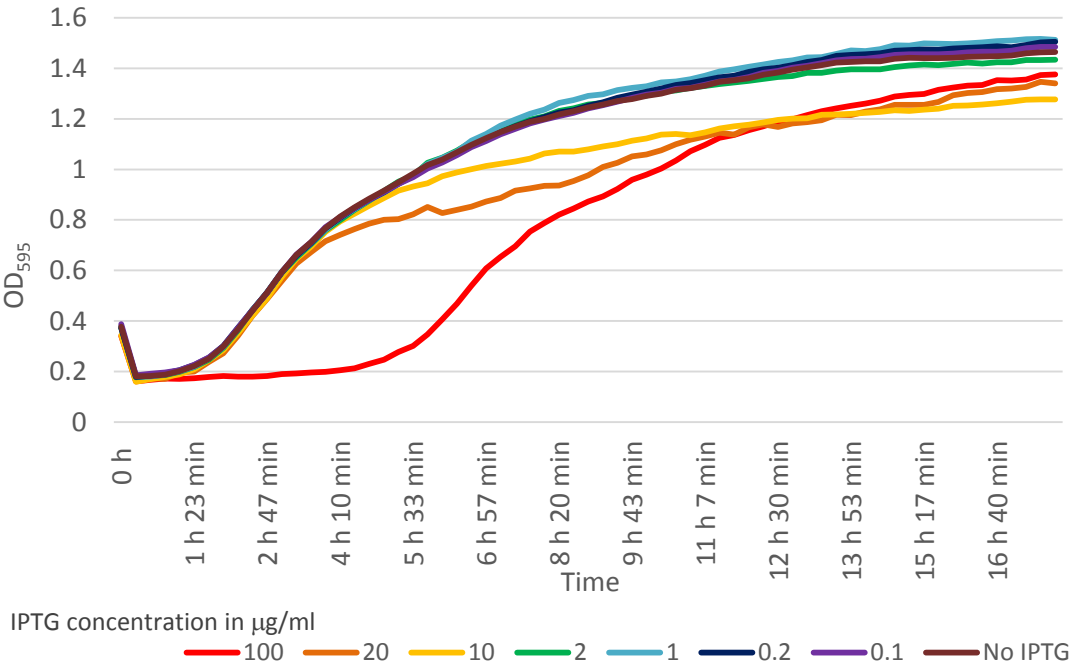


Figure 3.20. Graph showing OD_{595} over time of *E.coli* cells producing aS-Cerulean3 having been induced with varying concentrations of IPTG. Readings were taken simultaneously with the fluorescent measurements of the proceeding graph. 100 µg/ml IPTG induction has extremely reduced growth and fluorescence, 20 µg/ml has high levels of fluorescence and slightly reduced growth so will be used.

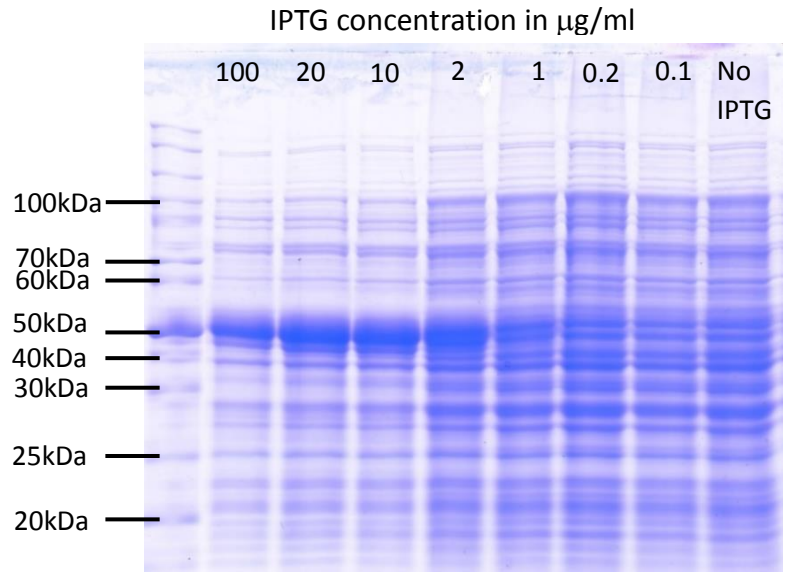


Figure 3.21. Coomassie Blue stained SDS-PAGE gel showing the level of protein produced by *E.coli* cells producing aS-Cerulean3 having been induced for 3 hours with varying concentrations of IPTG. IPTG concentrations range from zero to 100μg/ml. The highest levels of protein were produced when a final concentration of 2 to 20 μg/ml was used to induce protein production. Expected molecular weight of aS-Cerulean3 - 42.5 kDa.

3.4.2. Optimisation of starting OD_{595}

To optimise the starting OD_{595}, *E. coli* cultures at different starting OD_{595} values, expressing the aS-Venus-BiFC construct were incubated in a fluorescent plate reader, taking simultaneous readings for Venus fluorescence and OD_{595}. Overnight starter cultures of aS-Venus-BiFC with and without the plasmid for production of the NatB complex were used to inoculate new cultures which were grown to mid log, these were then sub cultured, to obtain cultures with OD_{595} values of 0.1 and 0.01. These cultures were then induced with 20μg/ml of IPTG and placed into 6 wells of a 96 well plate which was incubated in a CLARIOstar fluorescent plate reader. Graphs for the OD_{595} starting values of OD_{595}0.1 and OD_{595}0.01 are shown (**Figures 3.22 and 3.23**).

A starting OD_{595} of 0.01 gave a slightly longer lag phase for both OD_{595} growth and fluorescence, compared to that for a start OD_{595} 0.1. However, the culture with a starting OD_{595} of 0.01 gave the greatest difference in fluorescence values between cultures producing Nt-acetylated aS-Venus-BiFC and non NT-acetylated aS-Venus-BiFC.

A starting OD_{595} of 0.01 was used for future aS-Venus-BiFC assays.

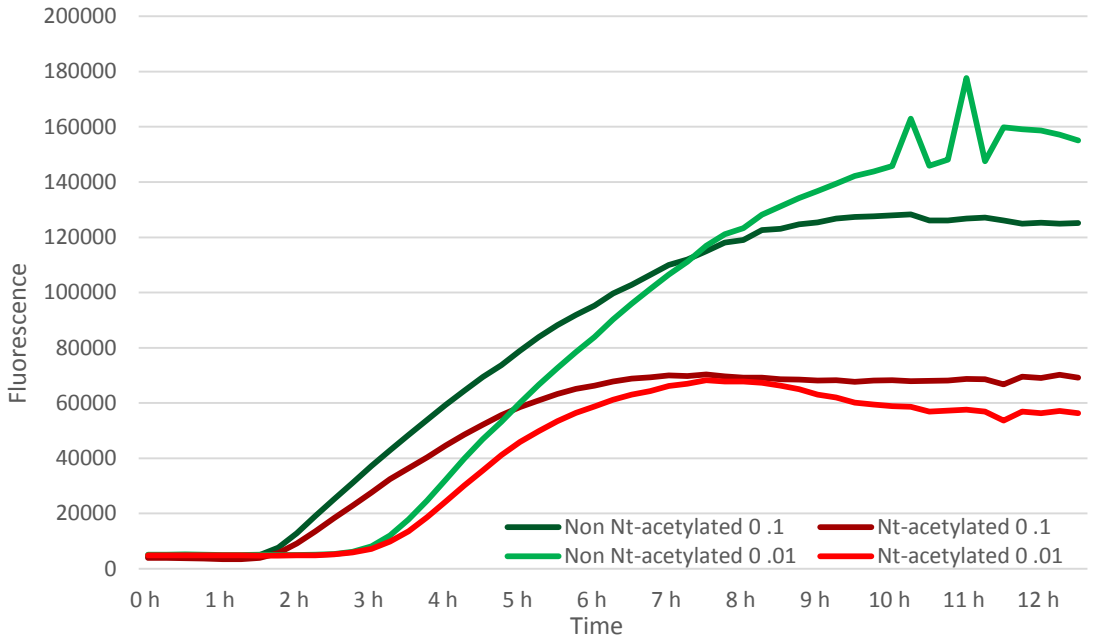


Figure 3.22. Graph showing the level of fluorescence over time of *E.coli* cells producing either Nt-acetylated or non Nt-acetylated aS-Venus BiFC, with an initial OD_{595} of 0.1 or 0.01. Cells were induced with a final concentrations of 20 μg/ml IPTG. A starting OD_{595} of 0.01 gave the greatest difference in fluorescence between Nt-acetylated and non Nt-acetylated aS-Venus BiFC.

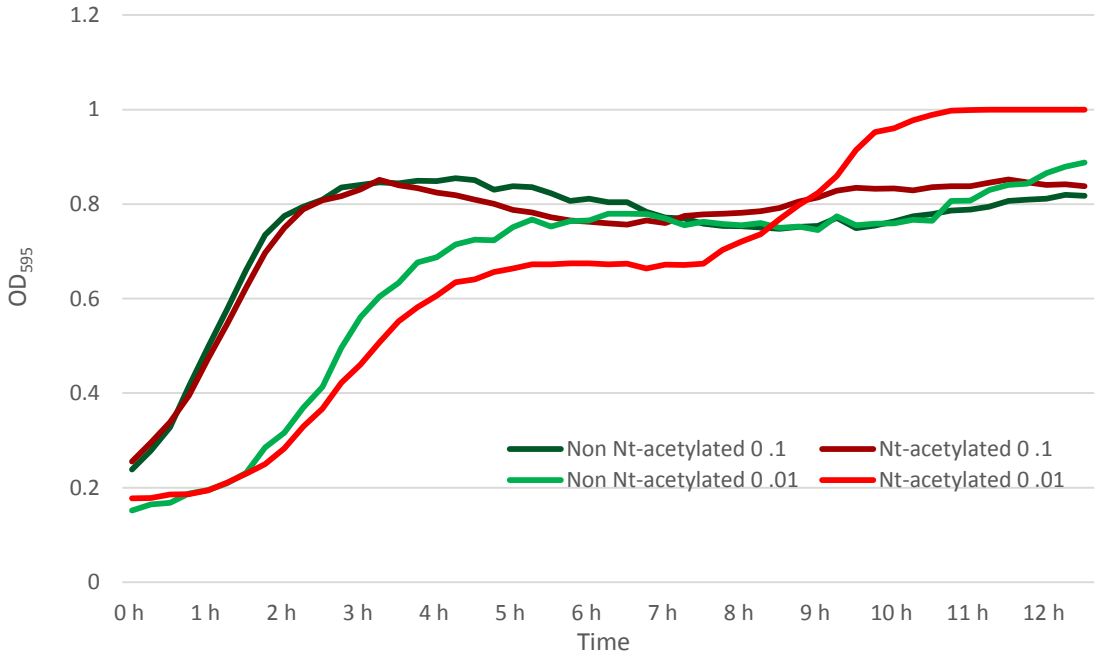


Figure 3.23. Graph showing OD_{595} values over time of *E.coli* cells producing either Nt-acetylated or non Nt-acetylated aS-Venus BiFC, with an initial OD_{595} of 0.1 or 0.01. Cells were induced with a final concentrations of 20 μg/ml IPTG. Readings taken simultaneously with fluorescent readings of the previous graph. Similar growth rates are seen in both cultures at each starting OD_{595}.

3.4.3. Optimisation of 96 well plates and plate position

Different types of 96 well plate were compared during aS-Venus-BiFC assays, black-walled clear bottomed plates, without cell culture coatings, with parafilm sealed lids, were found to give the most consistent results, with the best range of fluorescence values.

It was noted that there was a large difference in fluorescence when comparing results from exactly the same cell culture in different well positions. To examine this, a culture of *E. coli* expressing the aS-Venus-BiFC was grown in an temperature controlled, fluorescent plate reader, taking both fluorescence and OD_{595} readings in a 96 well plate. A heat map was created for the fluorescence graph according to the level of fluorescence, at each plate position (Figures 3.24). The same heat map colour coding was applied to the OD_{595} graph to show how the difference in fluorescence relates to cell growth (**Figures 3.24 and 3.25**).

A difference in growth showed an inverse correlation with fluorescence, however only a small reduction growth correlated with a large increase in fluorescence.

This difference in fluorescence in 3 separate assays was analysed to produce a heat map. Using the time point at which the highest fluorescence reading was taken, the relative difference from the lowest fluorescence reading was calculated for each well (**Figure 3.26**). A graph showing the average relative difference for each well, with error bars added to show the variation between the separate runs, also highlights the high level of variation between runs in wells around the outside of the plate (**Figure 3.27**).

Due to the results obtained examining the effect of plate position on aS-Venus-BiFC fluorescence, the outside wells were not used in subsequent assays. The relative difference figures were also used as a correction factor, to obtain more accurate results in further assays.

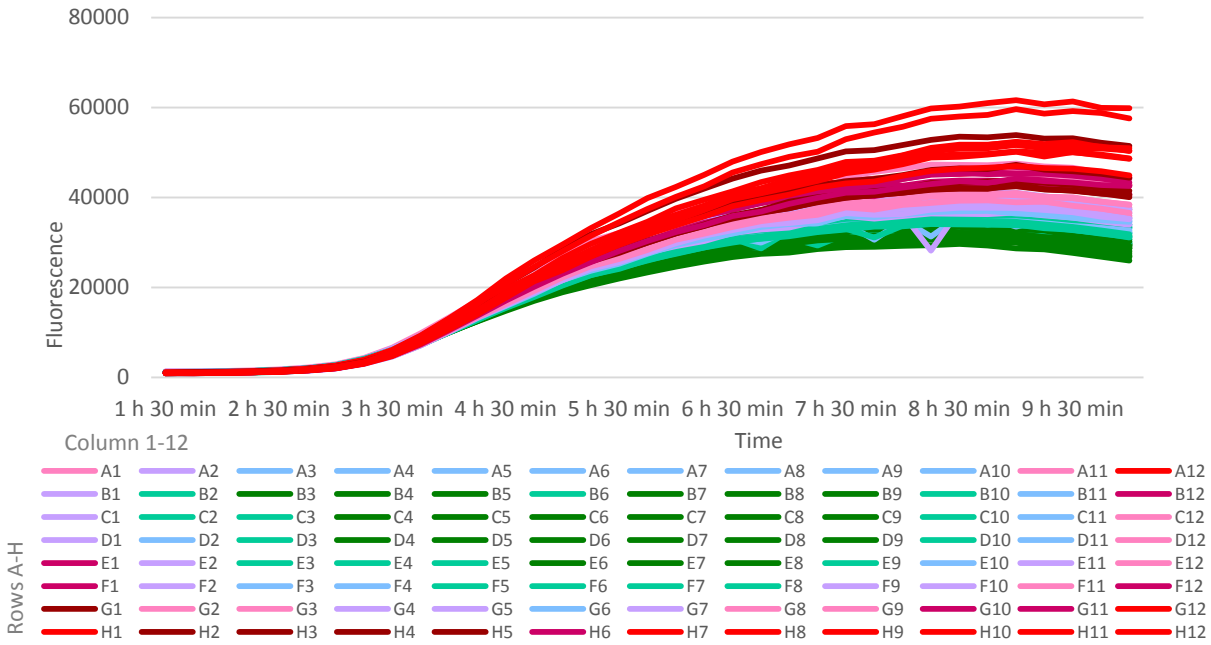


Figure 3.24. **Graph showing the level of Venus fluorescence over time of a single culture of *E.coli* cells producing non Nt-acetylated aS-Venus BiFC**. Cells at an initial OD_{595} of 0.01 were induced with a final concentrations of 20μg/ml IPTG. The level of fluorescence was found to vary with plate position as shown by comparing the graph colours to colours on the position table which corresponds to the position on 96 well plates.

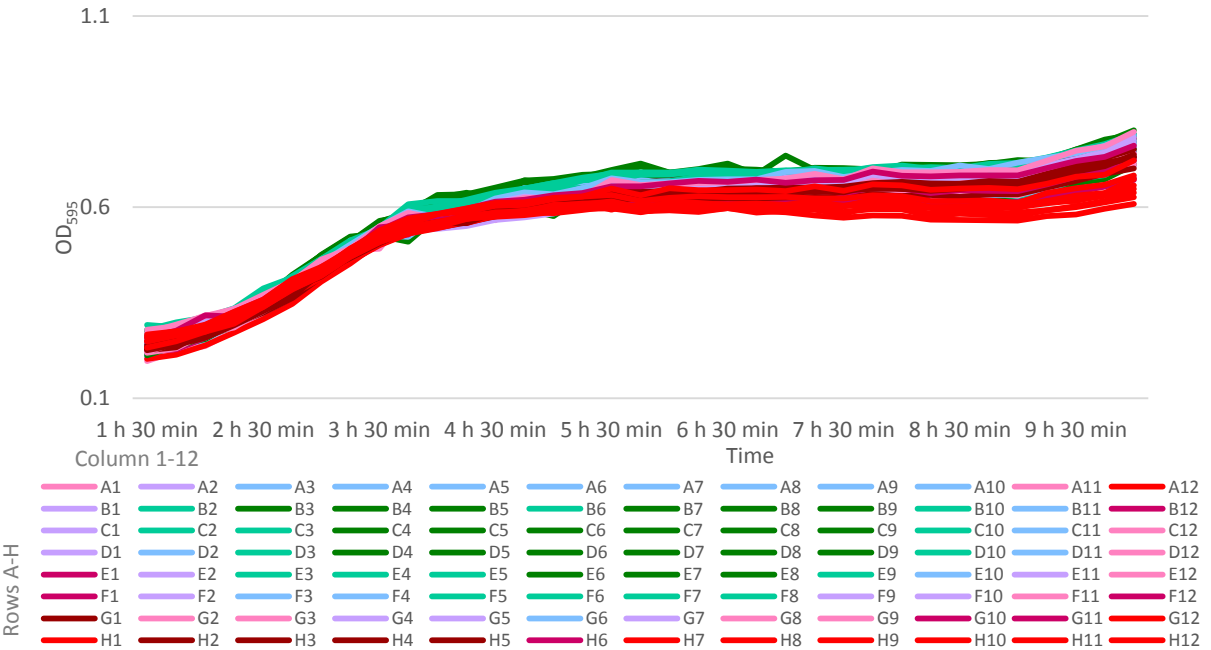


Figure 3.25. Graph showing OD_{595} values over time of a single culture of *E.coli* cells producing non Nt-acetylated aS-Venus BiFC. Cells with an initial OD_{595} of 0.01 were induced with a final concentrations of 20 μg/ml IPTG. Readings were taken simultaneously with fluorescent readings for the previous graph. OD_{595} values also varied with plate position as shown by comparing the graph colours to colours on the position table.

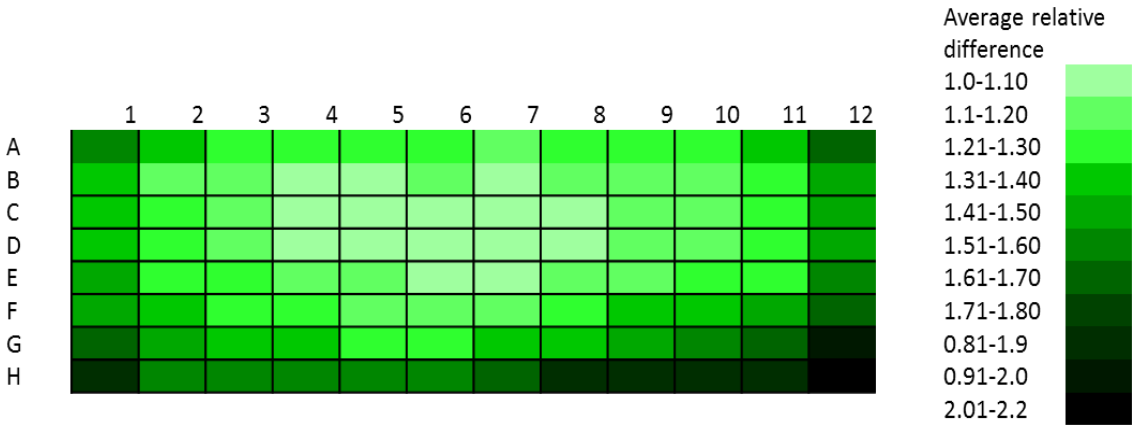


Figure 3.26. Heat map showing the average relative difference in fluorescence from the lowest fluorescence value at the time point when the highest level of fluorescence was reached, shown as position on a 96 well plate. Results were obtained using cultures of *E.coli* cells producing non Nt-acetylated aS-Venus BiFC, with an initial OD_{595} of 0.01 and having been induced with a final concentrations of 20 μg/ml IPTG. The greatest relative difference is seen at the corners bottom and sides of the plate.

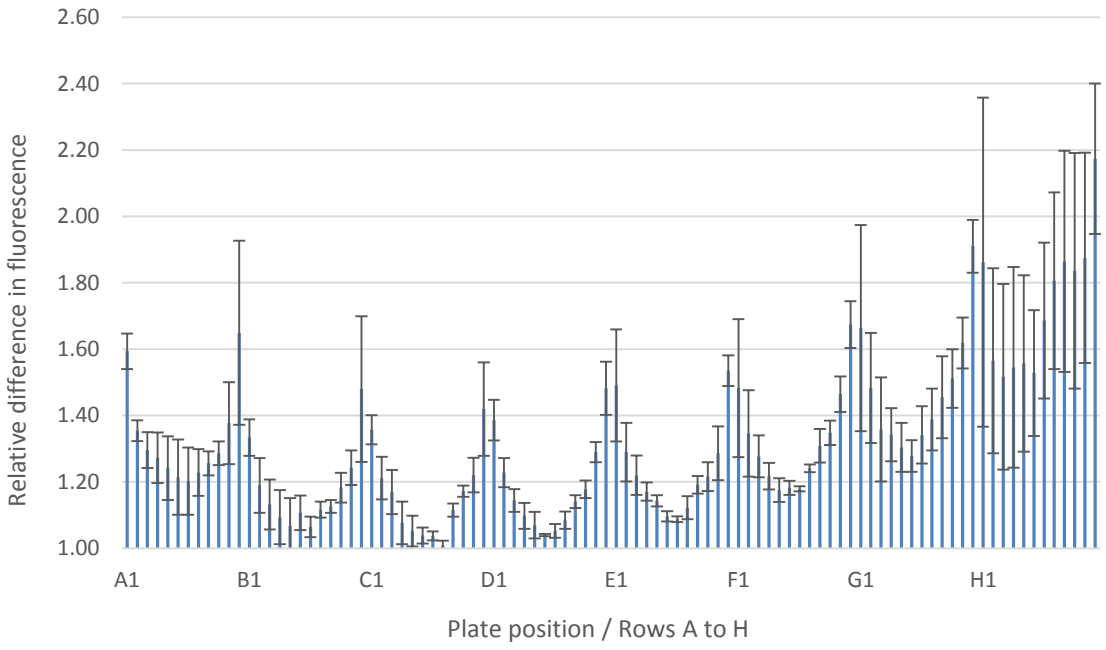


Figure 3.27. Graph showing average relative difference in fluorescence from the lowest fluorescence value at the time point when the highest level of fluorescence was reached. Shown as position row by row and including S.D. error bars.

3.5 Congo Red and NIAD-4 staining of live cells

aS is known to form β-sheet rich fibrils (Ross and Poirier, 2004). To examine whether the change in FRET observed in stationary cells could be due to this β-sheet formation, fluorescent dyes used in the identification of amyloid were added to live *E. coli* cultures. Congo Red and NIAD-4 fluorescently stain amyloid (Clement and Truong, 2014)(Brandenburg, Berlepsch and Koksch, 2012b), and both of these dyes were used to examine the development of amyloid within live *E. coli* cells expressing aS-Venus-BiFC, with and without the presence of the NatB complex, to produce both Nt-acetylated and non Nt-acetylated forms of the proteins.

Live *E.coli* cells were incubated in media containing each dye, whilst expressing the aS-Venus-BIFC construct. Images show clear amyloid formation within late log phase/ early stationary cells producing Nt-acetylated aS, predominantly at the cell poles. Only a small amount of amyloid formation is seen within cells producing non Nt-acetylated aS-Venus-BiFC (**Figure 3.28**).

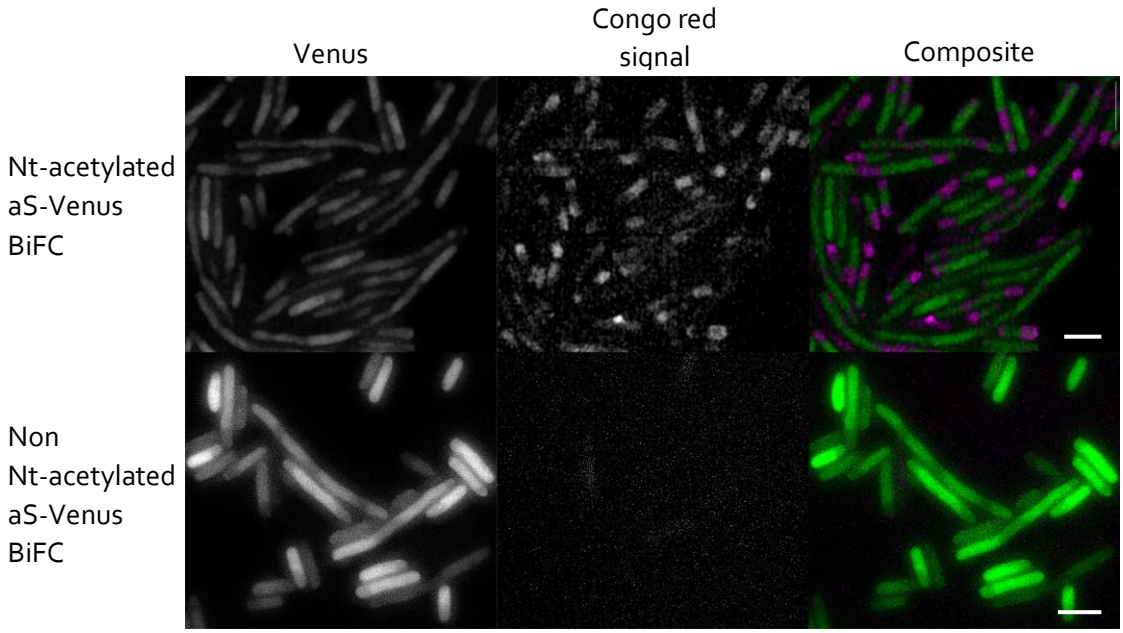


Figure 3.28. Images of *E. coli* producing aS-Venus BiFC induced with 100 μg/ml IPTG for 4 hours, with 0.001% Congo Red. Congo Red, red fluorescence indicates the formation of amyloid in areas of the cells producing Nt-acetylated aS-Venus BiFC but not in cells producing non Nt-acetylated aS-Venus BiFC. Scale bars 2 μm

(Eastwood *et al.*, 2017)

It was decided to examine this β-amyloid formation over time in live *E. coli* cells, as indicated by Congo Red fluorescence, in cells expressing the NatB complex and aS tagged with different yellow/green/blue fluorophores, as used during other FLIM and BiFC experiments. Congo Red was used in preference to NIAD-4 in further experiments due to its better aqueous solubility.

Cells expressing the different aS constructs were incubated in media containing Congo Red and imaged at 2, 4, 6 and 22 hours after induction with 100μg/ml IPTG. All cells within 3 fields of view were counted for each construct for each time point (a minimum of 381 cells for each) according to whether any red fluorescence could be seen within a cell or if only the fluorescence of the fluorophore could be seen. The percentage of cells showing red fluorescence and the percentage showing no red fluorescence were compared (**Figure 3.29**). The development of amyloid as indicated by Congo red fluorescence was found to be consistent with the different aS-fluorophore constructs.

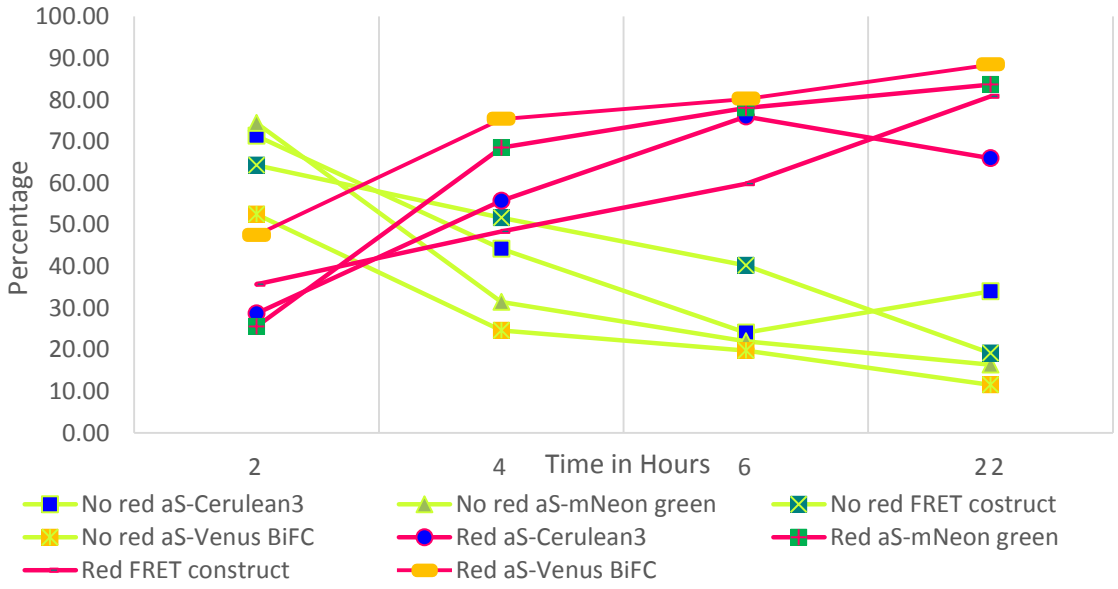


Figure 3.29. The percentage of *E.coli* cells with some Congo Red fluorescence indicating some amyloid formation versus the number of *E. coli* cell with no red fluorescence indicating the absence of any amyloid formation. All cells are producing Nt-acetylated aS attached to Cerulean3, mNeonGreen or both of these as a FRET construct or Venus BiFC. Similar results were obtained with all fluorophores and combinations (n = at least 381 cells per culture).

3.6 The use of BiFC to screen for aS-drug interactions

To examine the possibility of using the aS-Venus-BiFC assay as a screen to find drugs which interact with aS, 130 different drugs from the Selleckchem.com FDA Approved Drug Screening Library were screened using the aS-Venus BiFC assay.

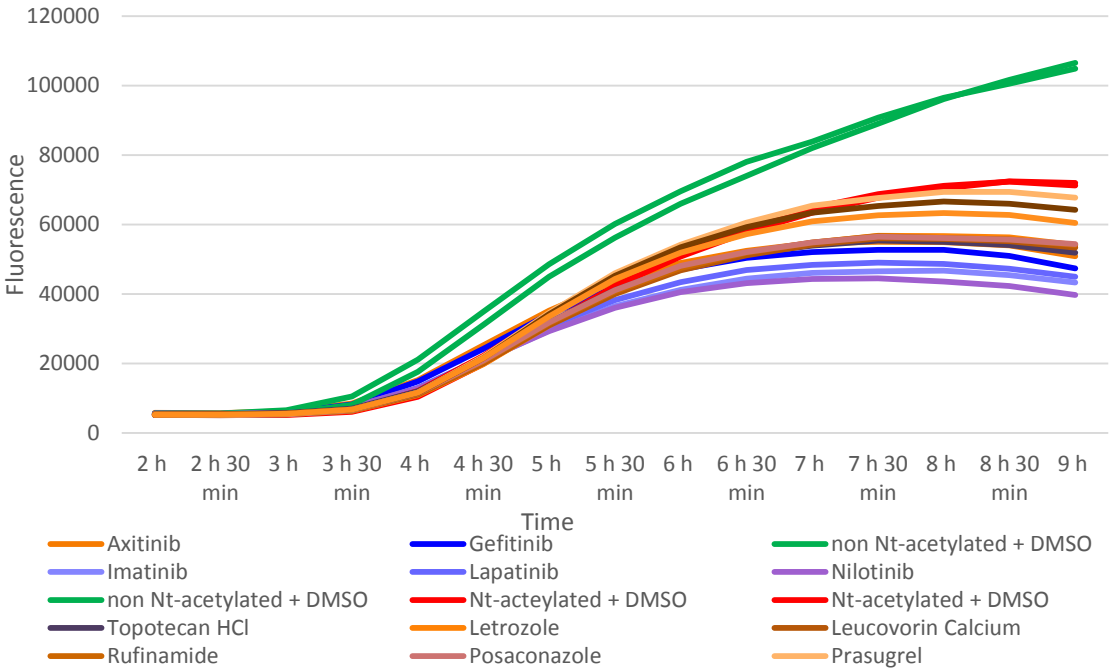


Figure 3.30. Graph showing the level of fluorescence over time of *E.coli* cells producing non Nt-acetylated aS-Venus-BiFC + DMSO controls, Nt-acetylated aS-Venus BiFC + DMSO controls or with the addition of a FDA approved drug at a final concentration of 1μM. Cultures were induced with a final concentrations of 20 μg/ml IPTG,

In initial assays four of the drugs, Gefitinib, Imatinib, Lapatinib and Nilotinib were found to have a larger effect on the level of BiFC fluorescence, all four are Tyrosine kinase inhibitors (**Figure 3.30**). New samples of three of these were purchased to confirm the original data.

In a confirmation assay using these drugs at a final concentration of 5μM, two drugs in particular reduced Nt-acetylated aS-Venus-BiFC fluorescence (**Figure 3.31**). Gefitinib is an inhibitor of epidermal growth factor receptor's (EGFR) tyrosine kinase and Lapatinib

is an inhibitor of EGFR and ErbB-2 (HER-2) tyrosine kinases. Both drugs are used in the treatment of adult cancers.

A further confirmation assay adding Gefitinib and Lapatinib to a lower final concentration of 0.5μM, also gave a reduction in Nt-acetylated aS-Venus-BiFC fluorescence (**Figure 3.32**).

Interestingly the anti-cancer drug Nilotinib, an inhibitor of Bcr-Abl tyrosine kinase activity, has been shown to reverse loss of dopamine neurones and improve motor behaviour in Parkinson's disease models (Hebron, Lonskaya and E-H Moussa, 2013).

Direct binding of one of these tyrosine kinase inhibitors, Gefitinib, to aS, was confirmed using Isothermal Titration Calorimetry (**Figure 3.33**) with measured binding affinities in the low micro molar range. ITC was conducted and data calculated by Charles River Ltd.

This work gives proof of concept for aS-Venus-BiFC as a potential drug screening method.

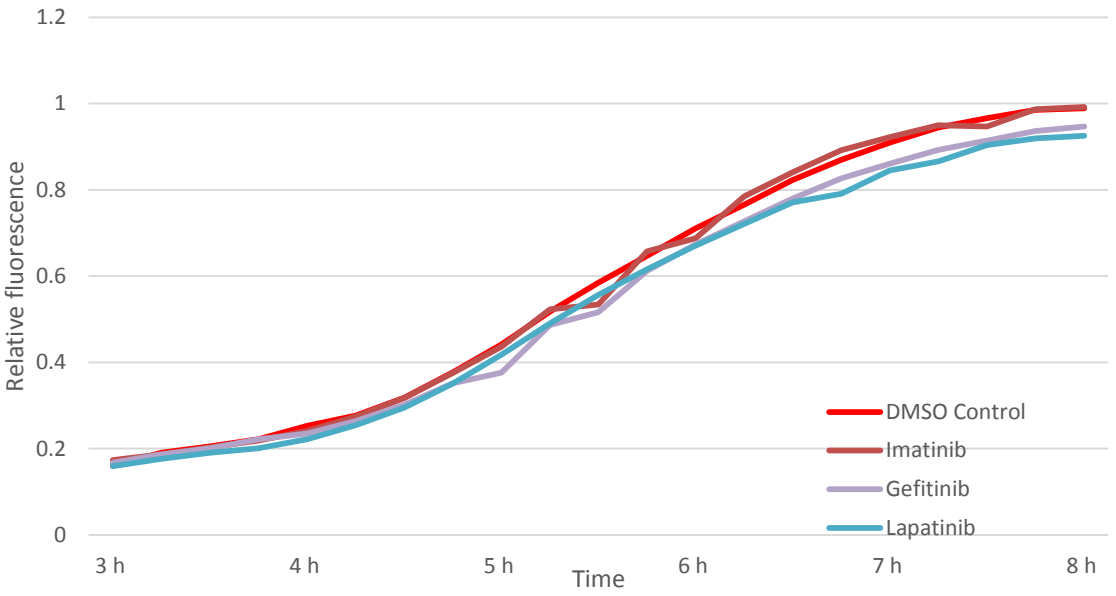


Figure 3.31. Graph showing the level of fluorescence over time of *E.coli* cells producing Nt-acetylated aS-Venus BiFC in the presence of Tyrosine kinase inhibitors. Cells were induced with a final concentrations of 20 μg/ml IPTG. A final concentration of 5 μM of each Tyrosine kinase inhibitors was also added. Two of these Gefitinib and Lapatinib saw a reduction in Venus BiFC relative fluorescence.

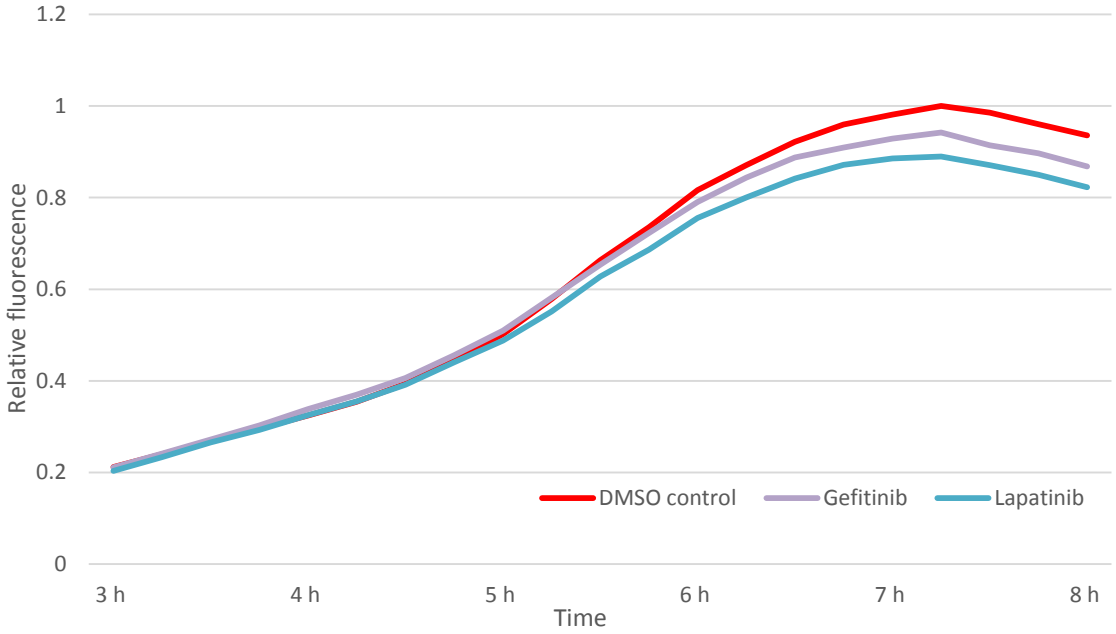


Figure 3.32. Graph showing the level of fluorescence over time of *E.coli* cells producing Nt-acetylated aS-Venus BiFC in the presence of 0.5μM Tyrosine kinase inhibitors. Cells were induced with a final concentrations of 20 μg/ml IPTG. A final concentration of 0.5 μM Gefitinib or Lapatinib was added to cultures and a reduction in relative fluorescence was seen at this reduced concentration.

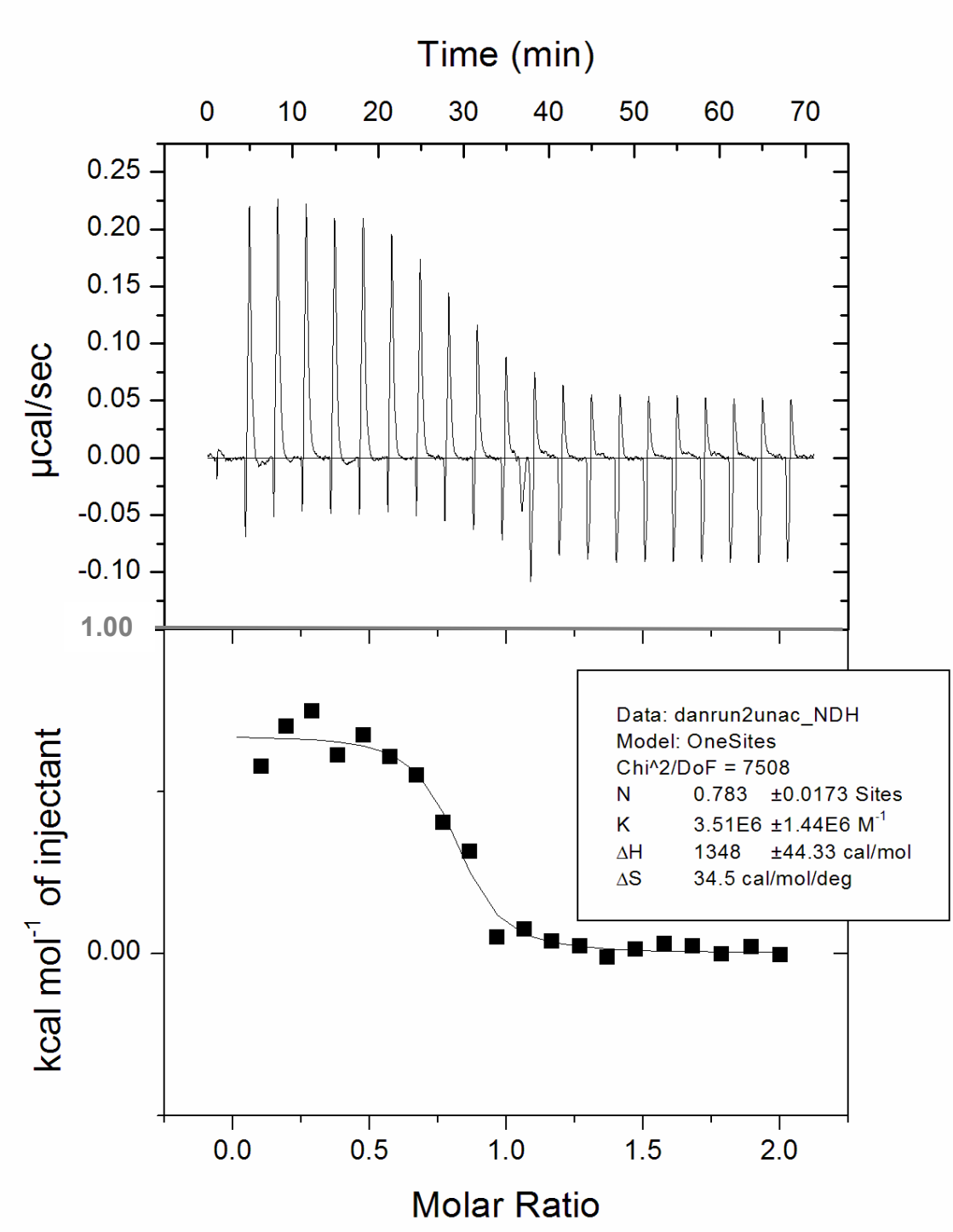


Figure 3.33. **ITC graphs showing energy transfer with time as Gefitinib was titrated into non Nt-acetylated aS.** A binding affinity of 3.51 µM ±1.44 µM. was calculated. ITC conducted and analysed with Charles River Ltd

3.7 Use of Venus-BiFC as a reporter of Nt-acetylation effects on Cdc8

Cdc8 is an α helical coiled coil protein, which forms dimers that then join end-to-end to produce polymers which can associate with actin-filaments. The Nt-acetylation of the yeast Tropomyosin, Cdc8 enhances these end-to-end contacts. These studies indicate that Nt-acetylation of Cdc8 stabilises the α-helical conformation of the amino terminus and stiffens the protein, resulting in the formation of longer filaments (East *et al.*, 2011) (Table 3.1). Other studies have shown that fusing Cerulean3 to the carboxyl terminus of Cdc8, disrupts the proteins ability to form end to end contacts and abolishes its ability to interact with actin and thus function within a cell (Brooker, Geeves and Mulvihill, 2016).

The use of Venus-BiFC to investigate Cdc8 polymerisation was examined. A Venus-BiFC construct was produced attached to the *Schizosaccharomyces pombe* tropomyosin, Cdc8. The Cdc8-Venus-BiFC construct enabled the simultaneous production of Cdc8-Venus-(start-154) and Cdc8-Venus-(155-end). As Cdc8 dimers form the two halves of the Venus fluorophore should form a complete Venus fluorophore, enabling the production of Venus fluorescence, and this was seen when the Cdc8-Venus BiFC construct was expressed in its non Nt-acetylated form. However a drop in fluorescence was seen when the protein was expressed in its Nt-acetylated form (Figure 3.34). This change in Cdc8-Venus-BiFC fluorescence is not due to differences in cell growth as shown by simultaneous readings for OD_{595} (**Figure 3.35**).

The theory was proposed that the two halves of the Venus fluorophore being smaller than the two complete Cerulean3 fluorophores used in previous studies (Brooker, Geeves and Mulvihill, 2016) could be forced apart by the more stable, stiffer Nt-acetylated Cdc8-Venus-BiFC, but not by the less stable more flexible non Nt-acetylated Cdc8-Venus-BiFC (**Figure 3.36**). This could be investigated further by examining the viscosity of each purified set of BiFC proteins, both Nt-acetylated and non Nt-acetylated.

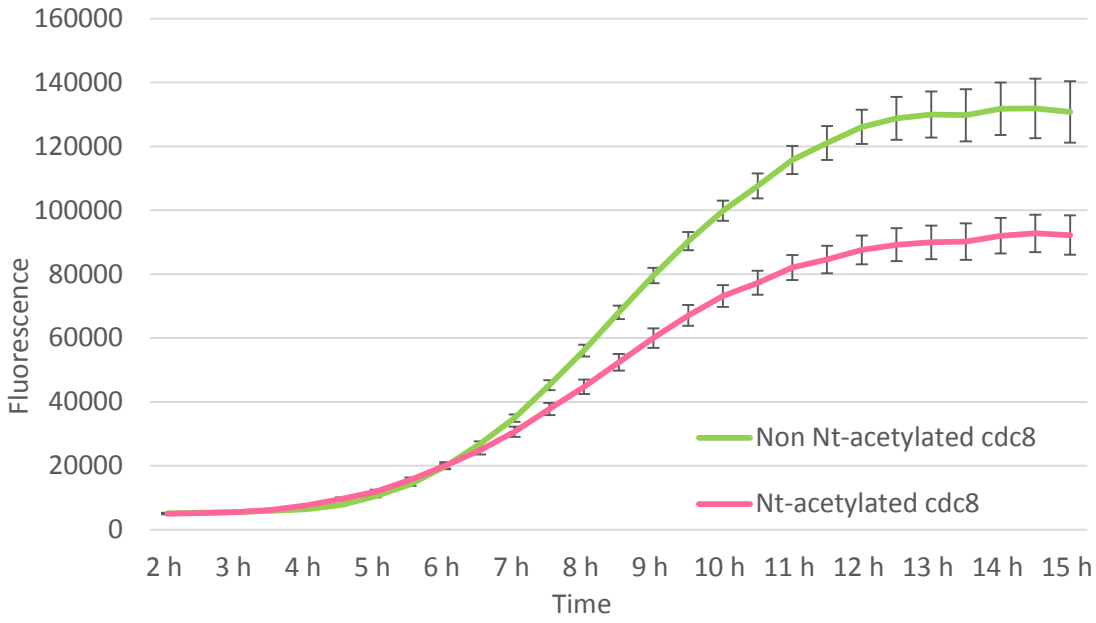


Figure 3.34. Graph showing the level of fluorescence over time of *E.coli* cells producing either Nt-acetylated or non Nt-acetylated cdc8-Venus BiFC. Cells were induced with a final concentration of 20 μg/ml IPTG. Results show Venus BiFC could potentially be used to investigate other protein interactions.

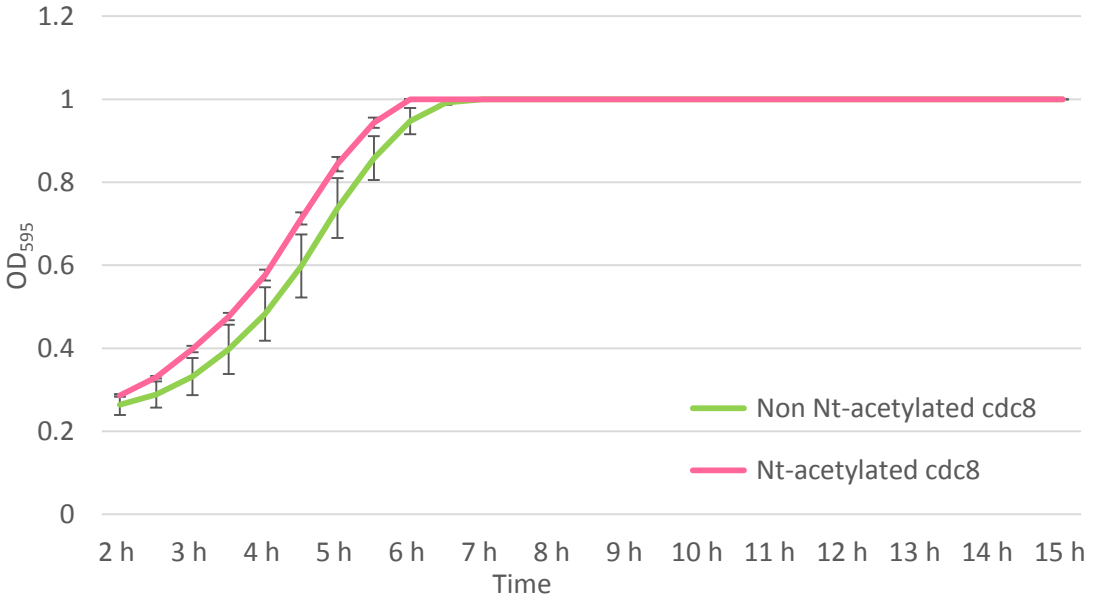


Figure 3.35. Graph showing the OD_{595} over time of *E.coli* cells producing either Nt-acetylated or non Nt-acetylated cdc8-Venus BiFC. Cells were induced with a final concentration of 20 μg/ml IPTG. Readings taken simultaneously with fluorescent readings for previous graph, show that differences in fluorescence are not due to differences in growth.

Protein	Single dimer	2x dimer	3x dimer	4 or more dimers
Cdc8 non Nt-acetylated	93.33%	6.67%	0	0
Cdc8 Nt-acetylated	74.05%	19.62%	5.70%	0.63%

Table 3.1. Polymer lengths of Cdc8 non Nt-acetylated and Cdc8 Nt-acetylated, calculated from electron micrographs (n>200). Adapted from East et al., 2011.

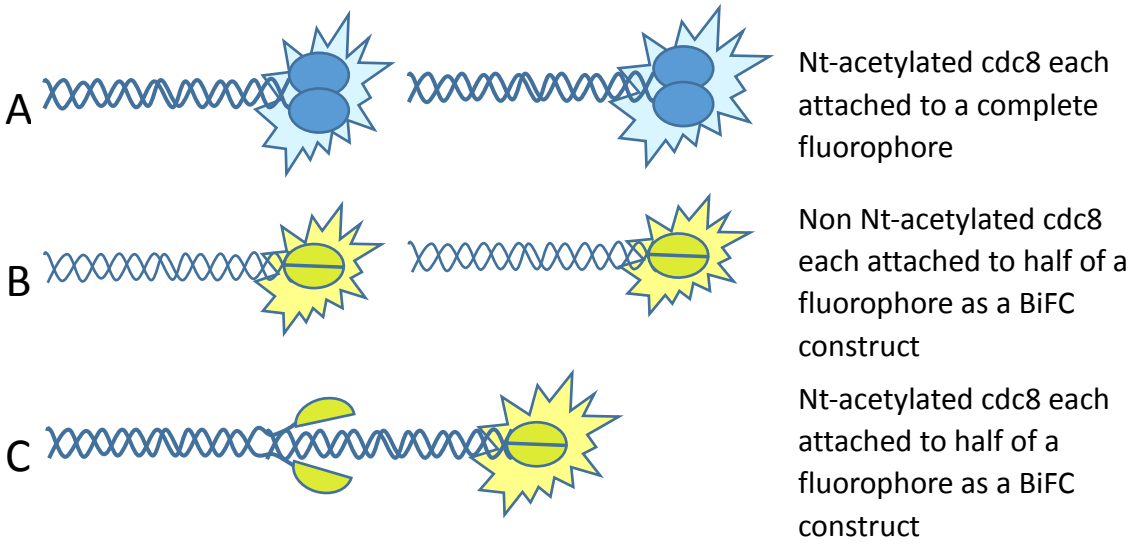


Figure 3.36. Schematic of proposed theory for differences in fluorescence between Nt-acetylated and non Nt-acetylated Cdc8-Venus-BiFC. When a complete fluorophore is attached to each Cdc8, polymers are unable to form (A). When half of a fluorophore is attached to each non Nt-acetylated Cdc8, polymers are unable to form (B). When half of a fluorophore is attached to each Nt-acetylated Cdc8 the two halves of the fluorophore can be forced apart enabling the formation of Cdc8 polymers (C).

3.8 Discussion

The use of aS-Venus-BiFC in this work has shown the need to optimise the techniques used. The results obtained using aS-Venus BiFC showed how starting cell density, rate of induction using IPTG, plate type and plate position, can all have a significant effect on the results obtained. By using optimal conditions, not using the outside wells of the 96 well plate and applying a plate position correction factor, consistent accurate results can be obtained using aS-Venus-BiFC.

This work has shown that Nt-acetylation causes changes to protein conformation and oligomerisation. Differences were shown to exist between both purified proteins *in vitro,* as shown by size exclusion results and *in vivo* in *E. coli,* as shown by Congo Red and NIAD-4 staining and by aS-Venus-BiFC assays in live *E. coli* and by FLIM in stationary cells.

Within *E. coli* Nt-acetylation enhanced the ability of aS to form oligomers leading to amyloid formation in cells, as shown by Congo Red and NIAD-4 staining in live *E. coli*.

The development and optimisation of aS-Venus-BiFC assays enabled this to be used as a novel rapid BiFC screen for drugs which may effect aS oligomerisation. Proof of concept was confirmed as ITC results show that Gefitinib, a drug identified as interacting with and reducing aS-Venus-BiFC fluorescence, interacted with non Nt-acetylated aS-Cerulean3 at a low micro molar concentration, a binding affinity of 3.51 μM ±1.44 μM was measured by ITC.

Interestingly the tyrosine residue Y39 which can be phosphorylated, lies within the known PD related mutations ranging from A30P to A53T.

Chapter 4: The effect of Nt-acetylation on aS membrane interactions

aS binds to membranes with this binding inducing the formation of an amphipathic helical structure, which is considered to be functionally important. Different N-terminal helical structures have been observed with different amounts of membrane binding from just 19 residues binding to approximately 100, and including a broken helix structure (Snead and Eliezer, 2014) and this membrane-induced α-helical folding, is enhanced by Nt-acetylation (Bartels *et al.*, 2014).

To examine the effect of Nt-acetylation on aS interactions with membranes, when produced within *E. coli*, fluorescent microscopy was first used to examine the localisation of aS fluorescently tagged with Cerulean3, within *E. coli* cells. It is difficult to examine the effect of Nt-acetylation of aS within eukaryotic cells as knockout of the NatB complex which Nt-acetylates aS results in the formation of abnormal cell growth, as seen with a *naa25* deletion *S. pombe* strain (Coulton *et al.*, 2010). Investigations into interactions of non Nt-acetylated aS with membranes within *E. coli,* which do not normally produce the NatB complex, do not encounter these problems. It is possible to use an additional plasmid to enable the simultaneous production of the NatB complex within *E. coli* to enable the formation of Nt-acetylated aS.

4.1 Comparison of Nt-acetylated versus non Nt-acetylated aS localisation using Widefield microscopy and TEM imaging

To compare the localisation of Nt-acetylated and non Nt-acetylated aS within *E. coli* cells, images were taken of *E. coli* BL21 DE3 cells producing aS-Cerulean3, both with and without the co-expression of NatB complex. The images obtained for the two forms of aS were very different. Cells producing non Nt-acetylated aS-Cerulean3 appeared to be surrounded by large aS-Cerulean3 filled vesicles, whereas cells producing Nt-

acetylated aS-Cerulean appeared to have areas of concentrated aS-Cerulean3 fluorescence within cells. Cells producing both forms of the protein, appeared to have areas of membrane binding around the outside of the cell (**Figure 4.1**).

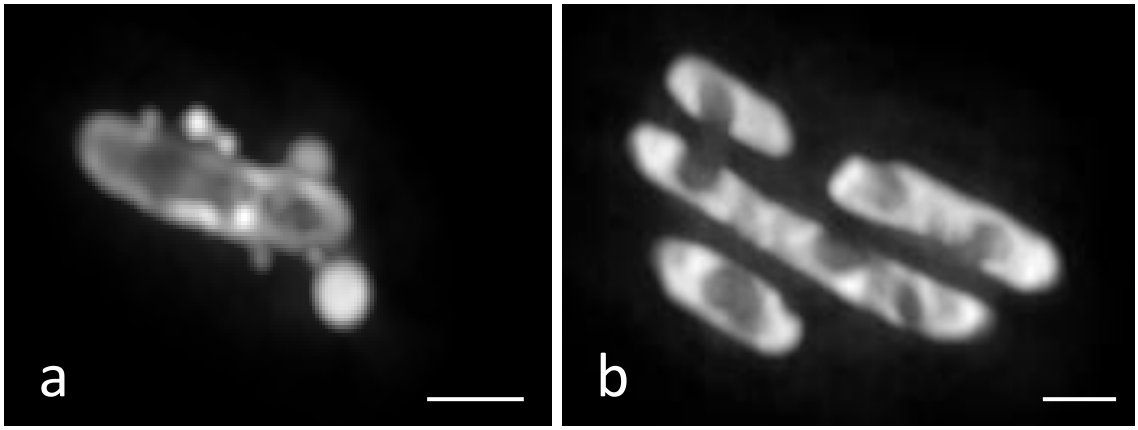


Figure 4.1. Widefield images of BL21 DE3 *E.coli* producing either Non Nt-acetylated or Nt-acetylated aS-Cerulean3, 3 hours post induction. Cells induced with 100μg/ml IPTG showing (a) non-Nt-acetylated aS-Cerulean3 localising to the outside of the cell and inside large extracellular vesicles and (b) Nt-acetylated aS-Cerulean3 localising to regions within cells. Scale: 1μm.

To examine whether the vesicles observed around cells producing non Nt-acetylated aS were membrane bound and whether the structures inside cells producing Nt-acetylated aS were membrane associated, aS-Cerulean3 was simultaneously expressed with CydAB-mCherry, using a pET Duet plasmid. CydAB encodes for CydA which is the cytochrome d, subunit I, and CydB which is the cytochrome d, subunit II. Together they form an inner membrane transmembrane complex, which is attached to the red fluorophore mCherry, (**Figures 4.2 and 4.3**). Cytochrome d is an aerobic terminal oxidase that catalyses the oxidation of ubiquinol-8 and the reduction of oxygen to water.

Cells producing non Nt-acetylated aS-Cerulean3 with CydAB-mCherry were observed associated with large vesicles. Most of these vesicles contained both aS-Cerulean3 and CydAB-mCherry indicating that these structures are membrane bound (**Figure 4.2**).
Cells producing Nt-acetylated aS-Cerulean3 with CydAB-mCherry in comparison were observed to have CydAB-mCherry fluorescence in the cell membranes with a few small areas of brighter fluorescence which were not co-localised with the areas of aS-Cerulean3 localisation which were again seen in cells (**Figure 4.3**).

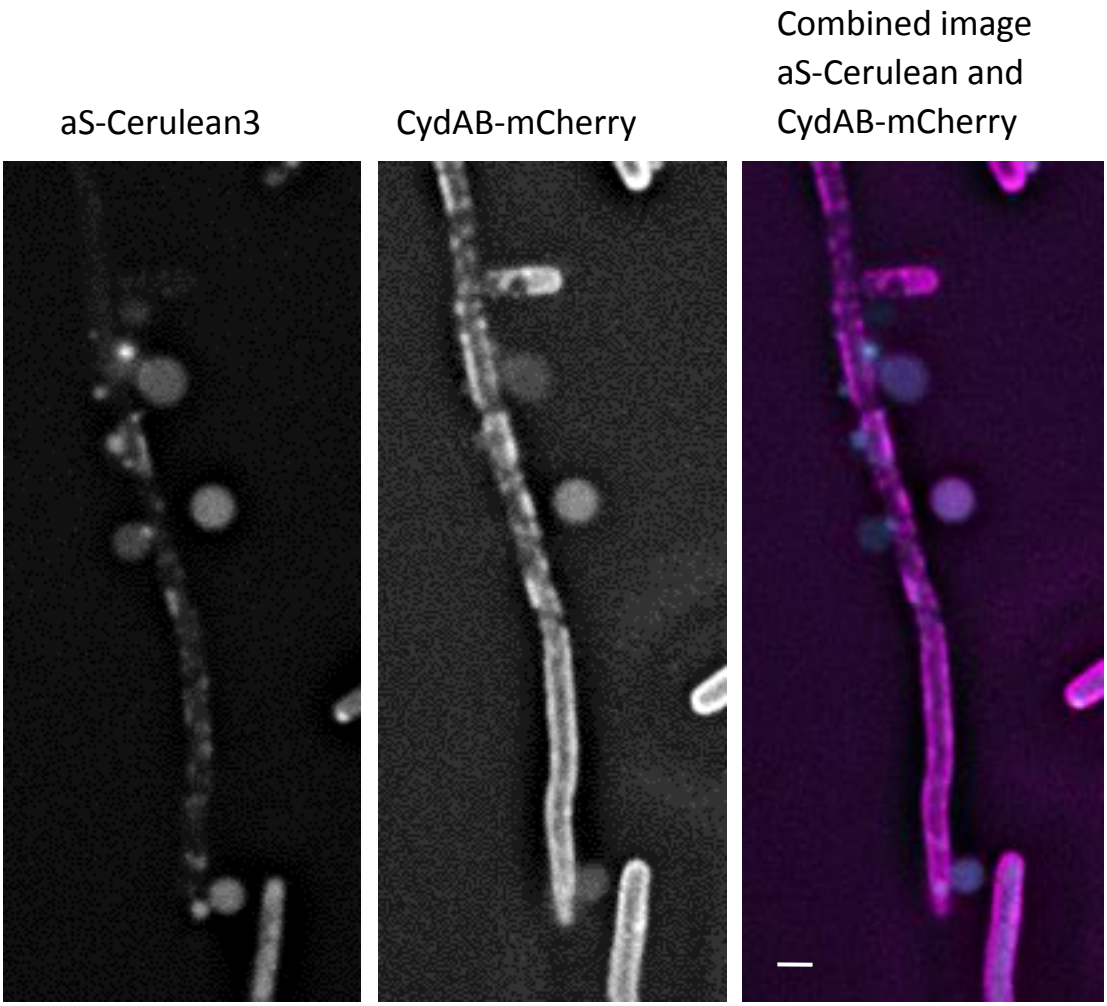


Figure 4.2. **Widefield images of BL21 DE3 *E.coli* producing non Nt-acetylated aS-Cerulean3 with CydAB-mCherry, 3 hours post induction.** Cells were induced with 100μg/ml IPTG. Images show non Nt-acetylated aS-Cerulean3 (blue) with CydAB-mCherry (magenta) large extra cellular vesicles can be seen around the cell, many clearly containing both aS-Cerulean3 and CydAB-mCherry. Scale: 1μm.

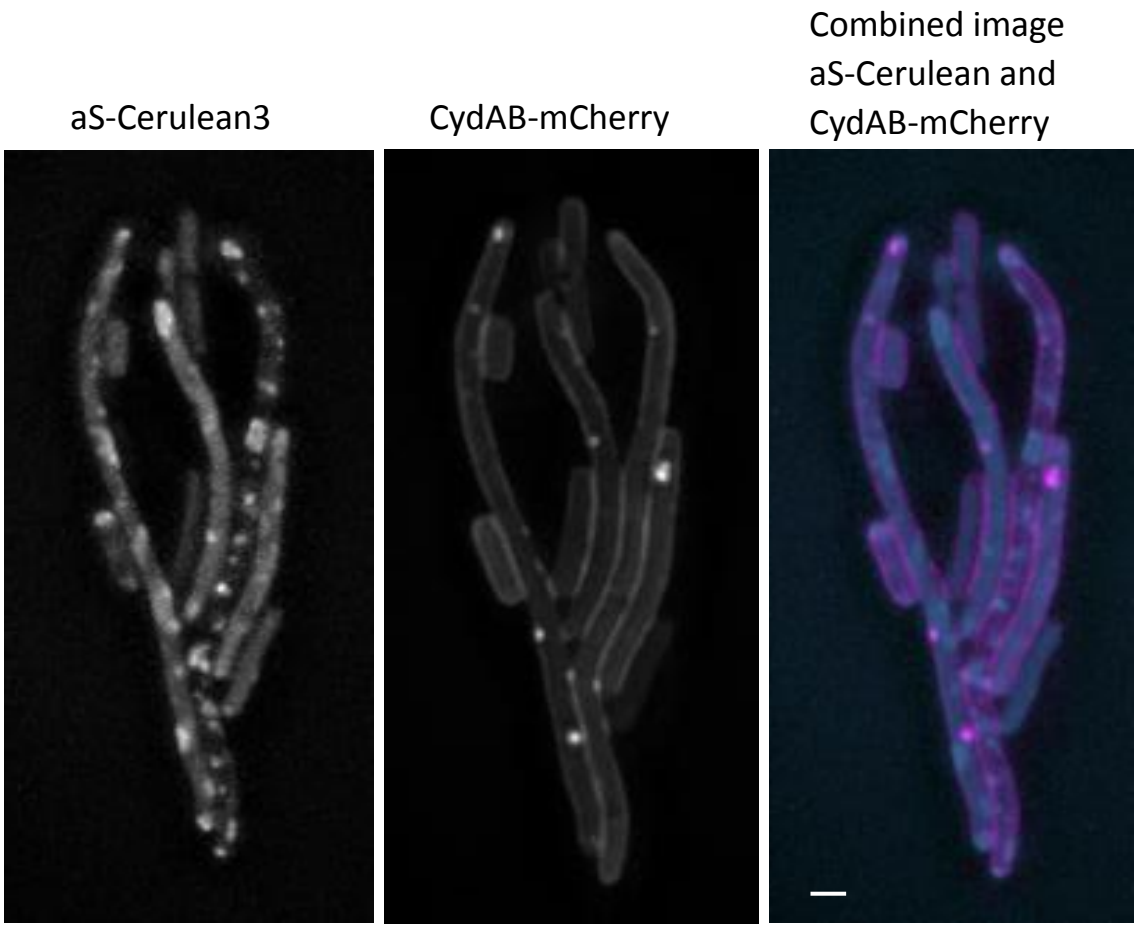


Figure 4.3. **Widefield images of BL21 DE3 *E.coli* producing Nt-acetylated aS-Cerulean3 with CydAB-mCherry 3 hours post induction.** Cells were induced with 100μg/ml IPTG producing Nt-acetylated aS-Cerulean3 (blue) with CydAB-mCherry (magenta) showing aS-Cerulean3 localising to areas within the cell and CydAB-mCherry mainly restricted to the membrane with a few small foci. Scale: 1μm.

Anti aS Immuno Electron Microscopy (E.M.) was also used to confirm the localisation on aS-Cerulean3 within *E. coli* cells. This is an immunogold technique where cells were induced with 100μg/ml IPTG to produce both Nt-acetylated and non Nt-acetylated aS-Cerulean3 for 2.5 hours, then prepared and treated with a primary antibody, Rabbit polyclonal anti aS antibody and then a secondary anti-rabbit antibody attached to 15nm gold discs that appear as black spots on the images. The gold discs do not show the exact location, due to the length of the two antibodies joined together which separate the gold disc and the aS protein that they connect to, which can be 15 to 30nm. The images obtained, indicated that aS is localised to the inside of the plasma membrane

of cells producing both Nt-acetylated and non Nt-acetylated aS-Cerulean3, localisation was observed in areas as seen using fluorescent microscopy (F**igure 4.4**).

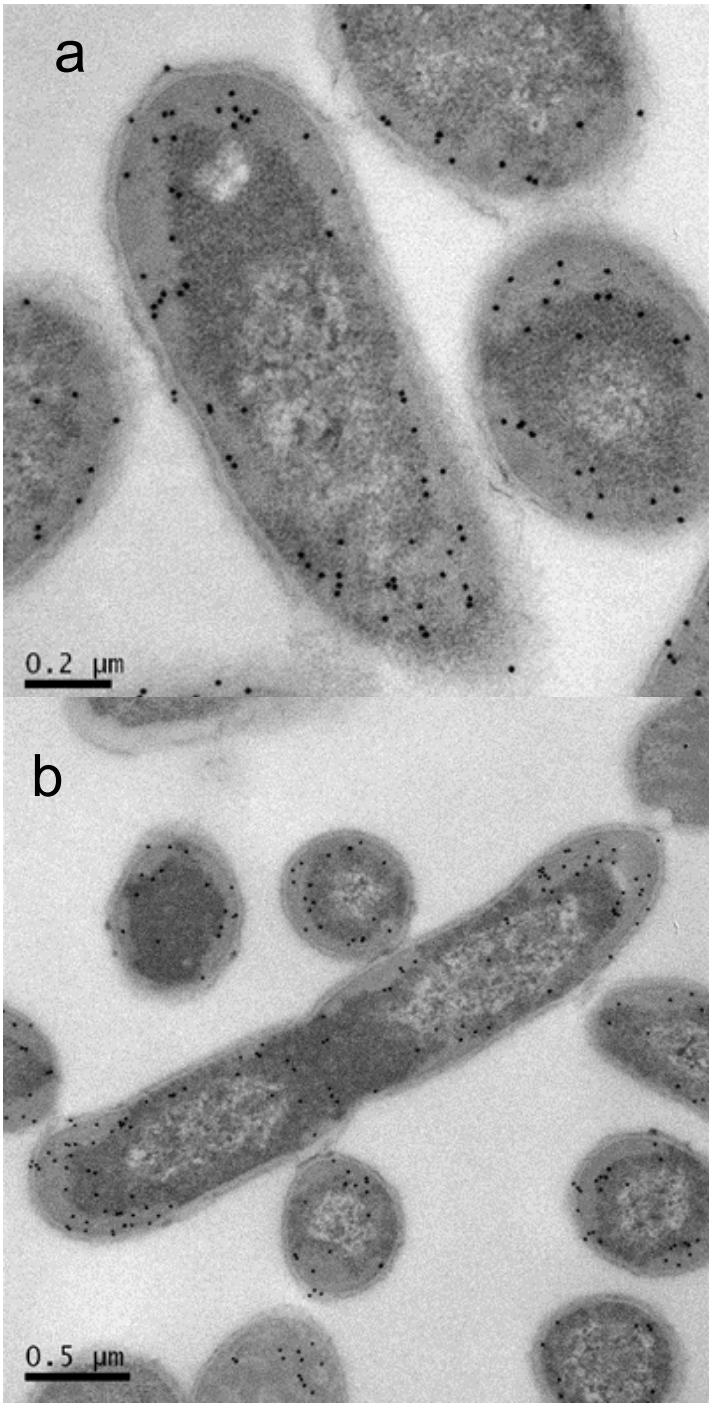


Figure 4.4. Immuno-EM images of BL21 DE3 *E.coli* producing either Non Nt-acetylated aS-Cerulean3 or Nt-acetylated aS-Cerulean3, 2 hours 40 minutes post induction. Cells were induced with 100µg/ml IPTG. Images show Non Nt-acetylated aS-Cerulean3 (a) or Nt-acetylated aS-Cerulean3 (b). Black dots located around the outside of cells are 15nm gold discs connected to aS by 15 to 30 nm of primary rabbit anti aS antibody and secondary anti rabbit antibody.

Transmission Electron Microscopy (TEM) was used to examine the vesicles and structures seen with fluorescent microscopy. Following initial preparation including embedding, cells were thin sectioned and stained with 5% uranyl acetate and 0.1% lead citrate. In images of JM109 *E. coli* cells producing non NT-acetylated aS, membranes can be seen deforming both out from and into cells (**Figure 4.5**). Vesicles which appear to be membrane-bound structures are seen around BL21 DE3 *E. coli* cells induced to produce non Nt-acetylated aS-Cerulean3. One larger vesicle seems to be in the process of forming, with a membrane that appears continuous around both the vesicle and parent cell (**Figure 4.6 a and b**). BL21 DE3 *E. coli* cells induced to produce Nt-acetylated aS-Cerulean3 however were observed to have tubular structures inside the cell membrane in the same areas of the cell as aS-Cerulean3 was shown to be located in Immuno E.M. images (**Figure 4.6 c, d and e**).

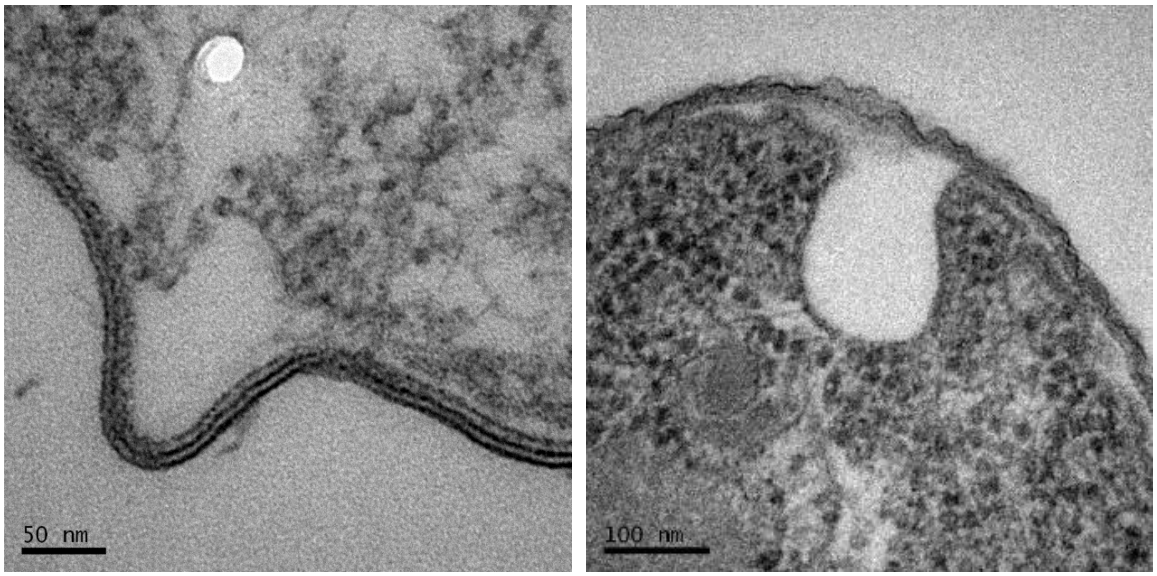


Figure 4.5. TEM images of JM109 *E.coli* producing non Nt-acetylated aS. Membranes can be seen deforming both out from and into the cell.

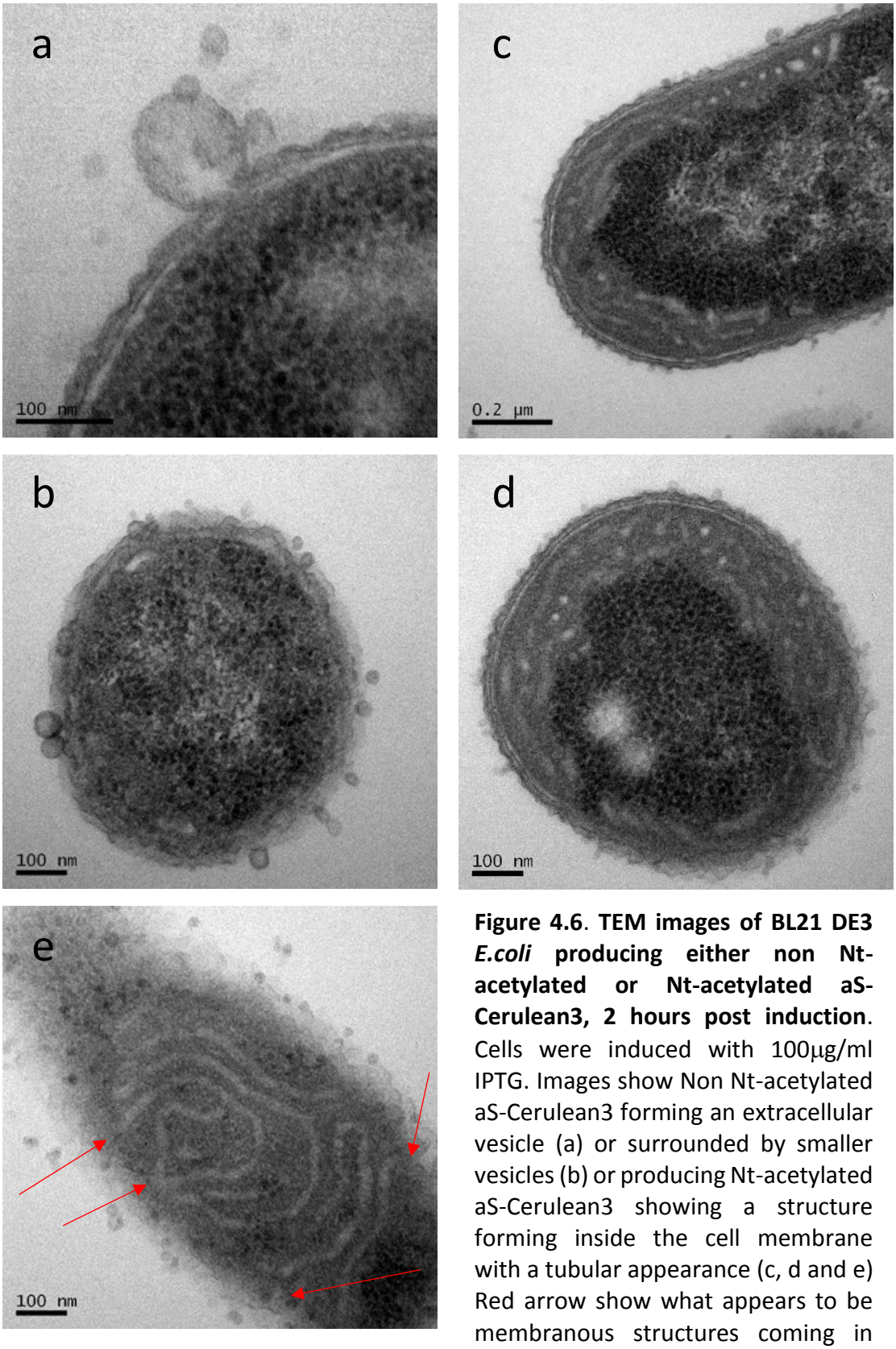


Figure 4.6. TEM images of BL21 DE3 *E.coli* producing either non Nt-acetylated or Nt-acetylated aS-Cerulean3, 2 hours post induction. Cells were induced with 100µg/ml IPTG. Images show Non Nt-acetylated aS-Cerulean3 forming an extracellular vesicle (a) or surrounded by smaller vesicles (b) or producing Nt-acetylated aS-Cerulean3 showing a structure forming inside the cell membrane with a tubular appearance (c, d and e) Red arrow show what appears to be membranous structures coming in from the plasma membrane.

Time-lapse imaging, using wide field fluorescent microscopy of *E. coli* BL21DE3 cells producing aS-mNeonGreen, using a Cellasics microfluidic system, was carried out to capture images of forming vesicles. Images were taken at a rate of 1 per minute. One large vesicle was captured forming, this was a rapid process with the vesicle only visible for 6 frames before it lefts the cell (**Figure 4.7 and Film 1**).

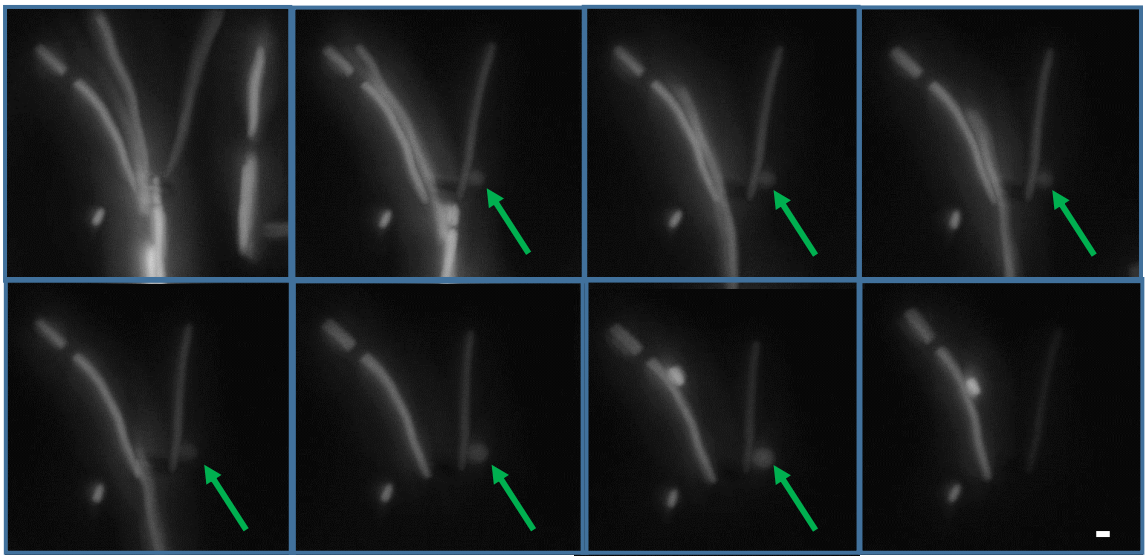


Figure 4.7. **Montage of time lapse images, showing the formation of an aS induced vesicle (green arrows).** Images taken at 1 minute intervals. Scale bar 1 μm.

4.2 Comparison of vesicle number and size, with varying C-terminal fluorophore

Observations were made during investigations into both aS membrane interactions and into aS oligomerisation, that vesicles formed when aS was attached to different C-terminal fluorophores, appeared to differ in numbers and in size. To investigate these observations, images of *E. coli* BL21DE3 cells producing aS-Cerulean3 or aS-mNeonGreen both non Nt-acetylated, were analysed and the size of all vesicles within a field of view were measured and counted (**Figure 4.8**).

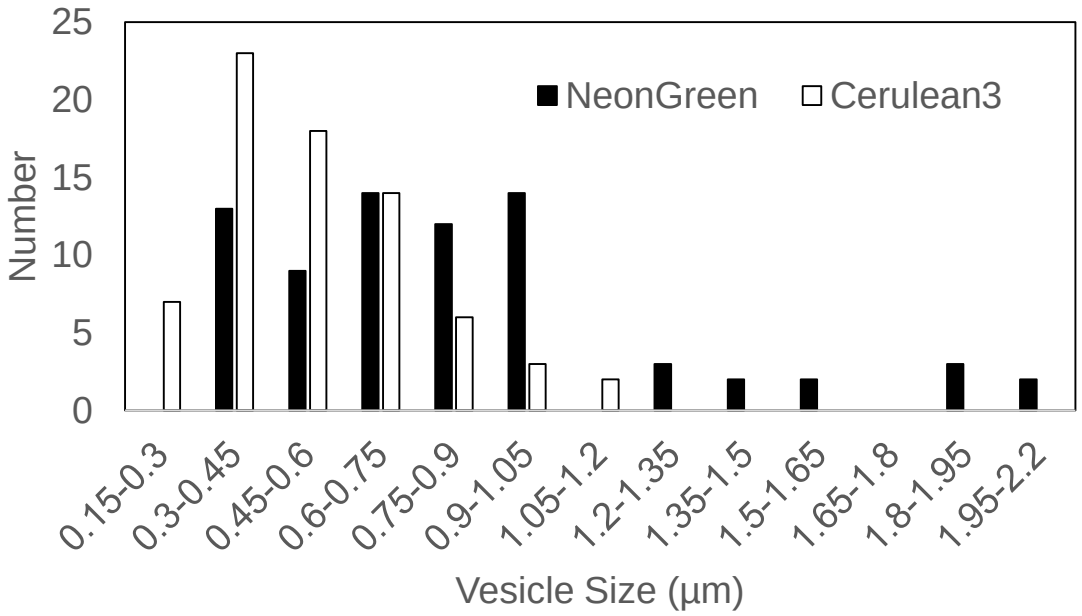


Figure 4.8. Comparison of size and number of vesicles in 1 image each of *E. coli* BL21 DE3 producing aS-Cerulean3 or aS-mNeonGreen-Pif6. Cells were induced with 100µg/ml IPTG. Larger vesicles were seen with cells producing aS-mNeonGreen and more, smaller vesicles with cells producing aS-Cerulean3.

This simple comparison indicated that the C-terminal fluorophore may have an effect on the size and number of vesicles formed. However, it has also been observed that the formation of vesicles is a transient stage. Any slight differences in plasmid uptake, induction timings, temperature and rate of induction, may also be influencing the size and number of vesicles seen at any particular time point.

To aid further investigations into vesicle formation, it would be beneficial to find optimum conditions and timings for vesicle formation with each different aS recombinant protein produced within *E.coli*.

4.3 The use of FLIM to examine membrane interactions

Having shown that the vesicles formed when non NT-acetylated aS is produced in *E. coli,* were membrane bound, it was decided to use FRET measured by FLIM to examine whether aS interacts with either the inner, outer or both membranes, when produced within *E. coli*.

Two new FRET constructs were produced using the pET Duet vector. The first construct was used to produce aS-Cerulean3 simultaneously with Citrine MinD. MinD is a protein which interacts with the inner membrane of *E. coli* due to an amphipathic helix at its C-terminal (Szeto *et al.*, 2002) which is fluorescently tagged at the N-terminal with Citrine. The second construct was created to produce aS-mNeonGreen simultaneously with mCherry fluorescently tagged Outer membrane protein A (Reusch, 2012), OmpA-mCherry.

Both fluorophore pairs are capable of FRET when in close proximity (less than 10nm). The emission wavelength for each donor fluorophore, Cerulean3 or mNeonGreen overlaps the excitation wavelength for the corresponding acceptor fluorophore, Citrine or mCherry.

Each construct was expressed in BL21 DE3 *E. coli* cells both with and without the NatB complex to enable the production of either Nt-acetylated or non Nt-acetylated aS. FLIM images were taken of cells from each culture which were then analysed.

A variation in FLIM can be seen across images of each type of cell culture by comparing colour, however the range of fluorescent lifetime represented by the same colour range is very different for different donor fluorophores. Where Cerulean3 acts as a donor fluorophore, a large difference was seen in the range of fluorescent lifetimes between *E. coli* producing Non Nt-acetylated aS-Cerulean3 alone, approximately 3150ps to 3900ps and for *E. coli* producing aS-Cerulean3 with Citrine-MinD, approximately 2550ps to 3200ps (**Figure 4.9**). A far smaller difference was seen in the range of fluorescent lifetimes where mNeonGreen acted as a donor fluorophore, with *E. coli* producing non Nt-acetylated aS-mNeonGreen alone having a range of fluorescent lifetimes of approximately and 2300ps to 2650ps and approximately 2250ps to 2600ps, in *E.coli* producing Non Nt-acetylated aS-mNeonGreen with OmpA-mCherry (**Figure 4.10**).

Non Nt-acetylated

aS-Cerulean3

aS-Cerulean3 with Citrine-MinD

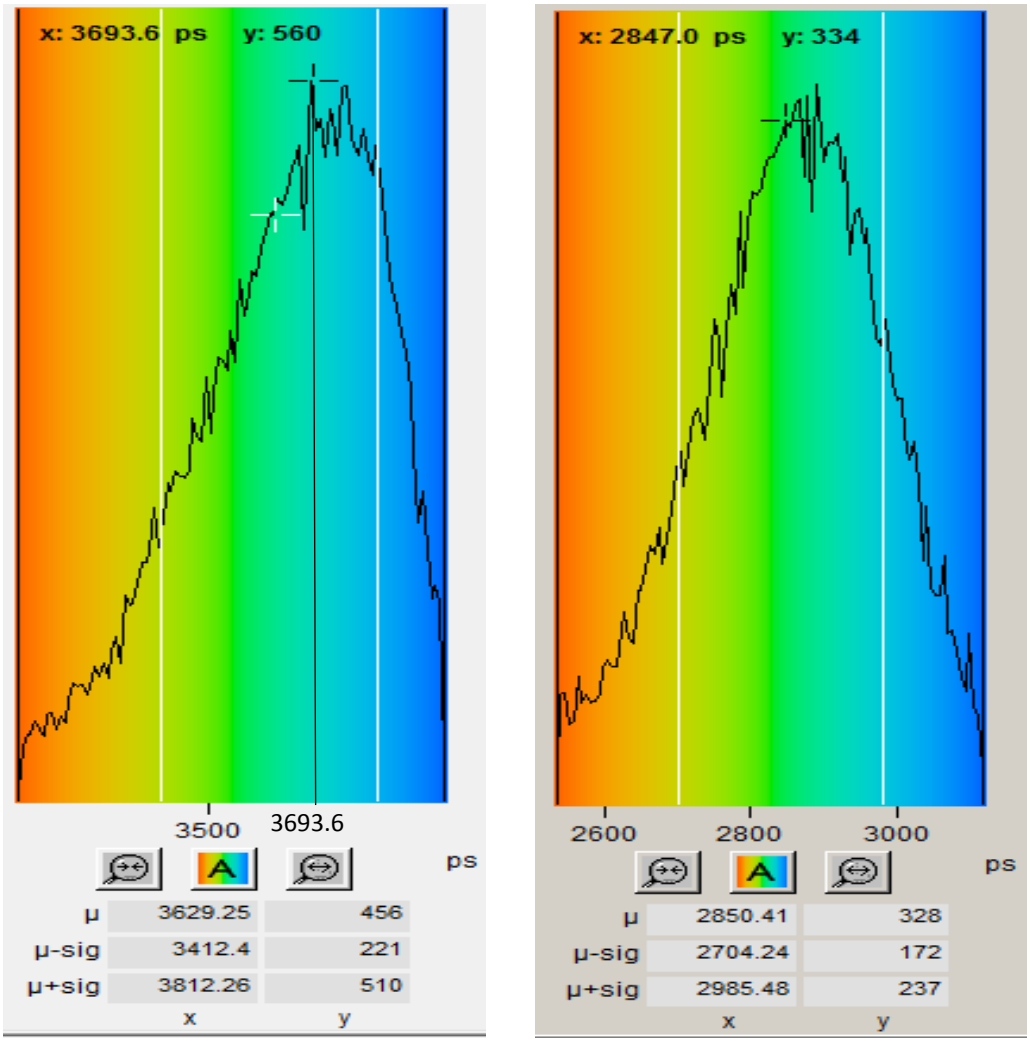


Figure 4.9. **Donor fluorophore fluorescent lifetime in pico seconds (ps) in *E. coli* cells producing non Nt-acetylated aS-Cerulean3 alone or aS-Cerulean3 with Citrine-MinD.** Values range from approximately 3150ps to 3900ps in *E. coli* producing non Nt-acetylated aS-Cerulean3 alone and 2550ps to 3200ps, in *E.coli* producing non Nt-acetylated aS-Cerulean3 with Citrine-MinD, an inner membrane binding protein.

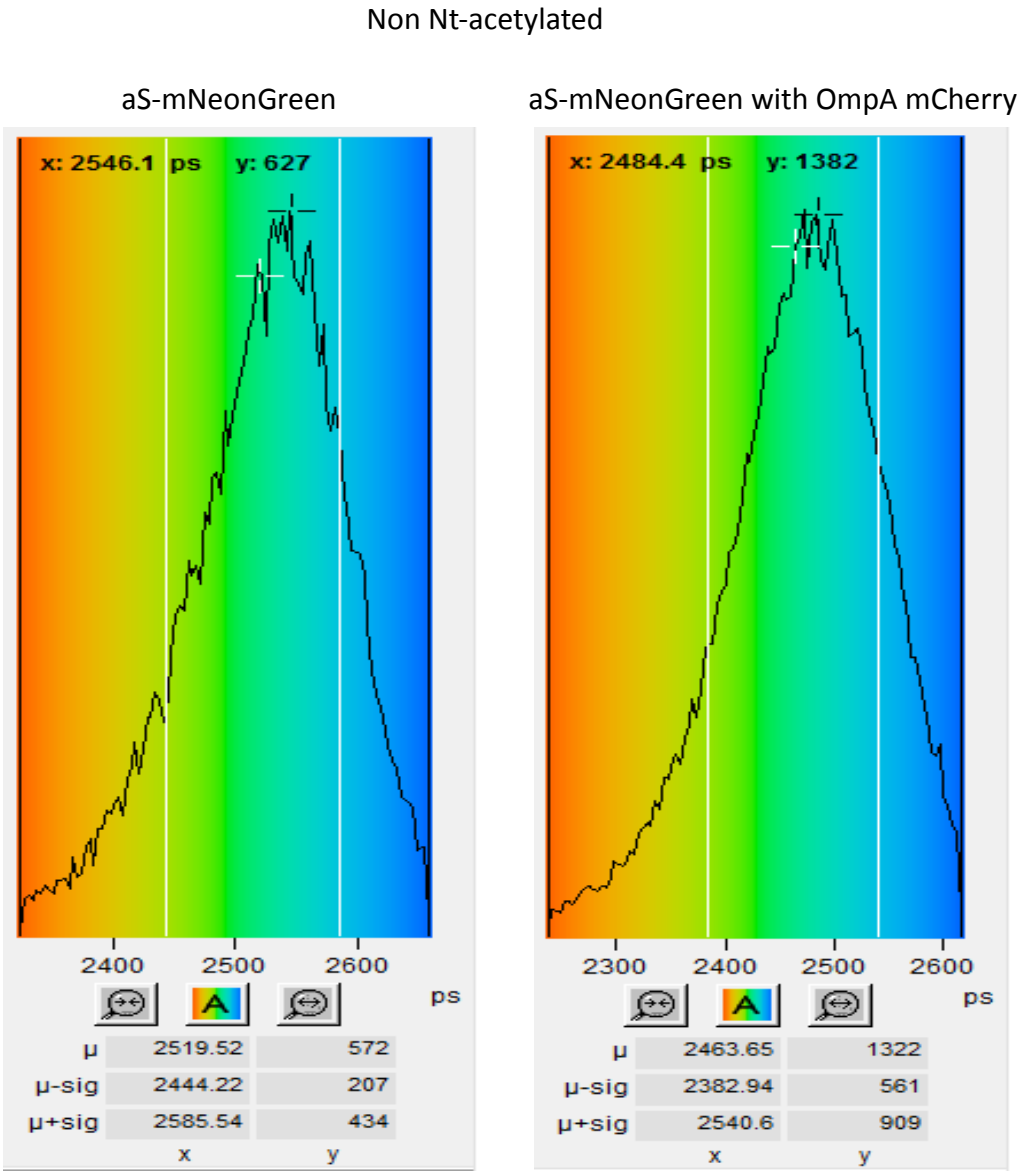


Figure 4.10. **Donor fluorophore fluorescent lifetime in pico seconds (ps) in *E. coli* cells producing Non Nt-acetylated aS-mNeonGreen alone or aS-mNeonGreen with OmpA-mCherry.** Values range from approximately 2300ps to 2650ps in *E. coli* producing Non Nt-acetylated aS-mNeonGreen alone and 2250ps to 2600ps, in *E.coli* producing Non Nt-acetylated aS-mNeonGreen with OmpA-mCherry, an outer

FLIM measurements were analysed by taking 18 individual pixel FLIM values from a line across an individual cell (**Figure 4.11**). These lines were drawn across cells at a point where there was the greatest colour range. The values for each of the 18 positions, were averaged between cells to obtain an average FLIM profile (**Figure 4.12**).

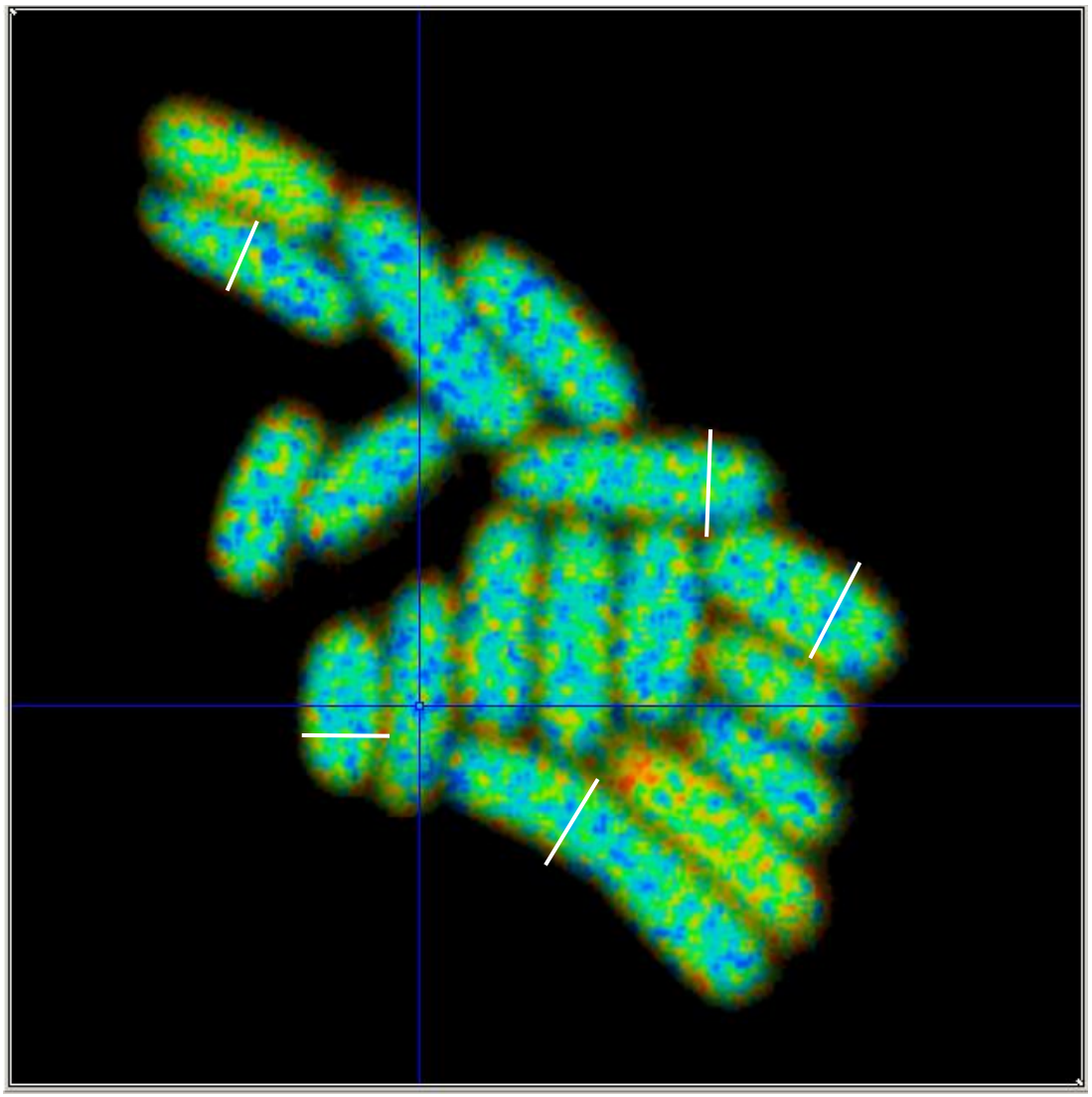


Figure 4.11. FLIM heat map image of *E. coli* producing non Nt-acetylated aS-Cerulean3 with Citrine-MinD. White lines show the cross sections along which 18 individual FLIM measurements were taken.

Very different shaped FLIM profiles were obtained for *E. coli* cells producing aS-mNeonGreen and OmpA-mCherry or aS-Cerulean3 and Citrine-MinD. The graphs obtained for cells producing aS-mNeonGreen and OmpA-mCherry are relatively flat with only a very small reduction in FLIM at the edges of the cells. The FLIM values

obtained were very close to the FLIM values obtained for aS-mNeonGreen alone. No change in FLIM means that FRET is not occurring, the minimal change in FLIM at the edges of the cells indicates that aS does not closely interact with the outer membrane. The Nt-acetylation of aS in cells producing aS-mNeonGreen and OmpA-mCherry does not appear to have any effect on the FLIM values measured.

The graphs obtained for cells producing aS-Cerulean3 and Citrine-MinD however have an arched shape. Cytoplasmic FLIM values were greatly reduced, from approximately 3500 ps for aS-Cerulean3 only controls, to approximately 3000 ps for non Nt-acetylated aS-Cerulean3 and Citrine-MinD and 2900 ps for Nt-acetylated aS-Cerulean3 and Citrine-MinD. This large reduction in FLIM indicated that FRET was occurring within the cells and that aS and MinD were interacting. The cytoplasmic FLIM values measured were very close to the levels measured for *E. coli* cells producing Non Nt-acetylated aS-Cerulean3 with aS-mNeonGreen at 3070ps (**Figure 3.12**).

An additional sharp decrease in FLIM was seen at the edges of the cells, indicating that there was an increase in FRET at the edges of the cell membrane. However the fluorescent intensities obtained at the edges of the cells were low and binning to overcome this, resulted in a loss of resolution, therefore, there can only be low confidence, in the results showing an increase in FRET at cell membranes. Improved data, at a higher magnification and with higher fluorescent intensities would need to be obtained to confirm this result.

Nt-acetylation of aS, in cells producing aS-Cerulean3 simultaneously with Citrine-MinD, does not appear to affect the shape of the FLIM graph obtained. A general small decrease in FLIM was observed across cells producing Nt-acetylated aS compared to those producing non Nt-acetylated aS.

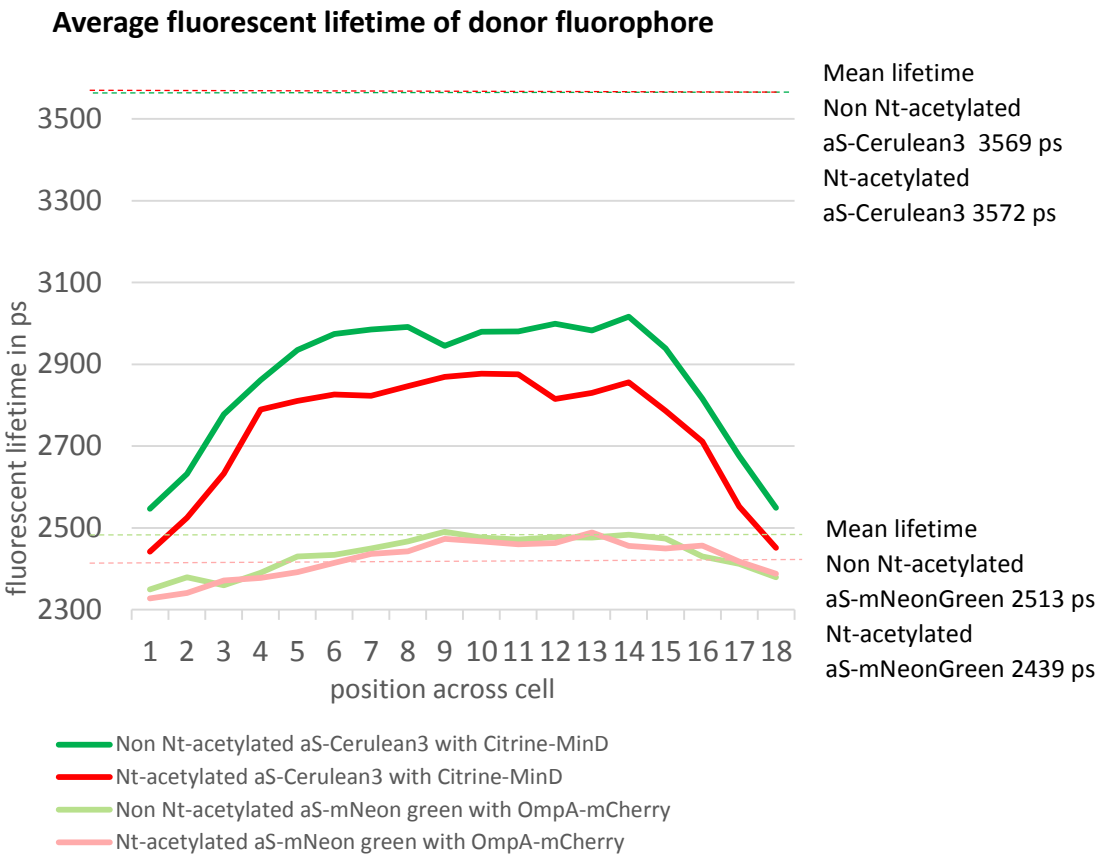


Figure 4.12. Average donor fluorophore fluorescent lifetimes in pico seconds across *E.coli* cells, producing either Non Nt-acetylated or Nt-acetylated aS-Cerulean3 with Citrine-MinD, an inner membrane marker, or Non Nt-acetylated or Nt-acetylated aS-mNeonGreen with OmpA-mCherry, an outer membrane marker. A reduction in fluorescent lifetime is seen in the cytoplasm of cells when aS-Cerulean3 is produced with Citrine-MinD indicating that FRET is occurring, FRET possibly increases further at the inner membrane. No significant reduction in fluorescent lifetime is seen when aS-mNeonGreen is produced with OmpA-mCherry indicating that FRET is not occurring within these cells. Average fluorescent lifetime for donor fluorophores on their own are shown as dotted lines.

aS-Cerulean3 and Citrine-MinD Non Nt-acetylated n=15 cells, Nt-acetylated n=15 cells.

aS-mNeonGreen and OmpA-mCherry Non Nt-acetylated n=10 cells, Nt-acetylated n=5 cells.

4.4 The use of Structured Illumination Microscopy (SIM) a Super resolution microscopy technique

SIM, a super resolution microscopy technique was used to further investigate the interaction of aS with both the inner and outer membranes of the *E. coli* in which it is produced, when both Nt-acetylated and non Nt-acetylated. SIM was used as this technique enables the acquisition of fluorescent images with a higher resolution, compared with basic fluorescent microscopy techniques, enabling the visualisation of fine structures. Confocal fluorescent microscopes can achieve resolutions of approximately 200-250nm, SIM however can achieve a resolution of approximately 100nm (Reusch, 2012)

SIM is a widefield microscopy technique which involves imaging a grating onto the sample to produce Moiré fringes. This technique is comparatively fast with imaging in the order of seconds and uses much lower laser powers than other Super resolution microscopy techniques and hence is suited to applications where limiting phototoxicity is important, such as when imaging live cells.

A new construct was made using a pET Duet vector to produce Citrine-MinD and OmpA-mCherry simultaneously to examine whether it was possible to differentiate the inner and outer membranes of *E. coli* (**Figure 4.13**). The images obtained show that it is possible to differentiate between these two membrane markers. Images do not show complete separation of the two fluorescent signals, but do show an area of co-localisation with Citrine fluorescence around the inside and mCherry fluorescence to the outside. Estimates of the periplasm thickness of *E. coli* vary from 10 nm to 50 nm (Sochacki *et al.*, 2011). When added to an inner membrane thickness of 7.5 nm and an outer membrane thickness of 7.5 nm to 10 nm, this give a total thickness from the inside of the inner membrane to the outside of the outer membrane of 25 nm to 67. 5nm, which is up to about two thirds of the resolution expected for SIM.

E.coli expressing the aS-mNeonGreen and OmpA-mCherry construct used in the FLIM investigation was imaged using SIM. An image obtained is shown compared with a widefield image of the same construct obtained using this labs widefield microscope in (**Figure 4.14**). The improved resolution of the SIM image enabled the clear visualisation

of many small vesicles. As seen previously cells producing non Nt-acetylated aS-mNeonGreen and OmpA-mCherry produced multiple large vesicles.

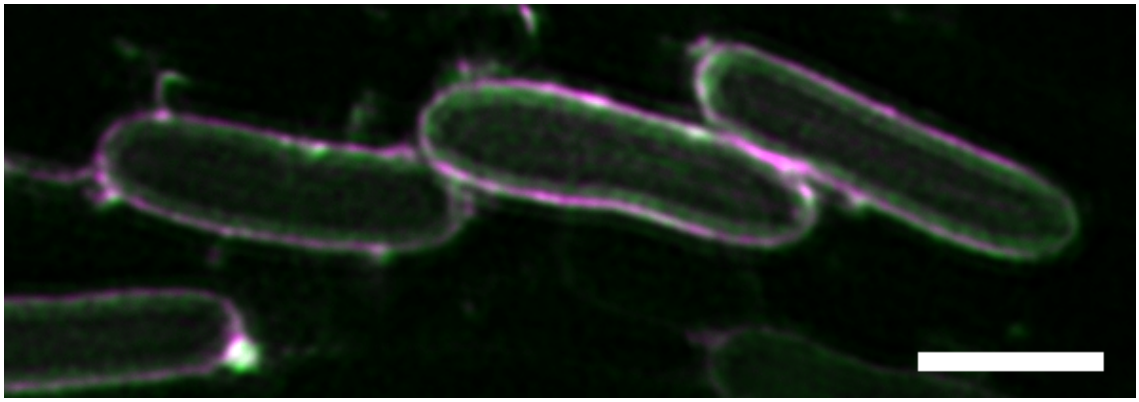


Figure 4.13. **SIM image of *E.coli* producing Citrine-MinD, inner membrane marker (green) and OmpA-mCherry, outer membrane marker (magenta).** Scale: 1µm.

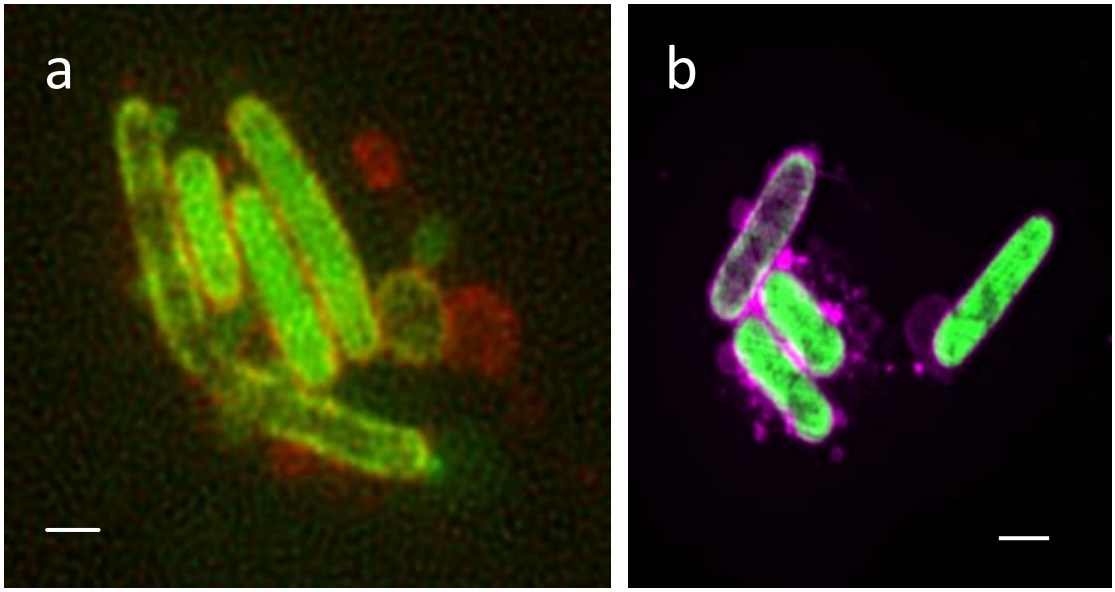


Figure 4.14. **Images of *E.coli* producing non Nt-acetylated aS-mNeonGreen (green) and OmpA-mCherry, (red and magenta) using widefield microscopy (a) and SIM (b).** Large outer membrane-bound vesicles can be seen around the cells. Scale: 1µm.

The aS-Cerulean3 and Citrine-MinD construct used in FLIM investigations and a new construct using different fluorophores producing, aS-mNeonGreen simultaneously with mScarlet-MinD, were used to investigate aS interactions with the inner membrane.

Similar images were obtained for both constructs, internal structures were seen with each construct, with and without the presence of the NatB complex to produce both Nt-acetylated and non Nt-acetylated aS (**Figure 4.15**). The localisation of these structures relates with the areas shown to produce structures with a tubular appearance in the TEM images obtained.

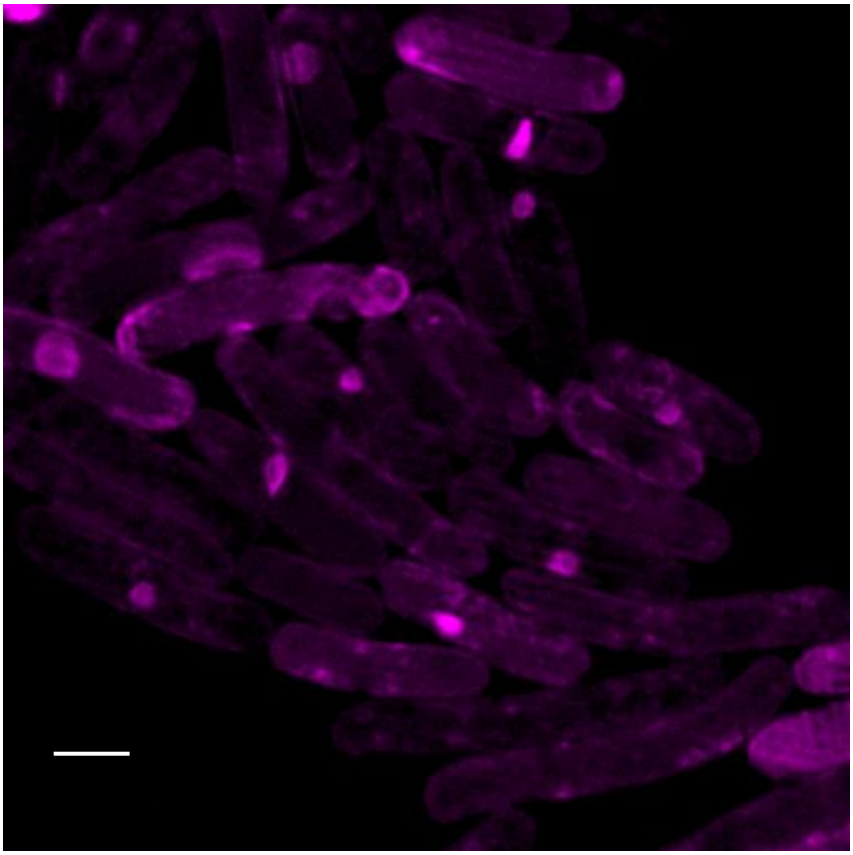


Figure 4.15. ***E.coli*** **producing non Nt-acetylated aS-mNeonGreen (not shown) and mScarlet-MinD inner membrane marker (magenta) obtained using SIM.** Internal structures appear to have formed from the inner membrane. Scale: 1µm.

One surprising difference was seen between images of *E. coli* producing non Nt-acetylated forms of the two sets of recombinant protein. When mScarlet-MinD was produced very few vesicles were seen. Those that were seen, were predominantly associated with cells with a reduced mScarlet signal. Membrane localisation of aS was also not seen as clearly when MinD was tagged with mScarlet compared to when it was

tagged with Citrine. This indicates that mScarlet may be interfering with membrane binding and that membrane binding is required for vesicle production (**Figure 4.16).**

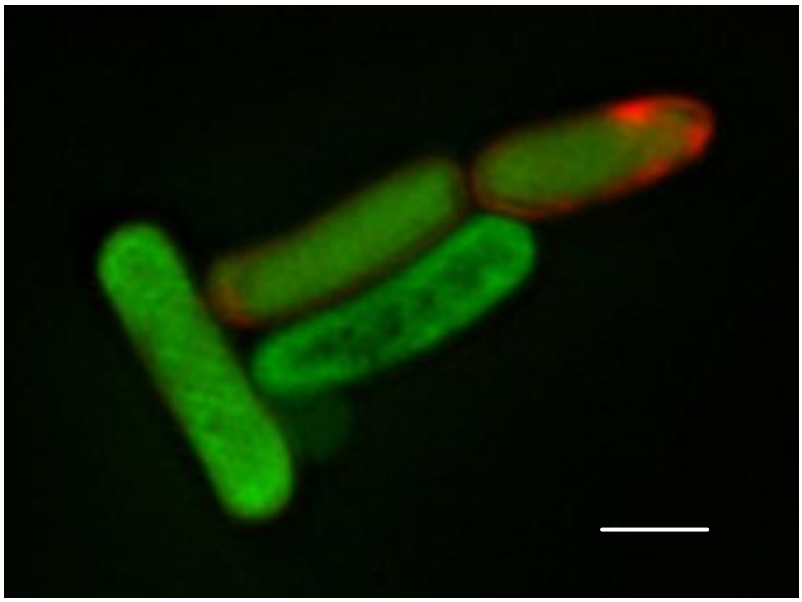


Figure 4.16. *E. coli* producing non Nt-acetylated aS-mNeonGreen (green) with mScarlet-MinD (red). Two cell showing clear production of mScarlet-MinD. A large vesicle is seen on the cells not clearly expressing mScarlet-MinD. Scale: 1μm.

4.5 The use of recombinant protein enhanced vesicle formation to facilitate large scale protein production

Protein-based therapeutics, are an important sector of the pharmaceutical industry with 2010 sales of $108 bln (Dimitrov, 2012). Many of these drugs are recombinant proteins produced in *E. coli.* If vesicles containing therapeutic proteins could be harvested allowing the protein to remain in a cytosolic environment, this could also improve protein stability, storage and drug delivery. If it is possible for recombinant therapeutic protein to be recovered from media or vesicles within media, the need to harvest biomass could be reduced and more protein could potentially be produced per fermenter run, reducing production costs.

The possibility of using these large aS induced vesicles to improve therapeutic protein production was investigated. Samples were taken from aS-Venus-BiFC cultures producing Nt-acetylated or non NT-acetylated aS induced with 100μg/ml IPTG, samples

were taken at 0, 1, 3, 5 and 7 hours post induction. Protein was precipitated from the cell cleared media and run on a Coomassie stained gel and western blot using Rabbit anti aS 1^{o} antibody. Protein including aS was shown to be present in the cell cleared media (**Figure 4.17**).

An induction with 20μg/ml IPTG would produce more protein, as shown in the previous chapter section (**3.4.1: Optimisation of aS induction**), but vesicle production has been seen most with induction at 100μg/ml. This is mainly due to the timing of vesicle production which is significantly delayed with a 20μg/ml IPTG induction. It is not known if this lower IPTG induction would affect the number of vesicles produced or the amount of protein released into the media.

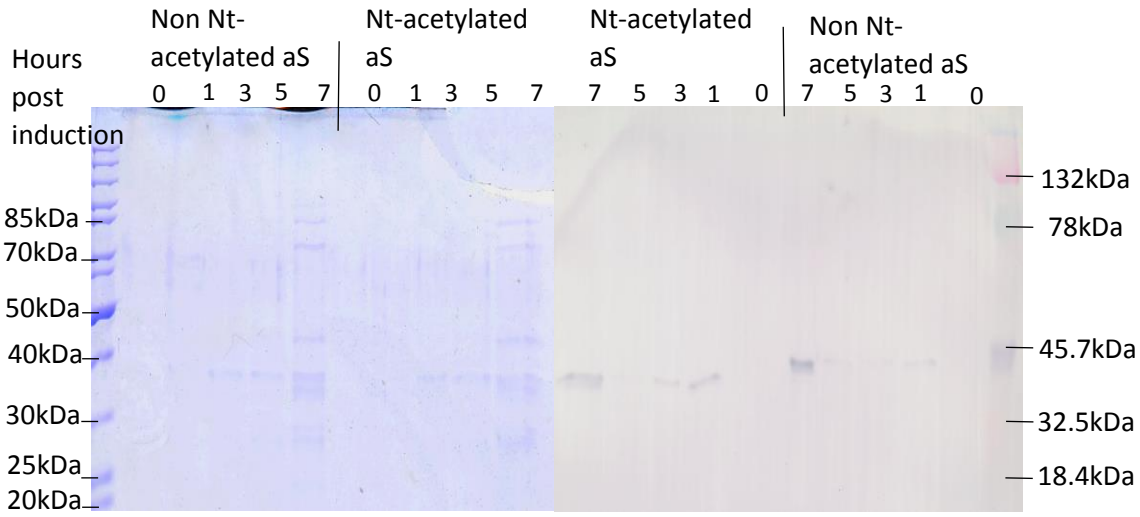


Figure 4.17. Coomassie Blue stained SDS-PAGE gel and matching western blot of protein precipitated from cell cleared media from aS-Venus BiFC cultures producing Non Nt-acetylated and Nt-acetylated aS. Faint traces of protein were detected by both Coomassie Blue stained SDS-PAGE gel and Western blot using Rabbit anti aS primary antibody. Expected molecular weights, aS-Venus C terminal - 24.1kDa and aS-Venus N terminal – 32.1kDa.

4.6 aS induced vesicles and human Growth Hormone (hGH)

Having shown the production of large aS induced vesicles and that protein could be recovered from cell cleared media, the possibility of improving large scale production of human Growth Hormone (hGH) using aS induced vesicles was examined.

The first plasmid used in this investigation was, pMK-RQ-aS-mNeonGreen-FLAG-hGH, obtained from Invitrogen. This plasmid has the strong, Tac promoter, which has been used in large scale fermenters (Rosano and Ceccarelli, 2014). Transformation of this plasmid into DH10β and BL21 DE3 *E. coli* cells proved unsuccessful, due to immediate, leaky aS expression by the Tac promoter.

To overcome the problem of leaky expression by the Tac promoter, the plasmid was successfully transformed into JM109 cells that carry a deletion of the proline biosynthetic operon [Δ(lac-proAB)] in the bacterial chromosome and the complementing proAB genes on the F'plasmid (obtained from Promega). These were grown in M9 minimal media, supplemented with additional glucose, $MgSO_4$ and Thiamine.

To enable the production of aS-mNeonGreen-FLAG-hGH using LB medium **(Table 2.1 I)** and BL21 DE3 *E. coli* competent cells and to enable the use of sequential induction with NatB (Eastwood *et al.*, 2017) a pETpRha plasmid, which requires the addition of rhamnose to induce protein production, was used. The pETpRha-aS-mNeonGreen-FLAG-hGH plasmid produced allows tightly controlled expression of aS-mNeonGreen-FLAG-hGH through the addition of varying concentrations of rhamnose.

The production of aS-mNeonGreen-FLAG-hGH using the new plasmid in both DH10β and BL21 DE3 *E. coli* cells was compared using the addition of varying concentrations of Rhamnose (**Figure 4.18**). A final concentration of 0.01% rhamnose was chosen for further investigations.

BL21 DE3 *E. coli* cells induced with 0.01% rhamnose to produce aS-mNeonGreen-FLAG hGH were imaged at 5 hours post induction. Large aS induce vesicles were observed around cells (**Figure 4.19**).

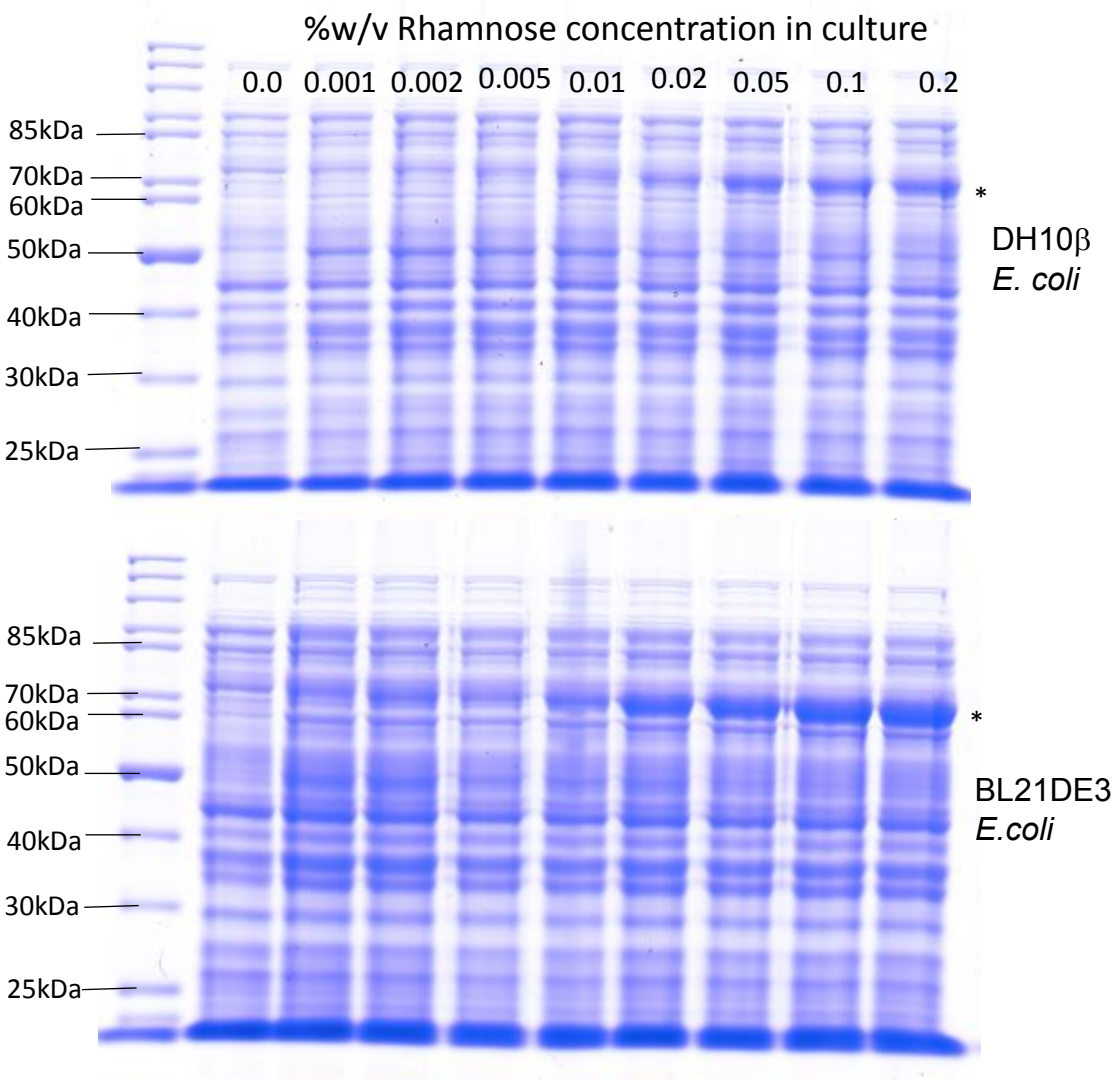


Figure 4.18. Coomassie Blue stained SDS-PAGE gels of cell extracts from *E. coli* strains DH10β and BL21 DE3 producing Non Nt-acetylated aS-mNeonGreen-FLAG-hGH. Cells were induced for 2 hours with various Rhamnose concentrations. Expected molecular weight of aS-mNeonGreen-FLAG-hGH is 65kDa (*)

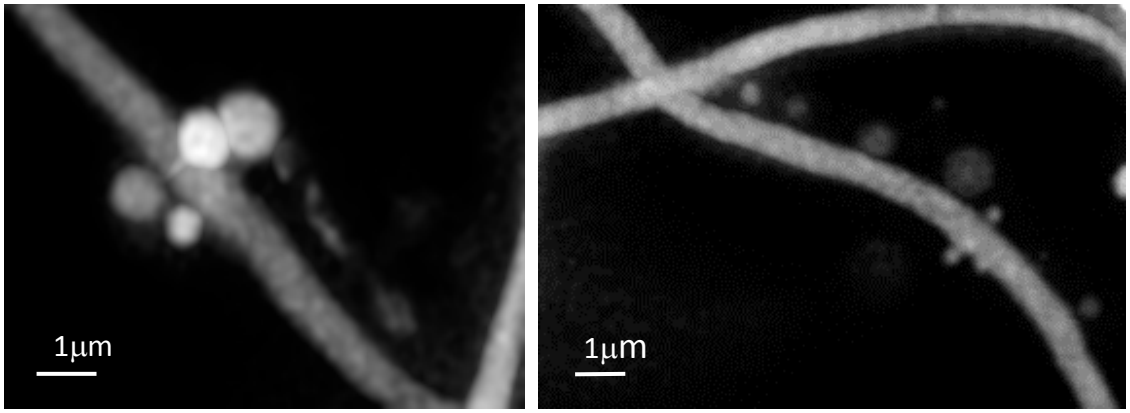


Figure 4.19. Images of *E. coli* induced for 5 hours with 0.01% Rhamnose producing non Nt-acetylated aS-mNeonGreen-FLAG-hGH. Images show large fluorescent vesicles around cells. Scale: 1μm.

The pETpRha plasmid was used to produce aS-mNeonGreen-FLAG-hGH within Ambr fermenters at Fujifilm-Diosynth. In four separate runs the presence of aS-mNeonGreen-FLAG-hGH was observed in both cell pellets and in media using an Anti FLAG 1^{o} antibody western blot (**Figure 4.20**). This result shows that *E. coli* cells containing the pETpRha-aS-mNeonGreen-FLAG-hGH plasmid can be grown within industrial Ambr250 fermenters, that aS-mNeonGreen-FLAG-hGH protein production could be induced and that vesicles and or aS-mNeonGreen-FLAG-hGH protein can be exported into the media.

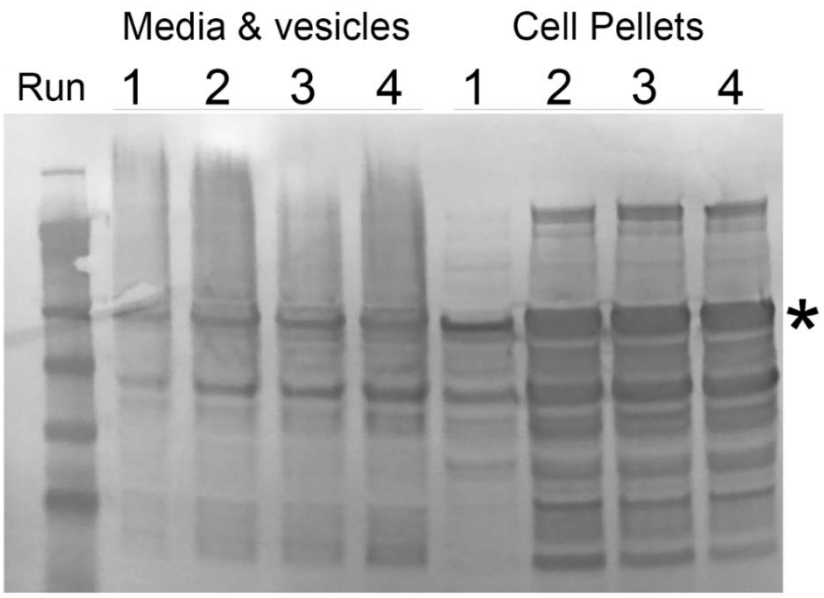


Figure 4.20. Anti-FLAG western shows expression and export to vesicles/media of αS-hGH fusion (highlighted by *) in four Ambr250 bioreactor runs. Data acquired by Fujifilm-Diosynth.

4.7 Purification of vesicles from cell culture

The potential to use intact, purified vesicles to improve the storage and delivery of therapeutic proteins within a cytosolic environment, was investigated. Initial investigations were carried out to see if intact vesicles could be purified from cell cultures, where vesicles were shown to be present by fluorescent microscopy. Vesicles purified from cell cultures producing aS-mNeonGreen-Pif6 and OmpA-mCherry were then compared with naturally-occurring vesicles purified from cell cultures producing OmpA-mCherry alone.

Samples of cell cultures where vesicles were seen, were centrifuged at various speeds for varying amounts of time and the supernatant then examined by fluorescent microscopy.

An optimal speed and time of 1000rcf for 30 minutes resulted in the presence of very few cells, but a clear presence of vesicles (**Figure 4.21**). Speeds above 1000rcf resulted in no intact vesicles being observed.

Samples of purified vesicles from cell cultures producing non Nt-acetylated aS-mNeonGreen-Pif6 with OmpA-mCherry, together with a control supernatant from cell cultures producing OmpA-mCherry alone, were subjected to Dynamic Light Scattering (DLS), a technique that is used to determine the size of small particles within a suspension. A monochromatic light source, is shone through a polarizer and into a sample. All of the molecules within the solution diffract the light in all directions. The scattered light then goes through a second polarizer where it is collected by a photomultiplier and the resulting image is analysed. The resultant graph shows the number and volume of different size particles. It also shows the intensity of light scattering by different sized particles, small numbers of larger particles produce high scattering intensities, so the presence of small numbers of large vesicles are shown by the intensity trace on the graphs.

The control supernatant contained a large numbers of particles of 0.7 to 2 nm and small numbers of larger particles from approximately 60 to 1500nm (**Figure 4.22**). The sample of purified vesicles from *E. coli* cells producing aS-mNeonGreen-Pif6 with OmpA-mCherry also had a high number of small particles of 0.6 to 2 nm and a small

number of larger particles from approximately 60 nm but in this sample much larger particles, possibly vesicles, were also measured up to approximately 5000 nm (**Figure 4.23**).

The aS induced vesicle containing sample also has another peak for particles of 10 to 20nm diameter which was not seen in the control sample. Interestingly a recent study looking at the Cryo-EM structure of aS fibrils formed from two protofilaments, measured their diameter at 10 nm (Guerrero-Ferreira *et al.*, 2018).

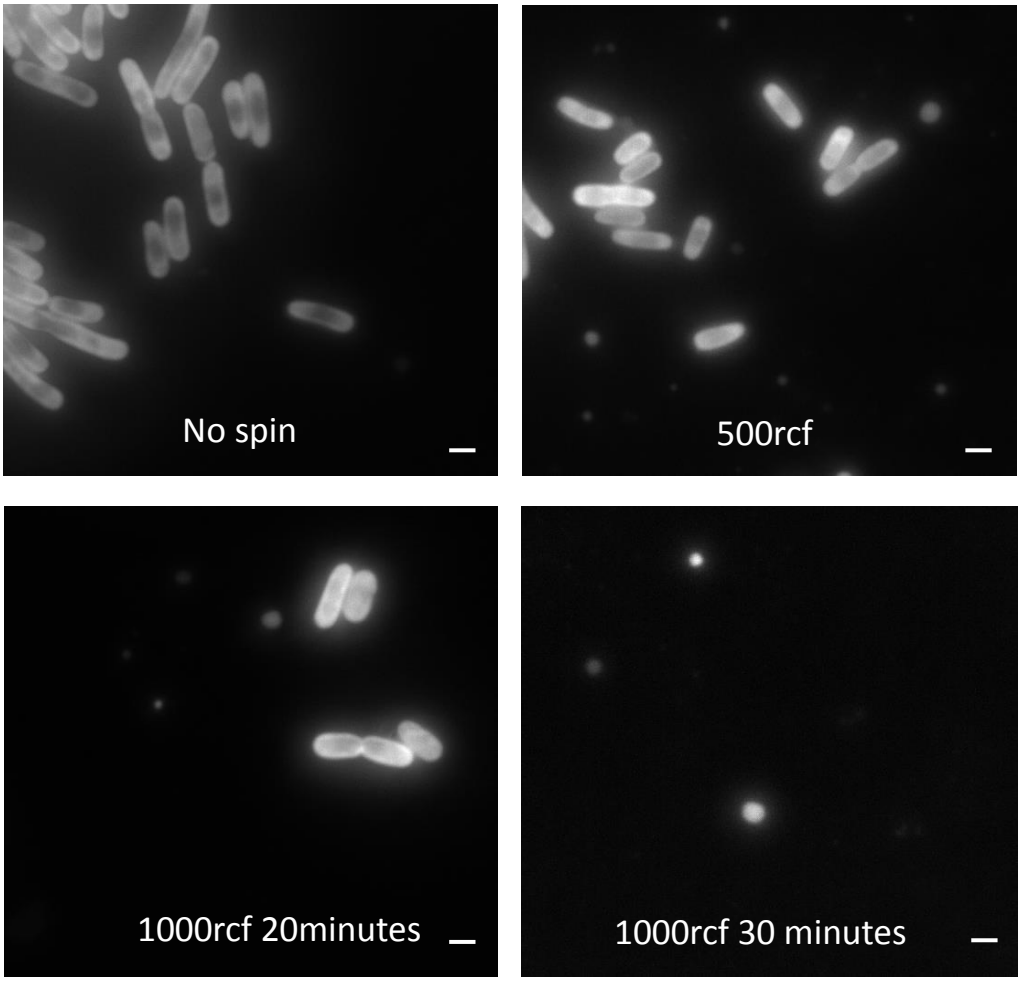


Figure 4.21. Images of supernatant from cell cultures centrifuged to remove cells from vesicle containing media. Vesicles produce by *E. coli* producing non Nt-acetylated aS-mNeonGreen-Pif6, induced for 5 hours with 100μg/ml IPTG. Scale: 1μm.

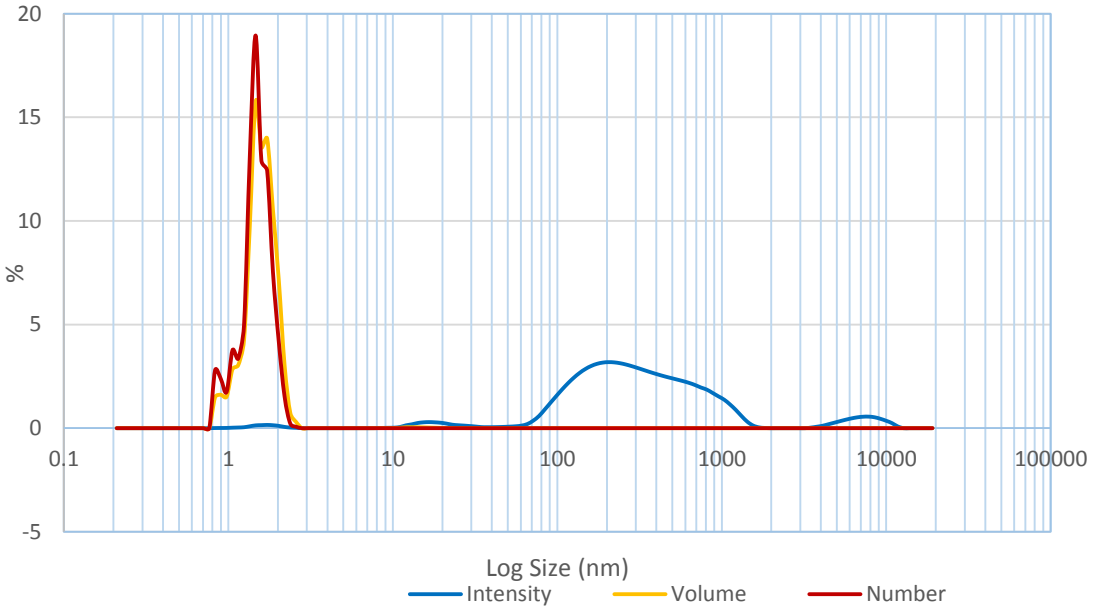


Figure 4.22. DLS graph of control supernatant from a culture of BL21 DE3 cells expressing OmpA-mCherry, centrifuged for 30 minutes at 1000rcf. The graph shows volume and number of particles of various sizes. The intensity trace indicates the presence of particles of different sizes up to approximately 1500nm diameter. Results obtained with the kind help of N. Manyanya.

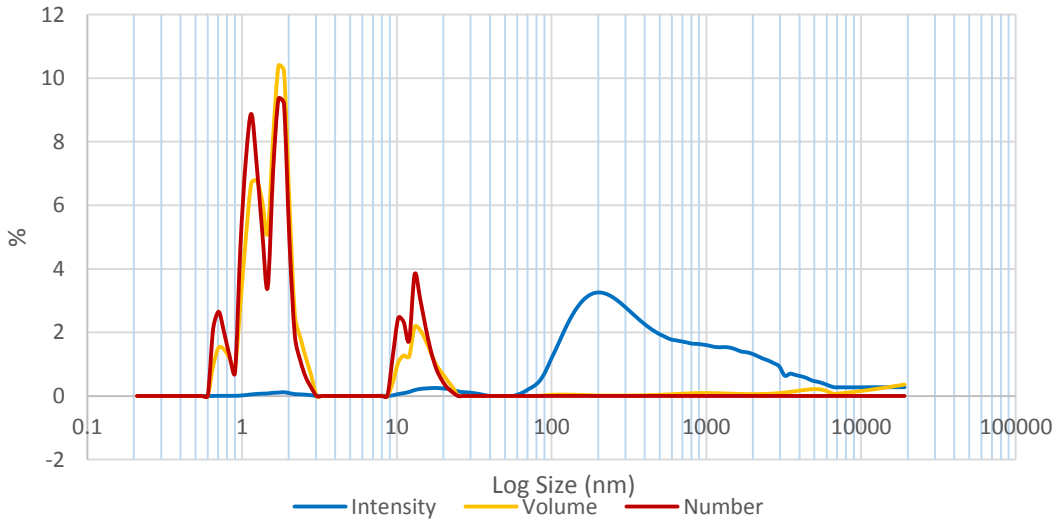


Figure 4.23. DLS graph of supernatant from a culture of BL21 DE3 cells expressing non Nt-acetylated aS-mNeonGreen-Pif6 and OmpA-mCherry, centrifuged for 30 minutes at 1000rcf. The graph shows volume and number of particles of various sizes. The intensity trace indicates the presence of particles of different sizes up to approximately 5000nm. Results obtained with the kind help of N. Manyanya.

4.8 Targeting of recombinant protein into vesicles

To optimise the use of large aS induced vesicles in therapeutic protein production, the therapeutic proteins need to be targeted into the vesicles as they form. The cytoplasmic protein content in vesicles appears to be random. Observing *E. coli* BL21 DE3 cells producing aS-mNeonGreen simultaneously with cytoplasmic mCherry, using fluorescent microscopy, some vesicles can be clearly seen to contain cytoplasmic fluorescent protein (**Figure 2.24**) but others do not.

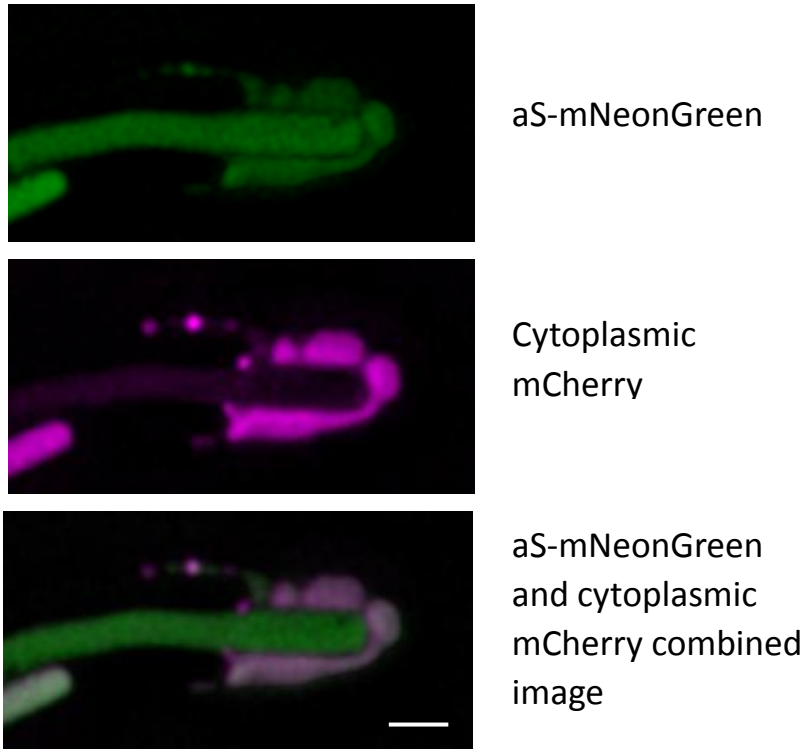


Figure 4.24. Widefield images of *E.coli* producing non Nt-acetylated aS-mNeonGreen (green) and cytoplasmic mCherry (magenta). Cytoplasmic mCherry can be seen within vesicles. Scale: 1µm.

Proteins can be targeted into vesicles by attaching them to aS, as the aS interacts with membranes and is thus drawn into vesicles as the membrane forms around. This can also be seen in SIM images of BL21 DE3 cells producing aS-mNeonGreen-FLAG-hGH simultaneously with OmpA-mCherry (**Figure 4.25**).

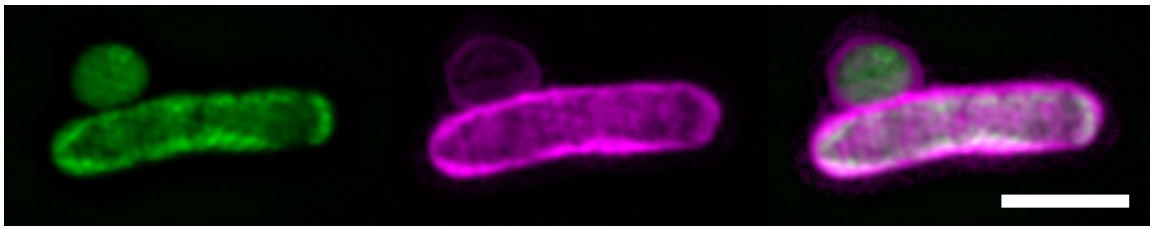


Figure 4.25. SIM images of *E.coli* producing non Nt-acetylated aS-mNeonGreen-FLAG-hGH (green) and OmpA-mCherry (magenta) outer membrane marker, show aS-mNeonGreen-FLAG-hGH packaged into the vesicle. Scale: 1µm.

A preliminary investigation was carried out into the possible use of optogenetics, to control the location of and target therapeutic proteins into aS induced vesicles. Optogenetics is a technique which uses two plant proteins, PhyB and Pif6. In the presence of phycocyanobilin (PCB) these proteins associate when exposed to 650nm red light and dissociate when exposed to 750nm far red light (**Figure 4.26).**

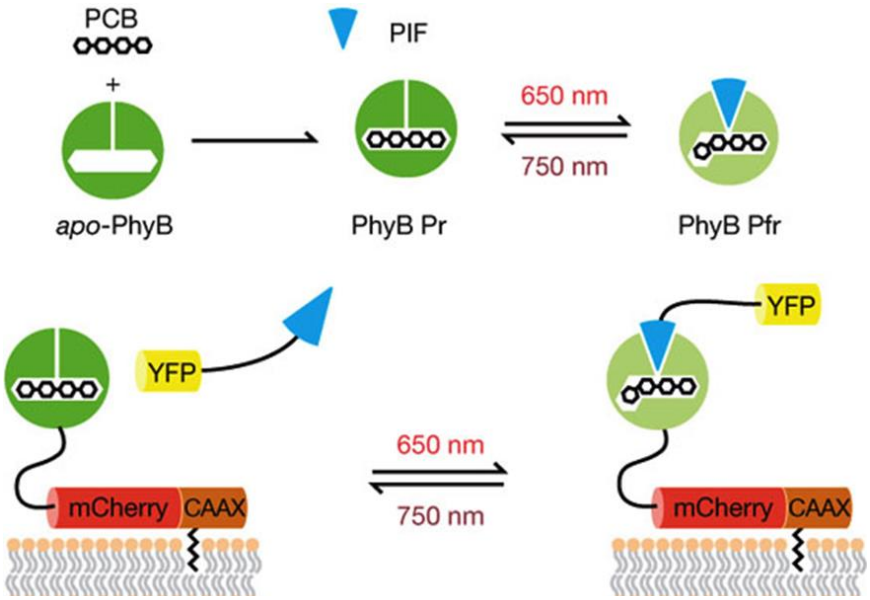


Figure 4.26. Schematic of optogenetics. Optogenetics uses two plant proteins, PhyB and Pif6. In the presence of PCB these proteins associate when exposed to 650nm red light and dissociate when exposed to 750nm far red light. By producing a recombinant protein attached to Pif6 it can be targeted to and released from PhyB attached to an anchor protein, thus controlling its location within a cell. From (Levskaya et al., 2009)

E. coli BL21 DE3 cells producing aS-mNeonGreen-Pif6 simultaneously with PhyB-mCherry were imaged after exposure to 650nm red light. The recombinant proteins were observed to co-localise (**Figure 4.27**). Unfortunately time restraints meant that this investigation was not pursued further

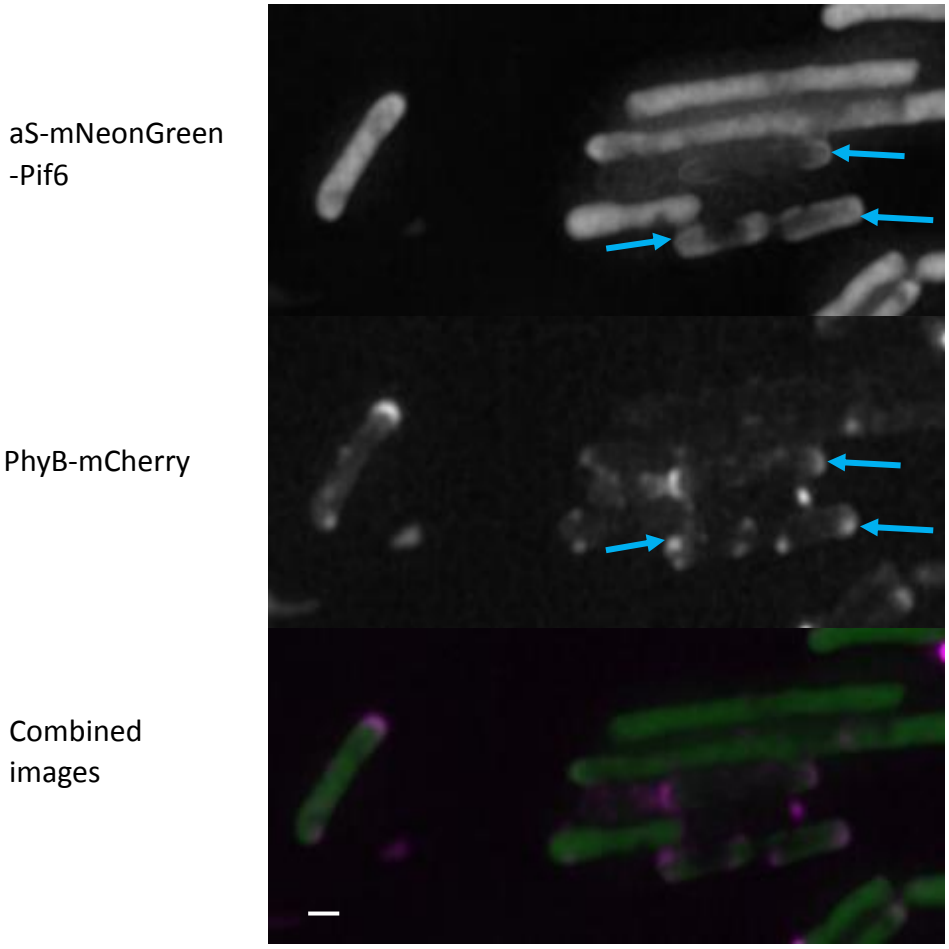


Figure 4.27. Widefield images of *E.coli* producing non Nt-acetylated aS-mNeonGreen-Pif6 (green) and PhyB-mCherry (magenta). Images obtained, post 10 minute exposure to 650nm red light, showing co-localisation (blue arrows). Scale: 1µm.

4.9 Lipid specific interactions

To better understand aS membrane interactions including vesicle formation, investigations were carried out to investigate aS interactions with single lipids.

PIP Strips™ membranes are designed for the identification of proteins possessing phosphoinositide recognition domains and for analysis of their lipid-binding specificities. PIP Strip™ membranes were used for an initial investigation into lipid specific binding. aS was shown to bind to specific lipids and a difference was observed between Nt-acetylated versus non Nt-acetylated aS-Cerulean3 in binding to Phosphatidic acid (PA) (**Figure 4.28**).

Purified aS-Cerulean3, both Nt-acetylated and non Nt-acetylated, was sent to Nyasha Manyanya for addition to single lipid vesicles formed from the membrane lipids, 1-palmitoyl-2-oleoyl-sn-glycero-3-phosphocholine (POPC) or 1,2-distearoyl-sn-glycero-3-phospho-(1'-rac-glycerol) (DSPG) and analysis by DLS. The size of POPC vesicles did not change when either protein was added to them. However, when non Nt-acetylated was added to DSPG vesicles, an increase in size was observed which was not seen when Nt-acetylated aS-Cerulean3 was added to the same vesicles (**Figure 4.29**). This indicates that aS interactions with membranes may differ according to the lipid content of the membrane and whether the aS is Nt-acetylated or not.

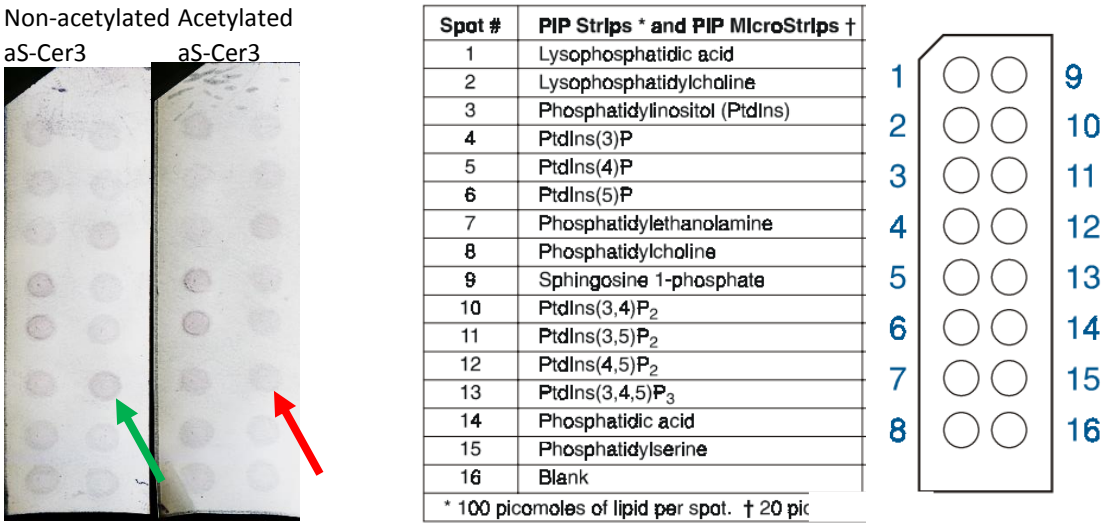


Figure 4.28. PIP strips showing aS-Cerulean3 binding to specific lipids. Non Nt-acetylated aS (green arrow) has a stronger affinity for Phosphatidic Acid compared to Nt-acetylated aS (red arrow).

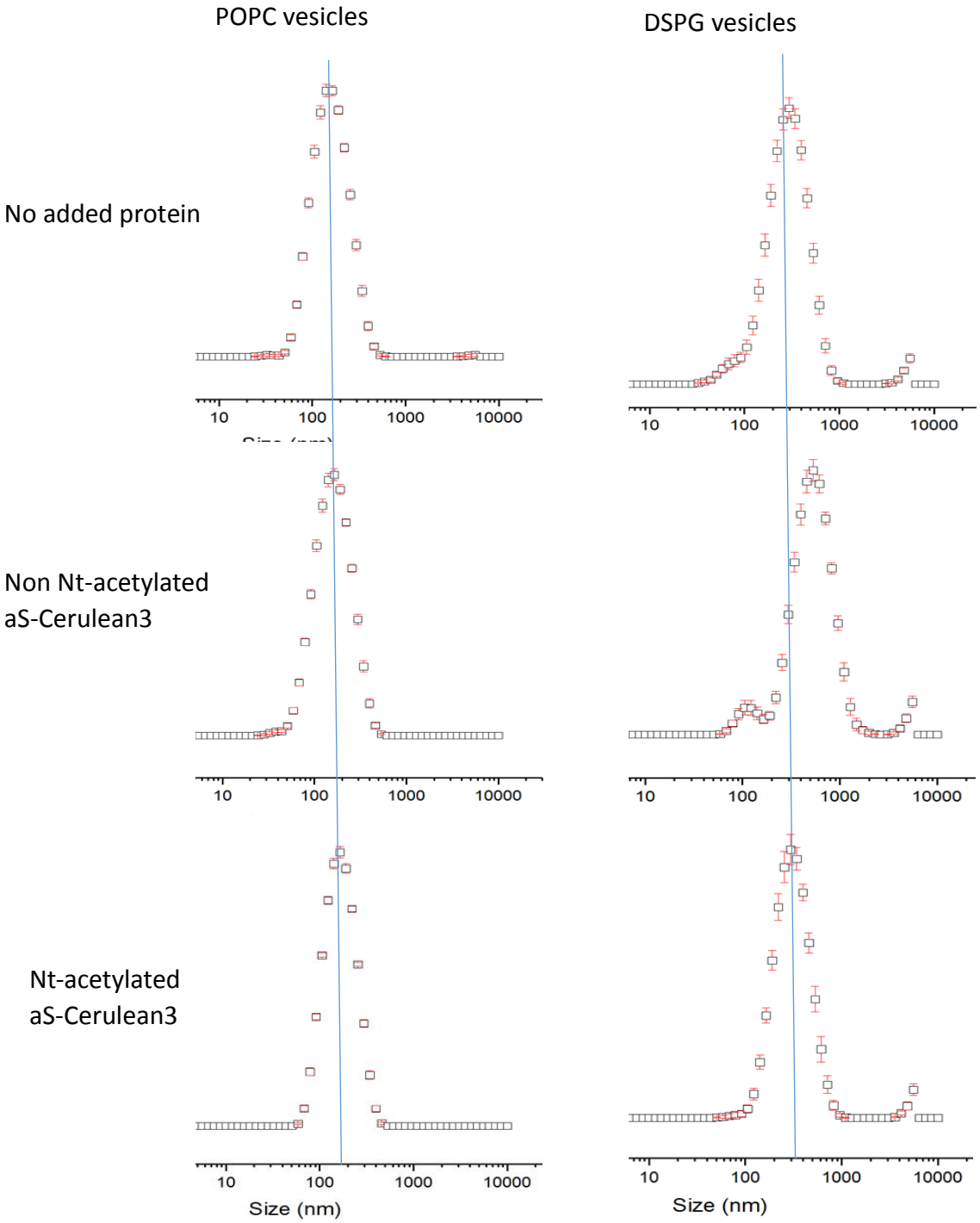


Figure 4.29. DLS measurements of vesicle size when either Nt-acetylated of non Nt-acetylated aS is added. No difference is seen in1-palmitoyl-2-oleoyl-sn-glycero-3-phosphocholine (POPC) vesicles when either Nt-acetylated of non Nt-acetylated aS is added. No difference in size is seen when Nt-acetylated aS is added to 1,2-distearoyl-sn-glycero-3-phospho-(1'-rac-glycerol) (DSPG) vesicles. However an increase in size is seen when non Nt-acetylated aS is added to DSPG vesicles. Results obtained with the kind help of Nya Manyanya.

4.10 aS and Microcompartments

Bacterial microcompartments are functional analogues of eukaryotic organelles, formed of a selectively permeable protein shell encapsulating an enzymatic core. Bacterial microcompartments can provide a defined microenvironment and are the subject of increasing interest in synthetic biology. The production of microcompartments within vesicles could potentially provide extra rigidity and stability to them, improving vesicle purification and a vesicle membrane surrounding a microcompartment could offer protection of microcompartment proteins from protease activity.

The possibility of producing microcompartments within aS-induced vesicles was investigated.

A construct to produce microcompartment proteins with aS-mCherry was obtained from Dr S.Frank (Parsons *et al.*, 2010). aS-mCherry-PduABJKNU was produced in *E. coli* JM109 cells which were imaged using widefield microscopy (**Figure 4.30) and** TEM (**Figure 4.31**). The TEM images obtained show aS induced vesicles larger than those seen previously by TEM, indicating that vesicle stability may be improved by the co-expression of microcompartment proteins. Cell extracts from this cell culture were run on a Coomassie stained gel to compare with a published SDS-page gel showing these microcompartment proteins (**Figure 4.32**).

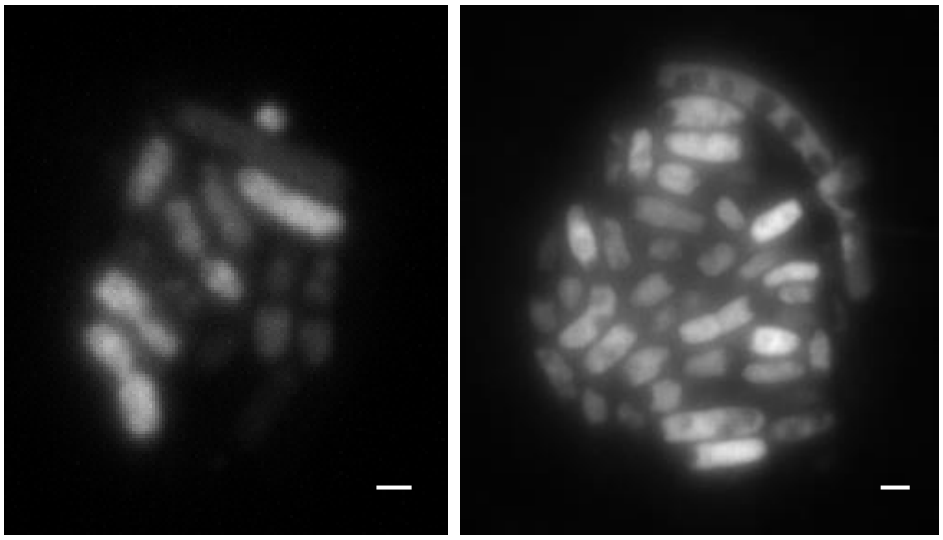


Figure 4.30. Widefield images of JM109 *E.coli* producing non Nt-acetylated aS-mCherry-PduABJKNU. A few vesicles were seen and lots of dark internal areas where cytoplasm appears to be excluded. Scale bar 1μm.

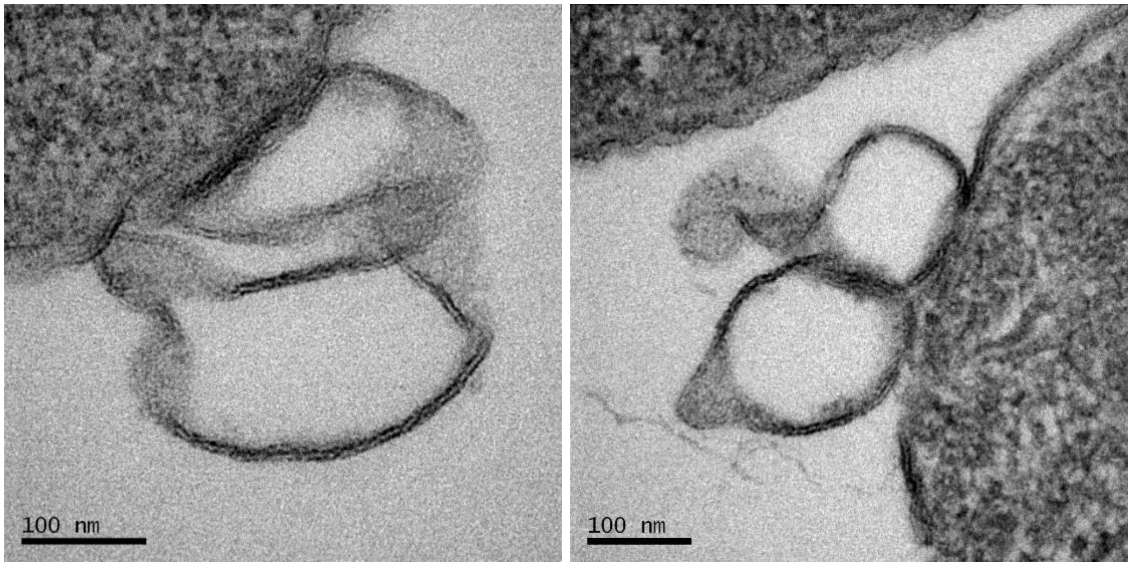


Figure 4.31. TEM images of JM109 *E.coli* producing non Nt-acetylated aS-mCherry-PduABJKNU. Extracellular vesicles larger than previously seen by TEM were visualised, which appear to be attached to cells.

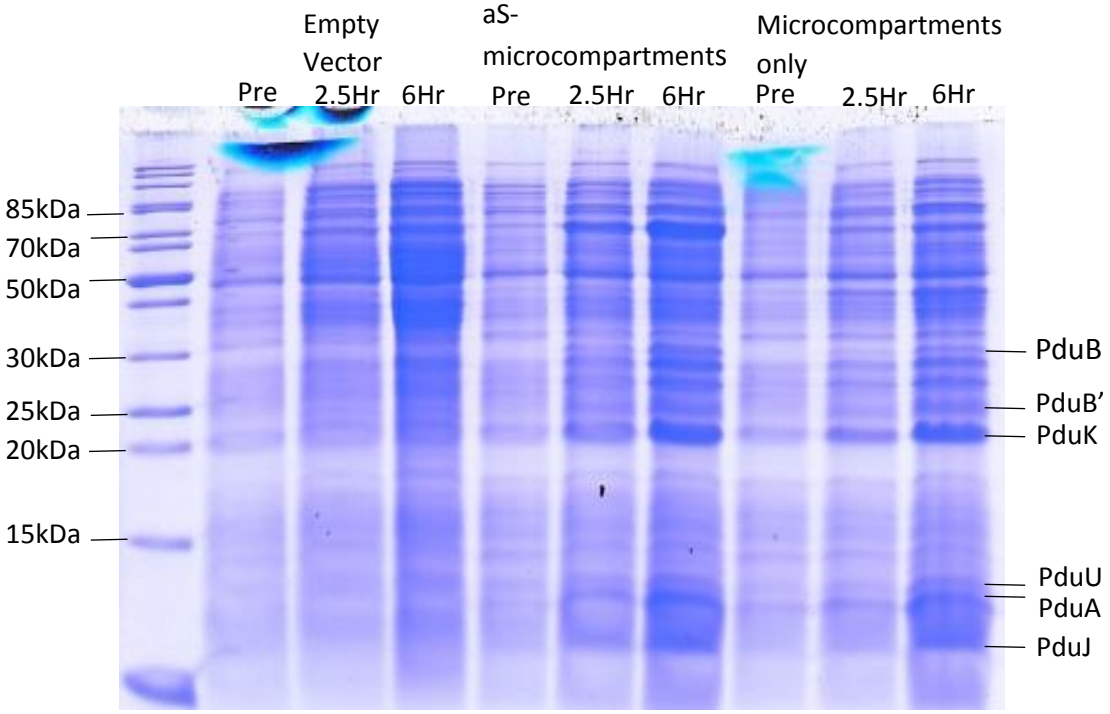


Figure 4.32. 17% SDS PAGE gel stained with Coomassie Blue, showing protein present in cell extracts from JM109 *E.coli* producing non Nt-acetylated aS-mCherry-PduABJKNU. Samples were taken at 2.5 and 6 hours post induction with 0.2% Rhamnose. Protein bands identified by comparison with a published SDS-page gel of Microcompartment proteins in Parsons *et al,* (2010).

4.11 Discussion

This investigation has shown that aS possibly interacts with the inner membrane of the *E. coli* in which it is produced, when either Nt-acetylated or non Nt-acetylated, but not with the outer membrane. aS interacts with MinD, an inner membrane binding protein and that this interaction possibly changes on membrane binding.

Clear differences were seen between the membrane interactions of Nt-acetylated and non Nt-acetylated aS. It was observed that when Nt-acetylated aS is produced within *E. coli* cells the formation of internal structures with a tubular appearance is more predominant, this was seen most clearly with TEM. It was also observed that vesicle formation predominantly occurs at dynamic membranes when non Nt-acetylated aS is produced within *E. coli* cells, this was seen most clearly with fluorescent microscopy.

Both vesicles and tubular structures are formed predominantly at dynamic membranes. The lipid content of different areas of cellular membranes varies. It has been shown with PIP Strip™ membrane assays and in DLS assays with single lipid vesicles, that Nt-acetylated and non Nt-acetylated aS interact with different lipids. This lipid specificity could potentially be a reason for aS localisation and the differing interactions with Nt-acetylated and non Nt-acetylated aS. This then raises the question as to whether different bacterial strains with different membrane lipid content would be more effective for vesicle formation.

Future use and development of aS induced vesicles for therapeutic protein production requires optimisation of vesicle formation for each required constructs, including optimisation of timings, induction rate and bacterial strains used. Future investigations could also look into improving targeting of therapeutic proteins into vesicles, for example by attachment to membrane proteins. The plasmid selection antibiotic used may also have an effect on vesicle formation, either directly by affecting the cell wall or indirectly through the loss of selection and should be further investigated.

Chapter 5: The effect of *naa-80* knockout in *C. elegans*

NatH which is comprised of a single unit N-α-acetyltransferase-80 (NAA-80) is a recently described, highly specific Nat, which post-translationally Nt-acetylates β-actin and γ-actin. The β and γ-actin Nt-acetylation increases the ratio of monomeric to filamentous actin, reduce the number of lamellipodia and filopodia and reduces cell hypermotility in studies using HAP1 and HAP1 *NAA80*-KO cell lines (Drazic *et al.*, 2018). The Mulvihill lab has an interest in Nt-acetylation and the actomyosin cytoskeleton in yeast and *C. elegans.*

The aim of this investigation was to examine the effect of *naa-80* knockout (KO) on the regulation of actin in *C. elegans,* to look for any *naa-80* KO specific phenotype.

5.1 Acquisition and generation of a *naa-80* deletion allele in *C. elegans*

To understand the physiological role of *naa-80* in a whole organism model the *naa-80* gene was targeted for knockout in *C. elegans*. Three *naa-80* knockout *C. elegans* strains were obtained from Knudra Transgenics (Utah USA). Each of these strains was produced using CRISPR-sdm transgenesis. This method uses two sgRNAs to guide cutting of the genome by Cas9 protein. An oligonucleotide donor homology guides repair of the cut genome, introducing an early stop (3 frame stop sequence-TAGATAGATAGA) after Proline 46, within Exon 2. The transgene remains 40bp shorter than the endogenous DNA sequence.

To confirm the knockout of *naa-80* in each of the acquired strains quantitative PCR (qPCR) was used. RNA was extracted from three biological replicates of the N2H control strain and each of the new *naa-80* KO strains and used to generate cDNA. qPCR was performed using each of these samples with control and *naa-80* specific oligo mixes. The extremely low relative amount of *naa-80* mRNA was detected for the acquired

strains compared with the N2H controls confirmed that they were all *naa-80* knockout strains (Figure 5.1).

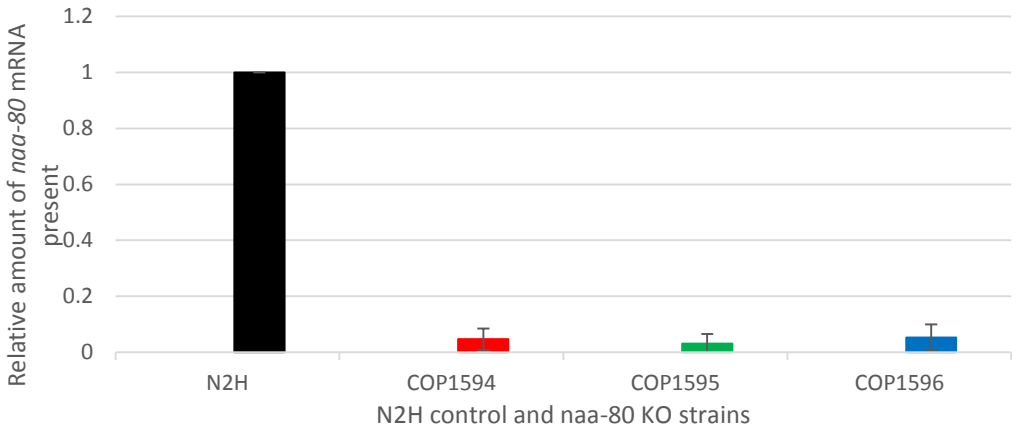


Figure 5.1. qPCR showing relative amounts of *naa-80* mRNA in N2H control and *naa-80* KO *C. elegans* strains COP1594, COP1595 and COP1596. Only very low values were obtained for the knockout strains, confirming the knockout of *naa-80*. Three biological repeats were used for each strain.

5.2 Initial brood size and age specific fecundity assays with knockout strains at 20°C

Fertility is a good read out of organismal health. This is easy to determine in C. elegans by counting the number of progeny they produce over their reproductive lifespan. To determine whether *naa-80* contributes to fertility the brood sizes of N2H controls were compared to that of all three *naa-80* knockout strains. No significant difference in brood size was seen in two out of three knockout strains, a difference was seen with the third strain, as calculated by students t test, p=0.006 against N2H controls (**Figure 5.2**). Total progeny counts from control and knockout strains demonstrated that in general *naa-80* does not contribute to the total progeny production of *C. elegans*.

It was noted after initial brood size assays that there were differences in the timing of when eggs were laid. This suggested that *naa-80* knockout *C. elegans* reached adulthood earlier and started laying eggs before their wild type counterparts. The results for the initial brood size assays were analysed on a day-to-day basis to compare age-specific fecundity (**Figure 5.3**). Age specific fecundity assays compare the number

of live offspring from eggs laid each day by parent *C. elegans*, which are of the same age. This is a way to compare the rate of development of parental *C. elegans* which were all hatched from synchronised, 2 hour, timed egg lays. Each repeat was analysed separately as parent worms used for the initial brood size assays were moved between plates at slightly different times of the day and so runs were not directly comparable with each other. Taken together the data suggests that *naa-80* may have an impact on developmental timing of the *C. elegans* larvae.

During these assays a high incidence of internal hatching was observed in the N2H controls, it was therefore decided to repeat brood size assays changing the incubation temperature from 20°C to 25°C which can reduce this phenotype. As all three *naa-80* knockout strains showed low levels of *naa-80* mRNA transcript (**Figure 5.1**) and all showed similar fecundity profiles only one was chosen to proceed with, COP1594.

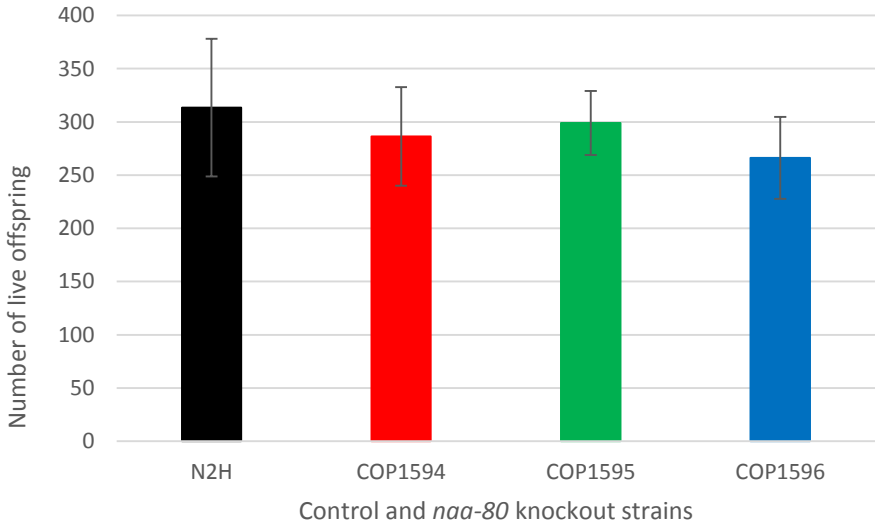


Figure 5.2. Average number of offspring for brood size assays carried out at 20°C using N2H control and *naa-80* knockout C. elegans strains COP1594, COP1595 and COP1596. Only strain COP1596 had a statistically significant difference using Student's t-test against N2H controls, N2H n=34, COP1594 n=31 p=0.119, COP1595 n=32 p=0.137, COP1596 n=30

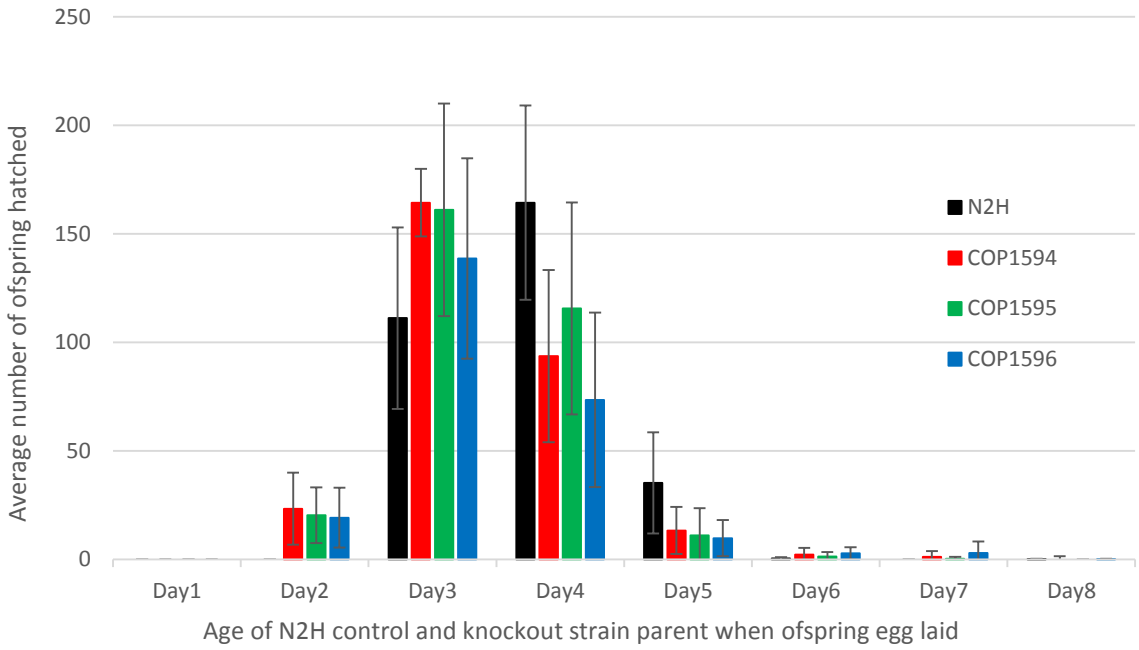


Figure 5.3. Age specific fecundity assay from a timed egg lay, at 20°C using N2H control and *naa-80* knockout *C. elegans* strains COP1594, COP1595 and COP1596. N2H control *C. elegans* parents were found not to lay eggs until placed on plates at 3 days after they were eggs themselves, compared with 2 days for the *naa-80* knockout strains and to reach peak egg laying rates a day later. N2H n=10, COP1594 n=10, COP1595 n=11, COP1596 n=11.

5.3 Initial assays at 25°C using a single knockout strain

Brood size assays were repeated at 25°C in an attempt to reduce the number of C. elegans experiencing internal hatching. A reduction in internal hatching when increasing the incubation temperature from 20°C to 25°C is a phenomenon previously observed by senior researchers within this lab. Parent *C. elegans* were moved at the same time each day so that comparable age specific fecundity results could be obtained for all runs. As larvae were counted, a number of unfertilised eggs were observed on the plates, these were also counted and compared. Larvae were also imaged at 1, 2 and 3 days post timed egg lay, these images were analysed using Optomorph software to measure larvae lengths in pixels.

A large difference was seen in brood size between N2H controls and the *naa-80* knockout strain (**Figure 5.4**) which appears to be due to very low brood sizes being

obtained for the N2H controls, far below what would be expected. Possible problems with the control strain as highlighted by the very low brood size must be taken into account when analysing the results obtained at 25°C.

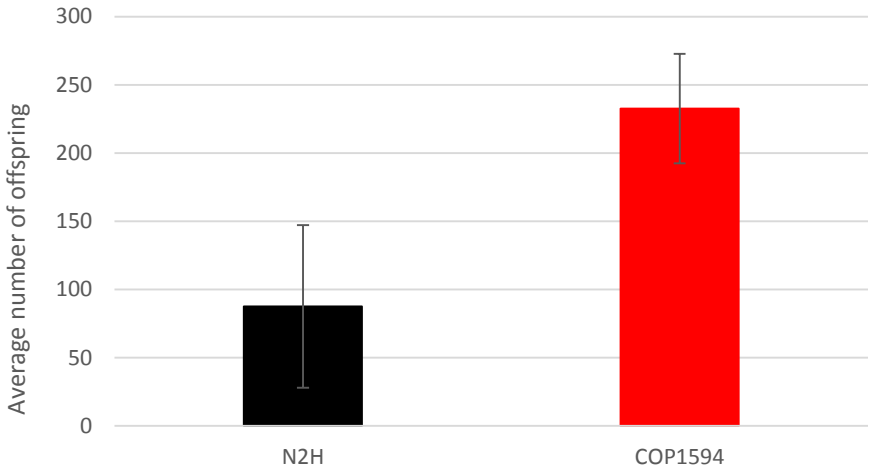


Figure 5.4. Brood size assays carried out at 25°C using N2H control and *naa-80* knockout *C. elegans* strain COP1594. N2H control *C. elegans* appeared to be unhealthy with reduced brood size, below what would normally be expected. N2H n=35, COP1594 n=34

Again a clear difference in age specific fecundity was seen with the *naa-80* knockout strain reaching peak egg lay a day before the N2H controls (**Figure 5.5**).

The average number of unfertilised eggs counted was much higher for the *naa-80* knockout strain compared to N2H controls. There was a large amount of variation in the number of unfertilised eggs laid between individual parent *C. elegans*, resulting in a very large standard deviation (**Figure 5.6**). This result may also have been affected by the N2H controls producing a low brood size.

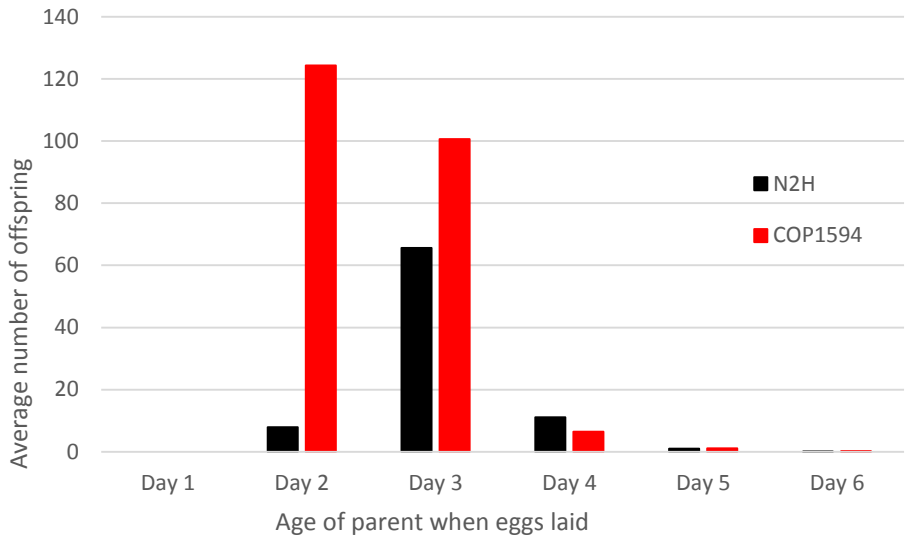


Figure 5.5. Averaged results from three Age specific fecundity assays at 25°C using N2H control and *naa-80* knockout *C. elegans* strain COP1594. N2H control *C. elegans* parents were found to reach peak egg laying rates a day later than the KO strain. N2H n=35, COP1594 n=34

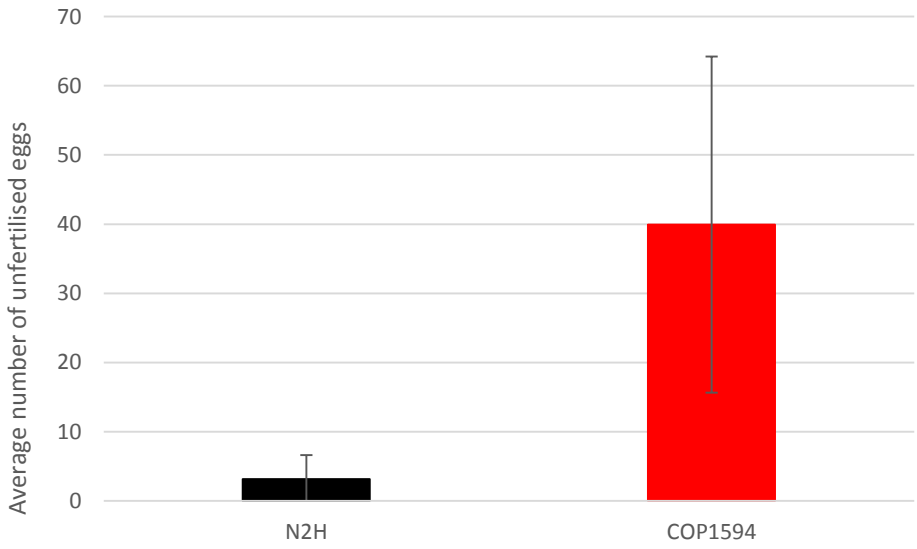


Figure 5.6. Average number of unfertilised eggs laid during the 25°C brood size assays. A large difference was seen between N2H controls and *naa-80* knockout *C. elegans* despite only small numbers of eggs being counted, a large S.D. was seen and the large difference in brood size should also be taken into consideration. N2H n=35, COP1594 n=34

As the age specific fecundity results obtained at both 20°C and 25°C indicated a possible difference in the rate of *C. elegans* development from embryo to egg laying, larvae

lengths were measured at 1, 2, and 3 days post timed egg lay, to compare the rate of larval development. The larvae lengths measured at 1, 2 and 3 days post timed egg lay all gave longer lengths for the *naa-80* knockout *C. elegans* compared with the N2H controls of the same age (**Figure 5.7**). The results for 1 and 2 days post timed egg lay were significant according to Student's t-test. Day 1 $p=7.2x10^{-7}$, Day2 p=0.03, at day 3 the difference was not found to be significant, Day3 p=0.18. This indicates that larvae development is accelerated in the *naa-80* knockout strain compared to the N2H controls for the first two days post hatching but that this accelerated development slows by day 3, when the difference in larvae length is no longer significant.



Figure 5.7. Average larvae lengths in pixels of N2H control and *naa*-80 knockout larvae. The *naa-80* knockout *C. elegans* strain COP1594 had longer lengths than N2H controls at the same age from timed egg lay. Day 1 N2H n=23, COP1594 n=22, Day 2 H2H n=37 COP1594 n=40, Day 3 N2H n=39 COP1594 n=45.

5.4 Production of outcrossed strains

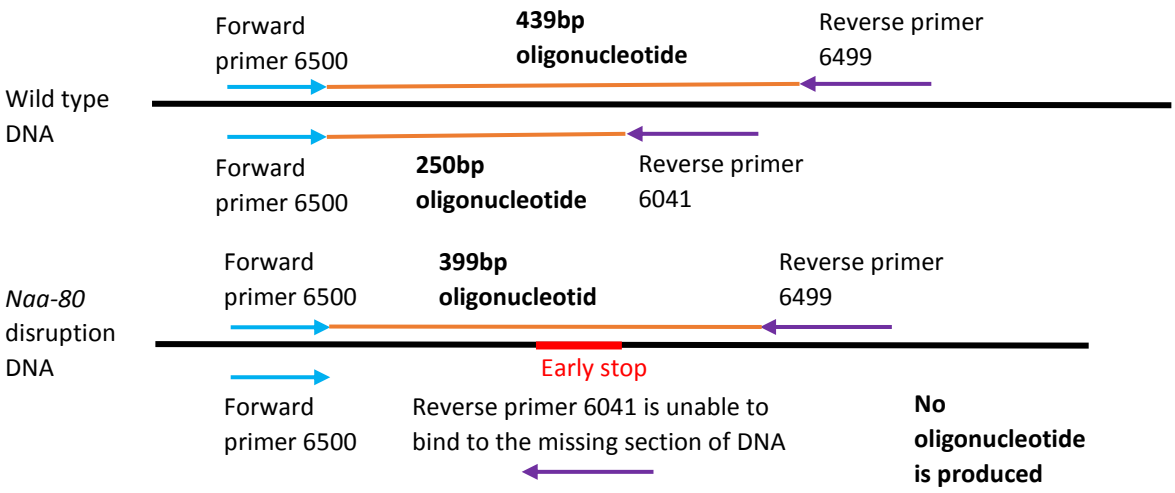
In order to show that any phenotype observed during initial assays was solely due to the *naa-80* knockout the acquired *naa-80* knockout strain COP1594 was back crossed into N2H *C. elegans.* This was completed 6 times to ensure that all *C. elegans* used in further assays had the same genetic background. It was necessary to ensure that only

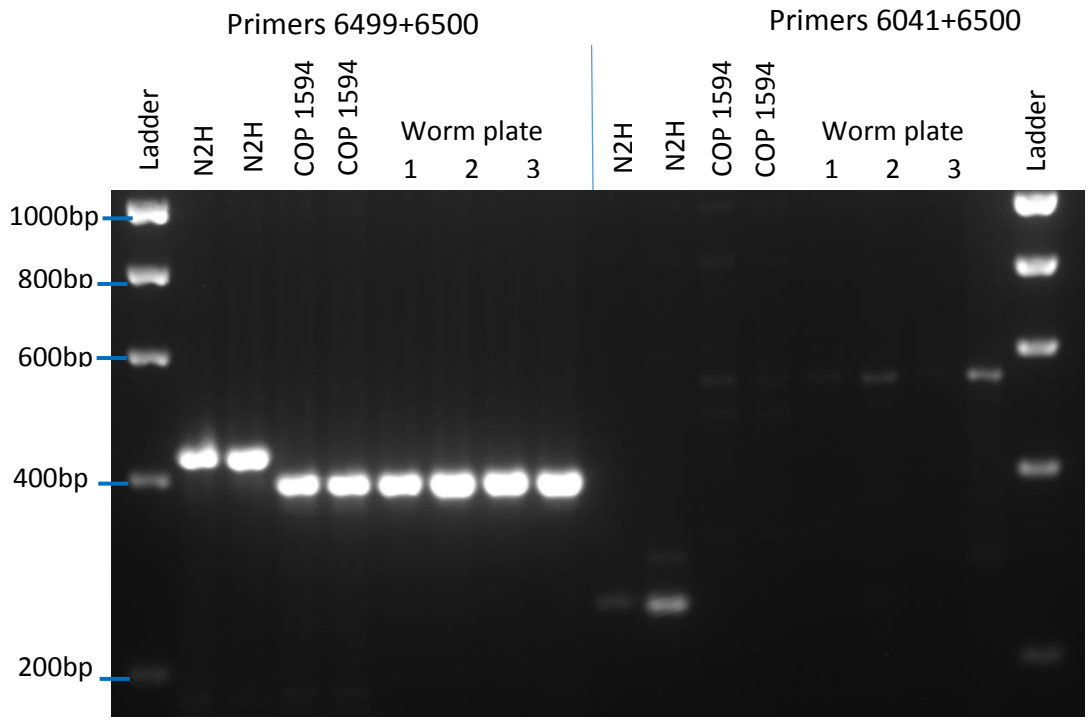
outcrossed *C. elegans* homozygous for the *naa-80* knockout were used for each following outcross. To ensure this, following each cross F2 generation *C. elegans* which had been individually isolated and allowed to lay eggs were lysed and used for Genotyping PCR using primers 6499 and 6500. If the outcrossed *C. elegans* are homozygous a single band of 399bp should be seen, whereas a 439bp band would be seen for wild type and heterozygous *C. elegans*. After every third cross, genotype PCR were carried out using multiple F3 generation *C. elegans* and splitting the lysate to use two different sets of primers 6499 and 6500 and 6500 and 6041, where the reverse primer initiates DNA replication within the section of *naa-80* which was deleted by CRISPR/CAS9. This means that no band should be seen for homozygous *C. elegans* and a 250bp band will be seen for wild type and heterozygous *C. elegans* (**Figure 5.8**). After the 6th outcross this was carried out with duplicate N2H and COP1594 *naa-80* knockout controls and with three separate 6th outcross plates (**Figure 5.8**).

Once this final 6th outcross was confirmed, it was used to repeat the previous assays. A new N2H hermaphrodite control strain line was produced from the N2H strain that the *naa-80* knockout strain was crossed into.

The 6th outcrossed strain was then also outcrossed once into two other strains BU70 and XW8490, producing either LifeAct-mRFP or mCHERRY-ACT-1 for use in fluorescent microscopy imaging.

LifeAct-mRFP is a peptide marker for imaging of filamentous actin LifeAct binds to filamentous actin only, the attached monomeric Red Fluorescent Protein allows filamentous actin to then be imaged in live C. elegans using fluorescent microscopy. ACT-1 is a single actin isoform which is produced in C. elegans. The expression of mCHERRY-ACT-1 enables the imaging of ACT-1 within live C. elegans using fluorescent microscopy, it can be seen in various structures but predominantly in striated muscle of the body wall.





Primers	N2H	Naa80Δ
6499+6500	439bp	399bp
6041+6500	250bp	No band

Figure 5.8. Genotyping PCR. Positioning of primers used for Genotyping PCR, showing the lengths of oligonucleotide produced with each primer pairing, for both wild type and naa-80 disruption C. elegans. Genotype PCR, on 2% agarose gel, giving final confirmation of *naa*-80 knockout in *C. elegans* from three separate plates of the 6th outcross of *naa*-80 knockout into N2H background. Duplicates of N2H control and COP1594 *naa*-80 knockout controls included. Expected band sizes are included in the table.

5.5 Assays with the outcrossed knockout strain

Brood size, age specific fecundity and larvae length assays were repeated with the outcrossed *naa-80* knockout strain and new N2H controls. Both of these strains appeared healthy and did not have a problem with internal hatching, because of this the assays were repeated at the more commonly used temperature of 20°C.

Three brood size assays were repeated at 20°C and although a slight difference was seen this was not significant according to student's t-test, p=0.10 (**Figure 5.9**).

The averaged results for age specific fecundity show the N2H control *C. elegans* producing live offspring slightly ahead of the naa-80 knockout *C. elegans,* contrary to the initial assay results. This difference was shown to be small but significant according to student's t-test on days 2 (p=0.0002) and 3 (p=0.0125) (**Figure 5.10**). However this is not a reliable result as only one of the three individual assay had any significant differences.

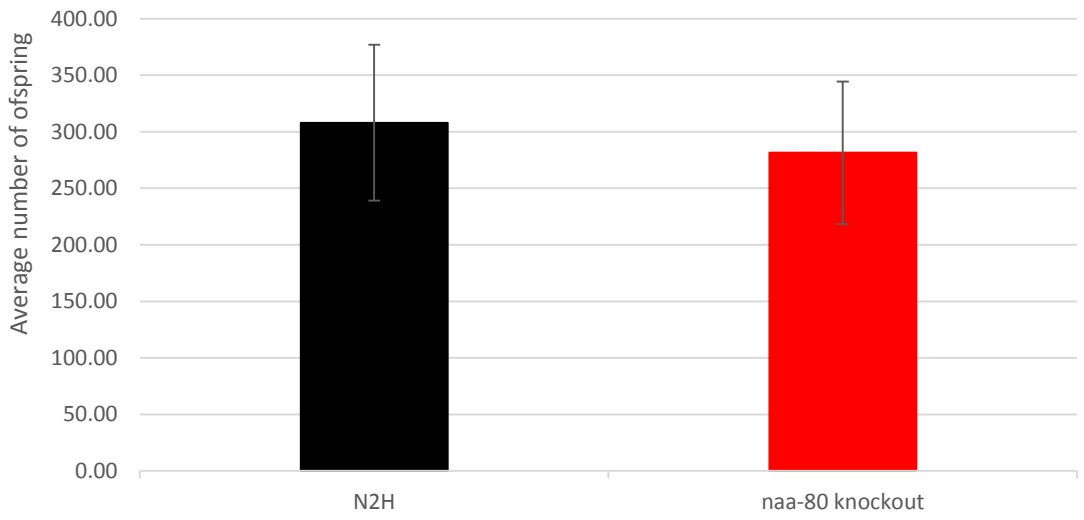


Figure 5.9. Results of brood size assays carried out at 20°C using N2H control and outcrossed *naa-80* knockout *C. elegans* strain. No significant difference in brood size was seen. N2H n=36, *naa-80* knockout n=36

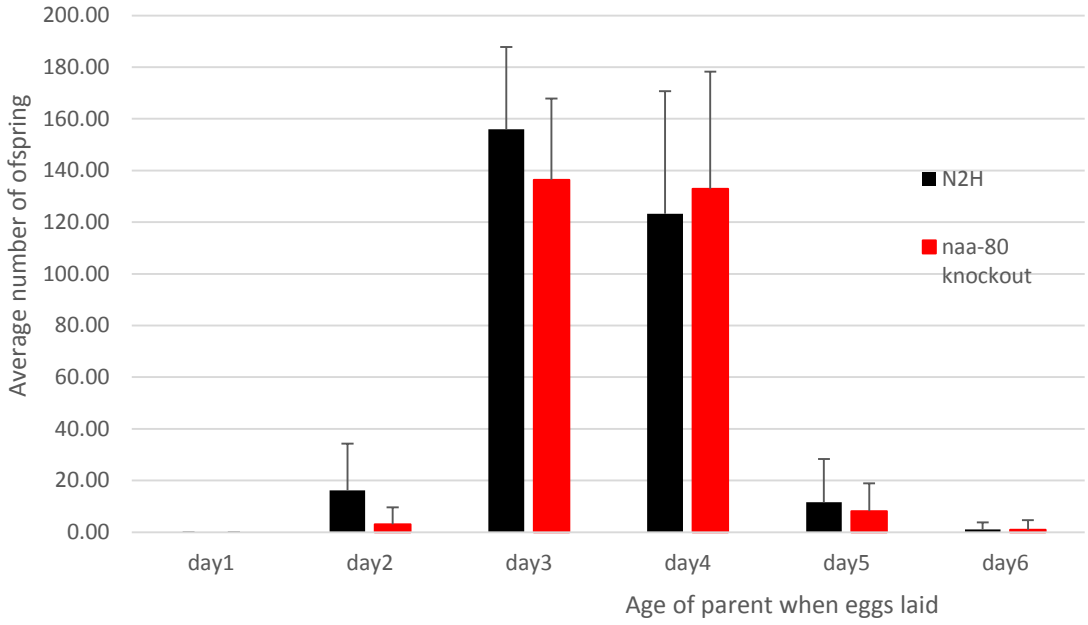


Figure 5.10. Averaged results from three Age specific fecundity assays at 20ºC using N2H control and outcrossed *naa-80* knockout *C. elegans*. N2H control *C. elegans* parents were found to reach peak egg laying rates the same day as the knockout strain, but had higher rates of egg lay on days 2 and 3, though this was only significant in one of the three individual runs. N2H n=36, *naa-80* knockout n=36

Very few unfertilised eggs were seen, this assay was not repeated as there were not enough unfertilised eggs to be statistically significant.

The Imaging and measurement of larvae lengths from timed egg lay was repeated, but inconsistent results were obtained. In the 1st run N2H control *C. elegans* lengths were consistently longer than for *naa-80* knockout *C. elegans*. In the 2nd run *C. elegans* of both strains were of very similar length and in the 3rd run the N2H control *C. elegans* lengths were consistently shorter than for *naa-80* knockout *C. elegans* (**Figure 5.11**).

It had been noticed by this point in the investigation that older *C. elegans* parents often laid eggs which were more developed, the ultimate expression of this being internal hatching in some older *C. elegans*. A further larvae length assay was performed using age synchronised parent *C. elegans* for the timed egg lay. Very similar results were

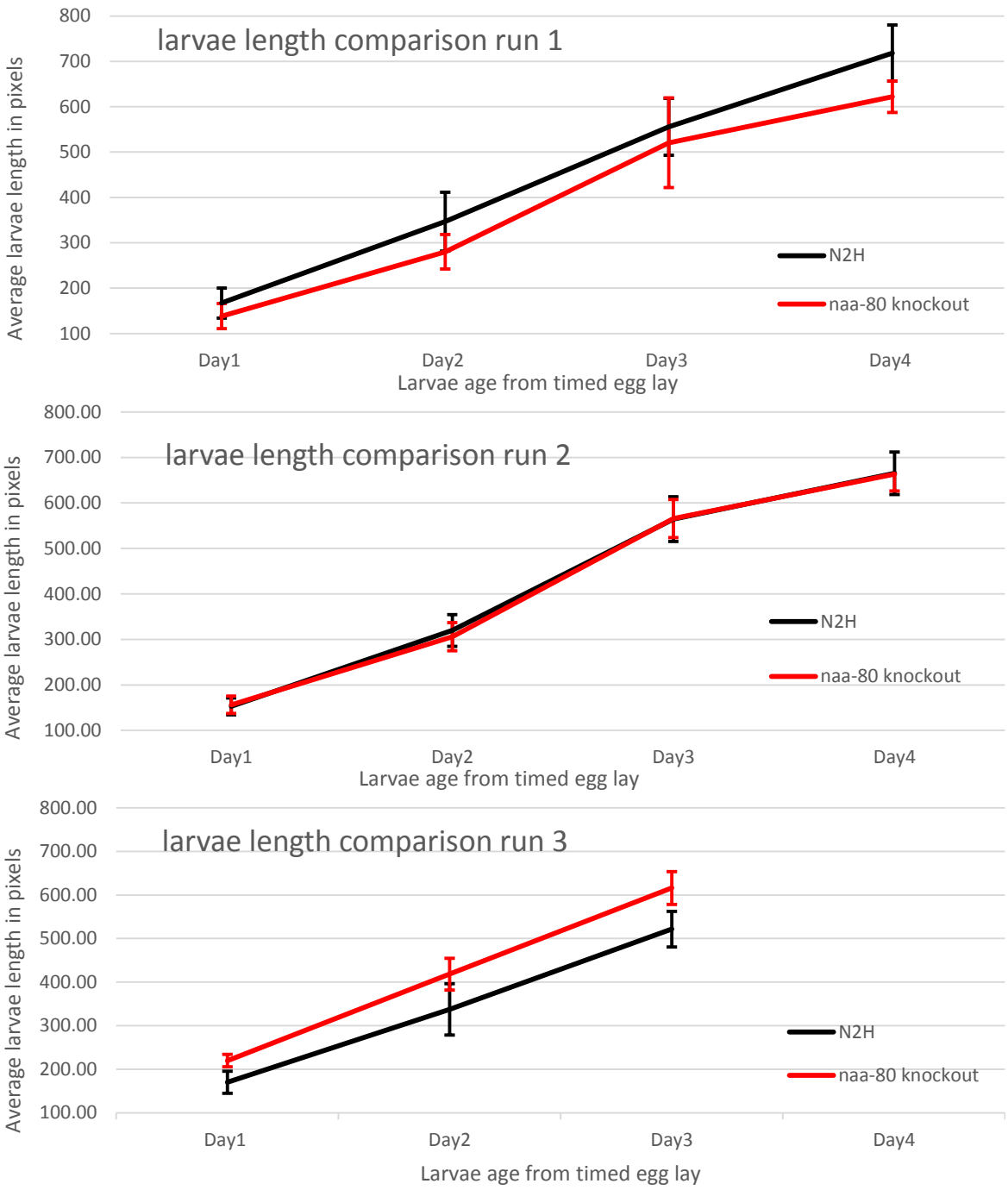


Figure 5.11. Average larvae length in pixels. Outcrossed *naa-80* knockout and N2H control *C. elegans* varied in length at the same age from timed egg lay. One run had no significant differences, however the other two runs did, in opposing directions.

Number measured	Run1				Run2				Run3		
	Day1	Day2	Day3	Day4	Day1	Day2	Day3	Day4	Day1	Day2	Day3
N2H	27	29	29	30	34	45	27	17	44	39	25
naa-80 knockout	27	29	29	30	29	26	37	23	38	28	25

obtained for both *C. elegans* strains and a reduction in standard deviation values was seen (**Figure 5.12**).

It was noticed whilst taking measurements that some of the slides imaged appeared to have two different populations of *C. elegans*. This was possibly due to a sudden increase in size when larvae went through moult. Moulting is a complex developmental step which involves extensive tissue remodelling. The first stage of moulting, Lethargus, is characterised by a gradual decrease in general activity and feeding, followed by separation of the old cuticle and eventual shedding and emergence from the old cuticle. Due to these large changes over a relatively short space of time, a small difference in timing could possibly result in a clear difference in larvae length.

A further investigation comparing body bends was also carried out with the outcrossed *naa-80* knockout and new N2H control *C. elegans* to look for differences in motility. One run was carried out using the body bend assay protocol as described in wormbook. This measurement included a considerable amount of dwelling time. Two further runs were carried out counting body bends during active movement (**Figure 5.13**). A very small difference was seen for the first run ($p=0.26$) and results for the second and third runs were almost identical (<1bend per minute different) for the two strains.

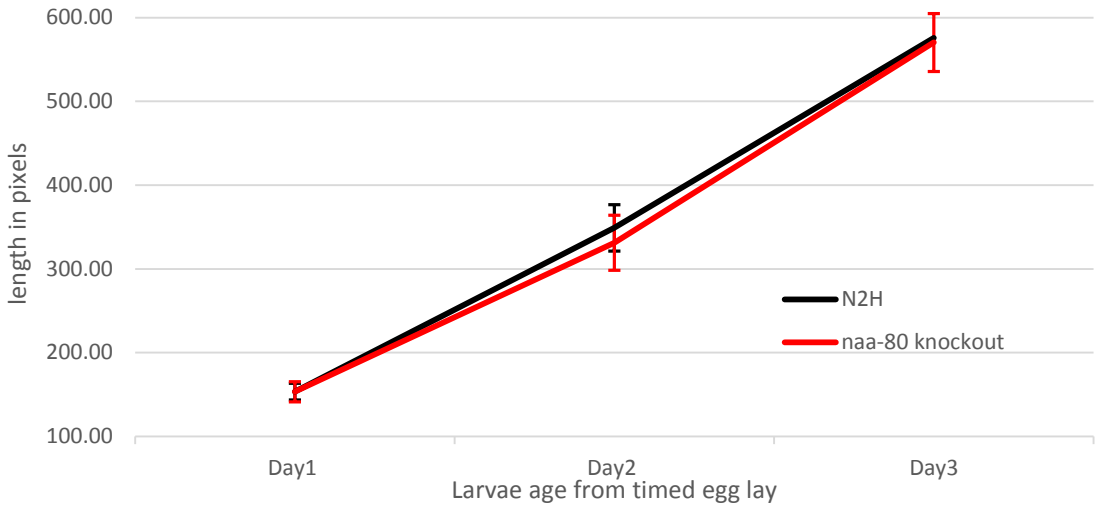


Figure 5.12. Average larvae length in pixels of outcrossed *naa-80* knockout and N2H control *C. elegans* from age synchronised parents. Larvae show no significant difference in length on days 1 and 3. A small but significant difference was seen on day 2. S.D. values were reduced by using synchronised parents for the timed egg lay.

	Day1	Day2	Day3
N2H n=	32	44	43
naa-80 knockout n=	22	46	46
Students t.test	0.998	0.006	0.445

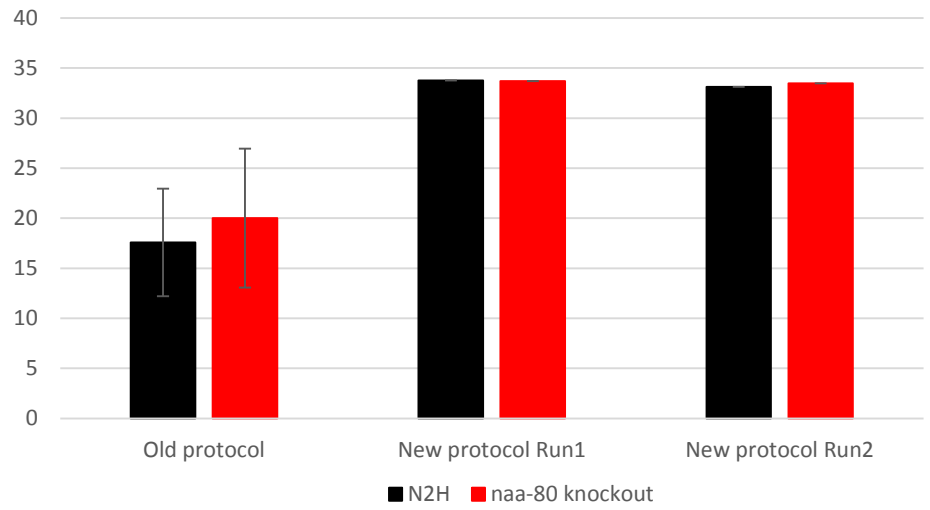


Figure 5.13. Average number of body bends per minute, of outcrossed *naa-80* knockout and N2H control *C. elegans.* Body bends were measured using the wormbook protocol (3 sets of 3 minutes for 12 of each worm strain) including dwelling time and the amended protocol counting body bends only during active movement (17 to 23 minutes per run per strain).

5.6 Optimisation of conditions for Time lapse imaging

Before time-lapse microscopy could be used for the comparison of embryo developmental timing and actin dynamics, both slide preparation and imaging conditions needed to be optimised.

Initially problems were encountered keeping embryos healthy and growing on a slide, over the long timespan needed to image embryos from 4 cells to hatch, approximately 11 to 12 hours. Eggs needed to be kept moist, but slides couldn't be sealed completely due to the need for gaseous exchange. Tapes and glues used to partially seal slides also had to be non-toxic. Eventually a successful technique for slide preparation was developed, as detailed in Methods and materials, section 2.7.5.

The optimum timing for time lapse imaging of embryo development was found to be 999 time lapse images at a rate of 1 per minute, over 16 hours 39 minutes. This is long enough for a healthy embryo to develop from a single cell to hatch at 21^{o}C.

When imaging LifeAct-mRFP and mCHERRY-ACT1 producing *C. elegans,* it was also necessary to minimise laser intensity and exposure times so as not to damage embryos or photo bleach the fluorophore.

5.7 Embryo developmental timing

16 hour 39 minute time-lapse images were used to compare embryo developmental timings.

By the time eggs had been dissected, slides prepared and the microscope focused on eggs, many had reached 2 or 4 cells before imaging began. The last image with 4 cells was used as the starting point for all time measurements. Time lapse films of both N2H control (n=12) and outcrossed naa-80 knockout (n=11) *C. elegans* were made (**Film 2. and Figure 5.14**). 3 different time points were used for measurements. Measurements were taken from 4 cells until the end of the first fold (when tail reaches the opposite end of the egg), start of 2nd fold (when tail starts to move back towards the head) and start of circling (when head has moved from one end of the egg to the other). Live developing embryos move, bend and stretch, so by measuring three different time

points for multiple *C. elegans* it was hoped to minimise variation due to this. No significant difference was seen in embryonic developmental timing (**Figure 5.15**).

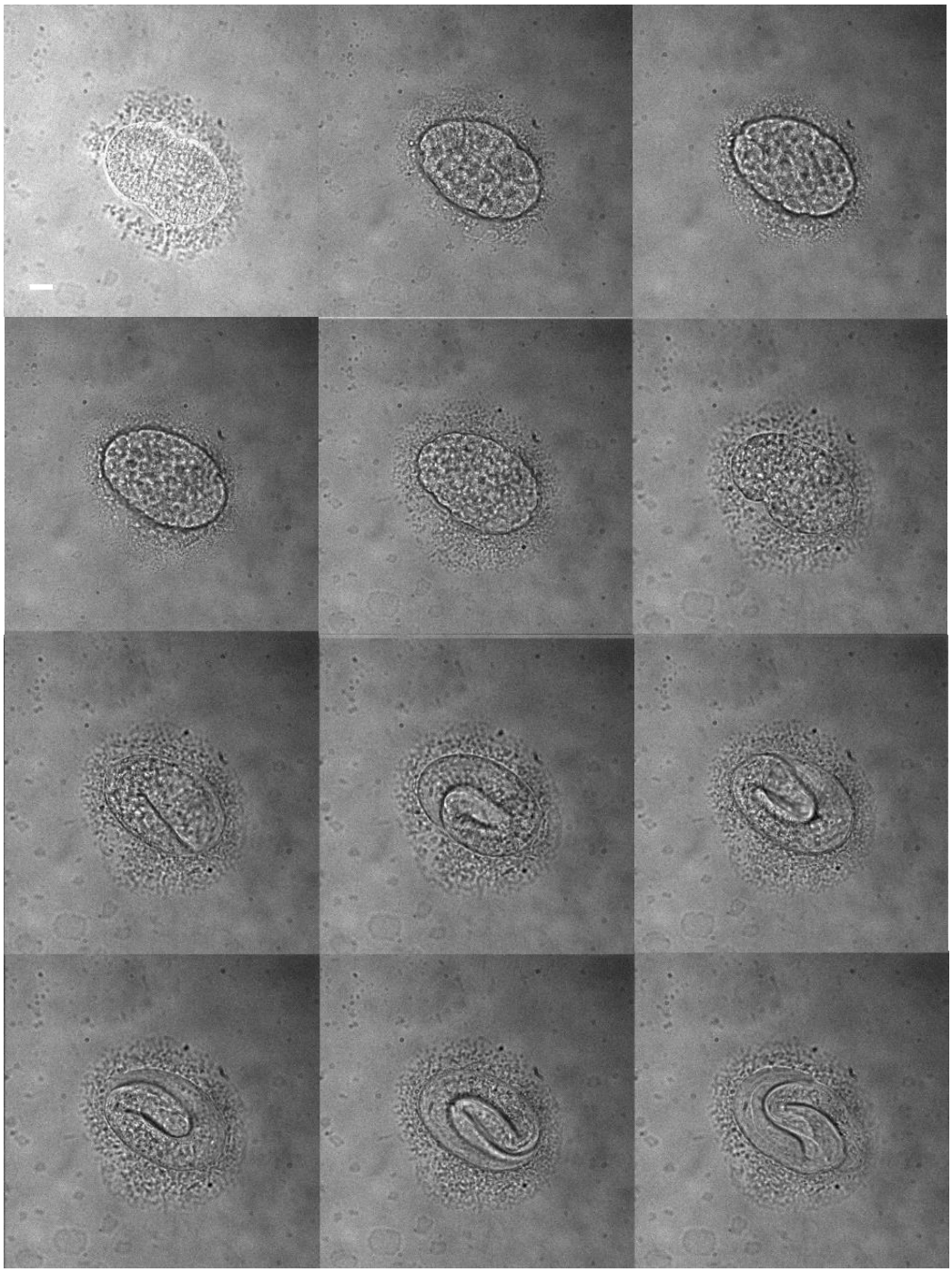


Figure 5.14. **Single frames from a time lapse film of an outcrossed *naa-80* knockout *C. elegans* embryo.** Bright field Images from every 80 minutes during development. Scale bars 10μm.

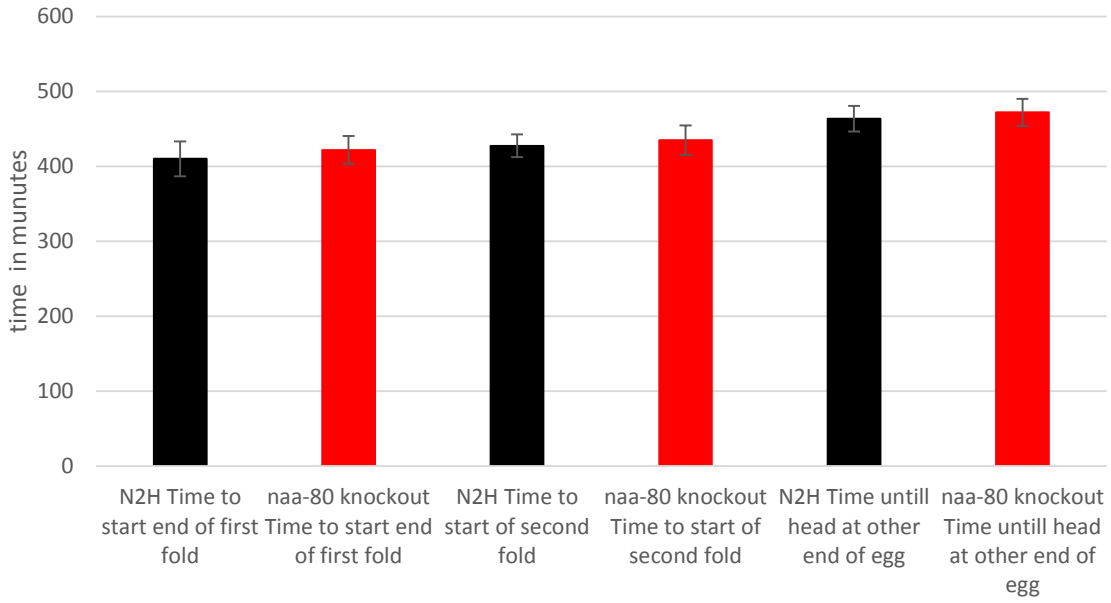


Figure 5.15. Average minutes until three different embryonic developmental stages are reached in N2H controls (n=12) and outcrossed *naa-80* knockout (n=11) *C. elegans*.

Time lapse images of *C. elegans* embryos producing LifeAct-mRFP both with and without having been outcrossed also showed no difference in developmental timings (**Film 3 and Figure 5.16)**. No difference in the development of filamentous actin within the embryos of these two strains could be seen either.

A timelapse film of *C. elegans* producing mCHERRY-ACT-1 showed that mCHERRY-ACT-1 fluorescence only started to be seen at a late point during embryo development, just before the embryo began to move within the egg (**Film 4 and Figure 5.17**). This meant that this strain was not useful for comparing early embryo development and it was not used for any further time lapse investigations.

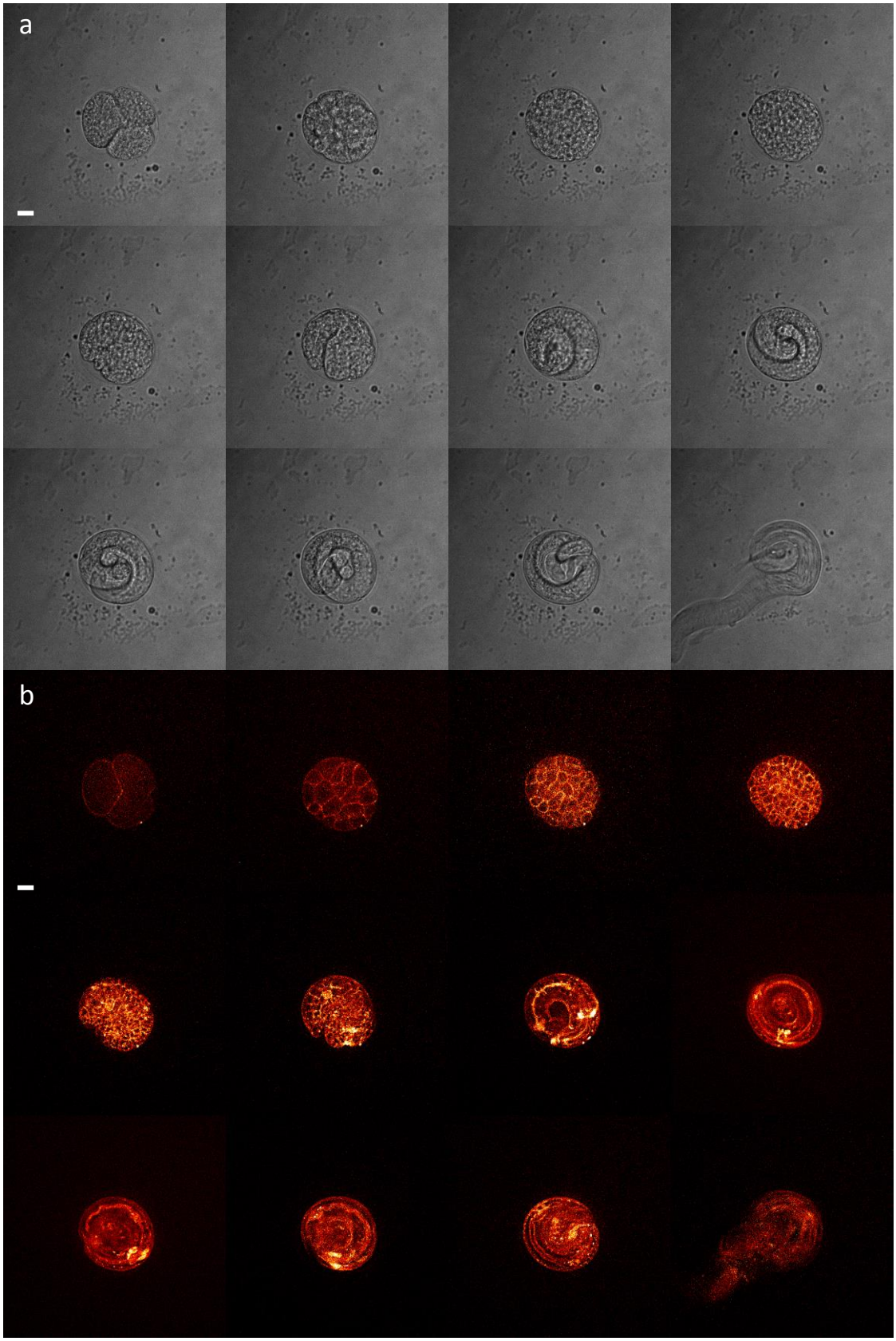


Figure 5.16. **Single frames from a time lapse film of a *C. elegans* embryo producing LifeAct-mRFP.** Images from every 80 minutes during development showing, Bright field images (a) and mRFP fluorescence images (b). Scale bars 10μm.

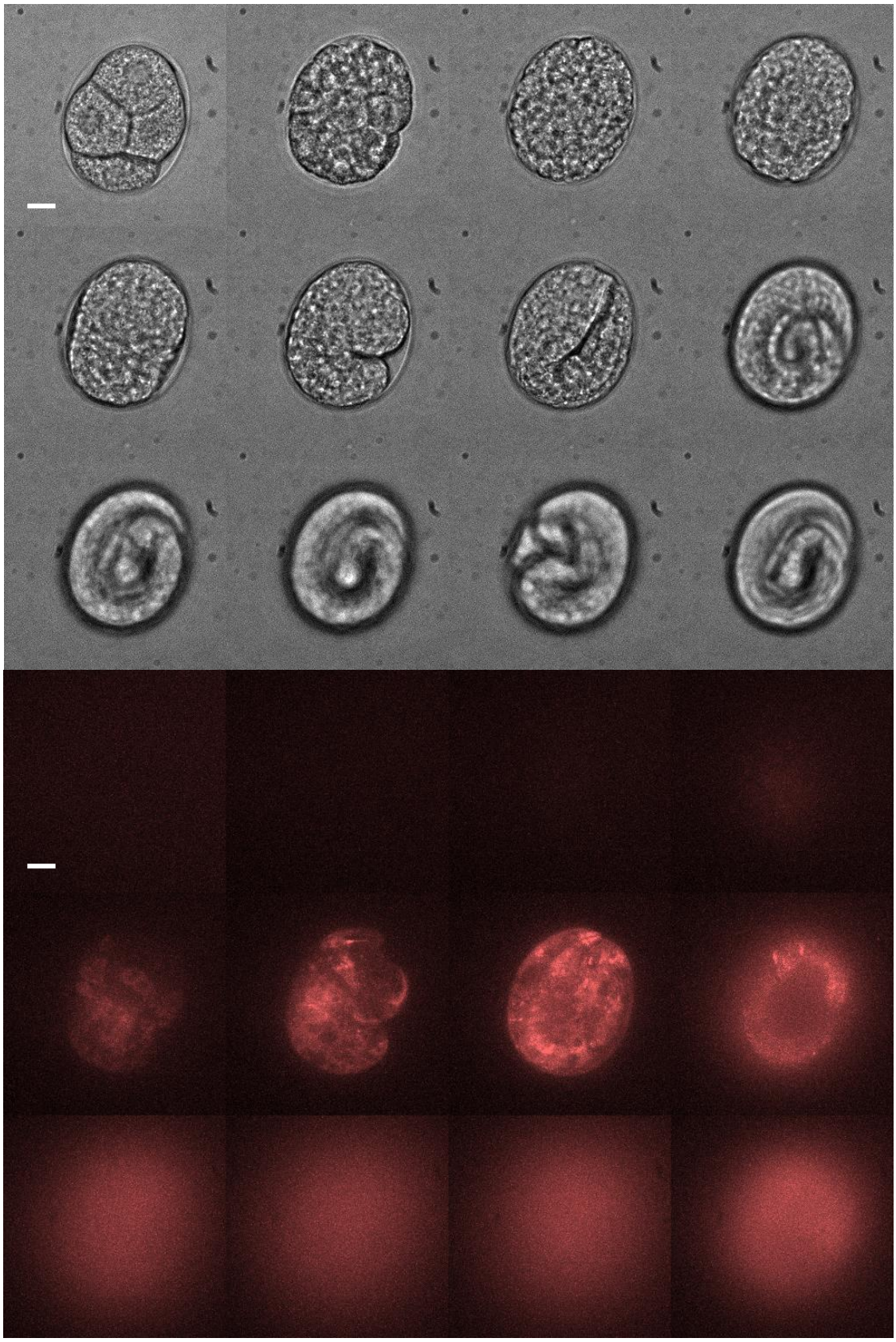


Figure 5.17. **Single frames from a time lapse film of a *C. elegans* embryo producing mCHERRY-ACT-1.** Images from every 80 minutes during development showing, Bright field images (a) and mCHERRY fluorescence images (b). Scale bars 10μm.

5.8 Rapid time lapse imaging to examine actin dynamics in early embryo development

Streaming, was used for rapid time lapse imaging, taking 10 frames per second to capture rapidly changing filamentous actin dynamics. *C. elegans* embryos were imaged producing LifeAct-mRFP both with and without having been crossed with the outcrossed *naa-80* knockout strain. Again no difference was seen in filamentous actin development or developmental timings (**Film 5**).

5.9 Comparison of images of *C. elegans* larvae and adult

Fluorescent images of *C. elegans* larvae and adults, producing LifeAct-mRFP both with and without having been crossed with the outcrossed *naa-80* knockout strain, were produced and compared. No differences beyond those due to positioning of the larvae or adults on the slides could be seen. Images of whole L2 larvae (**Figure 5.18**), adult heads (**Figure 5.19**) and central body sections of adults containing eggs with early stage developing embryos within them (**Figure 8.20**) are shown as examples.

Fluorescent images of *C. elegans* larvae and adults, producing mCHERRY-ACT-1 both with and without having been crossed with the outcrossed *naa-80* knockout strain, were produced and compared. No differences beyond those due to positioning of the larvae or adults on the slides was observed in images of L3 larvae (**Figure 5.21**). Close up images of L4/young adult heads (**Figure 5.22**) and of complete L4/young adults one producing HUM-1-GFP and mCHERRY-ACT-1 and one producing mCHERRY-ACT-1 crossed with the outcrossed *naa-80* knockout strain, (**Figure 5.24**) also show no differences beyond those due to positioning. Differences in the brightness of the spermatheca are believed to be partly due to differences in the brightness of the individual images, but mainly due to differences in the degree of stretch of the muscles forming them. The two strains could be differentiated due to the HUM-1-GFP structures seen in the head of the *Hum-1;gfp::hum-1;mCH::act-1 C. elegans. (***Figure 5.23**) HUM-1 is the *C. elegans* homolog of *H. sapiens* myosin 1E. It was used during this investigation to identify *C. elegans* producing mCHERRY-ACT-1 and wild type NAA-80 from *C. elegans* producing mCHERRY-ACT-1 without NAA-80.

Figures showing larger *C. elegans* have been stitched together using power point.

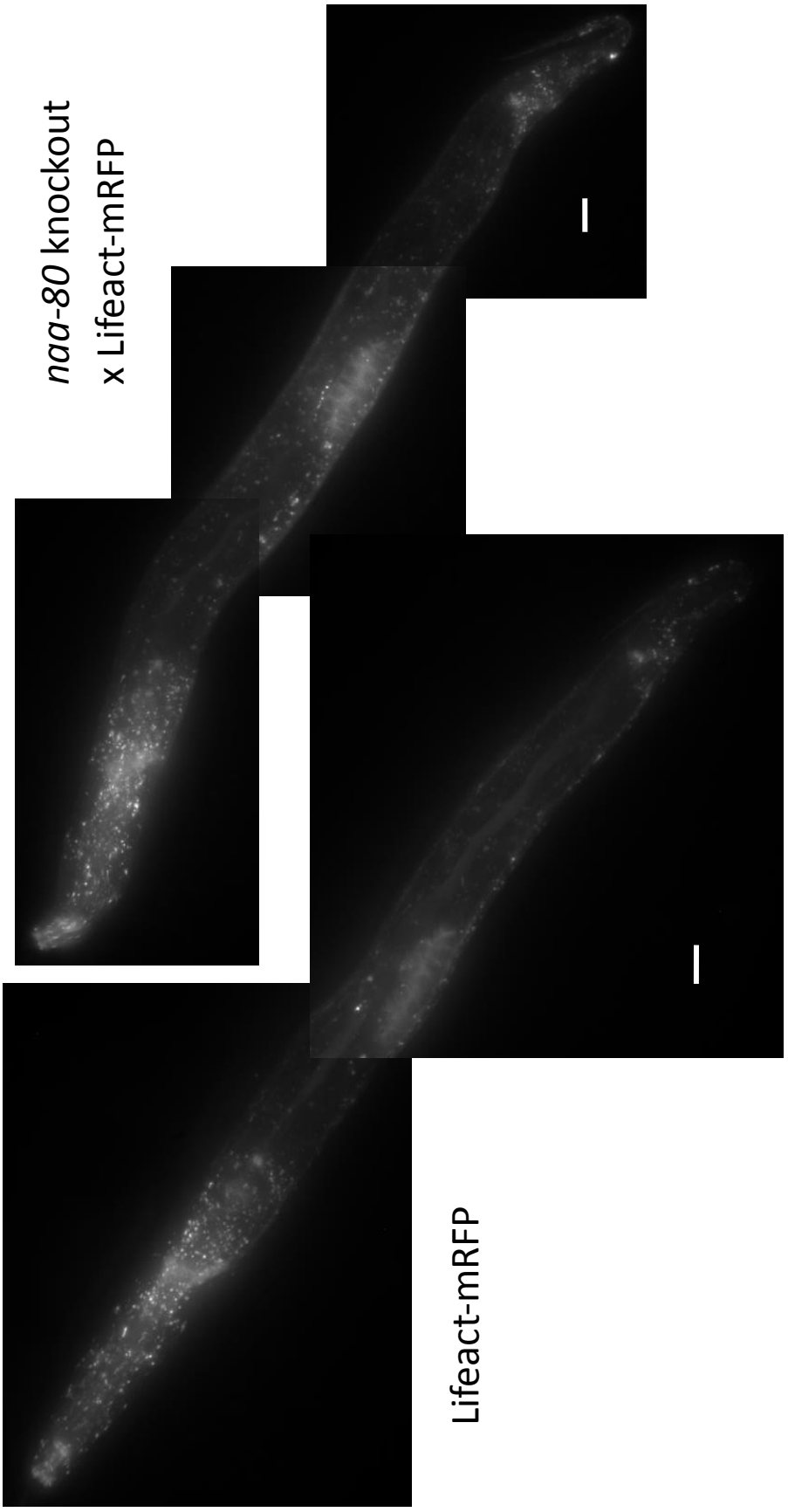


Figure 5.18. L2 larvae of LifeAct-mRFP *C. elegans* (left) and outcrossed *naa-80* knockout x LifeAct-mRFP *C. elegans* (right). Images show filamentous actin. No clear difference was observed between the images, only minor differences due to positioning.

Scale Bars 10μm

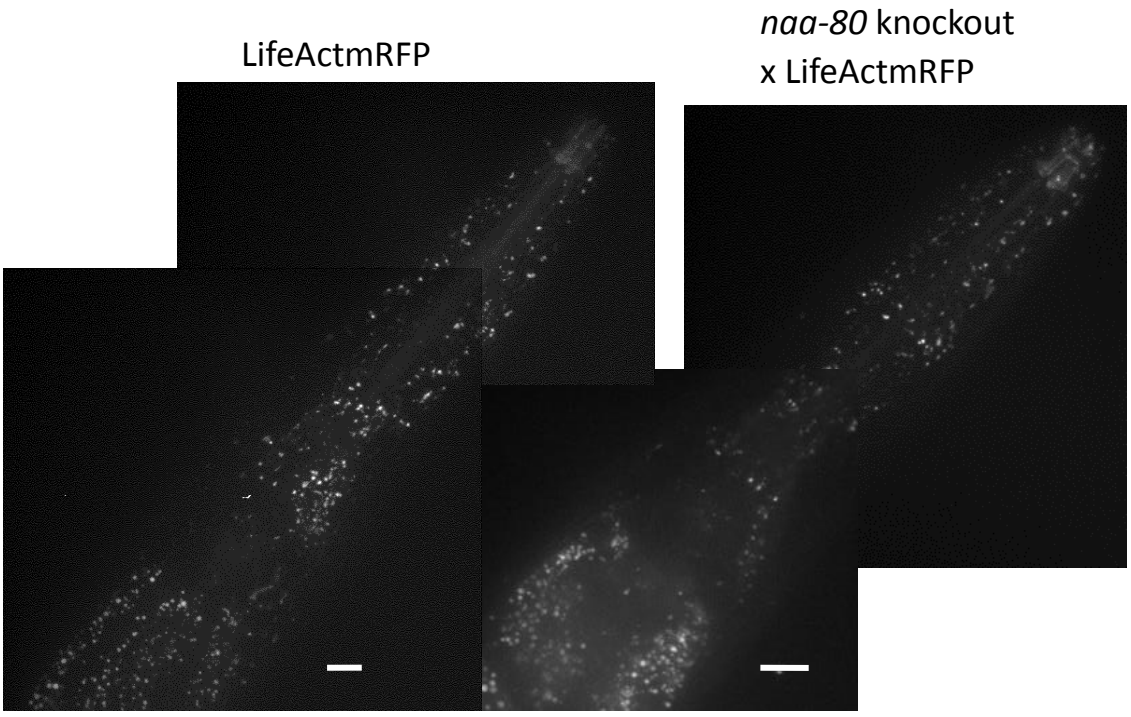


Figure 5.19. Heads of adult LifeAct-mRFP *C. elegans* (left) and outcrossed *naa-80* knockout x LifeAct-mRFP *C. elegans* (right). Images show filamentous actin. No clear difference was observed between the images, only minor differences due to positioning. Scale bars 10μm

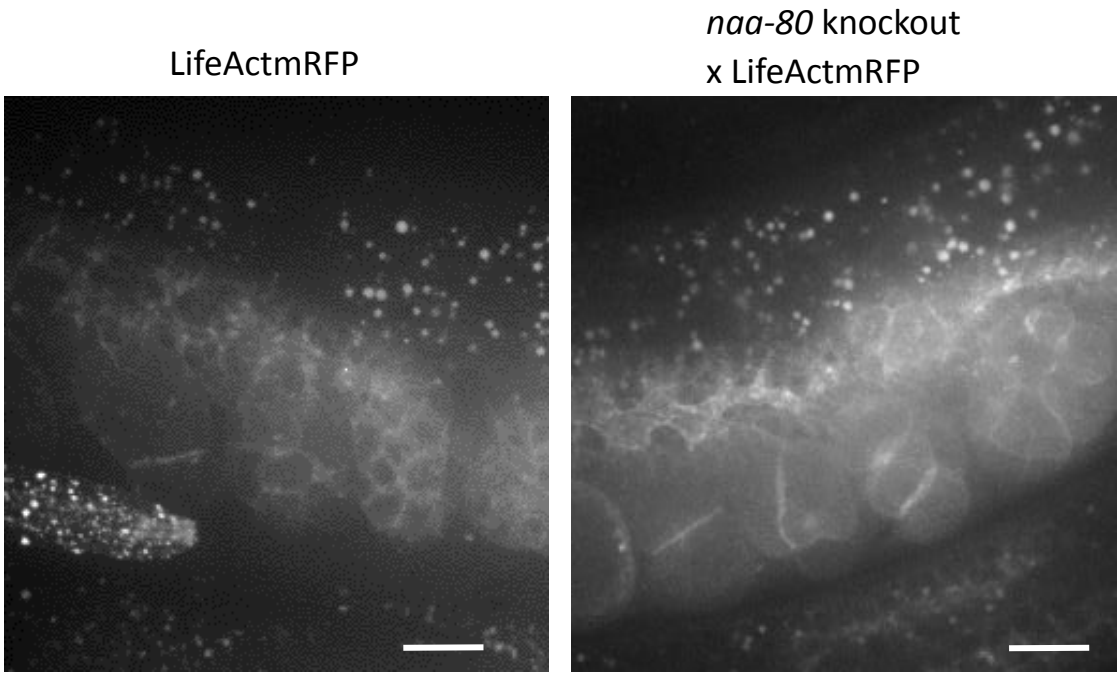


Figure 5.20. **Developing embryos inside adult of LifeAct-mRFP *C. elegans* (left) and outcrossed *naa-80* knockout x LifeAct-mRFP *C. elegans* (right).** Images show filamentous actin. No clear difference was observed between the images, only minor differences due to positioning. Scale Bars 10μm.



Figure 5.21. L3 larvae of mCherry-*Act*-1 *C. elegans* (left) and outcrossed *naa-80* knockout x mCherry-*Act*-1 *C. elegans* (right). Images show mCherry-ACT-1. No clear difference was observed between the images, only minor differences due to positioning. Scale Bars 10µm.

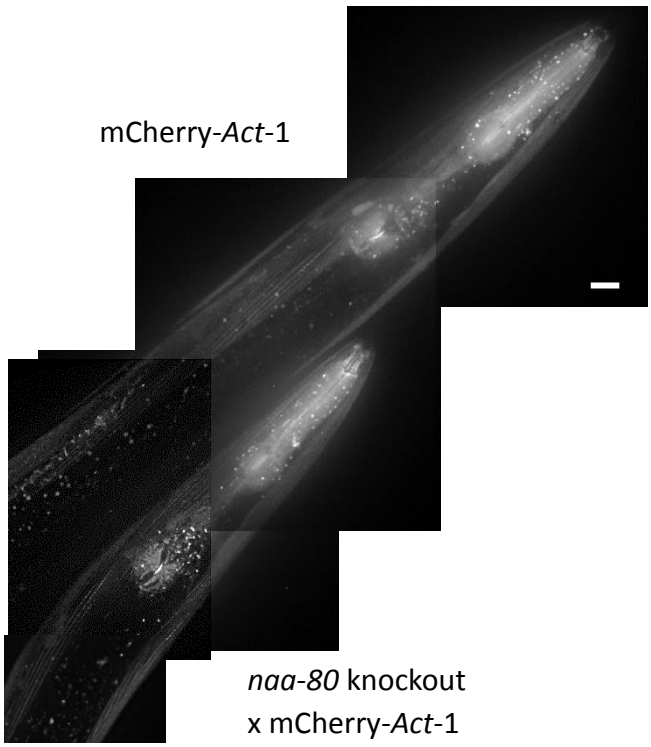


Figure 5.22. **Heads of L4/young adult mCherry-*Act*-1 *C. elegans* (top) and outcrossed *naa-80* knockout x mCherry-*Act*-1 *C. elegans* (bottom).** Images show mCherry-ACT-1. No clear difference is seen between the images, only minor differences due to positioning. Scale Bars 10μm.

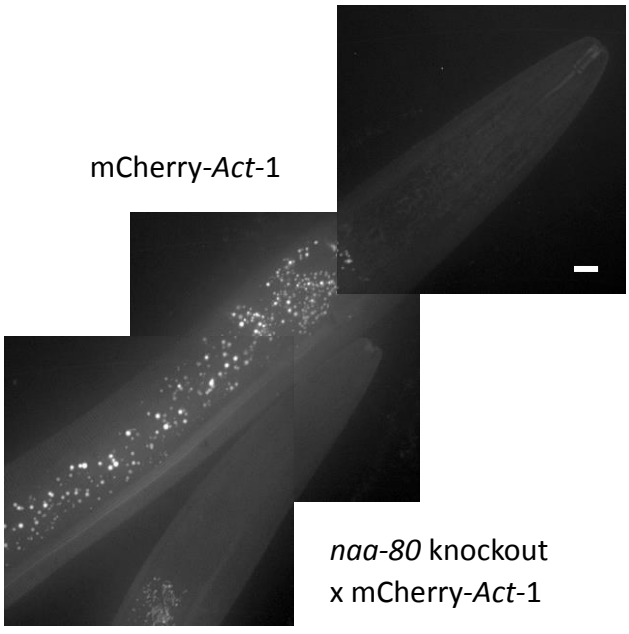


Figure 5.23. GFP image of L4/young adult mCherry-*Act*-1 *C. elegans* heads (top) and outcrossed *naa-80* knockout x mCherry-*Act*-1 *C. elegans* (bottom). Images show HUM-1-GFP structures in the head of the *Hum-1;gfp::hum-1;mCH::act-1 C. elegans,* enabling differentiation of the two strains. Scale Bar 10μm.

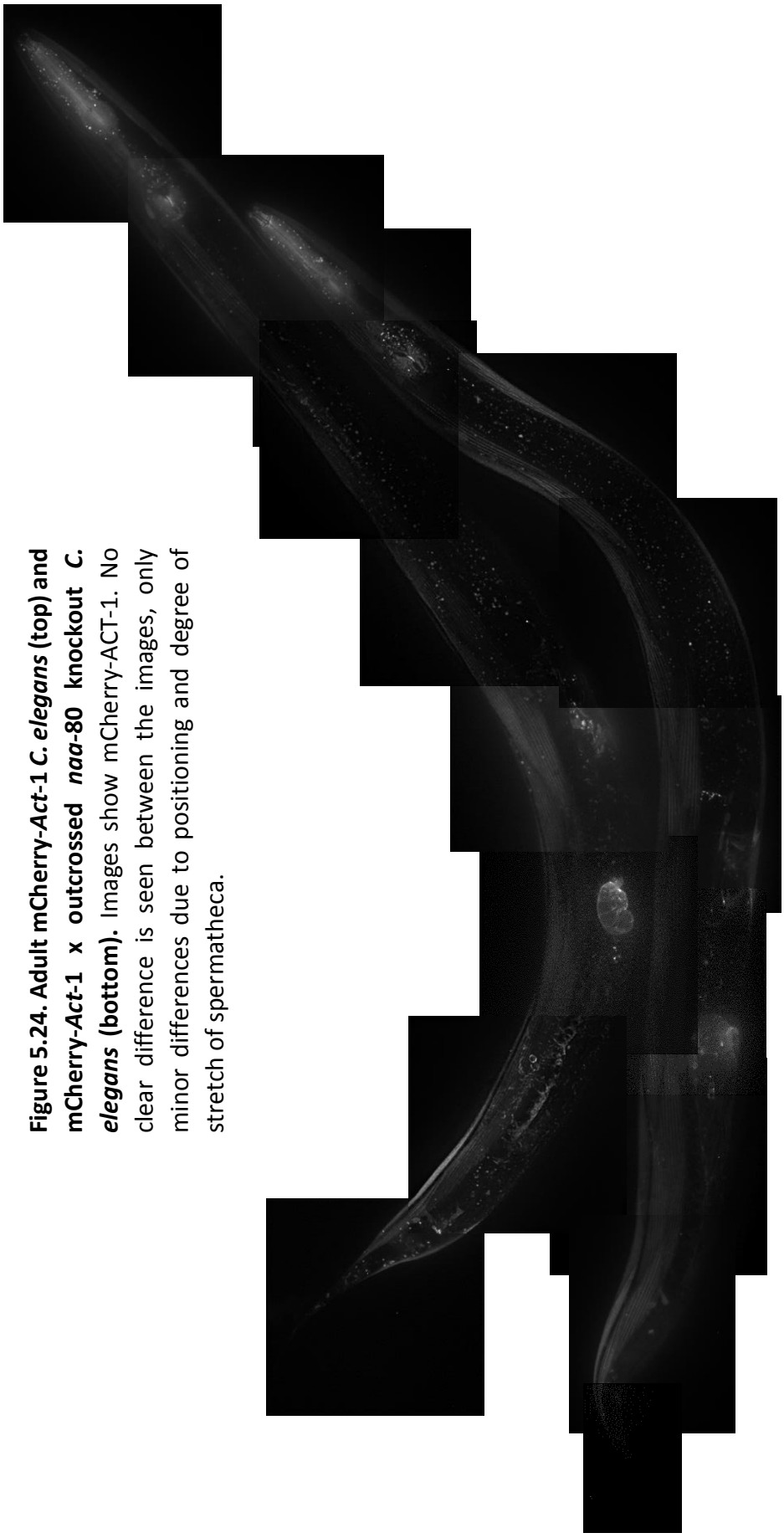


Figure 5.24. Adult mCherry-*Act*-1 *C. elegans* (top) and mCherry-*Act*-1 x outcrossed *naa*-80 knockout *C. elegans* (bottom). Images show mCherry-ACT-1. No clear difference is seen between the images, only minor differences due to positioning and degree of stretch of spermatheca.

5.10: Discussion

Despite early promising results it has so far not been possible to show a clear change in phenotype due to the knockout of *naa-80*.

This study has highlighted the need to create and use appropriate controls, as the difference in background genetics of the Knudra produced strains and the N2H control strains used, resulted in a difference in phenotype that was not due to the *naa-80* knockout.

Both the BU70LifeAct-mRFP and XW8490, strains producing LifeAct-mRFP and mCHERRY-ACT-1 that were crossed into were used as they were readily available strains, both though have limitations. LifeAct is known to affect actin filament dynamics (Courtemanche, Pollard and Chen, 2016) so should only be compared with and without the *naa-80* knockout and not with any other strains. The mCHERRY-ACT-1 having an N-terminal fluorophore cannot be Nt-acetylated. However as this is produced from an integrated transgene which does not affect the endogenous ACT-1, which will also be produced with or without NAA-80 Nt-acetylation. It should be noted that the N-terminal fluorescently tagged ACT-1 would not affect the Nt-acetylation of β or γ-actin.

Further work to discover a change in phenotype due to the knockout of *naa-80* could still be carried out, investigating other aspects of movement such as velocity, resting times, reversals, degree of body bend, exploratory behaviour and defecation frequency. Investigations could also be carried out into motoneuron development as β and γ actin have both been shown to have specific roles in motoneuron development (Moradi *et al.*, 2017)

Investigations could also be divided according to developmental stage.

Chapter 6: Discussion

6.1. The effect of naa-80 knockout in C. elegans

In the investigation into the effect of *naa-80* knockout in *C. elegans,* brood size and fecundity were investigated first, as fertility is a good indicator of organismal health. The use of developmental assays, comparing time taken by embryos to reach different developmental points, was also a good place to start to look for possible *naa-80* knockout phenotypes. Filamentous actin is important in cell division, the build-up of filamentous actin can be seen around cells and across the site of cell division in early embryos (Film 5.) within this investigation. The Nt-acetylation of actin has been found to have a significant effect on the turnover of filamentous actin. Cytoplasmic actin, a mixture of both β and γ isoforms, has elongation and depolymerisation rates approximately twofold faster for Nt-acetylated actin compared to Non Nt-acetylated actin. Non-Nt-acetylated actin filaments appear to be more stable, and cells containing Non Nt-acetylated actin also have a decrease in their ratio of monomeric to filamentous actin (Drazic *et al.*, 2018) (Aksnes *et al.*, 2018). It was thought that changes in the stability, turnover and ratio of monomeric to filamentous actin, might therefore have an impact on this early embryonic cell division. Early assays with *naa-80* knockout strains prior to outcrossing into the N2H control strain, also indicated that there may be a change in developmental timing during larvae growth, this was investigated by comparing larvae length.

Although NAA80 has only been formally demonstrated to Nt-acetylate class I, β and γ actin. NAA80 is predicted to Nt-acetylate all actins, including muscle actin. Images of *C. elegans* expressing mCHERRY-ACT-1, the single muscle actin isoform found in *C. elegans,* or LifeActmRFP, to visualise filamentous actin, both with and without *naa-80* knockout were therefore compared.

Unfortunately no change in phenotype associated with *naa-80* knockout in *C. elegans* could be found during this investigation. There are numerous other assays that could be used to investigate movement, including defecation assays and the use of computer software which can be used to examine many other aspect of movement including reversals, degree of body

bend, dwelling time, forwards velocity and which can be used to examine both adults and different larval stages.

α, β, and γ actin have roles in axon growth and collateral branch formation in motoneurones (Moradi *et al.*, 2017). HAP1 NAA80 knockout cells also show a fourfold increase in the numbers of filopodia seen and formed twice as many lamellipodia compared to controls. HAP1 NAA80 knockout cells also show increased motility with at least a doubling in speed for random cellular movement (Drazic *et al.*, 2018) (Aksnes *et al.*, 2018). With this in mind, sensory assays such as touch, chemotaxis and food sensing, may be good areas for further investigations into *naa-80* knockout phenotype.

One thing that was shown very clearly in this investigation, was the need for genetic background controls. Within this study *naa-80* knockout *C. elegans* were back crossed into N2H controls 6 times to produce a strain with >98% genetic identity, with the N2H control *C. elegans* used. This is a very time consuming, but essential process, as was shown in this investigation. Erroneous results were obtained from early assays with *naa-80* knockout *C. elegans*, as received from Knudra, due to background genetic variation.

In actin filaments, the actin N-termini are exposed and thus Nt-acetylation status may effect interactions with many actin binding proteins, such as myosin (Arnesen, Marmorstein and Dominguez, 2018) (Mentes *et al.*, 2018) (**Figure 1.7**). Changes in proteins binding to actin could also have an effect on many individual cellular processes.

6.2 Contradictory aS research

Papers publishing research into aS, in particular into protein structure, oligomerisation and membrane interactions are contradictory. Many of these differences may be in part explained by differences in the techniques and materials used. Much of the *in vitro* work carried out previously, has used recombinant protein produced in *E. coli*, which was not Nt-acetylated (Burré, Sharma and Südhof, 2014), some was produced in eukaryotic cells or as recombinant protein in *E. coli* with co-expression of NatB and was thus Nt-acetylated (Bartels *et al.*, 2014). Investigations into membrane binding *in vitro* have also used different sizes of synthetic vesicles, 40-120 nm (Dikiy and Eliezer, 2014) with different lipids (Bartels *et al.*, 2014)(Pirc and

Ulrih, 2015)(Varkey *et al.*, 2010) or rat synaptic vesicles (Fusco *et al.*, 2016), the differing compositions of which may contribute to difference seen in aS binding and or conformation. Differences in concentrations of IPTG added to cultures to produce recombinant aS also vary widely, from 0.05mM (Burré, Sharma and Südhof, 2014) to the most commonly used 1mM (Barinova *et al.*, 2017) often using IPTG concentrations, which could result in aS being produced at a rate which may have a toxic effect on *E. coli* and could impact on overall protein production. A 1mM IPTG induction has been shown to result in a high level of Tyr136Cys substitution, resulting in increased dimerization and reduced amyloid formation (Barinova *et al.*, 2017).

6.3: BiFC development

BiFC was found to be a very useful technique during this investigation and has the potential to be used in investigations into other protein-protein investigations, such as into Cdc8 polymer formation. It is particularly useful for measuring reactions in real time as readings are taken every 15 minutes. However this is a very sensitive assay where induction rate and starting OD_{595} may need to be optimised for each investigation. Variations due to plate position are also likely to differ between incubating fluorescent plate readers and therefore variations due to plate position and correction factors will should be investigated for each machine used.

6.4: aS Oligomerisation

In the investigation into aS oligomerisation, clear and consistent differences were seen between Nt-acetylated and Non Nt-acetylated aS. The size exclusion assays using purified protein showed that two different forms of aS were present in both protein samples. Nt-acetylated aS was present, predominantly in a larger state, where the protein forms either a larger conformation or oligomeric state, whereas Non Nt-acetylated aS was predominantly present in a smaller state, which may be due to most of the protein being in a smaller conformation or monomeric form. It was not possible to say from this whether the larger form was due to a conformational change or oligomerisation.

The investigations examining FRET, both in house and using FLIM to investigate FRET, show that with both forms of the protein FRET was occurring in vivo. This shows that the two fluorophores are being brought into close contact, within 10nm of each other. The average FLIM values for actively growing cultures did not differ much between Nt-acetylated and non Nt-acetylated aS producing cultures. A change was seen however in aS producing cultures which were held in stationary phase. By grouping FLIM values for individual cells into 100 ps bands it became clear that the cells producing Nt-acetylated aS formed two separate groups, one of which had an increase in fluorescent lifetime and thus a reduction in FRET. Cells producing non Nt-acetylated aS which were held in stationary phase, only produced one population, in which FRET was occurring.

The BiFC assay which was used to examine oligomerisation *in vivo,* also indicated that a different form of oligomerisation was occurring with the two different forms of aS. Similar levels of aS-Venus BiFC protein, produced approximately double the level of fluorescence then aS was not Nt-acetylated compared to when aS was Nt-acetylated. One possible explanation for this is that aS oligomers have a different conformation according to their Nt-acetylation status, with aS oligomers more often forming in an anti-parallel fashion when Nt-acetylated and thus holding the two halves of the Venus fluorophore apart and reducing the level of fluorescence.

A third method used to investigate differences in *in vivo* oligomerisation was the use of Fluorescent amyloid staining dyes. Live cells producing Nt-acetylated or non Nt-acetylated aS were incubated with Congo red dye. Imaging using fluorescent microscopy showed the development of red fluorescence, indicating the presence of amyloid in cells producing Nt-acetylated aS. This red fluorescence developed predominantly in areas of cells with dynamic membranes. Red fluorescence was rarely seen in cells producing non Nt-acetylated aS, which also suggests the presence of a different aS oligomeric state, which is resistant to amyloid formation. The development of Congo red, red fluorescence was seen to be consistent in cells producing four different forms of fluorescently tagged Nt-acetylated aS.

Although FRET, FLIM and BiFC assays indicate the presence of aS oligomerisation *in vivo* with both forms of aS, evidence of this is not often seen with non Nt-acetylated aS on Coomassie stained SDS-PAGE gels and western blots, bands of sizes expected for oligomeric non Nt-acetylated aS were only seen consistently in extracts from cultures held in stationary phase

for days. The size exclusion assay also showed purified non Nt-acetylated aS to be in a smaller form compared to Nt-acetylated aS. In contrast western blots of extracts from cells producing Nt-acetylated aS, especially those which have been producing Nt-acetylated aS for over 5 hours, showed aS at higher molecular weights indicating the presence of oligomeric species. One possible explanation for this is that Nt-acetylated aS forms a more stable oligomeric structure and that non Nt-acetylated aS forms a different, less stable oligomeric structure, which is broken down during protein purification and or preparation for Coomassie stained SDS-PAGE gels and western blots. This also indicated that changes in Nt-acetylated aS oligomerisation occur as cells become stressed, in stationary phase. Several Tyrosine kinase inhibitor drugs were seen to reduce BiFC fluorescence of the aS-Venus BiFC construct, indicating an effect on aS oligomerisation. ITC results for one of the drugs investigated, Gefitinib also confirmed an interaction with aS. This shows that several drugs may directly interact with aS and effect aS oligomerisation and behaviour *in vivo*.

6.5: aS Membrane interactions

Both Nt-acetylated and non Nt-acetylated aS are seen to localise at membranes, this is seen both with fluorescent microscopy and with immuno EM. However investigations into membrane interactions, show clear differences between how each form of aS effects membranes.

Widefield fluorescent microscopy images, show *E. coli* cells producing Nt-acetylated aS, predominantly develop areas of concentrated aS within the cell. Fluorescent SIM images of cells co expressing aS-mNeonGreen and mScarlet-MinD or aS-Cerulean3 and Citrine-MinD show internal structures which appear to be formed from the inner membrane. TEM images of *E. coli* producing aS-Cerulean3 also support this theory, as what appear to be membranous structures can be seen to originate at the plasma membrane and to form in the same areas as aS was shown to be present by immuno EM.

Cells producing non Nt-acetylated aS are also seen to develop areas of localisation, but to a far lesser extent. Cell producing non Nt-acetylated aS are however seen to produce large numbers of small outer membrane vesicles, as well as a number of large extracellular vesicles,

often in excess of 1μm, these have been seen up to approximately 5μm in diameter. These vesicles are commonly seen to contain fluorescently tagged aS and can also contain cytoplasmic protein, though this is not always seen. These aS induced vesicles differ from naturally occurring vesicles in several ways. Firstly in size, aS induced vesicles often exceed 1μm in diameter whereas naturally occurring vesicles are normally 20-400nm (Toyofuku, Nomura and Eberl, 2019). Secondly aS induced vesicles will often contain fluorescently tagged aS and can also contain cytoplasmic proteins, naturally occurring outer membrane vesicles do not normally contain cytoplasmic proteins. Thirdly naturally occurring Outer-inner membrane vesicles and Explosive outer membrane vesicles, which can contain cytoplasm, are produced by explosive lysis. Many cells producing aS induced vesicles commonly appear undamaged and able to continue growing as seen in widefield fluorescent microscopy of live cells, including time lapse images (**Figure 4.14**) (**Film. 1**).

The timing of vesicle production was found to vary with the rate of aS induction and to a lesser extent with the construct being used. Induction with 100μg/ml IPTG would typically result in the formation of vesicles from approximately 3 hours post induction, whereas induction with 20μg/ml IPTG would typically result in vesicle formation from 5 hours post induction. Imaging of cells producing aS induced vesicles was predominantly carried out with an induction of 100μg/ml to allow for imaging to be completed the same day, due to a more rapid vesicle formation.

A potential use of aS induced vesicles, for the improvement of therapeutic protein production, was identified and investigated in collaboration with Fujifilm-Diosynth. Despite early problems with toxicity, which highlighted the need for tight control of expression, it was shown to be possible to scale up production to produce aS-mNeonGreen-FLAG-hGH within their Ambr250 bioreactors and that this protein was exported to vesicles and or media.

As cytoplasmic proteins are only seen in approximately 50% of aS induced vesicles a preliminary investigation was carried out into the possible use of optogenetics to target therapeutics to vesicles. On exposure to 650nm red light PhyB-mCherry was seen to co-localise with aS-mNeonGreen-Pif6 but these investigations were not continued with, due to time constraints. For the remainder of this investigation the attachment of the therapeutic protein, hGH to aS-mNeonGreen via FLAG was found to be sufficient for targeting into aS induced vesicles.

As well as potentially increasing the yields of therapeutic protein produced per fermenter run, due to harvesting protein from media rather that by harvesting biomass, there are potential benefits to harvesting protein packaged within vesicles. The harvesting of therapeutic protein within a vesicle could improve the storage and delivery of these proteins, due to their being stored within a cytosolic environment. It is possible to purify intact vesicles, as shown by fluorescent microscopy and DLS. It has also been shown that it is possible to express the proteins for the formation of bacterial microcompartments tagged with aS-mCherry, this resulted in larger possibly more stable vesicles being imaged by TEM.

The vesicles induced by the production of non Nt-acetylated aS were predominantly seen to form at dynamic membranes, at the poles and what appeared to be sites of cell division, this was reminiscent of the Congo Red amyloid staining seen in cells producing Nt-acetylated aS, which was also seen predominantly at cell poles. This raised the question of why interactions were seen to occur at specific locations. It was decided to investigate whether Nt-acetylated and non Nt-acetylated aS had different binding affinities for different single lipids. Assays with single lipid vesicles and specific lipids on PIP strips™ were carried out and these indicated different lipid binding affinities. When non Nt-acetylated aS was added to DSPG vesicles this resulted in an increase in vesicle size, reminiscent of the vesicle assembly seen in Fusco *et al.*, (2016) (**Figure. 6.1**) when non Nt-acetylated aS was added to small unilamellar vesicles.

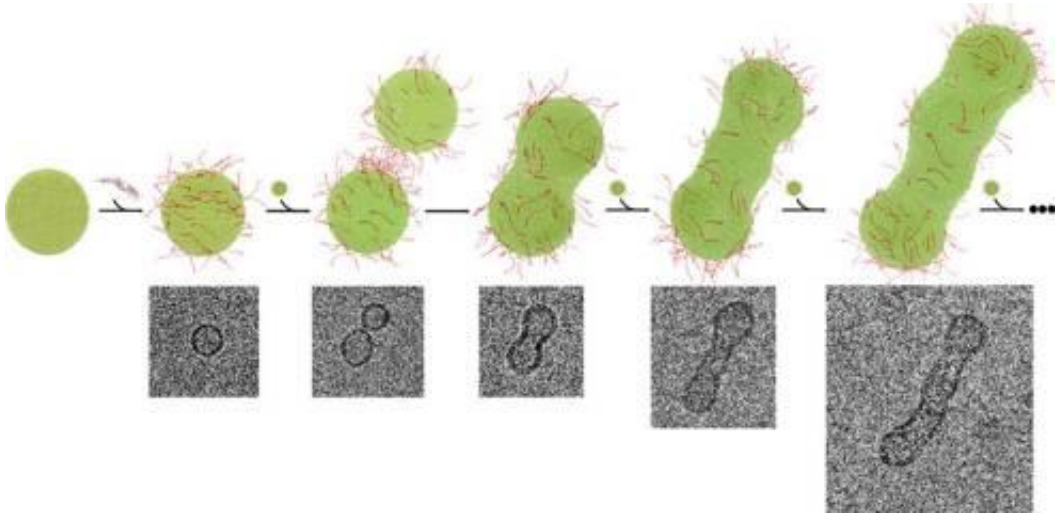


Figure. 6.1. A proposed scheme for the stepwise mechanism of vesicles assembly. From Fusco et al., 2016

FLIM results indicated that aS does not interact directly with the outer membrane, but that it does interact directly with MinD, an inner membrane binding protein. A decrease in FLIM was seen within the cytoplasm of cells producing aS-Cerulean3 and Citrine MinD. A further decrease in FLIM was also indicated at the cell membrane, however low confidence can be given to this result due to the low intensity readings at the very edge of cells. Binning of pixels which would improve intensities, resulted in an unacceptable loss of resolution when analysing the images obtained. It may be possible to obtain statistically significant results by imaging cells with a higher magnification to allow binning without such a large loss of resolution or a higher level of induction may be used to try to increase fluorescent intensities. The use of the slow maturing fluorophore, mScarlet, in membrane interaction investigations, was found not to be a good choice. Red fluorescence could not be seen in all cells and where it was seen, no membrane localisation could be seen, suggesting that steric hindrance may have been occurring.

6.6: Summary of aS findings

Finding	**Evidence**
Both Nt-acetylated and non Nt-acetylated aS form oligomers.	FRET, FLIM, SDS Page gel, WB, BiFC
Nt-acetylated and non Nt-acetylated aS form oligomers with different conformations.	BiFC, SEC.
Nt-acetylated aS dimers and oligomers are more stable than non Nt-acetylated aS dimers and oligomers.	SEC, SDS-PAGE gel, WB
3 Tyrosine Kinase inhibitors were found to effect dimer conformation with Nt-acetylated aS.	BiFC
Gefitinib a Tyrosine kinase inhibitor interacts with aS	ITC
Changes occur in oligomeric structure in older stationary cells producing Nt-acetylated aS but not in cells producing non Nt-acetylated aS.	FLIM
Areas of aS localisation are commonly seen in *E. coli* cells producing Nt-acetylated aS, these are only occasionally seen in *E. coli* cells producing non Nt-acetylated aS.	Fluorescent microscopy

E. coli producing Nt-acetylated aS form internal structures with a tubular appearance which are rarely seen in cells producing non Nt-acetylated aS.	TEM
E. coli producing Nt-acetylated aS show red fluorescence predominantly at their poles, when stained with Congo red indicating the presence of amyloid , this staining is rarely seen in cells producing non Nt-acetylated aS.	Congo red staining
Both Nt-acetylated and non Nt-acetylate aS localise at *E. coli* membranes	Fluorescent microscopy, Immuno EM
Non Nt-acetylated aS production in *E. coli* induces formation of large, membrane bound, extracellular vesicles, which can contain cytoplasm. These vesicles are only rarely seen with cells producing Nt-acetylated aS.	Fluorescent microscopy, TEM, DLS
aS induced vesicles can form rapidly, over approximately 7 minutes	Time lapse Film.1
aS induced extracellular vesicles can be purified from media.	Fluorescent microscopy, DLS
aS-mNeonGreen-FLAG-hGH can be exported into vesicles and or media when produced in large scale fermenters.	WB
Purified Nt-acetylated and non Nt-acetylated aS, have different binding affinities for Phosphatidic acid.	Pip strips
Non Nt-acetylated aS causes DSPG vesicles to increase in size, whereas Nt-acetylated aS does not.	DLS with single lipid vesicles
Toxic effects of both forms of aS, on *E. coli* are effected by induction rates.	Fluorescence and OD_{595} growth curves

Table. 6.1. **Summary of aS findings.**

6.7: Future work

The investigation into the effect of *naa-80* knockout in C. elegans was unable to identify a knockout specific phenotype. Only a limited number of investigations could be carried out during the time available, leaving many different assays which could be carried out in future investigations. Future investigations could include more detailed movement assays and sensory assays, in the search for a *naa-80* knockout specific phenotype.

Further investigations into aS oligomerisation could focus on the effect of cell stress, on oligomerisation. The changes in FLIM in stationary cells producing Nt-acetylated aS and the higher molecular weight proteins seen more often in extracts from cells producing Nt-acetylated aS, which have entered stationary phase, indicate that cell stress may influence Nt-acetylated aS oligomerisation. The effect of stress caused by rate of induction, holding cells in stationary phase as opposed to repeatedly sub-culturing and environmental stress could be investigated.

The main area for further investigation is the use of aS induced vesicles for the enhancement of therapeutic protein production. Investigations could look at optimising induction rates and how induction rates effect vesicle size and stability. Slightly smaller but more stable vesicles could be more desirable if they are easier to purify. The timing of vesicle production could also be examined with regard to slower induction and vesicle production and loss of antibiotic selection. The use of different selection antibiotics, may also have an influence on vesicle production due to their differing modes of action. The reason for the predominant localisation of vesicle production at dynamic membranes also requires further investigation, If interactions with specific lipids localised to these areas of membranes are promoting vesicle production, the use of different strains which have higher levels of these specific lipids in their membranes may be beneficial.

One area which will be the subject of future investigation in tandem with optimisation of aS induced vesicle production, is the scaling up of these processes for therapeutic protein production in large scale industrial fermenters. This is to be carried out with Fujifilm-Diosynth. Further into the future, the production of other therapeutic proteins, the use of other methods for targeting proteins into vesicles, purification methods and the use of a FLAG tag and sequential production of more than one protein construct could be investigated.

Bibliography

Henriette Aksnes, Petra Van Damme, Kris Gevaert, Thomas Arnesen (2015) 'An Organellar Nα-Acetyltransferase, Naa60, Acetylates Cytosolic N Termini of Transmembrane Proteins and Maintains Golgi Integrity', *CellReports*, 10, pp. 1362–1374. doi: 10.1016/j.celrep.2015.01.053.

Henriette Aksnes, Marianne Goris, Øyvind Strømland, Adrian Drazic, Qaiser Waheed, Nathalie Reuter, and Thomas Arnesen, (2017) 'Molecular determinants of the N-Terminal acetyltransferase Naa60 anchoring to the Golgi membrane', *Journal of Biological Chemistry*, 292, pp. 6821–6837. doi: 10.1074/jbc.M116.770362.

Henriette Aksnes, Michael Mariea, Thomas Arnesen, and Adrian Drazic (2018) 'Actin polymerization and cell motility are affected by NAA80-mediated posttranslational N-terminal acetylation of actin', *Communicative and Integrative Biology*. doi: 10.1080/19420889.2018.1526572.

Thomas Arnesena,, Petra Van Dammed, Bogdan Polevodaf, Kenny Helsensd, Rune Evjentha, Niklaas Colaertd, Jan Erik Varhaugb, Joe¨ l Vandekerckhoved, Johan R. Lillehauga, Fred Shermanf, and Kris Gevaertd (2009) 'Proteomics analyses reveal the evolutionary conservation and divergence of N-terminal acetyltransferases from yeast and humans', *Proceedings of the National Academy of Sciences*, 106, pp. 8157–8162. doi: 10.1073/pnas.0901931106.

Thomas Arnesen, Kristian K. Starheim, Petra Van Damme, Rune Evjenth, Huyen Dinh, Matthew J. Betts, Anita Ryningen, Joe¨l Vandekerckhove, Kris Gevaert, and Dave Anderson (2010) 'The Chaperone-Like Protein HYPK Acts Together with NatA in Cotranslational N-Terminal Acetylation and Prevention of Huntingtin Aggregation', M*olecular and Cellular Biology*, 30, pp. 1898–1909. doi: 10.1128/MCB.01199-09.

Arnesen, T., Marmorstein, R. and Dominguez, R. (2018) 'Actin's N-terminal acetyltransferase uncovered', *Cytoskeleton*, (April), pp. 1–5. doi: 10.1002/cm.21455.

Audagnotto, M. and Dal Peraro, M. (2017) 'Protein post-translational modifications: In silico prediction tools and molecular modeling', *Computational and Structural Biotechnology Journal*, pp. 307–319. doi: 10.1016/j.csbj.2017.03.004.

Bryce T. Bajar, Emily S. Wang, Shu Zhang, Michael Z. Lin and Jun Chu, (2016) 'A Guide to Fluorescent Protein FRET Pairs', *Sensors*. doi: 10.3390/s16091488.

Baltic S, Perovic M, Mladenovic A, Raicevic N, Ruzdijic S, Rakic L, Kanazir S. (2004) 'a-Synuclein is expressed in different tissues during human fetal development', Journal of Molecular Neuroscience, 22, pp. 199–203.l (2004) 'a-Synuclein is expressed in different tissues during human fetal development', *Journal of Molecular Neuroscience*, 22, pp. 199–203.

Barinova KV, Kuravsky ML, Arutyunyan AM, Serebryakova MV, Schmalhausen EV, Muronetz VI (2017) 'Dimerization of Tyr136Cys alpha-synuclein prevents amyloid transformation of

wild type alpha-synuclein', *International Journal of Biological Macromolecules*. Elsevier B.V., 96, pp. 35–43. doi: 10.1016/j.ijbiomac.2016.12.011.

Barnum, K. J. and O'Connell, M. J. (2014) 'Cell cycle regulation by checkpoints', *Methods in Molecular Biology*, 1170, pp. 29–40. doi: 10.1007/978-1-4939-0888-2_2.

Bartels T, Kim NC, Luth ES, Selkoe DJ. (2014) 'N-Alpha-Acetylation of a-Synuclein Increases Its Helical Folding Propensity, GM1 Binding Specificity and Resistance to Aggregation', *PLoS ONE*, 9(7), p. 103727. doi: 10.1371/journal.pone.0103727.

Bartels, T., Choi, J. G. and Selkoe, D. J. (2011) 'α-Synuclein occurs physiologically as a helically folded tetramer that resists aggregation', *Nature*, 477(7362), pp. 107–111. doi: 10.1038/nature10324.

Bengoa-Vergniory N, Roberts RF, Wade-Martins R, Alegre-Abarrategui J (2017) 'Alpha-synuclein oligomers: a new hope', *Acta Neuropathologica*, 134, pp. 819–838. doi: 10.1007/s00401-017-1755-1.

Bindels DS, Haarbosch L, van Weeren L, Postma M, Wiese KE, Mastop M, Aumonier S, Gotthard G, Royant A, Hink MA, Gadella TW Jr. (2016) 'MScarlet: A bright monomeric red fluorescent protein for cellular imaging', *Nature Methods*. Nature Publishing Group, 14, pp. 53–56. doi: 10.1038/nmeth.4074.

Bootman MD, Collins TJ, Peppiatt CM, Prothero LS, MacKenzie L, De Smet P, Travers M, Tovey SC, Seo JT, Berridge MJ, Ciccolini F, Lipp P. (2001) 'Calcium signalling---an overview', *Cell & Developmental Biology*, 12, pp. 3–10. doi: 10.1006/scdb.2000.0211.

Brandenburg, E., Berlepsch, H. V. and Koksch, B. (2012) 'Specific in situ discrimination of amyloid fibrils versus a-helical fibres by the fluorophore NIAD-4', *Molecular BioSystems*, 8, pp. 557–564. doi: 10.1039/c1mb05370a.

Brooker, H. R., Geeves, M. A. and Mulvihill, D. P. (2016) 'Analysis of biophysical and functional consequences of tropomyosin-fluorescent protein fusions', *FEBS Letters*. doi: 10.1002/1873-3468.12346.

Burré, J., Sharma, M. and Südhof, T. C. (2014) 'α-Synuclein assembles into higher-order multimers upon membrane binding to promote SNARE complex formation', *Proceedings of the National Academy of Sciences*, 111, pp. E4274–E4283. doi: 10.1073/pnas.1416598111.

Campbell RE, Tour O, Palmer AE, Steinbach PA, Baird GS, Zacharias DA, Tsien RY. (2002) 'A monomeric red fluorescent protein', *PNAS*, pp. 2877–7882. doi: 10.1073/pnas.082243699.

Clement, C. G. and Truong, L. D. (2014) 'An evaluation of Congo red fluorescence for the diagnosis of amyloidosis', *Human Pathology*, 45, pp. 1766–1772. doi: 10.1016/j.humpath.2014.04.016.

Cocucci, E. and Meldolesi, J. (2015) 'Ectosomes and exosomes: shedding the confusion between extracellular vesicles', *Trends in Cell Biology*, 25, pp. 364–372. doi: 10.1016/j.tcb.2015.01.004.

Coulton AT, East DA, Galinska-Rakoczy A, Lehman W, Mulvihill D. (2010) 'The recruitment of acetylated and unacetylated tropomyosin to distinct actin polymers permits the discrete

regulation of specific myosins in fission yeast', *Journal of Cell Science*, 123, pp. 3235–3243. doi: 10.1242/jcs.069971.

Courtemanche, N., Pollard, T. D. and Chen, Q. (2016) 'Avoiding artifacts when counting polymerized actin in live cells with Lifeact-fluorescent fusion proteins', *Nat Cell Biol*. doi: 10.1038/ncb3351.

Culley S, Tosheva KL, Matos Pereira P, Henriques R (2018) 'SRRF: Universal live-cell super-resolution microscopy', *International Journal of Biochemistry and Cell Biology*, pp. 74–79. doi: 10.1016/j.biocel.2018.05.014.

Van Damme P, Lasa M, Polevoda B, Gazquez C, Elosegui-Artola A, Kim DS, De Juan-Pardo E, Demeyer K, Hole K, Larrea E, Timmerman E, Prieto J, Arnesen T, Sherman F, Gevaert K, Aldabe R. (2012) 'N-terminal acetylome analyses and functional insights of the N-terminal acetyltransferase NatB', *Proceedings of the National Academy of Sciences*, 109, pp. 12449–12454. doi: 10.1073/pnas.1210303109.

Van Damme P, Hole K, Gevaert K, Arnesen T (2015) 'N-terminal acetylome analysis reveals the specificity of Naa50 (Nat5) and suggests a kinetic competition between N-terminal acetyltransferases and methionine aminopeptidases', *Proteomics*, 15, pp. 2436–2446. doi: 10.1002/pmic.201400575.

Van Damme P, Kalvik TV, Starheim KK, Jonckheere V, Myklebust LM, Menschaert G, Varhaug JE, Gevaert K, Arnesen T (2016) 'A Role for Human N-alpha Acetyltransferase 30 (Naa30) in Maintaining Mitochondrial Integrity', *Molecular & Cellular Proteomics*, 15, pp. 3361–3372. doi: 10.1074/mcp.M116.061010.

De Los Santos C, Chang CW, Mycek MA, Cardullo RA (2015) 'FRAP, FLIM, and FRET: Detection and analysis of cellular dynamics on a molecular scale using fluorescence microscopy', *Molecular Reproduction and Development*. doi: 10.1002/mrd.22501.

Dikiy, I. and Eliezer, D. (2014) 'N-terminal Acetylation stabilizes N-terminal Helicity in Lipid- and Micelle-bound α-Synuclein and increases its affinity for Physiological Membranes', *Journal of Biological Chemistry*, 289(6), pp. 3652–3665. doi: 10.1074/jbc.M113.512459.

Dimitrov, D. S. (2012) 'Therapeutic proteins', *Methods in Molecular Biology*. Humana Press, Totowa, NJ, 899, pp. 1–26. doi: 10.1007/978-1-61779-921-1_1.

Dinh TV, Bienvenut WV, Linster E, Feldman-Salit A, Jung VAinnel T, Hell R, Giglione C, Wirtz M (2015) 'Molecular identification and functional characterization of the first N-acetyltransferase in plastids by global acetylome profiling', *Proteomics*, 15, pp. 2426–2435. doi: 10.1002/pmic.201500025.

Drazic A, Myklebust LM, Ree R, Arnesen T. (2016) 'The world of protein acetylation', *BBA - Proteins and Proteomics*, 1864, pp. 1372–1401. doi: 10.1016/j.bbapap.2016.06.007.

Drazic A, Aksnes H, Marie M, Boczkowska M, Varland S, Timmerman E, Foyn H, Glomnes N, Rebowski G, Impens F, Gevaert K, Dominguez R, Arnesen T (2018) 'NAA80 is actin's N-terminal acetyltransferase and regulates cytoskeleton assembly and cell motility', *Proceedings of the National Academy of Sciences*, p. 201718336. doi: 10.1073/pnas.1718336115.

East DA, Sousa D, Martin SR, Edwards TA, Lehman W, Mulvihill DP (2011) 'Altering the stability of the Cdc8 overlap region modulates the ability of this tropomyosin to bind cooperatively to actin and regulate myosin.', *Biochem J*. 438 pp. 265-73. doi: 10.1042/BJ20101316.

Eastwood TA, Baker K, Brooker HR, Frank S, Mulvihill DP. (2017) 'An enhanced recombinant amino-terminal acetylation system and novel *in vivo* high-throughput screen for molecules affecting α-synuclein oligomerisation', *FEBS Letters*. Wiley-Blackwell, 591(6), pp. 833–841. doi: 10.1002/1873-3468.12597.

Ettinger, A. and Wittmann, T. (2014) 'Fluorescence live cell imaging', *Methods in Cell Biology*, 123, pp. 77–94. doi: 10.1016/B978-0-12-420138-5.00005-7.

Fauvet B, Fares MB, Samuel F, Dikiy I, Tandon A, Eliezer D, Lashuel HA. (2012) 'Characterization of semisynthetic and naturally N α- acetylated α-synuclein in vitro and in intact cells: Implications for aggregation and cellular properties of α-synuclein', *Journal of Biological Chemistry*, 287(34), pp. 28243–28262. doi: 10.1074/jbc.M112.383711.

Fay, D. S. (2013) 'Classical genetic methods', *WormBook*. WormBook, pp. 1–58. doi: 10.1895/wormbook.1.165.1.

Fiske M, White M, Valtierra S, Herrera S, Solvang K, Konnikova A, Debburman S. (2011) 'Familial Parkinson's Disease Mutant E46K α -Synuclein Localizes to Membranous Structures, Forms Aggregates, and Induces Toxicity in Yeast Models', *ISRN Neurology*, 2011, pp. 1–14. doi: 10.5402/2011/521847.

Fusco G, Pape T, Stephens AD, Mahou P, Costa AR, Kaminski CF, Kaminski Schierle GS, (2016) 'Structural basis of synaptic vesicle assembly promoted by a-synuclein', *Nature Communications*, 7. doi: 10.1038/ncomms12563.

GE Healthcare (2015) 'Size exclusion chromatography columns and media Selection guide', pp. 1–12. doi: 10.1111/j.1467-8330.1974.tb00606.x.

Goris M, Magin RS, Foyn H, Myklebust LM, Varland S, Ree R, Drazic A, Bhambra P, Støve SI, Baumann M, Haug BE, Marmorstein R, Arnesen T (2018) 'Structural determinants and cellular environment define processed actin as the sole substrate of the N-terminal acetyltransferase NAA80', *Proceedings of the National Academy of Sciences*, 1, p. 201719251. doi: 10.1073/pnas.1719251115.

Griesbeck O, Baird GS, Campbell RE, Zacharias DA, Tsien RY. (2001) *Reducing the Environmental Sensitivity of Yellow Fluorescent Protein: Mechanism and Applications*. JBC Papers in Press. Available at: http://www.jbc.org/.

Guerrero-Ferreira R, Taylor NM, Mona D, Ringler P, Lauer ME, Riek R, Britschgi M, Stahlberg H. (2018) 'Cryo-EM structure of alpha-synuclein fibrils', *eLife*, 7. doi: 10.7554/eLife.36402.

Hart, A. C. (2006) 'Behavior', in *The C. elegans Research Community,WormBook*. WormBook, pp. 211–216. doi: 10.1895/wormbook.1.87.1.

Hebron, M. L., Lonskaya, I. and E-H Moussa, C. (2013) 'Nilotinib reverses loss of dopamine neurons and improves motor behavior via autophagic degradation of a-synuclein in

Parkinson's disease models', *Human Molecular Genetics*. doi: 10.1093/hmg/ddt192.

Hole K, Van Damme P, Dalva M, Aksnes H, Glomnes N, Varhaug JE, Lillehaug JR, Gevaert K, Arnesen T. (2011) 'The human N-Alpha-acetyltransferase 40 (hNaa40p/hNatD) is conserved from yeast and N-terminally acetylates histones H2A and H4', *PLoS ONE*, 6. doi: 10.1371/journal.pone.0024713.

Huang J, Wang H, Chen Y, Wang X, Zhang H. (2012) 'Residual body removal during spermatogenesis in C. elegans requires genes that mediate cell corpse clearance.', *Development*, 139, pp. 4613–22. doi: 10.1242/dev.086769.

Johnson M, Coulton AT, Geeves MA, Mulvihill DP (2010) 'Targeted amino-terminal acetylation of recombinant proteins in E. coli', *PLoS ONE*, 5, p. 15801. doi: 10.1371/journal.pone.0015801.

Jost, A. P. T. and Weiner, O. D. (2015) 'Probing Yeast Polarity with Acute, Reversible, Optogenetic Inhibition of Protein Function', *ACS Synthetic Biology*, 4, pp. 1077–1085. doi: 10.1021/acssynbio.5b00053.

Ju J, Chen A, Deng Y, Liu M, Wang Y, Wang Y, Nie M, Wang C, Ding H, Yao B, Gui T, Li X, Xu Z, Ma C, Song Y, Kvansakul M, Zen K, Zhang CY, Luo C, Fang M, Huang DCS, Allis CD, Tan R1,, Zeng CK, Wei J, Zhao Q (2017) 'NatD promotes lung cancer progression by preventing histone H4 serine phosphorylation to activate Slug expression', *Nature Communications*, 8. doi: 10.1038/s41467-017-00988-5.

Kalvik, T. V. and Arnesen, T. (2013) 'Protein N-terminal acetyltransferases in cancer', *Oncogene*. Nature Publishing Group, 32, pp. 269–276. doi: 10.1038/onc.2012.82.

Kim, W. S., Kagedal, K. and Halliday, G. M. (2014) 'Alpha-synuclein biology in Lewy body diseases', *Alzheimer's Research and Therapy*, pp. 1–9. doi: 10.1186/s13195-014-0073-2.

Klucken J, Outeiro TF, Nguyen P, McLean PJ, Hyman BT. (2006) 'Detection of novel intracellular-synuclein oligomeric species by fluorescence lifetime imaging', *Research Communication J*, 20, pp. 2050–2057. doi: 10.1096/fj.05-5422com.

Koebnik, R., Locher, K. P. and Van Gelder, P. (2000) 'Structure and function of bacterial outer membrane proteins: barrels in a nutshell', *Molecular microbiology*, 37, pp. 239–253. doi: 10.1016/0029-554X(70)90374-5.

L. Hebron, M. (2014) 'Tyrosine Kinase Inhibition Regulates Early Systemic Immune Changes and Modulates the Neuroimmune Response in α-Synucleinopathy', *Journal of Clinical & Cellular Immunology*, 05, p. 259. doi: 10.4172/2155-9899.1000259.

Levskaya A, Weiner OD, Lim WA, Voigt CA. (2009) 'Spatiotemporal control of cell signalling using a light-switchable protein interaction', *Nature*, 461, pp. 997–1001. doi: 10.1038/nature08446.

Li, L. and Yang, X.-J. (2000) 'Tubulin acetylation: responsible enzymes, biological functions and human diseases', *Cellular and Molecular Life Sciences*, 72. doi: 10.1007/s00018-015-2000-5.

Liszczak G, Goldberg JM, Foyn H, Petersson EJ, Arnesen T, Marmorstein R. (2013) 'Molecular

basis for N-terminal acetylation by the heterodimeric NatA complex', *Nature Structural and Molecular Biology*, 20, pp. 1098–1105. doi: 10.1038/nsmb.2636.

Lööv C, Scherzer CR, Hyman BT, Breakefield XO, Ingelsson M. (2016) 'α-Synuclein in Extracellular Vesicles: Functional Implications and Diagnostic Opportunities', *Cellular and Molecular Neurobiology*, pp. 437–448. doi: 10.1007/s10571-015-0317-0.

Lopez, D. (2015) 'Molecular composition of functional microdomains in bacterial membranes', *Chemistry and Physics of Lipids*, 192, pp. 3–11. doi: 10.1016/j.chemphyslip.2015.08.015.

Malnou, C. E., Bonnaud, E. M. and Suberbielle, E. (2016) 'Histone acetylation in neuronal (dys)function', *BioMol Concepts*, 7, pp. 103–116. doi: 10.1515/bmc-2016-0002.

Maltsev, A. S., Ying, J. and Bax, A. (2012) 'Impact of N-terminal acetylation of α-synuclein on its random coil and lipid binding properties', *Biochemistry*, 51, pp. 5004–5013. doi: 10.1021/bi300642h.

Markwardt M, Kremers GJ, Kraft CA, Ray K, Cranfill PJ, Wilson KA, Day RN, Wachter RM, Davidson MW, Rizzo MA. (2011) 'An Improved Cerulean Fluorescent Protein with Enhanced Brightness and Reduced Reversible Photoswitching', *PLoS ONE*, 6, p. 17896. doi: 10.1371/journal.pone.0017896.

McNulty, B. C., Young, G. B. and Pielak, G. J. (2006) 'Macromolecular crowding in the Escherichia coli periplasm maintains α-synuclein disorder', *Journal of Molecular Biology*, 355, pp. 893–897. doi: 10.1016/j.jmb.2005.11.033.

Mentes A, Huehn A, Liu X, Zwolak A, Dominguez R, Shuman H, Ostap EM, Sindelar CV (2018) 'High-resolution cryo-EM structures of actin-bound myosin states reveal the mechanism of myosin force sensing', *Proceedings of the National Academy of Sciences*, p. 201718316. doi: 10.1073/pnas.1718316115.

Moradi M, Sivadasan R, Saal L, Lüningschrör P, Dombert B, Rathod RJ, Dieterich DC, Blum R, Sendtner M. (2017) 'Differential roles of α-, β-, and γ-actin in axon growth and collateral branch formation in motoneurons', *The Journal of cell biology*, 216, pp. 793–814. doi: 10.1083/jcb.201604117.

Nguyen KT, Mun SH, Lee CS, Hwang CS (2018) 'Control of protein degradation by N-terminal acetylation and the N-end rule pathway', *Experimental & Molecular Medicine*, 50, p. 91. doi: 10.1038/s12276-018-0097-y.

Outeiro TF, Putcha P, Tetzlaff JE, Spoelgen R, Koker M, Carvalho F, Hyman BT, McLean PJ. (2008) 'Formation of toxic oligomeric α-synuclein species in living cells', *PLoS ONE*, 3(4). doi: 10.1371/journal.pone.0001867.

Paleologou, K. E. and El-Agnaf, O. M. A. (2012) 'α-Synuclein Aggregation and Modulating Factors', in *Protein Aggregation and Fibrillogenesis in Cerebral and Systemic Amyloid Disease*, pp. 109–164. doi: 10.1007/978-94-007-5416-4_6.

Parsons JB, Frank S, Bhella D, Liang M, Prentice MB, Mulvihill DP, Warren MJ. (2010) 'Synthesis of Empty Bacterial Microcompartments, Directed Organelle Protein

Incorporation, and Evidence of Filament-Associated Organelle Movement', *Molecular Cell*, 38, pp. 305–315. doi: 10.1016/j.molcel.2010.04.008.

Perrin, B. J. and Ervasti, J. M. (2010) 'The actin gene family: Function follows isoform', *Cytoskeleton*, 67(10), pp. 630–634. doi: 10.1002/cm.20475.

Peter, M. and Ameer-Beg, S. M. (2004) 'Imaging molecular interactions by multiphoton FLIM', *Biology of the Cell*, 96, pp. 231–236. doi: 10.1016/j.biolcel.2003.12.006.

Pirc, K. and Ulrih, N. P. (2015) 'α-Synuclein interactions with phospholipid model membranes: Key roles for electrostatic interactions and lipid-bilayer structure', *BBA - Biomembranes*, 1848, pp. 2002–2012. doi: 10.1016/j.bbamem.2015.06.021.

Polevoda, B., Arnesen, T. and Sherman, F. (2009) 'A synopsis of eukaryotic Nα-terminal acetyltransferases: nomenclature, subunits and substrates', *BMC Proceedings*, 3, p. S2. doi: 10.1186/1753-6561-3-s6-s2.

Pollard, T. D. (2016) 'Actin and actin-binding proteins', *Cold Spring Harbor Perspectives in Biology*, 8. doi: 10.1101/cshperspect.a018226.

Pratt MR, Abeywardana T, Marotta NP. (2015) 'Synthetic Proteins and Peptides for the Direct Interrogation of α-Synuclein Posttranslational Modifications', *Biomolecules*, 5, pp. 1210–1227. doi: 10.3390/biom5031210.

Prigsheim T, Jette N, Frolkis A, S. T. D. L. (2014) 'The Prevalence of Parkinson's disease: A systematic review and meta-analysis', *Movement Disorders*, 29, pp. 1583–1590. doi: 10.1002/mds.26643.

Ree, R., Varland, S. and Arnesen, T. (2018) 'Spotlight on protein N-terminal acetylation', *Experimental & Molecular Medicine*, 50, p. 90. doi: 10.1038/s12276-018-0116-z.

Ren G, Wang X, Hao S, Hu H, Wang CC. (2007) 'Translocation of-Synuclein Expressed in Escherichia coli', *JOURNAL OF BACTERIOLOGY*, 189(7), pp. 2777–2786. doi: 10.1128/JB.01406-06.

Reusch, R. N. (2012) 'Insights into the structure and assembly of Escherichia coli outer membrane protein A', *FEBS Journal*, pp. 894–909. doi: 10.1111/j.1742-4658.2012.08484.x.

Ritchie, C. M. and Thomas, P. J. (2012) 'Alpha-synuclein truncation and disease', *Health*, 04, pp. 1167–1177. doi: 10.4236/health.2012.431175.

Rope AF, Wang K, Evjenth R, Xing J, Johnston JJ, Swensen JJ, Johnson WE, Moore B, Huff CD, Bird LM, Carey JC, Opitz JM, Stevens CA, Jiang T, Schank C, Fain HD, Robison R, Dalley B, Chin S, South ST, Pysher TJ, Jorde LB, Hakonarson H, Lillehaug JR, Biesecker LG, Yandell M, Arnesen T, Lyon GJ. (2011) 'Using VAAST to Identify an X-Linked Disorder Resulting in Lethality in Male Infants Due to N-Terminal Acetyltransferase Deficiency', *The American Journal of Human Genetics*, 89, pp. 28–43. doi: 10.1016/j.ajhg.2011.05.017.

Rosano, G. L. and Ceccarelli, E. A. (2014) 'Recombinant protein expression in Escherichia coli: Advances and challenges', *Frontiers in Microbiology*. doi: 10.3389/fmicb.2014.00172.

Ross, C. A. and Poirier, M. A. (2004) 'Protein aggregation and neurodegenerative disease',

Nat Med. doi: 10.1038/nml066.

Rothfield, L. I., Shih, Y.-L. and King, G. (2001) *Minireview Polar Explorers: Membrane Proteins that Determine Division Site Placement*, *Cell*. Available at: https://www.cell.com/action/showPdf?pii=S0092-8674%2801%2900432-9 .

Ruzafa D, Hernandez-Gomez YS, Bisello G, Broersen K, Morel B, Conejero-Lara F. (2017) 'The influence of N-terminal acetylation on micelle-induced conformational changes and aggregation of α-Synuclein', *PLoS ONE*, 12. doi: 10.1371/journal.pone.0178576.

Safarian S, Rajendran C, Müller H, Preu J, Langer JD, Ovchinnikov S, Hirose T, Kusumoto T, Sakamoto J, Michel H. (2016) 'Structure of a bd oxidase indicates similar mechanisms for membrane integrated oxygen reductases', *Science*, 352, pp. 583–586. doi: 10.1126/science.aaf2477.

Saunier C, Støve SI, Popp B, Gérard B, Blenski M, AhMew N, de Bie C, Goldenberg P, Isidor B, Keren B, Leheup B, Lampert L, Mignot C, Tezcan K, Mancini GM, Nava C, Wasserstein M, Bruel AL, Thevenon J, Masurel A, Duffourd Y, Kuentz P, Huet F, Rivière JB, van Slegtenhorst M, Faivre L, Piton A, Reis A, Arnesen T, Thauvin-Robinet C, Zweier C. (2016) 'Expanding the Phenotype Associated with NAA10-Related N-Terminal Acetylation Deficiency', *Human Mutation*, 37, pp. 755–764. doi: 10.1002/humu.23001.

Schiza V, Molina-Serrano D, Kyriakou D, Hadjiantoniou A, Kirmizis A. (2013) 'N-alpha-terminal Acetylation of Histone H4 Regulates Arginine Methylation and Ribosomal DNA Silencing', *PLoS Genet*, 9, p. 1003805. doi: 10.1371/journal.pgen.1003805.

Schmid AW, Fauvet B, Moniatte M, Lashuel HA. (2013) 'Alpha-synuclein Post-translational Modifications as Potential Biomarkers for Parkinson Disease and Other Synucleinopathies', *Molecular & Cellular Proteomics*. MCP Papers in Press, 12, pp. 3543–3558. doi: 10.1074/mcp.R113.032730.

Setty SR, Strochlic TI, Tong AH, Boone C, Burd CG. (2004) 'Golgi targeting of Arf-like GTPase Arl3p requires its Nα-acetylation and the integral membrane protein Sys1p', *Nature Cell Biology*, 6, pp. 414–419. doi: 10.1038/ncb1121.

Shaner NC, Campbell RE, Steinbach PA, Giepmans BN, Palmer AE, Tsien RY. (2004) 'Improved monomeric red, orange and yellow fluorescent proteins derived from Discosoma sp. red fluorescent protein', *Nature Biotechnology*, 22, pp. 1567–1572. doi: 10.1038/nbt1037.

Shaner NC1, Lambert GG, Chammas A, Ni Y, Cranfill PJ, Baird MA, Sell BR, Allen JR, Day RN, Israelsson M, Davidson MW, Wang J. (2013) 'A bright monomeric green fluorescent protein derived from Branchiostoma lanceolatum', *Nature Methods*, 10, pp. 407–409. doi: 10.1038/nmeth.2413.

Sheikh TI, de Paz AM, Akhtar S, Ausió J, Vincent JB. (2017) 'MeCP2_E1 N-terminal modifications affect its degradation rate and are disrupted by the Ala2Val Rett mutation', *Human Molecular Genetics*, 26, pp. 4132–4141. doi: 10.1093/hmg/ddx300.

Shyu YJ, Liu H, Deng X, Hu CD. (2006) 'Identification of new fluorescent protein fragments for bimolecular fluorescence complementation analysis under physiological conditions', *BioTechniques*, 40, pp. 61–66. doi: 10.2144/000112036.

Snead, D. and Eliezer, D. (2014) 'Alpha-Synuclein Function and Dysfunction on Cellular Membranes', *Experimental Neurobiology*, 23, p. 292. doi: 10.5607/en.2014.23.4.292.

Sochacki KA, Shkel IA, Record MT, Weisshaar JC. (2011) 'Protein Diffusion in the Periplasm of E. coli under Osmotic Stress', *Biophysj*, 100, pp. 22–31. doi: 10.1016/j.bpj.2010.11.044.

Sohlenkamp, C. and Geiger, O. (2016) 'Bacterial membrane lipids: diversity in structures and pathways', *FEMS Microbiology Reviews*, 008, pp. 133–159. doi: 10.1093/femsre/fuv008.

Starheim, K. K., Gevaert, K. and Arnesen, T. (2012) 'Protein N-terminal acetyltransferases: when the start matters', *Trends in Biochemical Sciences*, 37, pp. 152–161. doi: 10.1016/j.tibs.2012.02.003.

Stetefeld, J., McKenna, S. A. and Patel, T. R. (2016) 'Dynamic light scattering: a practical guide and applications in biomedical sciences', *Biophysical Reviews*, pp. 409–427. doi: 10.1007/s12551-016-0218-6.

Stiernagle, T. (2006) 'Maintenance of C. elegans', *WormBook*. doi: 10.1895/wormbook.1.101.1.

Szeto TH, Rowland SL, Rothfield LI, King GF. (2002) 'Membrane localization of MinD is mediated by a C-terminal motif that is conserved across eubacteria, archaea, and chloroplasts', *Proceedings of the National Academy of Sciences*, 99, pp. 15693–15698. doi: 10.1016/S0361-1124(75)80066-9.

Toettcher J Gong D Lim W Weiner O (2011) Llight control of plasma membrane recruitment using the phy-pif system', *Methods Enzymol*, pp. 409–423.

Toyofuku, M., Nomura, N. and Eberl, L. (2019) 'Types and origins of bacterial membrane vesicles', *Nature Reviews Microbiology*. 17, pp. 13–24. doi: 10.1038/s41579-018-0112-2.

Trexler, A. J. and Rhoades, E. (2012) 'N-terminal acetylation is critical for forming a-helical oligomer of a-synuclein', *Protein Science*, 21, pp. 601–605. doi: 10.1002/pro.2056.

Varkey J, Isas JM, Mizuno N, Jensen MB, Bhatia VK, Jao CC, Petrlova J, Voss JC, Stamou DG, Steven AC, Langen R. (2010) 'Membrane curvature induction and tubulation are common features of synucleins and apolipoproteins', *Journal of Biological Chemistry*, 285, pp. 32486–32493. doi: 10.1074/jbc.M110.139576.

Varshavsky, A. (2011) 'The N-end rule pathway and regulation by proteolysis', *Protein Science*, pp. 1298–1345. doi: 10.1002/pro.666.

Wallace, W., Schaefer, L. H. and Swedlow, J. R. (2001) 'A workingperson's guide to deconvolution in light microscopy', *BioTechniques*, pp. 1076–1097. doi: 11730015.

Wang W, Perovic I, Chittuluru J, Kaganovich A, Nguyen LT, Liao J, Auclair JR, Johnson D, Landeru A, Simorellis AK, Ju S, Cookson MR, Asturias FJ, Agar JN, Webb BN, Kang C, Ringe D, Petsko GA, Pochapsky TC, Hoang QQ. (2011) 'A soluble -synuclein construct forms a dynamic tetramer', *Proceedings of the National Academy of Sciences*, 108, pp. 17797–17802. doi: 10.1073/pnas.1113260108.

Yang, X. J. (2004) 'The diverse superfamily of lysine acetyltransferases and their roles in

leukemia and other diseases', *Nucleic Acids Research*, pp. 959–976. doi: 10.1093/nar/gkh252.

Yutaka Kodama and Hu, C.-D. (2010) 'An improved bimolecular fluorescence complementation assay with a high signal-to-noise ratio', *Bio Techniques*, 49, pp. 793–805. doi: 10.2144/000113519.